

# **Novel applications of advanced optical microscopy for microbiology**

**Liam Mark Rooney**

Submitted in fulfilment of the requirements for the degree of Doctor of Philosophy

Strathclyde Institute of Pharmacy and Biomedical Sciences

Faculty of Science

University of Strathclyde

March 2020

*For Michael, Michael and Mamie*



# Declaration of authenticity and author's rights

This thesis is the result of the author's original research. It has been composed by the author and has not been previously submitted for examination which has led to the award of a degree.

Collaborations with other researchers have been identified and credited where appropriate in the text, and stated clearly for each Chapter below;

- Chapter 2 – the background correction pipeline for IRM data was developed and written specifically for this project by Lisa Kölln (University of Strathclyde, UK). All background corrected in figures presented in Chapter 2 were performed by the Author.

The analysis scripts for the model lens specimen used in Chapter 2 were developed and written by Ross Scrimgeour (University of Strathclyde, UK). Analysis of lens specimens was carried out in collaboration with Dr. Scrimgeour.

*Myxococcus xanthus* strains were kindly gifted by Prof. Lotte Sogaard-Andersen (Max Planck Institute for Terrestrial Microbiology, Germany).

- Chapter 3 – *Escherichia coli* JM105-miniTn7 strains were provided by Ainsley Beaton (University of Strathclyde, UK). The pJM058 plasmid (arabinose biosensor) was gifted by Dr. Nicola Holden (James Hutton Institute, UK).
- Chapter 4 – Dr. Lionel Dupuy (James Hutton Institute, UK) provided a small batch of unprocessed Nafion pre-cursors and an aliquot of sulphorhodamine-B-stained transparent soil. Cryomilling was performed by the Author in Dr. Dupuy's lab, and all subsequent work was carried out by the Author at the University of Strathclyde.

Figure legends also indicate where figures have been adapted or reproduced from previously published works, and appropriate citation is provided in agreement with publisher guidelines and copyright law.

Permission was granted from publishers where reproduced figures were not originally published under an Open Access Creative Commons licence. Specifically, these agreements are in reference to Figure 1.2c (Springer Nature: Nature Protocols – licence number 4834211316065) and Figure 1.16b (Annual Reviews, Inc.: Annual Review of Microbiology – licence number 1036737-1).

The copyright of this thesis belongs to the author under the terms of the United Kingdom Copyright Acts as qualified by University of Strathclyde Regulation 3.50. Due acknowledgement must always be made of the use of any material contained in, or derived from, this thesis.

A handwritten signature in black ink, appearing to read 'L. Rooney', with a long horizontal flourish extending to the right.

Liam Mark Rooney

21<sup>st</sup> May 2020

# Abstract

The study of bacteria often requires visualisation by optical microscopy, but the use of advanced optical microscopy methods is uncommon by many microbiologists. Therefore, there remains many areas of microbiology which require exploration using newly developed techniques. This thesis describes the application of advanced optical microscopy methods to three distinct microbiological questions centred on bacterial gliding motility, the spatial organisation of biofilms, and the growth of bacteria in a mimetic three-dimensional (3D) culture environment.

The gliding motility of *Myxococcus xanthus* has been described as a lateral process, and it was unclear if single bacteria were capable of moving in three dimensions. This was due to three-dimensional imaging of bacteria often being unachievable by optical methods due to the height of a bacterial cell being on the order as the axial resolution of the conventional optical microscope. To overcome this a novel variant of the live-cell label-free technique, interference reflection microscopy (IRM), was developed. This method relies on the interference of multiple wavelengths of incident and reflected light and results in a series of intensity maxima and minima which encode 3D information. A specimen of known geometry was used to characterise this method before application to gliding *M. xanthus* cells. Multi-wavelength confocal IRM revealed that *M. xanthus* exhibited aperiodic oscillations during gliding, which challenged the theory that gliding motility was a lateral phenomenon. By use of deleterious mutants, it was deduced that the oscillatory behaviours were not linked to the main driving force of gliding, proton motive force. A hypothesis was proposed which suggested that these behaviours were caused by recoil and force transmission along the cell body following firing of the Type IV pili.

Bacterial biofilms have been studied by conventional microscopy methods for over 50 years; however due to a technology gap, the structure of large microbial aggregates remained unclear. The development of the Mesolens, an optical system which uniquely allows simultaneous imaging of individual bacteria over a 36 mm<sup>2</sup> field of view, enabled the study of mature *Escherichia coli* macro-colony biofilm architecture like never before. The Mesolens enabled the discovery of intra-colony channels on the order of 10 µm in diameter that are integral to *E. coli* macro-colony biofilms and form as an emergent property of biofilm growth. These channels have a characteristic structure and reform after total mechanical disaggregation of the colony, facilitate transport of particles, and play a role in the acquisition of and distribution of nutrients through the biofilm. Furthermore, intra-colony channels potentially offer a previously unobserved route for the delivery of dispersal agents or antimicrobial drugs to biofilms, which would ultimately lower their impact on public health and industry.

The practice of bacterial culture has remained unchanged for over a century. Therefore, almost all observations of bacterial behaviour have been made using synthetic laboratory condition which are not representative of the natural environment. To address this, a mimetic 3D transparent soil culture medium was fabricated and designed specifically for bacterial culture. This novel culture medium was optimised for two wide-ranging genera of soil bacteria, *Streptomyces coelicolor* and *Bacillus subtilis*. Following careful design of the transparent soil platform, each strain was imaged using the Mesolens to provide a better understanding of how they colonised their natural habitat. Each species was found to colonise the surface of soil independently of their growth behaviours on traditional two-dimensional culture methods. Moreover, the viability of bacteria grown in transparent soil was found to be uncompromised. Therefore, transparent soil stands as a readily tailored platform for

bacterial culture and is compatible with any optical microscope to study bacterial behaviours in a mimetic soil environment.

# Acknowledgements

I have a lot of people to thank for getting me where I am today. My family, friends, colleagues, those who have guided and mentored me, encouraged me, and supported me. It's difficult to put into words how thankful I am to those who have been on this journey with me, but I'll try my best. I've been told numerous times that I like to waffle when I write, but this is the one time I don't think I can cut back. Bear with me... it's a long one!

First of all, I thank Gail. Gail is perhaps one of the most modest people I know, and I can already see her breathing into a pretend paper bag and wincing in anticipation as to what I'm about to write. I've been truly lucky to have Gail as a supervisor over the past three and a half years. She has taught me everything I know about physics, microscopy, academia, gin, and how to (unsuccessfully) hide my glaikit facial expressions during meetings. Gail has been a constant source of encouragement throughout my time at Strathclyde. She has provided me with countless opportunities to present my work, meet new people, attend conferences, supervise students, contribute to grants and afforded me the freedom to collaborate on exciting projects. She works incredibly hard and has always had the best intentions of her group in mind, pushing them forward and championing them whenever possible. She is one of the most selfless academics I know, and I respect her greatly because of it. I know that as I move on from Strathclyde that I do so a greater scientist because of Gail. I don't think I could have done it without her motivation and guidance. Thank you.

I also thank Hoskie. It's unusual for a second supervisor to invest so much time and resource in a student, but since day one Paul has made me feel like part of the family. Having not only come to physics as a complete novice, I also was by no means a microbiologist. I thank Paul for all of his patience, guidance and, again, the numerous

opportunities he has put me forward for. I don't think I've ever been to a meeting with Paul where he hasn't taken the time to introduce me to the most illustrious PI in the room, or a time where he's let my pint glass run dry. So, Paul, thank you for all of your input and help over the past few years, and for making it a wee bit easier to accept my new identity as a microbiologist.

Thank you to Brad. Brad has been a wise and all-knowing figure during my PhD, and at times I've thought of him as a third supervisor. I don't think I've ever asked him about a problem which he hasn't either conjured up a hand-fashioned instrument to solve it or explained the solution by means of an insightful personal anecdote. He has been a steering hand since the start of my PhD (since I unwittingly explained to him how a confocal works during my interview), and I thank him for his valuable insights, fruitful discussions and contributions to my work. Additionally, I'd like to thank Brad for his uncanny catalogue of impersonations and entertaining stories during his visits to Glasgow and in Plymouth. I also thank him for maintaining control of his handbrake when reverse parking at the Queen Anne's Battery Marina in Plymouth while I was squished in the back of his car.

I would like to thank the other PIs of HW Level 6 for building a friendly and open research environment, which isn't always easy to come by. Thank you to Nick Tucker, Kate Duncan, Arnaud Javelle, and Iain Hunter. Thank you to Paul Herron for letting me rip apart and rebuild your widefield system, for your (many) experimental suggestions, and for being subjugated to my progress reports over the years. Thank you to Morgan Feeney, who is one of the most knowledgeable microbiologists I know, for her manuscript advice and experimental suggestions. Many thanks to John Dempster, who has kept the MesoScan and MesoCam software alive without which the Mesolens would have been be a much more difficult beast to tackle.

Thank you to the many bodies who have given me money to attend meetings, sponsored prizes, supervise students and organise symposia. Thank you to the Royal Microscopical Society, the Microbiology Society, the Society for Applied Microbiology, Medical Research Scotland, the European Organisation for Molecular Biology, the Medical Research Council, the University of Strathclyde, Zeiss and Nikon. Thank you also to the fantastic and generous collaborators I've had the chance to work with over my PhD. Thank you to Lionel Dupuy (James Hutton Institute, Dundee, UK) for his help with the transparent soil. Thank you to Rut-Carballido Lopez (Institut National de la Recherche Agronomique, Paris, France) for the kind donation of the *Bacillus* strains. Thank you to Lotte Søgaaard-Andersen, Dobromir Szadkowski, and Anke Treuner-Lange (Max Planck Institute for Terrestrial Microbiology, Marburg, Germany) and Dave Whitworth (Aberystwyth University, Aberystwyth, UK) for their guidance with the Myxo. Thank you to Margaret O'Prey (CRUK, Beatson Institute, Glasgow, UK) for her help with and kind donation of an Olympus FV1000.

Working between biophotonics (or whatever we're called now!) and microbiology has given me the pleasure of working with a diverse range of talented scientists. This has meant that I'm never far from a friendly face to bounce ideas off of, collaborate with, or have snacks with. Gail's group, past and present, have been incredible to work with. I was welcomed into the group as "the biologist" in 2016, and ever since the others have been patient and understanding, helping me to grasp some basic understanding of physics and microscopy. I only hope I've managed to help teach some biology in return along the way. I thank Calum, Peter, Jan, Jana, Gill, Lee, Katrina, Shannan, Mollie, and Bea. I would also like to extend a special thanks to Lisa "KÖLLN!" and Ross for being particularly patient and for being such great co-authors to work with on our Myxo paper. Thank you to Eliana for explaining so many physics concepts to me and for patiently sense-checking my Introduction. Also, thanks to



David for being a great, although sometimes annoying, office neighbour – I'll think of you fondly whenever I see a 5 kg bag of rice. Thank you all for making the 5<sup>th</sup> floor so fun. Oh, and Mollie, congratulations on your paper (again) and for inviting me to *your* paper celebration!

Working as part of HW601 has been amazing. Thank you to everyone for being so supportive over the years, I'll miss working with such a fantastic group of amazing researchers! There are so many people to thank. Thank you to Molly, Elmira, Eilidh, Darren, Adriana, Lily, Dave, Charlie, Parra, Laia, Ally, Emily, Gordon, Tiago, Sarah, Gaetan, Anna and of course Jonny for making the office so fun, and for countless gins together over the years! Thank you to all the amazing Post Docs who have always been there to answer silly questions and stop me from setting my bench on fire (again). Thank you to Post Docs past and present; John, Stuart, Kirsty, Gillian and Walid. I'd like to specifically thank three of my closest friends from Level 6 for all of their support, guidance, laughs, drinks, good times, and for agreeing to be my bridesmaids. Thank you, Lis, for always being there to listen and helping me solve numerous problems. Thank you for supplying me with Jamón and veggies, and for attempting to teach me Spanish. Thank you to Ainsley, for giving me all those fluorescent strains way back and getting me started, for always coming up with weird and wonderful things to look at under the Mesolens, and for being a wide-legged woman who has always been there to quote obscure early-2000s references with me. Thank you to Becca, for being an amazing bench neighbour over the past 3 years, all the brilliant nights out, hungover sunglasses-adorned keynote lectures and for never making me look like the drunkest person in the room. Thank you for always being there to bounce ideas off of, and for coming up with new and exciting experiments. All three of you are amazing friends and awe-inspiring scientists. I'll really miss working alongside you all every day.

Thank you to my amazing pals Kerry, Olivia, Jonny (again) and Twiggy for all their help during our undergrad, and for listening to me grumble about science for the past three and a half years.

My family have been supportive of everything I've ever done, and they're the reason I've made it this far. Since I was wee I've been given every opportunity to learn and explore whatever areas of science take my fancy. Thank you to Mum and Dad. Thank you for always pushing me to do my homework and making me study, even when I didn't want to. Thank you for all you've given up, all your time, all you've pushed me and all of your patience over the years. I'm really lucky to have two people I can always rely on, and who try their hardest to understand me when I talk about biofilm formation and how microscopes work. Thank you to Michelle and Will. My Auntie Michelle is without-a-doubt, 100% to blame for me becoming a scientist. Thank you for all the trips to museums, science centres, castles and Dynamic Earth, for encouraging my curiosity, and for always offering to read drafts for me. Thank you to both of my Grans, Sandra and Sandra, for all of their support and kindness. Thank you to those who I've lost during my PhD, to my two Papas, Michael and Michael, and to Mamie, to whom this thesis is dedicated to. Your support meant the world to me. Thank you to my adopted families, the Wilsons and the McGaws. Thank you to Sarah, Allan, Kirsty, Callum, Melinda, John, Hayley, Erin, and Finlay. Thank you for always being interested in my work, and for listening to me ramble about science. Thank you to GMa for teaching me how to communicate my work effectively, and to never start a sentence with "so". Thank you everyone.

Finally, thank you to Fraser. Without Fraser I wouldn't have made it to this point. Your support, kindness, motivation, constant enthusiasm and love has kept me going. I'm so lucky to have your encouragement, and I've always been thankful for your patience and understanding. I'm sorry for being so grumpy while writing these past few months.

I don't think I'd have remained sane without having you to ground me and supply me with snacks. You have always been selfless when it comes to my studies. Thank you for pushing me to take every opportunity, apply for every grant, write every word and think about every result. You've helped me more than you can ever know, and far more than I can put into words. Thank you for putting up with me, and for agreeing to spend the rest of our lives together. I hope you realise that you've got many more years of science-talk ahead of you!

Thank you.

\*post-*viva* amendment;

Having prepared for and sat my *viva* during the peak of the SARS-CoV-2 pandemic, I would like to thank my friends and family even more for their support even after writing and submitting my thesis. Also, thank you my examination committee (Seamus Holden, Brian Patton and Christian Wozney) for taking the time to read and provide informed feedback on my thesis, and for giving me an enjoyable online *viva* experience under the strange circumstances.

# Research output

## Published and submitted works (refer to Appendix III)

Rooney, L.M., Kölln, L.S., Scrimgeour, R., Amos, W.B., Hoskisson, P.A., McConnell, G., (2020). Three-Dimensional Observations of an Aperiodic Oscillatory Gliding Behavior in *Myxococcus xanthus* Using Confocal Interference Reflection Microscopy. *mSphere*, **5**; e00846-19. <https://doi.org/10.1128/mSphere.00846-19>.

Rooney, L.M., Amos, W.B., Hoskisson, P.A., McConnell, G., (2020). Intra-colony channels in *E. coli* function as a nutrient uptake system. *ISME J.* <https://doi.org/10.1038/s41396-020-0700-9>.

## Oral presentations

- **Scottish Microscopy Group AGM 2017, Glasgow, November 2017.**

“Applying the Mesolens to Microbiology: visualising biofilm architecture and substructure”

- **Microbiology Society AGM 2018, Birmingham, April 2018.**

“Applying the Mesolens to Microbiology: visualising biofilm architecture and substructure”

- **University of Strathclyde Doctoral School Multidisciplinary Symposium, Glasgow, July 2018.**

“Of Microbes and the Mesolens: Investigating the Internal Architecture of *Escherichia coli* Biofilms”

- **Microbiology Society AGM 2019, Belfast, April 2019.**

“Of microscopes and microbes: the need for new imaging techniques in microbiology”

- **Junior Awards for Microbiology 2018/19, Birmingham, May 2019.**

“Applying the Mesolens to Microbiology: visualising the internal architecture of bacterial biofilms”

*\*Winner of the 2019 Junior Award for Microbiology*

- **Federation of European Microbiology Societies (FEMS) AGM 2019, Glasgow, July 2019.**

“Of microscopes and microbes: characterising a novel nutrient acquisition system in *Escherichia coli* biofilms”

- **Glasgow Imaging Network 2019, Glasgow, August 2019.**

“What can the Mesolens do for microbiologists? Exploring a novel nutrient acquisition system in *E. coli* biofilms”

- **Eurobiofilms 2019, Glasgow, September 2019.**

“Visualising the structure of bacterial communities: characterising a novel nutrient uptake system in *Escherichia coli* biofilms”

- **Midlands Molecular Microbiology Meeting 2019, Nottingham, September 2019.**

“Mesoscopic Microbiology: exploring the inner workings of *E. coli* biofilms using the Mesolens”

- **Aurox online optical microscopy symposium – Aurox Ltd., April 2020.**

“Mesoscopic Microbiology: exploring the inner workings of *E. coli* biofilms using the Mesolens”

## **Poster presentations**

- **Spatiotemporal Organisation of Bacterial Cells, Marburg, March 2018.**

“Interference Reflection Microscopy Shows Novel Insights to Bacterial Gliding Motility”

- **EMBO Practical Course on Advanced Optical Microscopy for Cell Biology, Plymouth, April 2018.**

“Interference Reflection Microscopy Shows Novel Insights to Bacterial Gliding Motility”

*\*Winner of Best Poster*

- **Scottish Universities Life Sciences Association (SULSA) Antimicrobial Resistance Conference, Glasgow, April 2018.**

“Applying the Mesolens to Microbiology: visualising biofilm architecture and substructure”

- **European Light Microscopy Initiative (ELMI) AGM 2018, Dublin, June 2018.**

“Applying the Mesolens to Microbiology: visualising biofilm architecture and substructure” and “Interference Reflection Microscopy Shows Novel Insights to Bacterial Gliding Motility”

- **Frontiers in Bioluminescence 2018, Glasgow, July 2018.**

“Applying the Mesolens to Microbiology: investigating the structural organisation of bacterial biofilms”

- **University of Strathclyde Doctoral School Launch, Glasgow, October 2018.**

“Applying the Mesolens to Microbiology: investigating the structural organisation of bacterial biofilms”

*\*Winner of Best Presentation*

- **Photonex Glasgow 2019, Glasgow, June 2019.**

“Visualising the structure of bacterial communities: characterising a novel nutrient uptake system in *Escherichia coli* biofilms”

- **Federation of European Microbiology Societies (FEMS) AGM 2019, Glasgow, July 2019.**

“Of microscopes and microbes: characterising a novel nutrient acquisition system in *Escherichia coli* biofilms”

# List of figures and tables

## Chapter 1

Figure 1.1. Resolution criteria in optical microscopy

Figure 1.2. Diffraction limited resolution in optical microscopy.

Figure 1.3. Image formation in the compound microscope.

Figure 1.4. Label-free contrast enhancement by dark field, DIC and phase contrast microscopy.

Figure 1.5. Fluorescence excitation and emission

Figure 1.6. Stoke shifts in fluorescence microscopy.

Figure 1.7. Widefield epifluorescence and confocal laser scanning microscopes.

Figure 1.8. Label-free 3D confocal reflection microscopy.

Figure 1.9.  $4\pi$  microscopy as a method of resolution enhancement.

Figure 1.10. Generation of a standing wave by means of a plane reflector.

Figure 1.11. Interference reflection microscopy.

Figure 1.12. High-resolution large FOV imaging using the Mesolens

Figure 1.13. An overview of the confocal laser scanning setup of the Mesolens.

Figure 1.14. The complex lifecycle of *Myxococcus xanthus*.

Figure 1.15. Canonical gliding motility mechanisms in *Myxococcus xanthus*

Figure 1.16. Development and regulation of biofilms.

**Figure 1.17. Extracellular components of *E. coli* which promote biofilm formation**

**Figure 1.18. Population sectoring in mature bacterial biofilms**

**Figure 1.19. The role of cell-cell and cell-surface interactions in biofilm patterning.**

## **Chapter 2**

**Figure 2.1. Schematic of the IRM model.**

**Figure 2.2. Extracting 3D information from 2D IRM image data**

**Figure 2.3. Axial resolution in IRM is independent of numerical aperture.**

**Figure 2.4. Low NA objective lenses can result in erroneous intensity artefacts**

**Figure 2.5. Using multiwavelength IRM to fill the information gap.**

**Figure 2.6. 3D reconstruction of a plano-convex lens specimen**

**Figure 2.7. Improving the axial resolution of IRM using a difference operation**

**Figure 2.8. *Myxococcus xanthus* exhibits 3D gliding behaviours**

**Figure 2.9. Understanding the 3D behaviour of *M. xanthus* during gliding.**

**Figure 2.10. Changing interference fringe patterns are indicative of changing gliding topographies.**

**Figure 2.11. Image correction workflow for IRM data**

**Figure 2.12. Selecting a k-value for IRM background correction**

**Figure 2.13. Image correction does not alter the position of fringe maxima and minima.**

**Figure 2.14. Image correction increases contrast and does not alter the position of intensity peaks.**



**Figure 2.15. Widefield IRM does not provide sufficient contrast to reveal sub-diffraction limited changes in the adhesion profile of gliding bacteria.**

**Figure 2.16. Multi-wavelength confocal IRM reveals axial movements along the cell body during gliding motility.**

**Figure 2.17. Understanding the 3D topography of gliding cells.**

**Figure 2.18. Axial gliding behaviours are independent of PMF-driven motility mechanisms.**

**Figure 2.19. IRM as a method for measuring the velocity of adherent cells.**

**Figure 2.20. Type IV pili deletions prevent cell attachment and are not applicable for study with IRM.**

## **Chapter 3**

**Figure 3.1. Schematic for bacterial culture and imaging mould.**

**Figure 3.2. Schematic of specimen preparation for mesoscopic imaging.**

**Figure 3.3. An overview of the miniTn7 photoprotein system.**

**Figure 3.4. Induction of the arabinose operon.**

**Figure 3.5. GFP production by JM105-pJM058 is dependent on the presence of L-arabinose.**

**Figure 3.6. Identification of an intra-colony channel system in *E. coli* macro-colony biofilms.**

**Figure 3.7. Increasing the quality of widefield mesolens data with deconvolution.**

**Figure 3.8. Confocal laser scanning mesoscopy revealed that intra-colony spatial patterns are not an artefact of the deconvolution process.**

**Figure 3.9. A mature *E. coli* biofilm analysed by BiofilmQ.**

**Figure 3.10. Cells are densely packed along the borders of intra-colony channels**

**Figure 3.11. Spatial resolution is too low to sufficiently resolve intra-colony channels by stereomicroscopy**

**Figure 3.12. Comparison of conventional low-NA widefield epifluorescence microscopy and high-NA mesoscopy.**

**Figure 3.13. Structural assessment of intra-colony channels.**

**Figure 3.14. Intra-colony channels are occupied by a protein-based structural matrix**

**Figure 3.15. Structural fluorescent dyes do not drastically alter the viability of JM105 strains.**

**Figure 3.16. Intra-colony channels form as an emergent property of biofilm formation.**

**Figure 3.17. Intra-colony channels are confined within clonal populations and unable to cross strain boundaries.**

**Figure 3.18. The miniTn7 insert location is conserved between JM105-miniTn7-*gfp* and JM105-miniTn7-*HcRed1***

**Figure 3.19. Fluorescein does not enter macro-colonies via intra-colony channels.**

**Figure 3.20. Intra-colony channels facilitate transport of nanoscopic particles.**

**Figure 3.21. Intra-colony channels play a functional role in nutrient acquisition and transport to the centre of bacterial biofilms.**

**Figure 3.22. Injection of fluorescein into solid medium resulted in rapid diffusion.**

**Figure 3.23. Perfusion of fluorescein into solid medium maintains a higher concentration over time compared to injection**

**Figure 3.24. Fluorescence emission of JM105-pJM058 during diauxic growth conditions.**

**Figure 3.25. Colistin was selected as the appropriate test antibiotic**

**Figure 3.26. Filter rings have comparable antibiotic diffusion properties to filter disks.**

**Figure 3.27. Intra-colony channels can be exploited to facilitate antimicrobial uptake.**

## **Chapter 4**

**Figure 4.1 The developmental lifecycle of Streptomyces**

**Figure 4.2 The chemical structure of Nafion™ co-polymers**

**Figure 4.3 Transparent soil culture method for mesoscopic imaging**

**Figure 4.4. Streptomyces grow as a differentiated mycelium under conventional culture conditions**

**Figure 4.5. *Bacillus subtilis* strains grown using conventional culture methods**

**Figure 4.6. Sulphorhodamine-B labelled transparent soil particles**

**Figure 4.7. Sucrose refractive index curve for Nafion™ refractive index matching**

**Figure 4.8. Determining the carbon auxotrophies of *Bacillus* strains for downstream refractive index matching.**

**Figure 4.9. Refractive index curves of D-xylose and D-arabinose for Nafion™ refractive index matching.**

**Figure 4.10. Refractive index curve of Percoll® for Nafion™ refractive index matching**

**Figure 4.11. Autofluorescence emission and reflection imaging of Nafion™ soils by confocal laser scanning microscopy**

**Figure 4.12. Autofluorescence emission of Nafion™ soils by widefield mesoscopy**

**Figure 4.13. Quantitative analysis of Nafion™ soil autofluorescence using the Mesolens**

**Figure 4.14. Streptomyces grow as hyphal pellets in a transparent soil environment**

**Figure 4.15. *Bacillus subtilis* colonises mimetic soil environments using two different behaviours**

**Figure 4.16. Confocal mesoscopy confirms the two colonisation methods used by *Bacillus subtilis* in a mimetic soil environment**

**Figure 4.17. Bacteria remain viable when cultured in a transparent soil environment**

# List of abbreviations

2D – Two dimensional

2p-RAM – 2-photon random access microscope

2x YT – 2x Yeast-Tryptone

3D – Three dimensional

ABS – Acrylonitrile butadiene styrene

Ag43 – Antigen 43

ATP – Adenosine triphosphate

BGCs – Biosynthetic gene clusters

BSA – Bovine serum albumin

BSAC – British Society for Antimicrobial Chemotherapy

c-di-GMP – cyclic-di-guanosine monophosphate

cAMP – cyclic-adenosine monophosphate

CCD – Charge-coupled device

CFU – Colony-forming units

CFW – Calcofluor-White

CLEM – Correlative light-electron microscopy

CLSM – Confocal laser scanning microscopy

CMLE – Classical maximum likelihood estimation

CMOS – Complementary metal oxide semiconductor

CPU – Central processing units

CRM – Confocal reflection microscopy

DCYE – Double casitone yeast extract

ddH<sub>2</sub>O – deionised distilled H<sub>2</sub>O

DMSO – Dimethyl sulfoxide

DNA – Deoxyribonucleic acid

dNTP – Deoxyribonucleotide triphosphate

ECM – Extracellular matrix

eDNA – extracellular DNA

EDTA – Ethylenediaminetetraacetic acid

EGFP – Enhanced green fluorescent protein

EHEC – Enteropathogenic *Escherichia coli*

EPS – Exopolysaccharide

EUCAST – European Committee on Antimicrobial Standardised Testing

FAC – Focal adhesion complex

FEP – Fluorinated ethylene propylene

FIJI – FIJI is just ImageJ

FITC-WGA – Fluorescein isothiocyanate-wheatgerm agglutinin

FOV – Field of view

FRAP – Fluorescence recovery after photobleaching

FWHM – Full-width half maximum

GFP – green fluorescent protein

I<sup>2</sup>M – Image interference microscopy

I<sup>3</sup>M – Incoherent interference illumination microscopy

I<sup>5</sup>M – I<sup>2</sup>M + I<sup>3</sup>M

IRM – Interference reflection microscopy

iSCAT – Interferometric scattering microscopy

KEGG – Kyoto encyclopaedia of genes and genomes

LB – Luria Bertani/Lysogeny broth

LED – Light emitting diode

LUT – Look up table

MS – Mannitol-Soya

MSCRAMMs – Microbial surface components recognising adhesive matrix molecules

NA – numerical aperture

NTC – No template control

OD<sub>600</sub> – Optical Density (at 600 nm)

OMV – Outer-membrane vesicle

PBS – Phosphate-buffered saline

PCR – Polymerase chain reaction

PI – Propidium iodide

PMF – Proton motive force

PMT – Photomultiplier tube

PSF – Point spread function

RAM – Random access memory

RGB – Red/green/blue

RICM – Reflection interference contrast microscopy

ROS – reactive oxygen species

RPM – Revolutions per minute

RT – Room temperature

SDCM – Spinning disk confocal microscopy

SIM – Structured illumination microscopy

SM – Spizizen minimal

SMLM – Single molecule localisation microscopy

SMM – Supplemented minimal medium

SNR – Signal-to-noise ratio

SPIM – Selective plane illumination microscopy

STED – Stimulated emission depletion

STORM – Stochastic optical reconstruction microscopy

SWFM – Standing wave fluorescence microscopy

T4P – Type IV pili

TAE – Tris:acetate:EDTA

TES - Tris[hydroxymethyl]methyl-2-amino-ethanesulphonic acid

TIRF – Total internal reflection fluorescence

UPEC – Uropathogenic *Escherichia coli*

UV – Ultraviolet

WGA – Wheatgerm agglutinin

YEME – Yeast extract malt extract



# Contents

<b>Chapter 1 Introduction.....</b>	<b>2</b>
<b>1.1 Fundamentals of optical microscopy.....</b>	<b>3</b>
1.1.1 Spatial resolution in optical microscopy .....	3
1.1.2 Contrast generation and enhancement in optical microscopy .....	7
1.1.3 Fluorescence for biological imaging .....	9
<b>1.2 Conventional fluorescence microscopy techniques .....</b>	<b>14</b>
1.2.1 Widefield epifluorescence microscopy .....	14
1.2.2 Confocal laser scanning microscopy .....	15
<b>1.3 Reflection and interference-based microscopy .....</b>	<b>17</b>
1.3.1 Confocal reflection microscopy .....	17
1.3.2 Total internal reflection fluorescence microscopy .....	18
1.3.3 $4\pi$ microscopy .....	19
1.3.4 Standing wave fluorescence microscopy .....	21
1.3.5 Interference reflection microscopy .....	23
<b>1.4 Optical mesoscopy .....</b>	<b>25</b>
1.4.1 The Mesolens .....	25
1.4.2 Other high-resolution, large FOV methods for bioimaging .....	27
<b>1.5 The gliding motility of <i>Myxococcus xanthus</i>.....</b>	<b>29</b>
<b>1.6 An overview of bacterial biofilms .....</b>	<b>33</b>
1.6.1 Bacterial biofilms .....	33
1.6.2 Spatial patterning in bacterial biofilms .....	38
<b>1.7 Microbial soil ecology.....</b>	<b>43</b>
<b>1.8 Research aims and objectives .....</b>	<b>45</b>
<b>Chapter 2 Multi-wavelength confocal interference reflection microscopy reveals novel gliding behaviours in <i>Myxococcus xanthus</i>.....</b>	<b>46</b>
<b>2.1 Introduction .....</b>	<b>47</b>
2.1.1 Bacterial gliding motility.....	47
2.1.2 Background theory for IRM .....	48
2.1.3 Interference reflection microscopy for bacterial imaging .....	50
2.1.4 Experimental aims .....	52
<b>2.2 Materials and Methods .....</b>	<b>52</b>

2.2.1 Bacterial cell culture .....	52
2.2.2 Interference reflection microscopy .....	53
2.2.3 Image processing and analysis .....	54
2.2.3.1 Image processing .....	54
2.2.3.2 Background correction for multi- $\lambda$ IRM data .....	55
2.2.3.3 Lens analysis and reconstruction .....	55
<b>2.3 Results .....</b>	<b>56</b>
2.3.1 Characterisation of a model plano-convex lens specimen for IRM .....	56
2.3.2 Application of multi-wavelength confocal IRM to a model specimen ..	60
2.3.3 Further improving the axial resolution of IRM using a difference operation .....	63
2.3.4 Single-wavelength IRM reveals axial gliding behaviours in <i>M. xanthus</i> .....	65
2.3.6 Multi-wavelength IRM reveals 3D behaviours of gliding bacteria .....	69
2.3.7 Understanding the mechanism behind the aperiodic oscillatory 3D gliding motility of <i>M. xanthus</i> .....	77
<b>2.4 Discussion .....</b>	<b>80</b>
<b>2.5 Conclusions .....</b>	<b>85</b>
<b>Chapter 3 Characterisation of a novel intra-colony channel system in Escherichia coli biofilms using the Mesolens .....</b>	<b>87</b>
<b>3.1 Introduction .....</b>	<b>88</b>
3.1.1 Spatial organisation in bacterial communities .....	88
3.1.2 The Mesolens as a tool for biofilm imaging .....	89
3.1.3 The use of antibiotics for biofilm clearance .....	90
3.1.4 Experimental aims .....	91
<b>3.2 Materials and Methods .....</b>	<b>92</b>
3.2.1 Specimen preparation .....	92
3.2.1.1 Designing and 3D-printing an imaging chamber for biofilm mesoscopy ..	92
3.2.1.2 Bacterial cell culture .....	93
3.2.2 Imaging conditions .....	95
3.2.2.1 Stereomicroscopy .....	95
3.2.2.2 Conventional widefield epifluorescence microscopy .....	95
3.2.2.3 Widefield epifluorescence mesoscopy .....	95
3.2.2.4 Confocal laser scanning mesoscopy .....	96
3.2.3 Characterising the structure of intra-colony channels .....	96
3.2.3.1 Assessment of channel composition by reflection confocal mesoscopy ..	97
3.2.3.2 Determining the distribution of non-viable cells in <i>E. coli</i> biofilms .....	97
3.2.3.3 Determining the distribution of exopolysaccharides in <i>E. coli</i> biofilms ....	98
3.2.3.4 Determining the distribution of cellulose in <i>E. coli</i> biofilms .....	98
3.2.3.5 Determining the distribution of lipids in <i>E. coli</i> biofilms .....	98
3.2.3.6 Determining the distribution of proteins in <i>E. coli</i> biofilms .....	99
3.2.3.7 Viability screening with structural dyes .....	99

3.2.4 Disruption and recovery of intra-colony channel structures .....	100
3.2.5 Strain mixing.....	100
3.2.6 Verification of mini-Tn7 insertion by colony PCR.....	101
3.2.7 Determining the function of intra-colony channels .....	102
3.2.7.1 Fluorescein uptake assay .....	102
3.2.7.2 Fluorescent microsphere uptake assay .....	103
3.2.7.3 Assessing channel-mediated nutrient uptake .....	103
3.2.7.4 Testing intra-colony channel-mediated antibiotic transport.....	107
3.2.8 Image processing and analysis .....	110
<b>3.3 Results .....</b>	<b>112</b>
3.3.1 Identification of a network of intra-colony channels in <i>E. coli</i> biofilms .....	112
3.3.1.1 Intra-colony channels discovered in mature <i>E. coli</i> biofilms.....	112
3.3.1.2 Demonstrating the benefits of mesoscopy for studying biofilm architecture .....	117
3.3.2 A structural assessment of intra-colony channels .....	118
3.3.2.1 Intra-colony channels are not composed of solid growth medium or air .....	118
3.3.2.2 Biofilm channels are not composed of non-viable cells, EPS, cellulose or lipids .....	120
3.3.2.3 Intra-colony channels contain protein.....	122
3.3.2.4 Fluorescent probes used for structural staining have minimal impact on cell viability .....	122
3.3.3 Understanding the formation of intra-colony channels .....	124
3.3.3.1 Channel formation is an emergent property of biofilm formation .....	124
3.3.3.2 Channels are unable to cross strain boundaries in mixed cultures .....	126
3.3.4 Determining a functional role for intra-colony channels.....	128
3.3.4.1 Intra-colony channels do not facilitate fluorescein transport when submerged in a fluorescein solution.....	128
3.3.4.2 Intra-colony channels create a capillary effect and act as uptake systems for fluorescent microspheres .....	128
3.3.4.3 Intra-colony channels facilitate nutrient transport in mature <i>E. coli</i> macro-colonies.....	131
3.3.5 Exploiting the role of intra-colony channels for antibiotic uptake .....	136
3.3.5.1 Selecting the appropriate test antibiotic .....	136
3.3.5.2 Comparison of filter disks and filter rings for antimicrobial susceptibility assays.....	137
3.3.5.3 Non-viable cells accumulate within intra-colony channels following antibiotic treatment.....	138
<b>3.4 Discussion.....</b>	<b>140</b>
<b>3.5 Conclusions .....</b>	<b>146</b>
<b>Chapter 4 Visualising the growth behaviours of soil bacteria using a transparent soil environment .....</b>	<b>147</b>
<b>4.1 Introduction.....</b>	<b>148</b>
4.1.1 <i>Streptomyces</i> spp. in the environment .....	149
4.1.2 <i>Bacillus</i> spp. in the environment .....	152

4.1.3 Transparent soil as an imaging tool for soil microbes .....	153
4.1.4 Experimental aims .....	156
<b>4.2 Materials and Methods .....</b>	<b>156</b>
4.2.1 Specimen preparation .....	156
4.2.1.1 Bacterial cell culture .....	156
4.2.1.2 Schwedock staining for Streptomyces .....	157
4.2.2 Constructing transparent soil for bacterial culture .....	159
4.2.2.1 Particle size reduction .....	159
4.2.2.2 Conversion of Nafion™ to an acid form and surface purification to ensure cationic exchange .....	160
4.2.2.3 Sulphorhodamine-B staining of processed Nafion™ particles .....	161
4.2.3 Preparing chemically processed Nafion™ particles for bacterial culture .....	161
4.2.3.1 Selecting the appropriate Streptomyces nutrient medium for use with transparent soil .....	162
4.2.3.2 Selecting the appropriate <i>Bacillus subtilis</i> nutrient medium for use with transparent soil .....	163
4.2.4 Refractive index matching for transparent soils .....	163
4.2.4.1 Refractive index matching for <i>S. coelicolor</i> soils .....	164
4.2.4.2 Refractive index matching for <i>B. subtilis</i> soils .....	164
4.2.4.3 Comparison of refractive index matching sugars to commercial colloid silica solutions .....	166
4.2.5 Development of an imaging workflow for the Mesolens .....	167
4.2.5.1 Sample preparation for Streptomyces imaging .....	167
4.2.5.2 Sample preparation for <i>Bacillus subtilis</i> imaging .....	168
4.2.5.3 Ensuring specimen viability in transparent soil media .....	169
4.2.6 Imaging conditions .....	170
4.2.6.1 Widefield microscopy .....	170
4.2.6.2 Confocal laser scanning microscopy .....	170
4.2.6.3 Widefield mesoscopy .....	171
4.2.6.4 Confocal laser scanning mesoscopy .....	171
4.2.7 Image processing and analysis .....	172
<b>4.3 Results .....</b>	<b>172</b>
4.3.1 Morphologies of test species under normal laboratory conditions ...	172
4.3.2 Optimisation of transparent soil for bacterial culture .....	174
4.3.2.1 Refractive index matching soils for Streptomyces culture using sucrose .....	175
4.3.2.2 Refractive index matching soils for <i>B. subtilis</i> culture using sucrose ....	176
4.3.2.3 Comparing commercial colloid silica and sugar refractive index matching preparations .....	178
4.3.3 Assessing the autofluorescence of transparent soils .....	178
4.3.4 Colonisation phenotypes of soil bacteria in a mimetic 3D environment .....	183
4.3.4.1 Growth behaviour of Streptomyces in transparent soil .....	183
4.3.4.2 Growth behaviour of <i>Bacillus subtilis</i> in transparent soil .....	185
<b>4.4 Discussion .....</b>	<b>189</b>

<b>4.5 Conclusions .....</b>	<b>194</b>
<b>Chapter 5 Concluding remarks and recommendations for future work .....</b>	<b>195</b>
<b>5.1 Summary.....</b>	<b>196</b>
<b>5.2 Recommendations for future work.....</b>	<b>198</b>
<b>References.....</b>	<b>202</b>
<b>Appendix I Bacterial Strains .....</b>	<b>231</b>
<b>Appendix II Bacterial growth media and buffers .....</b>	<b>233</b>
<b>Appendix III Published works .....</b>	<b>240</b>

*“Finty Tint.”*

Ronald Villiers

# Chapter 1

## Introduction

This Chapter provides a general overview of the principles underpinning optical microscopy and introduces various routine optical microscopy techniques which are used, or of particular relevance, in this work. I will first review the importance of spatial resolution and contrast in image formation, before introducing fluorescence-based microscopy methods. I will then introduce reflection and interference techniques, and optical mesoscopy, which are most relevant to the work in Chapters 2, 3 and 4. I will then introduce some background information about the gliding motility mechanisms of *Myxococcus xanthus*, the fundamentals of biofilm formation, and a brief introduction to microbial soil ecology with the aims of providing context to the biological questions answered by subsequent Chapters. The microscopical methods which are used directly are discussed in more detail alongside their biological applications in each Chapter. Finally, the research aims, motivations and objectives will be outlined for each Chapter of this thesis.

## **1.1 Fundamentals of optical microscopy**

Since its invention in the early 1600s, the optical microscope has set the stage for some of the most ground-breaking achievements in modern science<sup>1-3</sup>. The principals of light microscopy are based on the manipulation and control of light to form an image which has been magnified to reveal the fine details of the sample under observation. The quality of these observations is governed by two concepts; spatial resolution and contrast.

### **1.1.1 Spatial resolution in optical microscopy**

Resolution can be discussed in terms of spatial resolution, i.e. lateral (in  $x$ ,  $y$ , parallel with the focal plane) or axial resolution (in  $z$ , parallel with the propagation direction), or temporal resolution (the minimum time required to acquire two consecutive images). Spatial resolution in optical microscopy is defined as the smallest discernible distance between two distinct point objects<sup>4</sup> and is governed by a series of equations which illustrate the importance of the optical components of a microscope in image acquisition.

There are a number of criteria which can be used to describe the resolving power of an optical microscope. There are those based on the point spread function such as the Rayleigh or Sparrow limits and full-width half maximum (FWHM), or Abbe's theory of diffraction-limited resolution (Figure 1.1). The first description of a resolution limit was by Ernst Abbe in 1873, when he showed that spatial resolution was limited by diffraction of light caused by the specimen and optical elements of the microscope, and that microscopes could be designed to reduce optical aberrations that would lower image quality<sup>5</sup>.

One commonality that links different resolution criteria is the formation of an Airy disk diffraction pattern which occurs when light is focused through an optical microscope.



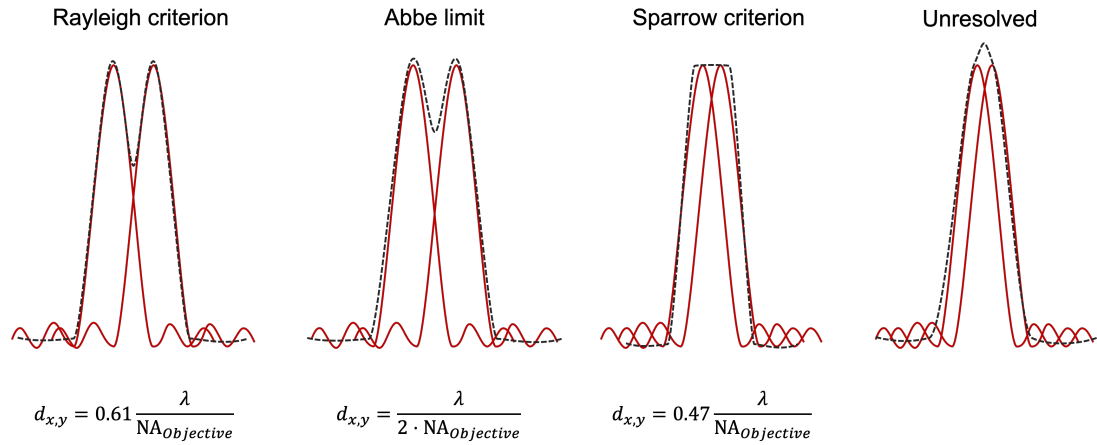


**Figure 1.1. Resolution criteria in optical microscopy.** Spatial resolution in optical microscopy can be determined by applying one of many resolution criteria. The Rayleigh, Abbe and Sparrow criteria are presented above, where the spatial resolution limit is shown using two adjacent Airy disks placed at their resolvable limits (Red = Airy Disk intensity profiles, black = predicted image intensity profile of the two closely spaced point emitters). Two unresolved point objects are also shown where the Airy Disks overlap and are no longer separately distinguished.  $d_{x,y}$  = lateral resolution limit,  $\lambda$  = wavelength, NA = numerical aperture.

An Airy disk pattern is generated by the diffraction of light caused by the object. It results in a central focal spot with concentric maxima and minima which decrease in intensity as they move from the centre<sup>6</sup>. As shown in Figure 1.2a and 1.2b, the lateral resolution limit can be determined by two adjacent closely spaced Airy disks. As the space separating these disks narrows, the Rayleigh limit is noted as the point where the first order maximum of the second disk aligns with the first order minimum of the first disk<sup>7</sup> (Figure 1.2b). The intensity profile of an Airy disk can be measured and reconstructed into a three-dimensional (3D) representation called the Point Spread Function (PSF) (Figure 1.2c). Taking the PSF into consideration, the diameter from the centre of the focal spot to the first minima defines the resolution limit set by the Rayleigh criterion.

The Rayleigh resolution can be calculated based on Abbe's principles of image

formation, which states that spatial resolution ( $d$ ) is dependent on the wavelength of light ( $\lambda$ ) and the numerical aperture (NA)<sup>8</sup>. The NA is calculated by the product of the refractive index of the sample medium ( $n$ ) and the half-angle ( $\theta$ ) of the cone of light which is collected by the objective lens or that is transmitted through the condenser lens (Equation 1.1).

$$NA = n \sin \theta \quad [1.1]$$

The lateral resolution for a diascopic or transmission microscope can be provided by Equation 1.2, whereas the limit for an episcopic microscope where incident and collected light propagate through the same objective lens can be given by Equation

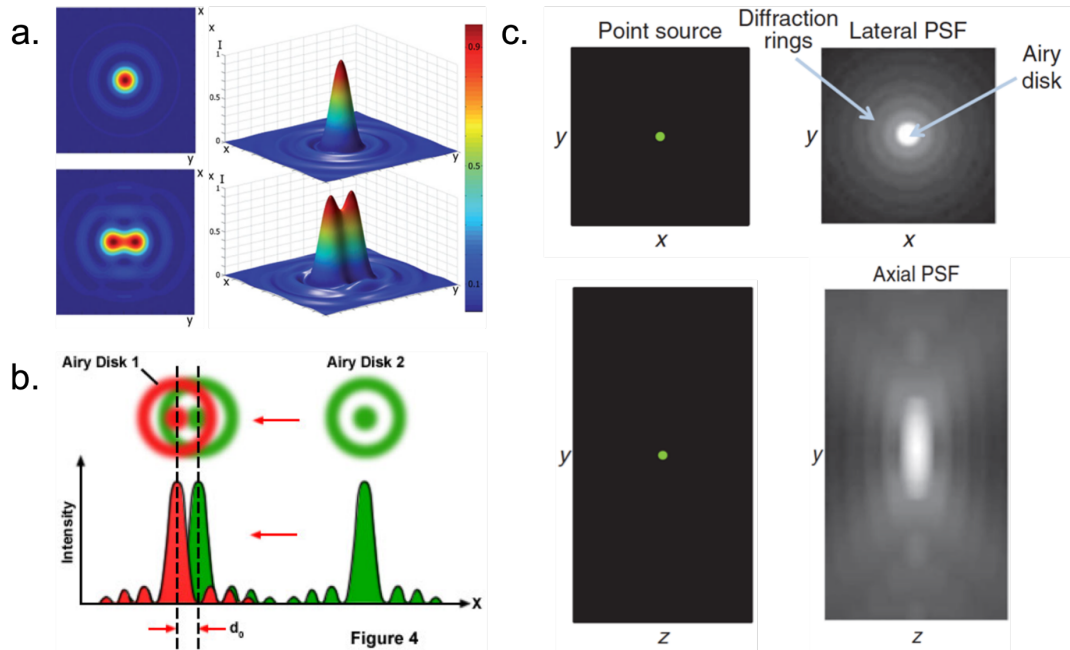


**Figure 1.2. Diffraction limited resolution in optical microscopy. (a)** A single Airy disk and two adjacent Airy disks close to their resolvable limit and corresponding intensity plots of each Airy disk. The colour table corresponds to the intensity. **(b)** The resolution limit exemplified by two Airy disks moving closer to one another. The Rayleigh criterion ( $d_0$ ) is shown, where the central maxima of Airy disk 2 overlaps with the first order minima of Airy disk 1. **(c)** Experimental data showing the lateral and axial PSFs from a single point source. Note the elongation of the axial PSF caused by the geometry of optical elements within the imaging system. Adapted from <sup>4,7,16</sup>.

1.3.

$$d_{x, y} = 1.22 \frac{\lambda}{NA_{Objective} + NA_{Condensor}} \quad [1.2]$$

$$d_{x, y} = 0.61 \frac{\lambda}{NA_{Objective}} \quad [1.3]$$

The axial diffraction-limited resolution of an optical microscope can be similarly understood. Two point objects will be resolved axially if they are separated by more than the distance from the focal spot to the first order minimum (Figure 1.2c). This can be calculated using Equation 1.4<sup>9</sup>.

$$d_z = \frac{2n\lambda}{(NA_{Objective})^2} \quad [1.4]$$

The axial resolution describes the achievable resolution in the  $z$ -dimension and is vital for 3D imaging of a biological sample. Like the equations governing lateral resolution, the axial diffraction-limited resolution can be calculated using the wavelength of incident light ( $\lambda$ ), the NA of the objective lens and the refractive index of the mounting medium ( $n$ ). The axial PSF is elongated along the optical axis of the microscope due to the non-symmetrical wavefront that propagates from the objective lens<sup>10</sup> and, like the lateral PSF, has concentric maxima and minima which define the axial resolution<sup>7,11</sup>.

Abbe's work showed that the diffraction-limited resolution of a microscope was not dependent on chromatic or spherical aberrations, although they are capable of decreasing image quality<sup>8</sup>. Monochromatic aberrations are wavelength independent and include spherical aberrations, coma, astigmatism, field curvature and distortion, while chromatic aberrations are dependent on the wavelength(s) of light used and can manifest either longitudinally or laterally<sup>12</sup>. To overcome these phenomena, multiple lenses can be used in the optical setup of the microscope to bring all divergent wavelengths of light into focus for chromatic aberrations<sup>9</sup>; or in the case of spherical

aberrations, by reducing the lens diameter (however this approach will lower the NA of the lens)<sup>13</sup>.

### **1.1.2 Contrast generation and enhancement in optical microscopy**

Contrast is perhaps the most important aspect of image formation. Image contrast can be described as the relative difference in signal between an object and the background. Without contrast there would be no visible detail in the image and contrast must be enhanced in many microscopy applications due to the transparency of many biological specimens. This can be achieved by several means. For example, absorption-based chemical dyes are used to increase contrast in brightfield microscopy. Alternatively, a phase difference can be generated between the incident and collected light which reveals previously unobservable features in the sample (e.g. in differential interference contrast (DIC)<sup>14</sup> and phase contrast microscopy<sup>15</sup>).

To understand the benefits of these contrast enhancement techniques one must first discuss the development of brightfield transmission microscopy. This method is perhaps the most readily available optical microscopy technique and was spawned from the work of Ernst Abbe and Carl Zeiss<sup>4</sup>. Widely regarded as the founding instrument of modern microscopy, the compound microscope was a transmission brightfield instrument which used multiple optical elements to correct aberrations and to focus an incoherent light source onto the specimen. Transmitted light was then collected by an objective lens and an image was formed in several conjugate image planes throughout the microscope before passing through the ocular lenses<sup>16</sup>. Homogeneous illumination is key to ensure optimum contrast in the resulting image, which is achieved by Köhler illumination. Köhler illumination is now the standard method for ensuring homogenous illumination across the field of view of the microscope and was developed by August Köhler<sup>9</sup>. This method relies on precise alignment of the conjugate image and aperture planes, which occur along the image-

forming paths (Figure 1.3). The result is an evenly illuminated field of view and maximum contrast between the specimen and the background.

Dark field microscopy improves contrast by introducing incident light at a high angle, such that a hollow cone of incident light is formed by means of a condenser annulus. Contrast arises from highly scattering objects in the sample, and scattered light is collected by the objective lens. Dark field is therefore able to reveal the edges of cells and highly scattering cellular components<sup>17</sup> (Figure 1.4a).

Phase contrast microscopy is another label-free method of contrast enhancement. A phase difference is introduced using a condenser annulus and a corresponding phase ring placed at the back focal plane of the objective lens. This results in propagation of a hollow cone of light which is refracted by the specimen wherever there is a refractive index boundary and collected by the objective lens. The phase ring introduces a phase shift in the collected non-diffracted light, resulting in a high contrast border

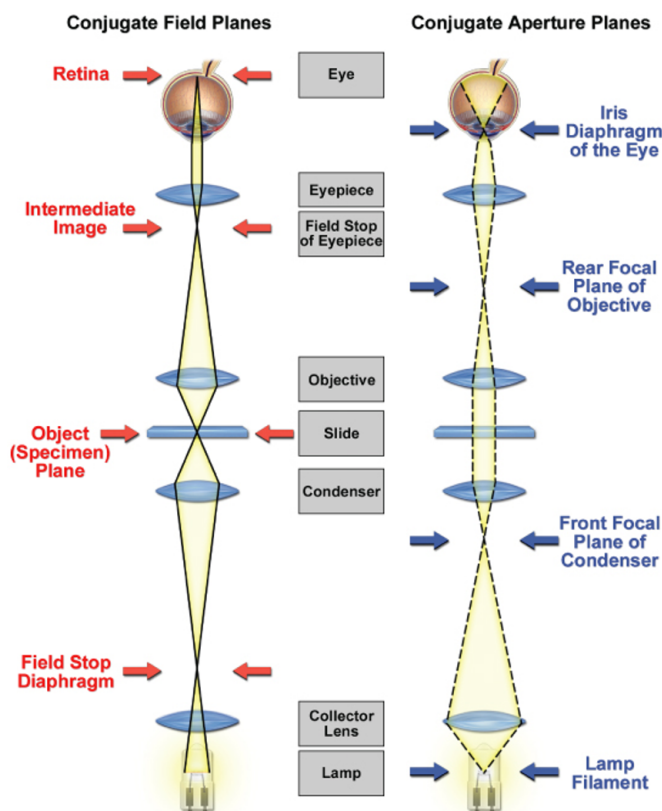


**Figure 1.3. Image formation in the compound microscope.**

The conjugate field (image) and aperture planes are shown which are present in the image formation path of a compound microscope. The alignment of these image formation planes results in an even field illumination and optimal contrast in the formed image. Reproduced from <sup>16</sup>.

surrounding objects which have a higher refractive index than their surrounding medium<sup>17,18</sup> (Figure 1.4b).

Differential phase contrast microscopy also relies on refractive index boundaries within the specimen to generate contrast. Linearly polarised light is split into two orthogonally polarised rays using a Wollaston prism and transmitted through the sample as two spatially separated rays. Particularly thick, or high refractive index regions of the sample will result in a change in optical path length before the two transmitted rays are then recombined by a second Wollaston prism and passed through an analyser. This results in interference of the transmitted light depending on how much the relative phase has been changed by the sample, in turn increasing the contrast of the resulting image<sup>19,20</sup> (Figure 1.4c).

### 1.1.3 Fluorescence for biological imaging

Another commonly used mechanism of contrast enhancement is the use fluorescent labelling to identify subcellular structures and is applicable to a wide variety of microscopy techniques. Fluorescence-based applications for biological imaging are now commonplace and serve as a vital tool for a variety of techniques including

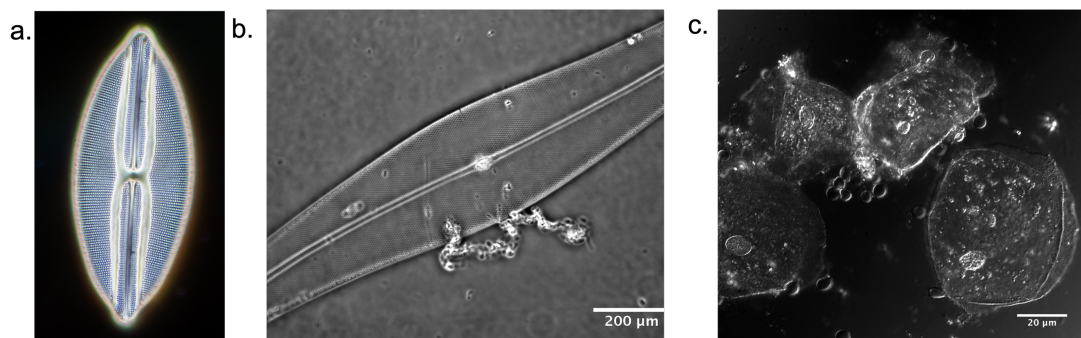


**Figure 1.4. Label-free contrast enhancement by dark field, DIC and phase contrast microscopy. a)** dark field image of a marine diatom (*Navicula* sp.) (Copyright © 2012 Waldo Neil; adapted from <https://tinyurl.com/diatomimaging>). **b)** A phase contrast image of a marine diatom (*Pleurosigma* sp.) collected from Queen Anne's Battery Marina, Plymouth, UK in April 2018. **c)** a DIC image of human buccal epithelial cells.

protein localisation and organelle staining and in routine laboratory fluorescence-based assays. Fluorescence microscopy was pioneered by Oskar Heimstädt in 1911 and was primarily used for observing autofluorescent specimens<sup>21</sup>. The technique was refined in 1937 when Haitinger developed non-autofluorescent compounds (fluorochromes/fluorophores) for staining cellular structures<sup>22</sup>. In the 1950s the concept of molecular specificity was expanded by the use of antibody conjugates of fluorophores to accurately target individual proteins<sup>23,24</sup>.

The underpinning theory of fluorescence in biological imaging is best described by understanding the excitation states of the outer electrons of a fluorophore. This can be explained using a Jablonski diagram which shows different excitation states that outer electrons can occupy when excited and their decay which results in the release of a photon which is then detected as an emission signal in microscopy (Figure 1.5). As the electrons are excited by an incident photon, they shift to the lower singlet state ( $S_1$ ) or the higher singlet state ( $S_2$ ) and photon can be emitted as the energy is converted within the fluorophore and returns to the ground state ( $S_0$ )<sup>25,26</sup>. This photo-induced process comprises four main phases (excitation, internal conversion, vibrational relaxation and fluorescence) and the process from beginning to end takes several nanoseconds to result in emission. Fluorescence emission maxima have a longer wavelength in comparison to their excitation maxima due to absorption of energy during excitation, which is termed the Stokes shift between a fluorophore's absorption and emission spectra (Figure 1.6)<sup>27</sup>.

Fluorescence microscopy took a huge leap forward in the late-20<sup>th</sup> century with the discovery and subsequent manipulation of the photoprotein, Green Fluorescent Protein (GFP). In 1962, Osamu Shimomura and his team isolated the luminescent protein, Aequorin, from the jellyfish, *Aequorea victoria*<sup>28</sup>. This protein was later renamed GFP and used to fluorescently label live cells to elucidate their sub-cellular

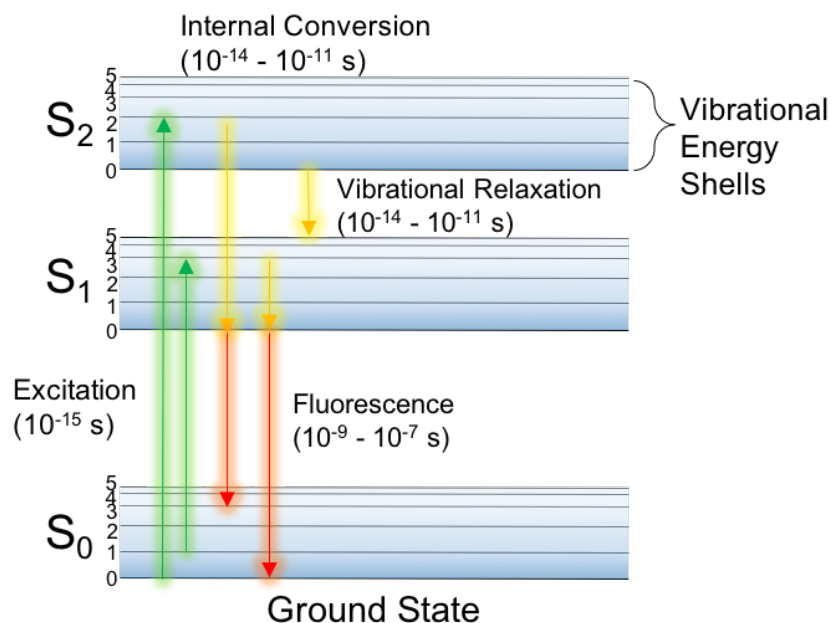


**Figure 1.5. Fluorescence excitation and emission.** A simplified Jablonski diagram showing the energy transfer of an electron which results in emission of fluorescence. As an electron is excited, its energy is transferred to a higher state ( $S_1$  or  $S_2$ ) and upon its return to the ground state ( $S_0$ ) a photon can be released. This process takes place in under a microsecond and results in a fast on/off switch which is vital in biological imaging. Adapted from <sup>26</sup>.

protein organisation and functionality<sup>29</sup>. Transcriptional or translational GFP fusion products are now routinely used throughout biology, allowing the spatiotemporal study of a specific protein within live cells. Additionally, attachment of GFP to specific targets via antibody conjugates can allow researchers to selectively tag their chosen protein in a biological specimen (so-called immunofluorescence). Either method allows visualisation, quantification and subcellular tracking of individual molecules<sup>30,31</sup>.

Other variants of GFP have since been developed from the mid-2000s and there is now a rainbow of available photoproteins as well as synthetically engineered photoproteins<sup>32-35</sup>. In the early 2000's another monomeric photoprotein, DsRed, was isolated from luminescent corals and manipulated to provide a range of red-emitting photoproteins<sup>32,36</sup>. The development of multiple coloured photoproteins has allowed



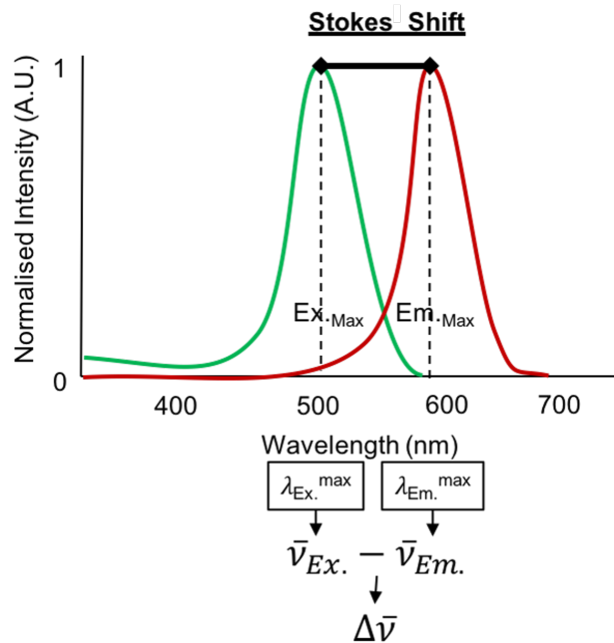


**Figure 1.6. Stoke shifts in fluorescence microscopy.** The representative absorption and emission spectra of a fluorescent molecule. The peak excitation wavelength is noted by  $Ex_{Max}$  and the peak emission wavelength by  $Em_{Max}$ . The Stokes shift ( $\Delta\bar{\nu}$ ) is shown by the difference between  $Ex_{Max}$  and  $Em_{Max}$ .

for multiple fluorescent tags to be added to a single specimen to enable multi-label imaging and determination of protein co-localisation and differences in protein expression in live cells.

The benefit of using fluorescent probes over the absorption-dependent chemical dyes that came before not only lie in their tagging specificities, but also in their biocompatibility increased detection sensitivity<sup>27</sup>. Absorption-specific dyes can often be non-specific and cytotoxic towards the target cell and therefore have the potential to not only give a high background signal due to non-specific binding but also compromised cell viability. Fluorescent tagging can also have similar problems, such as if the endogenous protein concentration is high in the specimen then unspecific binding can occur when using antibody conjugates hence why antibody-blocking is required<sup>9,37</sup>. By applying the Beer-Lambert law (which provides a measure of the absorbance of light by a material), the concentration of absorption-dependant dyes needs to be very high to improve contrast in comparison to antibody conjugates or fluorescent proteins. This high concentration of dye is often cytotoxic and prevents live cell imaging or can prevent a true representation of *in vivo* dynamics.

That being said, fluorescent dyes and photoproteins can also cause cytotoxic effects either through protein-induced toxicity or phototoxicity. Phototoxicity can occur when Reactive Oxygen Species (ROS) are generated by a fluorescent protein and acts to decrease cell viability. Phototoxicity can also occur or through excessive excitation power which compromises the viability of the biological specimen. The barrel structure of many photoproteins causes ROS to be trapped within the protein and results in a build-up of free radicals which in turn results in compromised cell viability<sup>38,39</sup>. More recently, the development of red photoproteins with lower cytotoxicity have been developed and the use of oxygen scavenging molecules has also been implemented in biological imaging applications to lower the effects of cytotoxicity<sup>40,41</sup>. Of course, it is recommended that the irradiance of the excitation source should be controlled at the specimen plane to minimise these effects and maintain cell viability during fluorescence imaging<sup>42</sup>.

There is however another fundamental problem that can occur when using any fluorescence application to biological specimens; photobleaching. Photobleaching is a destructive phenomenon where excessive excitation light results in degradation of the fluorochrome<sup>9</sup>. The destruction of fluorochromes in the singlet or triplet state results in a net loss in available ground state fluorophores. Therefore, the potential to image single molecules and cellular structures is significantly decreased and less information can be gleaned from a specimen. However, techniques such as Fluorescence Recovery After Photobleaching (FRAP) can use photobleaching to their advantage, where protein mobility and the rate diffusion in a sample can be observed<sup>43,44</sup>.

## 1.2 Conventional fluorescence microscopy techniques

### 1.2.1 Widefield epifluorescence microscopy

Following strides in the development of fluorescent probes and photoproteins, microscopes were developed that were capable of visualising fluorescently labelled specimens. Epifluorescence microscopes are routinely used for fluorescence imaging, where fluorophores are excited by means of non-coherent metal-halide arc lamps, light emitting diodes (LEDs), or a coherent laser source. It is crucial that an epifluorescence microscope is able to spectrally separate the excitation and emission light which propagate along the optical path<sup>45</sup>. This can be achieved using a dichroic mirror, which is composed of several thin layers of glass and has different reflection and transmission properties.

The modern widefield epifluorescence microscope was pioneered by Ploem in 1967 and is capable of imaging dynamic cellular events with diffraction-limited resolution<sup>46</sup>. The temporal resolution of widefield epifluorescence microscopy is high and is often limited by the frame rate of the detector. Additionally, widefield systems can be built in either inverted or upright configurations, can be adapted and are often sold commercially with added modalities such as DIC or phase contrast. Figure 1.7a shows a representative schematic of a typical upright widefield epifluorescence microscope. However, there are drawbacks to this method, particularly for thicker specimens. A high background signal is generated by collection from out-of-focus planes which lowers the contrast of the acquired image. Moreover, excitation is not limited to a single focal plane, and so photobleaching can occur even in focal planes outside the depth of field of the objective lens<sup>47</sup>. Nevertheless, widefield methods remain the basis for a number of optical techniques such as light sheet or selective plane illumination microscopy (SPIM)<sup>48,49</sup>, total internal reflection fluorescence (TIRF)

microscopy<sup>50–52</sup>, single molecule localisation microscopy (SMLM)<sup>53–55</sup> and structured illumination microscopy (SIM)<sup>56</sup>. To improve on the optical sectioning strength of the widefield epifluorescence microscope, confocal microscopy was later developed which allowed for higher contrast 3D images to be acquired.

### **1.2.2 Confocal laser scanning microscopy**

Confocal microscopy was first developed in the 1950s by Marvin Minsky to fulfil a requirement for an improved signal-to-noise ratio (SNR) and to improve the fluorescence-based contrast of widefield epifluorescence microscopes. A confocal mode was achieved by introducing a pinhole aperture before the detector which rejected out-of-focus contributions from the specimen<sup>57,58</sup>. The confocal microscope was improved on by the adoption of a scanning technique and incorporation of laser excitation sources in the late-1980s. This allowed for further improvement of background noise elimination and attainable resolution (although the spatial resolution of confocal laser scanning microscopy (CLSM) remained diffraction-limited)<sup>47</sup>. The use of a coherent excitation source resulted in diffraction-limited point illumination, while the confocal pinhole allowed for the removal of background irradiance from adjacent focal planes, optical sectioning and acquisition of 3D data sets. As shown in Figure 1.7b, a typical CLSM scans a laser source, using a scanning mirror, which has been focused to a diffraction-limited spot within the specimen. Like Minsky's original confocal microscope, a CLSM also has a pinhole aperture which lies before the detector (often a photomultiplier tube (PMT)) and rejects out-of-focus signal from the specimen to improve the SNR and image contrast. This also has the effect of restricting the imaging volume to a thin optical section depending on the excitation wavelength, NA of the objective lens, refractive index of the mounting medium and the diameter of the pinhole aperture<sup>47,59,60</sup>. The confocal optical section thickness typically ranges between 500 nm to 700 nm for a modern optical setup. The diameter

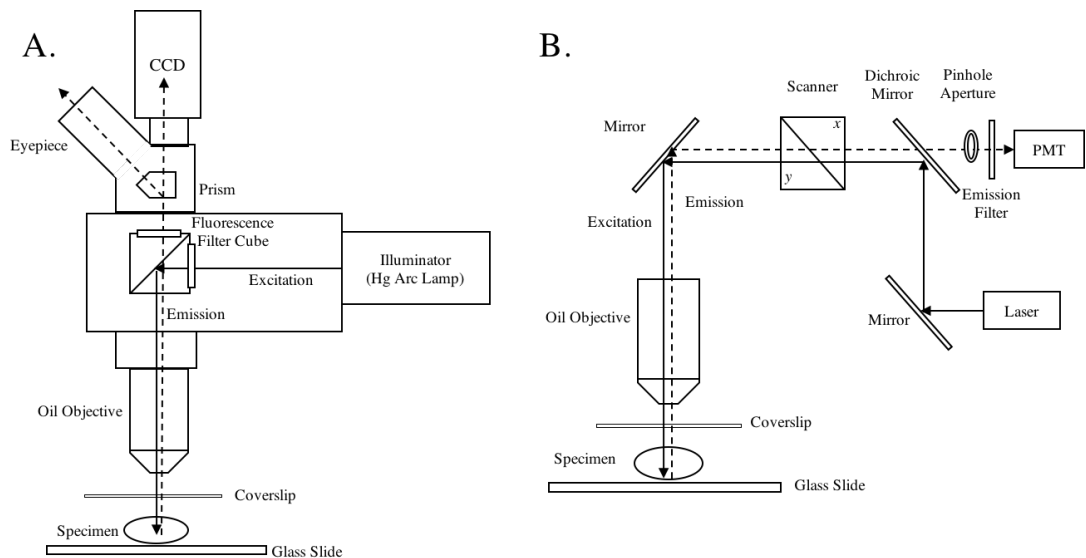


**Figure 1.7. Widefield epifluorescence and confocal laser scanning microscopes. a)**

diagram of an upright widefield epifluorescence microscope using a Mercury arc lamp illuminator and CCD-camera detector. Polychromatic light is directed through a selected excitation filter to provide the excitation wavelength required for the application. Filtered excitation light is focused onto the specimen via the objective lens and emitted light from excited fluorophores is collected by the objective lens and passed through the emission filter before being directed either to the eyepiece or detector via a prism. **b)** A CLSM uses a laser excitation source, where the beam is directed to the specimen through a series of mirrors and scanned using a scanning mirror. Emission light is passed through a dichroic mirror proximal to the PMT detector. A pinhole aperture rejects out-of-focus emission signals from above and below the focal plane, thereby resulting in higher quality images. Solid lines = excitation light, dashed lines = emission light. Adapted from <sup>9</sup>.

of the pinhole aperture is imperative to the optical sectioning strength and is optimally set to the diameter of 1 Airy unit (given by  $d_{x,y}$ ).

Despite the advantages of laser scanning microscopy for 3D imaging, there are still trade-offs to consider. Point scanning methods often have a lower temporal resolution than widefield methods as the excitation point source has to be scanned over the entire field (multiple times if averaging is required). Therefore, imaging dynamic

cellular events by CLSM can be challenging, however, there are ways to compensate for this. As discussed by Jonkman & Brown, the acquisition rate of a 1024 by 1024-pixel image with a 1  $\mu$ s pixel dwell time is around 1 frame per second, but the scanning frequency (temporal resolution) can be increased at the expense of spatial resolution<sup>61</sup>. This limitation can also be overcome by Spinning Disk Confocal Microscopy (SDCM), where a disk containing an array of pinholes is spun at approximately 5000 revolutions per minute to increase temporal resolution without sacrificing spatial resolution<sup>62</sup>. Other adaptations to the CLSM have increased the performance of this instrument to suit a variety of needs such as multi-photon imaging for use with thick or highly scattering samples<sup>63,64</sup>.

## **1.3 Reflection and interference-based microscopy**

Reflection and interference are two phenomena which can be used to generate contrast in optical microscopy and can be adopted by both widefield and confocal microscopes. There are a number of techniques which use these methods, including DIC and phase contrast (refer to Section 1.1.2). However, this Section shall provide an introduction to those related and most relevant to this thesis.

### **1.3.1 Confocal reflection microscopy**

Reflection-based methods typically rely on differences in refractive index within the specimen. Refractive index boundaries (i.e. at the glass-medium or medium-cell interface) result in reflection of incident light, which can be collected by the objective lens and detected by a PMT detector with no source blocking filter in place<sup>65</sup>. Confocal reflection microscopy (CRM) is capable of diffraction-limited 3D imaging and has the same temporal resolution as CLSM. As the contrast mechanism in confocal reflection microscopy relies on reflectivity, live cells can be imaged label-free (Figure 1.8). At a refractive index boundary, reflection signals also have a higher intensity than

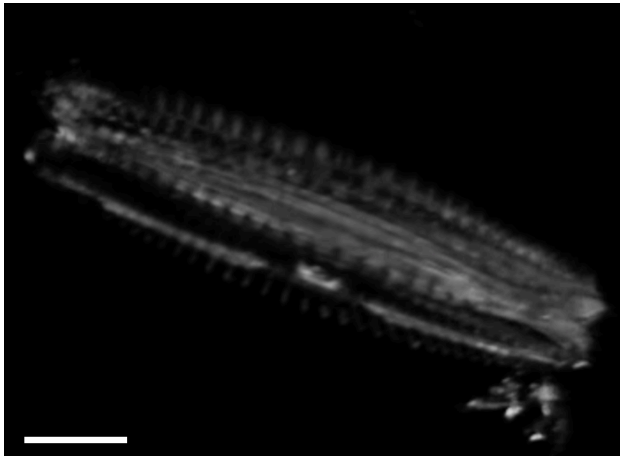


**Figure 1.8. Label-free 3D confocal reflection microscopy.** A maximum intensity projection of a marine diatom (*Amphora sp.*) imaged in 3D by confocal reflection microscopy. Scale bar = 20  $\mu\text{m}$ . Collected from Queen Anne's Battery Marina, Plymouth, UK in April 2018.

fluorescence emission (given the same incident power), and so less power is required for CRM than conventional fluorescence microscopy (*personal communication*; Amos, W.B., 2018). Therefore, there is less exposure of the sample to light compared to CLSM which maintains the viability of cells for longer periods. Nevertheless, CRM remains an underused method when compared to CLSM, for example, due to the benefits of molecular specificity that fluorescence affords while CRM relies only on refractive index boundaries.

### 1.3.2 Total internal reflection fluorescence microscopy

Total internal reflection fluorescence microscopy was pioneered by Axelrod in 1981 as a method of obtaining images of the basal membrane and adhesion properties of mammalian cells<sup>50</sup>. These cellular processes, which only occur at the basolateral membrane, can be selectively observed using TIRF microscopy due to the generation of an evanescent wave perpendicular to the substrate (i.e. the coverglass on which the specimen is mounted). The evanescent field is generated as incident light is directed to the coverglass at the critical angle of reflection ( $\theta_c$ ) where the incident light is refracted along the length of the coverglass. The critical angle (Equation 1.5) can be derived by from Snell's Law (Equation 1.6), where  $n_1$  and  $n_2$  are the refractive

indices of the immersion medium (e.g. water) and substrate, and  $\theta_i$  and  $\theta_2$  are the incident and refractive angle, respectively<sup>51</sup>.

$$n_1 \cdot \sin \theta_1 = n_2 \cdot \sin \theta_2 \quad [1.5]$$

$$\theta_c = \sin^{-1}(n_2/n_1) \quad [1.6]$$

The resulting evanescent wave limits excitation of any fluorophores to the basolateral surface of the specimen. However, due to the evanescent nature of the wave front the intensity of the wave will decrease exponentially along the optical axis. This means that any fluorophores beyond the TIRF field depth will remain unexcited and will therefore not contribute to the acquired fluorescence image. Moreover, this method of selectively imaging the bottom 100 nm or so of a specimen decreases the background signal that would have otherwise been detected by widefield epifluorescence or CLSM<sup>50,51,66</sup>.

### 1.3.3 $4\pi$ microscopy

As described in Section 1.1.1, the size of the PSF in a diffraction-limited optical microscope is governed by the NA of the objective lens and the collected wavelength of light. To decrease the size of the PSF, and so increase spatial resolution, one can either decrease the wavelength (which is not ideal for fluorescence imaging due to the fixed excitation and emission maxima of a given fluorophore, and increased cytotoxicity of using shorter wavelengths) or can increase the NA of the objective lens. The latter is only feasible until  $NA \approx 1.45$  due to the limitations of optical design<sup>9</sup>. However, the NA can effectively be increased by means of a  $4\pi$  geometry. This confocal method was developed in 1992 by Stefan Hell and reduces the PSF to a sphere<sup>67,68</sup>. The aim was to have two opposing objective lenses collect light over  $4\pi$  steradians (equal to 12.5667 steradians), compared to conventional epi-detection which is only able to collect light over  $2\pi$ <sup>9</sup> (Figure 1.9). The reduction of the PSF to a



sphere is a result of the interference caused by the two counter-propagating spherical wave fronts which reduces the elongation of the PSF<sup>67–69</sup>. In practice however, the PSF is not perfectly spherical which is due to the collection angle of high NA objective lenses being approximately 280°, and not 360°<sup>67</sup> (Figure 1.9b). Nevertheless, this method provides images of higher axial resolution than conventional diffraction-limited widefield epifluorescence or confocal microscopy and can be as low as 100 nm<sup>70–72</sup>. This is accompanied with the cost of delicate alignment of the two opposing objectives to avoid any phase differences between the two excitation and emission rays<sup>9</sup>. It is important to consider that the nature of  $4\pi$  microscopy can give rise to side-lobes in the reduced PSF; however, these can be removed by adopting a two-photon method<sup>73,74</sup> or by deconvolution<sup>75,76</sup>.

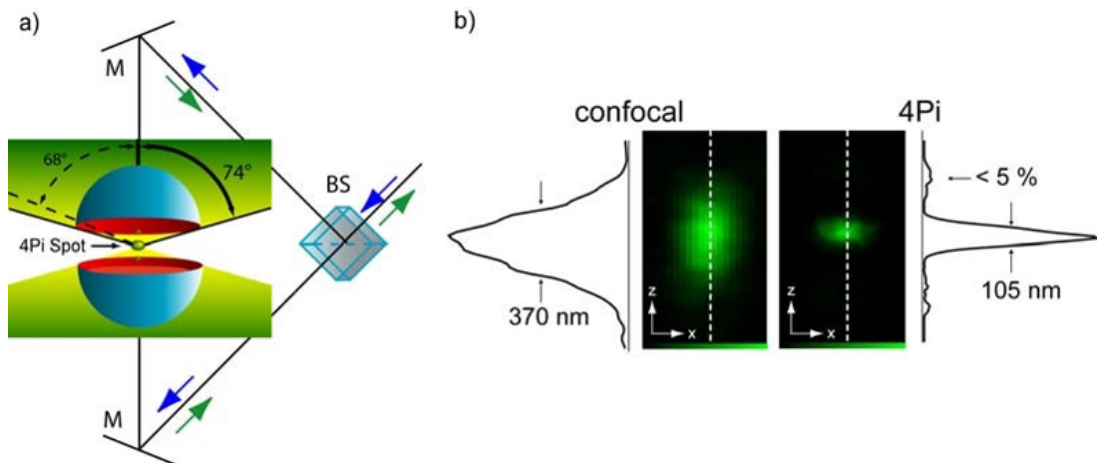


**Figure 1.9.  $4\pi$  microscopy as a method of resolution enhancement.** **a)** A diagram showing  $4\pi$  geometry, where fluorescence emission is detected by two opposing objective lenses. The excitation and emission array are separated and directed to and from each objective using a beam splitter (BS) and two mirrors (M). **b)** Intensity profiles and fluorescence images of axial PSFs from a confocal laser scanning microscope and a  $4\pi$  microscope. The PSF is reduced to a sphere, and results in higher spatial resolution. Reproduced from <sup>74</sup>.

Similar to  $4\pi$  microscopy, a technique named  $I^5M$  was developed by Gustafsson in 1999 which was a combination of two previously developed techniques; Image interference microscopy ( $I^2M$ ), and incoherent interference illumination ( $I^3M$ )<sup>77</sup>. This combination results in a widefield setup with  $4\pi$  geometry, thereby maintaining high spatial resolution (approx. 100 nm) while increasing the temporal resolution as point scanning is not required<sup>73,77,78</sup>. In  $I^5M$ , non-coherent light source is aligned for Köhler illumination for both objective lenses, and interference occurs at the specimen plane and emission is collected by both objective lenses and interferes to generate the final image<sup>77</sup>. Again, deconvolution methods can be used to suppress the side lobe artefacts present in  $I^5M$ <sup>75,76</sup>.

#### **1.3.4 Standing wave fluorescence microscopy**

Standing wave fluorescence microscopy (SWFM) is a fluorescence-based technique that can be adapted for widefield or confocal microscopes. This method was first demonstrated experimentally by Wiener in 1890<sup>79</sup>, and later refined by Frederick Lanni<sup>80,81</sup>. The standing wave method relies on the interference of two counter-propagating waves of the same wavelength with a relative phase shift equal to  $\pi$  ( $180^\circ$ ) at the sample plane<sup>80</sup> (Figure 1.10). This can be achieved by one of two ways; using a  $4\pi$  geometry where excitation light propagates from two opposing objective lenses to interfere and form a standing wave<sup>67,68,71,82</sup>, or by placing the specimen upon a plane reflector and using a conventional epifluorescence microscope<sup>80,81,83,84</sup>. The end result provides a five-fold improvement in the axial resolution ( $d_z \approx 90$  nm) and no compromise in the lateral or temporal resolution when compared to diffraction-limited CLSM, for example<sup>83</sup>. This method is capable of acquiring 3D information in a single two-dimensional (2D) image by generating what appears as a “contour map” of the specimen. The generation of a standing wave restricts fluorescence excitation to

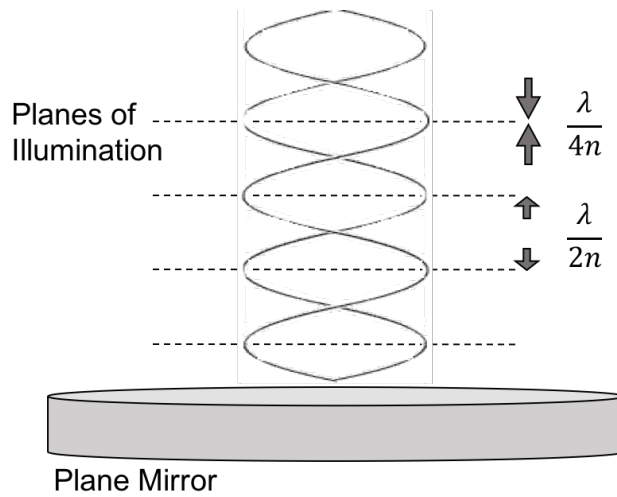


**Figure 1.10. Generation of a standing wave by means of a plane reflector.** A diagram of a SWFM setup is shown in plane reflector-configuration. Incident excitation light propagates towards the plane reflector, which when reflected undergoes a  $180^\circ$  phase-shift and counter-propagates relative to the incident light. Interference occurs between the incident and reflected waves resulting in thin antinodal planes of illumination separated by dark nodal planes. Excitation of any fluorophores in the sample will be localised to the antinodal planes. A 2D image is acquired where 3D information is encoded in fringes separated in the  $z$ -dimension by a regular antinodal spacing.

narrow antinodal bands of illumination which are separated axially by a factor of  $\lambda/2n$  and have a FWHM of  $\lambda/4n$ , where  $\lambda$  = excitation wavelength and  $n$  = refractive index of mounting medium<sup>80</sup>. Recently, this theory was applied to widefield SWFM of live red blood cells to generate 3D reconstructions of membrane dynamics at high temporal resolution<sup>85</sup>.

Standing wave fluorescence microscopy has also been combined with other super resolution techniques to increase the spatial resolution further. In 2016, SWFM was combined with stimulated emission depletion (STED) microscopy (which uses a “doughnut-shaped” depletion beam to increase spatial resolution by minimising the effective area of excitation at the focal point<sup>86</sup>) to achieve axial resolution of  $19 \text{ nm}$ <sup>87</sup>. Additionally, the standing wave principle has been applied to stochastic optical

reconstruction microscopy (STORM) (which is a widefield localisation technique that localises single point emitters by acquiring multiple images of chemically induced photo-switchable fluorophores<sup>53,88</sup>) to enhance fluorescence intensities in the near field<sup>89</sup>.

### 1.3.5 Interference reflection microscopy

Interference reflection microscopy (IRM) is a label-free method which was first described for biological imaging by Adam Curtis in 1964. Curtis used IRM to study the adhesion of embryonic chick heart fibroblasts to a glass slide and claimed to determine the separation distance between the pseudopodia and the coverglass by as little as  $50\text{\AA}$ <sup>90</sup>. Since the 1960s, IRM has been used to further study the focal adhesion sites in eukaryotic cells on glass substrates<sup>90–97</sup>, microtubule dynamics<sup>98–100</sup> and has also been applied briefly to the study of bacterial motility<sup>101–104</sup>.

In IRM, contrast results from reflections at refractive index boundaries, such as at the medium-cell interface (Figure 1.11). Constructive and destructive interference of

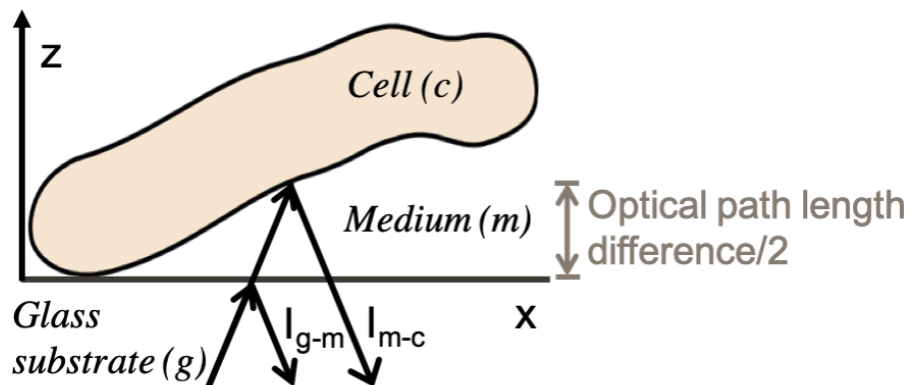


**Figure 1.11. Interference reflection microscopy.** A diagram illustrating the reflection boundaries at the coverglass (*g*), medium (*m*) and cell (*c*) boundaries. Incident light is reflected at the glass-medium interface and the medium-cell interface. The two reflected waves  $I_{g-m}$  and  $I_{m-c}$  interfere to generate maxima and minima which appear in the acquired image as a series of bright and dark fringes which encode axial information. Reproduced from <sup>145</sup>.

reflected light originating from the coverslip-medium and medium-cell interfaces result in a fringe pattern which can be translated to the axial profile of the basolateral surface of the cell<sup>105,106</sup>. Like SWFM, IRM provides a five-fold axial resolution enhancement over conventional widefield or point-scanning microscopy techniques, where 3D information can be extracted from a 2D image thus overcoming the limitations in optical sectioning of thin specimens (e.g. bacteria)<sup>90,105,106</sup>. Additionally, the interference fringes present in IRM data are separated axially by a factor of  $\lambda/2n$  and have a FWHM of  $\lambda/4n$ , where  $\lambda$  = incident wavelength and  $n$  = refractive index of mounting medium<sup>107</sup>. Interference reflection microscopy can be easily coupled into existing widefield and confocal microscopes by replacing the emission dichroic with a beam splitter and setting the spectral range of the detector to match the wavelength of incident light. However, one must consider that contrast will be decreased in widefield IRM due to the use of an incoherent light source and increased detection of out-of-focus signal<sup>105</sup>.

Other similar techniques to IRM include reflection interference contrast microscopy (RICM) and interferometric scattering microscopy (iSCAT). The differences between these techniques and IRM are subtle. RICM uses polarising filters and a specially designed antireflective objective lens to filter out reflected light from above and below the specimen plane, supposedly resulting in a higher contrast image<sup>105,107,108</sup>. iSCAT works on the basis of detecting both the reflected and scattered portions of light which interfere at the detector plane<sup>109</sup>.

Chapter 2 goes on to introduce IRM in more detail, and in particular its application to bacterial specimens. Furthermore, the development of a novel multi-wavelength confocal variation of IRM is described where multiple wavelengths are used to determine directionality of the specimen based on colour-ordering.

## 1.4 Optical mesoscopy

### 1.4.1 The Mesolens

Conventional optical microscopy methods are limited by a trade-off between the size of the field of view (FOV) and the attainable spatial resolution. This problem is due to the relationship between magnification and NA in conventional objective lens design, meaning that small features cannot be adequately resolved over large FOVs. To address this, a stitching and tiling method can be used where multiple images are acquired using a high magnification, high NA objective lens and digitally stitched together post-acquisition. However, this process often causes checker-board artefacts due to inhomogeneities in illumination, varying densities across the specimen which can result in light scattering, and stage drift which causes alterations in the focal plane of different tile images<sup>110</sup>. Stitching and tiling also comes with a lower temporal resolution compared to acquiring a single image of the whole field which must be considered for any live cell applications. Alternatively, a new method of high-resolution large specimen imaging can be used where fine details can be resolved across large areas of a specimen without any requirement for stitching and tiling. The Mesolens is one such instrument capable of acquiring images in this way, and since its development over the last decade has proven to be a useful tool for imaging large specimens at high spatial resolution. Furthermore, the Mesolens has proven to be a powerful tool in the fields of developmental and neurobiology<sup>111–113</sup>, however it has never been used to study any form of microbiological specimens.

The Mesolens is an optical mesoscope developed at the University of Strathclyde centred around a large objective lens and is perhaps the most radical re-design of the microscope objective lens in over a century. The Mesolens has a unique combination of a fixed 4x magnification with an NA of 0.47, which is approximately five-times

greater than that of a conventional 4x objective lens<sup>111</sup>. The low magnification results in a FOV measuring approximately 36 mm<sup>2</sup>, while the lens prescription provides a working distance of 3 mm. Thanks to the unusually high NA, the Mesolens has a lateral resolution of 700 nm and axial resolution of 7  $\mu$ m throughout the entire 108 mm<sup>3</sup> imaging volume<sup>111</sup>. It is important to note that observing subcellular structures with the Mesolens does not require any change in lens magnification as with traditional microscopes. Instead, one can observe sub-cellular structures simply by manipulating the digital zoom on any image analysis or viewing software (Figure 1.12). Moreover, the lens is chromatically corrected across the visible spectrum and designed to be compatible with various immersion fluids, which further sets it apart from other optical mesoscopy techniques. Currently, the Mesolens is fitted with confocal laser scanning and widefield epifluorescence modalities<sup>111,112</sup>, but has

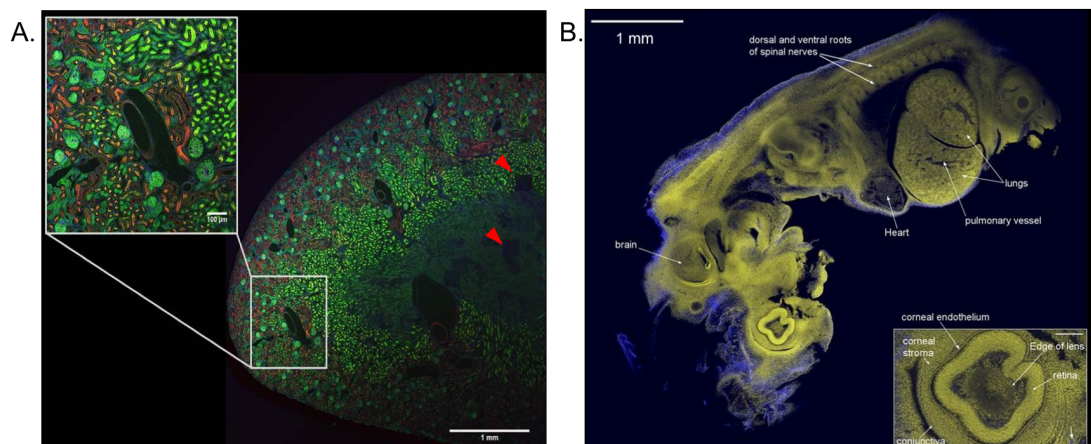


**Figure 1.12. High-resolution large FOV imaging using the Mesolens. a)** A widefield epifluorescence Mesolens image of a 16  $\mu$ m-thick mouse kidney section stained with Alexa488-Wheatgerm Agglutinin (green), Alexa568-Phalloidin (red), DAPI (blue) acquired using confocal mesoscopy. Regions where photobleaching has occurred after imaging of smaller sections with a conventional confocal microscope are indicated by red arrows. **b)** Single confocal Mesolens laser scanning image of a 12.5-day-old mouse embryo stained with acridine orange (yellow) and an Alexa594- $\beta$ -III-tubulin conjugate staining neuronal axons (blue). Adapted from <sup>111</sup>.

recently had the addition of HiLo microscopy<sup>113</sup> and development is ongoing for dark field, differential phase contrast, light sheet and TIRF modalities.

In confocal laser scanning mode, the optical setup of the Mesolens follows that of a conventional CLSM. The Mesolens itself measures approximately 55 cm long and is composed of 15 optical elements measuring up to 63 mm in diameter with an additional anti-reflection compensator plate and chromatic reflector for epifluorescence imaging<sup>111</sup> (Figure 1.13). In confocal mode, two PMTs are used for multi-channel imaging, and a high pixel-number camera can be used for widefield imaging. In order to sample as close to the Nyquist limit as possible, Mesolens images have to be approximately 20,000 pixels wide, which is only currently achievable in widefield mode by using a camera detector which has a chip-shifting modality<sup>111</sup>. The large images generated by the Mesolens leads to equally large datafiles, for example a 3-channel full-volume z-stack would produce a dataset >1.5 terabytes. Therefore, handling and storage of Mesolens data must be carefully managed.

#### **1.4.2 Other high-resolution, large FOV methods for bioimaging**

Aside from the Mesolens, other recent advances in optical microscopy have also allowed for imaging of relatively large live samples with high spatial resolution. Light sheet microscopy has been used as a “gentler” alternative to confocal laser scanning techniques with increased temporal resolution for imaging a variety of relatively large biological samples<sup>114</sup>. Due to the lower levels of phototoxicity and photobleaching observed during light sheet microscopy, images can be acquired over long periods to observe complex biological processes such as plant root growth<sup>115</sup>, development of insect larvae<sup>116</sup> and *in vivo* immune cell dynamics in live zebrafish<sup>117</sup>. However, the axial resolution of lightsheet microscopy is often compromised when imaging large samples due to the nature of Gaussian optics (i.e. the narrower the beam waist, the faster it diverges). In reference to the Mesolens, to achieve a light sheet which could



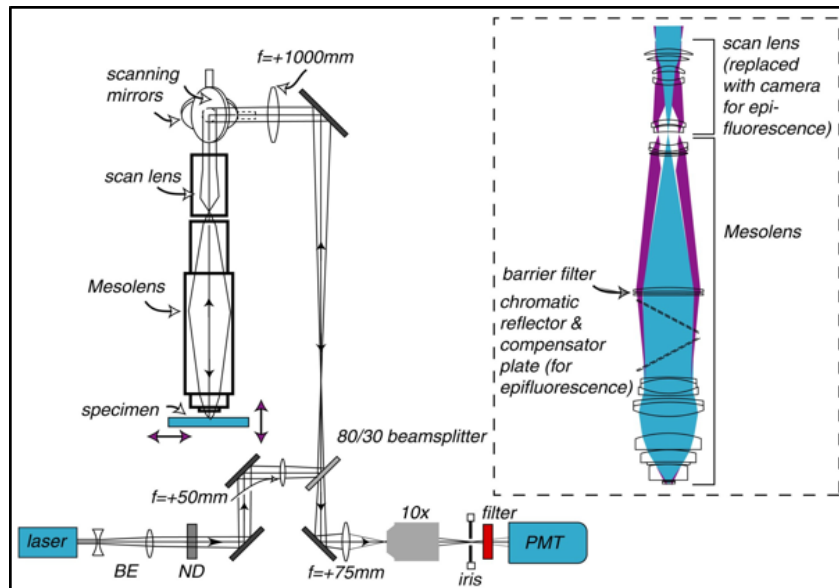


**Figure 1.13. An overview of the confocal laser scanning setup of the Mesolens.** The Mesolens itself is in the form of a large objective lens coupled to a large scanner and a confocal laser scanning system. In confocal mode, incident light is provided by a laser source and propagated through a series of optical elements before being directed towards two large aluminium-coated scanning mirrors and on through the scan lens and Mesolens. In the Mesolens itself (dashed cut-out) there are 15 optical elements up to 63 mm in diameter, hence why this instrument is not able to be implemented into a standard CLSM system. For widefield epifluorescence mode an additional compensator plate and chromatic reflector can be fitted, and incident light is source from a from a series of LEDs coupled into the optical path. Reproduced from <sup>111</sup>.

propagate over a full 6 mm FOV and achieve comparable axial resolution to that of the Mesolens, the beam waist would have to be on the order of 40-50  $\mu\text{m}$ , which would be inadequate to study the dynamics of, for example, live bacterial colonies as discussed in Chapter 3. Recent work has sought to address this by engineering different types of non-diffracting beams such as Bessel and Airy beams<sup>118–122</sup>.

However, these approaches have not yet been able to produce a lightsheet which would be suitable for imaging large microbiological specimens.

In regard to other comparable large FOV imaging techniques, a recently developed 2-photon random access microscope (2p-RAM) has been developed which has a FOV of 5 mm and sub-cellular resolution throughout the field<sup>123</sup>. However, the 2p-RAM is limited by a 1 mm imaging depth and is only suitable for use with a fixed wavelength infra-red excitation source, whereas the Mesolens has a comparative imaging depth of 3 mm and is chromatically corrected across the visible spectrum. Other optical imaging techniques such as ultrasound<sup>124,125</sup>, optical coherence tomography and photoacoustic tomography<sup>126–128</sup> are capable of imaging samples at the mesoscale, however the spatial resolution of these techniques is lower than that of the other mesoscopic imaging methods. As previously introduced, stitching and tiling offers a method of high resolution large FOV imaging, and have been previously used to investigate the structure of microbiological specimens. Others working in the field of biofilm imaging have used tile-scanning microscopes or automated scanning microscopes which change the location of the FOV or focal plane to match growing colonies. In doing so others have been able to image live biofilms over multiple spatial scales, from  $1 \times 10^1$ - $1 \times 10^4$  cells<sup>129–131</sup>, however using the Mesolens one can visualise bacterial colonies in excess of  $1 \times 10^9$  cells while maintaining sub-micron resolution throughout the entire  $36 \text{ mm}^2$  field within a single image. Therefore, in comparison with other large specimen imaging techniques, the Mesolens stands as a novel and appropriate method for *in situ* imaging of live bacterial communities.

## 1.5 The gliding motility of *Myxococcus xanthus*

*Myxococcus xanthus* traverses its environment by means of gliding motility which is relatively rare among bacterial motility mechanisms. These Gram-negative rod-

shaped bacteria do not express flagella or cilia like other many other motile microorganisms, instead they use a combination of slime extrusion, pili expression and intracellular motor complexes to propel themselves over the underlying substrate<sup>132,133</sup>. These bacteria exhibit three behavioural traits linked to their nutrient requirements; swarming occurs during the search for nutrient sources in groups of cells; predation occurs when single cells 'hunt' for their prey (e.g. *E. coli*); and fruiting body formation when nutrients are scarce, resulting in sporulation and formation of spore-bearing structures which hold and disseminate their spores<sup>134,135</sup> (Figure 1.14). The earlier work of Blackhart & Zusman demonstrated that *M. xanthus* glides at a speed of approximately 5  $\mu\text{m}/\text{minute}$  and interestingly exhibits a time-dependant directional change, where motile cells will reverse their trajectory every 7-8 minutes on average<sup>136,137</sup>. As described by Nan & Zusman, *M. xanthus* can also use its gliding motility for two distinct purposes; social (S) motility and adventurous (A) motility<sup>134</sup>. Social motility is used for groups of cells which move together and facilitates the swarming of communities of cells in the search for nutrients. This is achieved through retraction of type IV pili which attach to an exopolysaccharide matrix to generate mechanical force which pulls the cell forward<sup>138</sup>.

On the other hand, A-motility is used for the predation segment of the bacterium's life cycle. The mechanism of A-motility has been debated in recent years; however, it is now regarded as a combination of both slime extrusion and the activity of transient adhesion complexes which much like eukaryotic apicomplexan motility observed in amoeboid protozoa<sup>133,137–139</sup> (Figure 1.15). In 2002, Wolgemuth *et al.* discussed a conserved motility mechanism involving slime extrusion across several bacterial species. They showed that slime is produced by specialised nozzle-shaped organelles expressed at the lagging-pole of the cell<sup>132</sup> (Figure 1.15a). It was argued several years later that slime extrusion alone could not be responsible for the motility

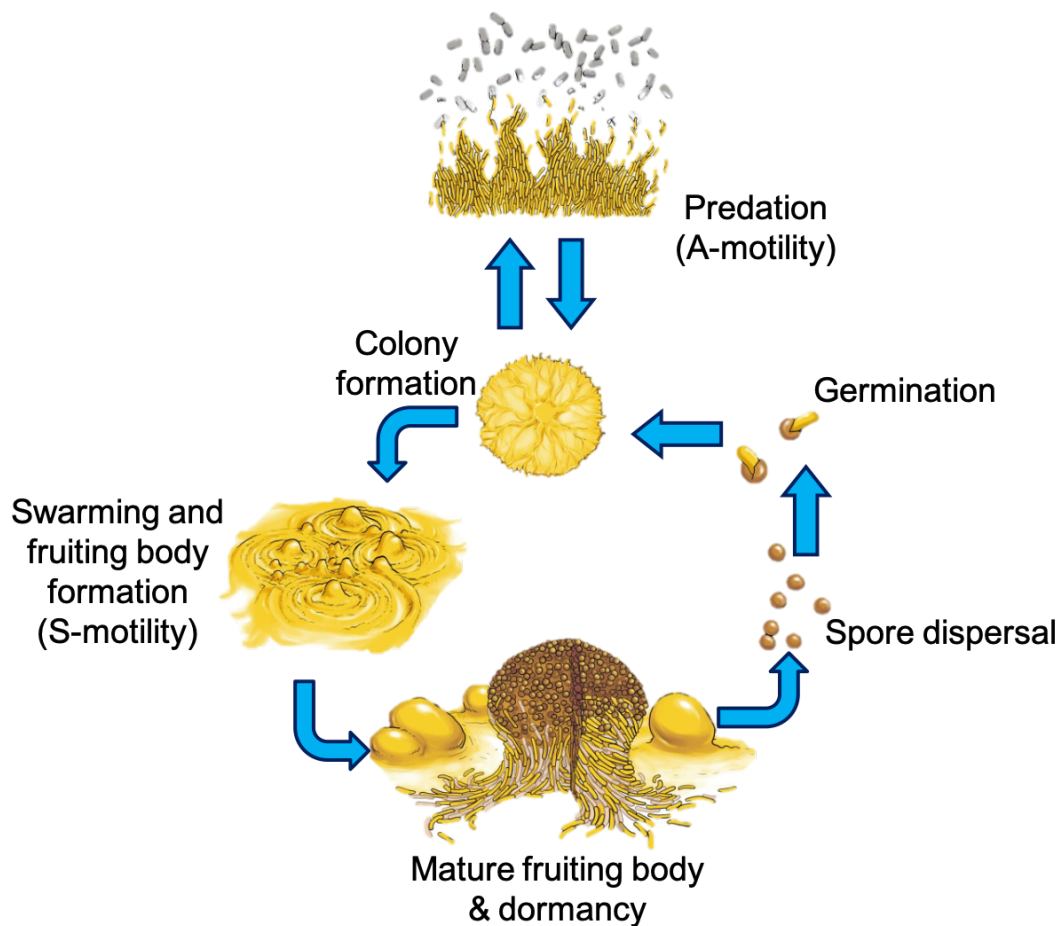


**Figure 1.14. The complex lifecycle of *Myxococcus xanthus*.** *Myxococcus xanthus* exhibits several developmental stages during different environmental conditions. During favourable conditions, spore germinate, and cells aggregate to form dense colonies. Adventurous (A) motility drives predation as *M. xanthus* spreads throughout the local environment in search of prey. Swarming is facilitated by social (S) motility in nutrient-deprived conditions where cells come together and form macroscopic 3D differentiated fruiting bodies. Sporulation occurs to protect cells from desiccation and remain dormant until favourable conditions arise again. Adapted from <sup>135</sup>.

of *M. xanthus*. Instead, Mignot *et al.* suggested that although slime production may be a factor in the gliding mechanism, that a focal adhesion theory would more likely be the driving force behind gliding motility<sup>139</sup>. This hypothesis seems to concur with other studies which show rotational movement of the cytoskeleton and slime extrusion in *Cytophaga spp.* and *Flavobacterium johnsoniae*, which are examples of gliding

bacteria belonging to the *Bacteroidetes* phylum<sup>101,140</sup>. The rotational mechanism of gliding was elucidated in *M. xanthus* by the characterisation of the AgmU complex; an inner-membrane-spanning A-motility protein complex (Figure 1.15b). The AgmU complex was found to interact with the MreB cytoskeleton and drive rotational movement using proton motive force. This rotational movement distorts the surface of the cell and generated pressure waves due to an increased resistance between the cell membrane and the slime layer. Rotational movement of the MreB cytoskeleton can be facilitated through interaction with MotAB homologues which act to push against the cytoskeletal tract<sup>141</sup>. Another conflicting hypothesis has also been outlined which suggests that motility is achieved by postulated cell-surface adhesin proteins which propel the motor complexes<sup>142,143</sup>. A recent study has also suggested the role of exopolysaccharide microchannels in the organisation and motility of *M. xanthus*.

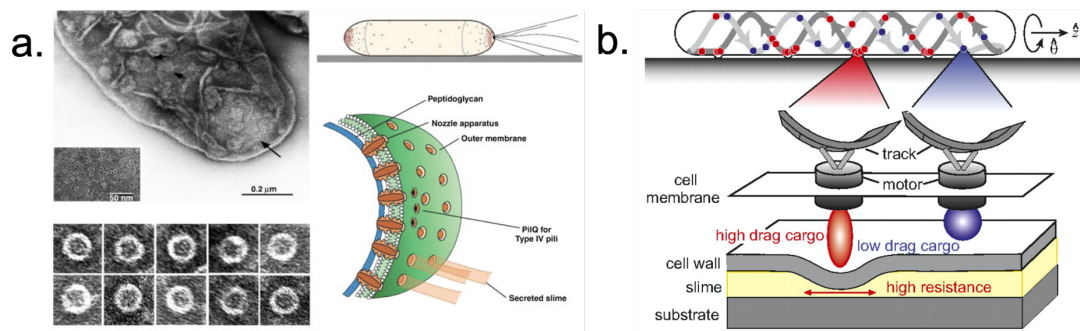


**Figure 1.15. Canonical gliding motility mechanisms in *Myxococcus xanthus*.** The mechanism of gliding motility in *M. xanthus* has been widely accepted to be caused by a combination of slime extrusion from the poles of the cell and interactions with the MreB cytoskeleton. **a)** Specialised nozzle-shaped organelles expressed on the outer-membrane at the cell's poles. Type IV pili may also be involved here during S-motility in the leading pole. Electron micrographs of the lagging pole of an *M. xanthus* cell showing the nozzle-shaped apparatus measuring 14 nm in diameter. **b)** The AgmU complex, an inner-membrane-spanning complex which attaches to MreB via MotAB proteins. Proton motive force results in movement of the cytoskeleton and directional movement over the substrate. Adapted from <sup>132,141</sup>.

*Myxococcus xanthus* has been shown to produce a 3D exopolysaccharide matrix which not only organises the directionality of cells but also provides structural support for the formation of fruiting bodies<sup>144</sup>.

Almost all documented gliding behaviours of *M. xanthus* have been reported using conventional widefield and confocal laser scanning methods. Due to the small size of bacteria, 3D optical imaging has historically proven challenging, and so the 3D behaviour of live bacteria remains unknown. However, as shown in Chapter 2 and by Rooney *et al.*, 3D bacterial imaging is possible using IRM and can be used to show that bacterial gliding motility is not merely limited to a single lateral plane<sup>145</sup>. Chapter 2 will provide an overview of how *M. xanthus* is able to move in all three dimensions by means of an aperiodic oscillatory behaviour.

## 1.6 An overview of bacterial biofilms

### 1.6.1 Bacterial biofilms

Biofilms are large aggregates of cells and extracellular materials which attach and grow typically at an interface between two surfaces, biotic or abiotic (i.e. either air, liquid or a solid surface)<sup>146,147</sup>. The cells which make up these biofilms produce an extracellular matrix (ECM) typically containing exopolysaccharides (EPS), signalling molecules and other proteins<sup>148,149</sup>.

The formation of a biofilm begins with the attachment of planktonic cells to an interface where they will begin to produce ECM components, continue to divide and attract other planktonic cells. Biofilms form by adhesion of planktonic (freely motile) cells to an interface where they will start to produce an ECM, continue to divide and attract other planktonic cells<sup>147</sup>. As the mass increases a macroscopic structure forms where cells can break free of the biofilm to become planktonic once more and restart the biofilm formation cycle<sup>150,151</sup> (Figure 1.16a). The process of biofilm formation is tightly

regulated and involves multiple signal cascades which cause planktonic bacteria to coalesce at an interface and aggregate (Figure 1.16b). Briefly, the most important of these cascades involve the intracellular secondary messenger cyclic-di-guanosine monophosphate (c-di-GMP). Following activation of membrane-bound signalling receptors (e.g. WspA), c-di-GMP is activated and goes on to upregulate EPS and alginate biosynthesis, adhesion proteins, and membrane pumps, while downregulating motility genes<sup>152–154</sup>. The second important pathway is that involving cyclic-adenosine monophosphate (cAMP), which upregulates biofilm formation by decreasing motility, increasing adhesion and increasing EPS production<sup>153,155,156</sup>. Aside from these widely conserved secondary messenger systems, processes such as quorum sensing, cell wall stress, mechanical sensing and environmental toxicity can all lead to biofilm formation<sup>153</sup>.

Due to their composition, biofilms offer an inherent protection to their constituent bacteria from both mechanical and chemical factors. Therefore, they are an emerging problem in public health, being involved in 80% of all chronic infections<sup>157</sup>, due to their ability to confer resistance to antimicrobial compounds<sup>158</sup>. Their resilience to antimicrobials can arise in several ways; high cell densities result in decreased penetration of the drug into the biofilm, high expression of  $\beta$ -lactamases which degrade certain antibiotics and the adaptation of persister cells which promote resistance by initiating horizontal gene transfer after the application of an antimicrobial<sup>159</sup>. Aside from public health, biofilms have also become a significant problem in industries such as brewing, water management and food processing due to their resilience to mechanical and chemical clearing<sup>160–164</sup>.

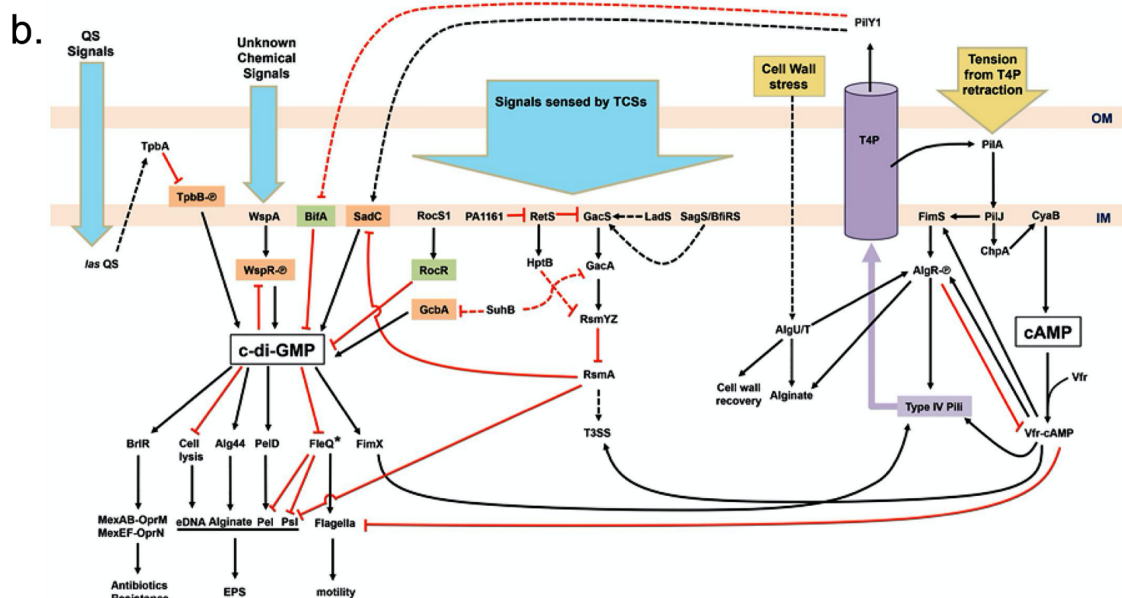
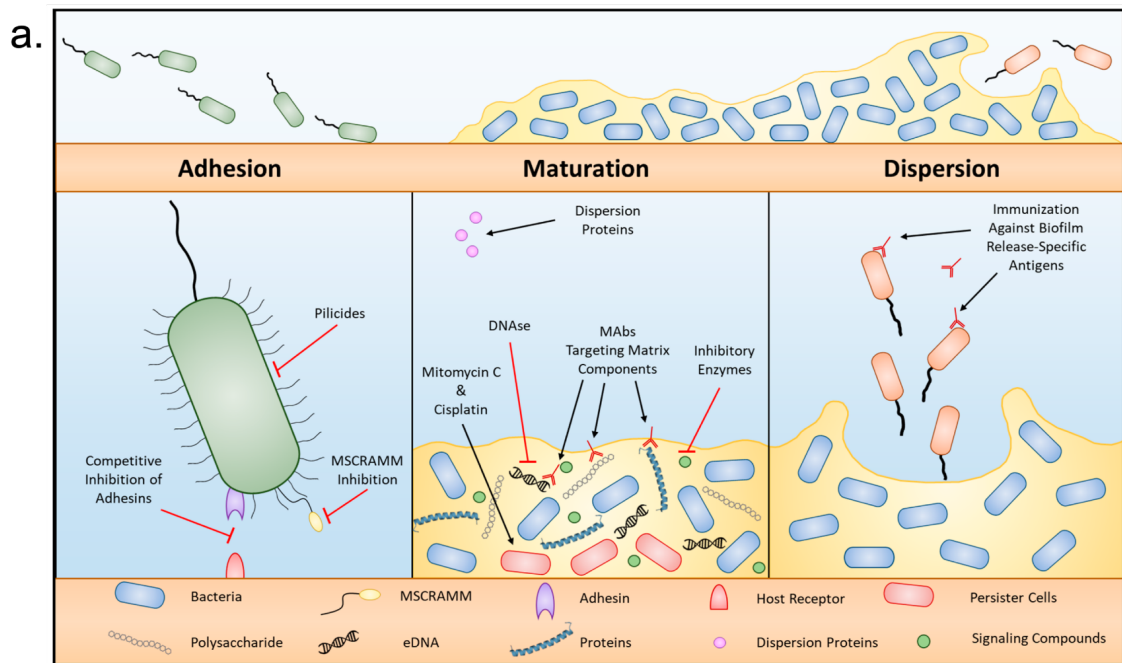


**Figure 1.16. Development and regulation of biofilms.** **a)** A diagram of the key stages in biofilm formation. Following adhesion of motile planktonic cells, the biofilm is established and matures as the ECM is deposited by cells. Mature biofilms can then shed cells to disperse them throughout the environment and re-colonise other surfaces. Some common biofilm dispersal agents and matrix components are also presented, including microbial surface components recognizing adhesive matrix molecules (MSCRAMMs), extracellular DNA (eDNA) and EPS. **b)** The regulation of biofilm formation detailing the main c-di-GMP and cAMP pathways. This diagram outlines biofilm regulation for *Pseudomonas* spp., but many of the key processes are conserved across species. Panel a) adapted from <sup>151</sup>, Panel b) adapted from <sup>154</sup>.



The study of biofilm architecture has developed over the past several years and has explored the role of extracellular components and secreted macromolecules which provide the biofilm with spatial organisation and structural support. Among these surface structures are type I pili (fimbriae), antigen43 (Ag43), colanic acid, cellulose, curli and flagella<sup>165</sup> (Figure 1.17). Fimbriae allow for attachment of *E. coli* onto solid surfaces and are key to the infection cycle of strains such as Uropathogenic *E. coli* (UPEC) and Enterohaemorrhagic *E. coli* (EHEC) O157:H7. These tubular structures (5 nm x 2 nm) are expressed across the cell's surface, with as much as 500 fimbriae per cell, and in the presence of mannose will bind to various host cell surface receptors and abiotic targets to ensure attachment<sup>166</sup>. Antigen 43 is another widely expressed extracellular component of both commensal and pathogenic *E. coli*. This protein facilitates attachment between cells, instead of attachment to a solid surface, and promotes aggregation of *E. coli* leading to the three-dimensional colonies which we observe on agar plates<sup>167,168</sup>. When environmental conditions are unfavourable colanic acid forms a protective capsule around the bacterium and is secreted into the extracellular matrix. Colanic acid synthesis is upregulated in mature biofilms and serves to protect from chemical and environmental factors which would disrupt the biofilm<sup>165</sup>. Cellulose is another extracellular polysaccharide component of biofilms

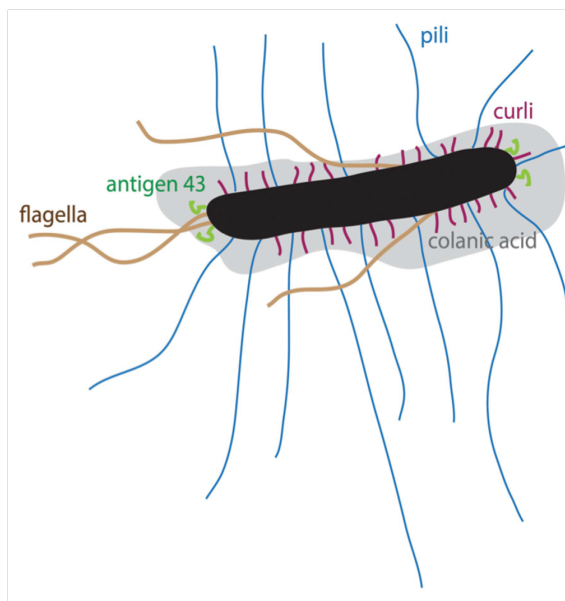


**Figure 1.17. Extracellular components of *E. coli* which promote biofilm formation.** A diagram of the extracellular components expressed in biofilm-forming bacteria. Reproduced from <sup>189</sup>.

which allows for structural support in mature biofilms and the formation of bacterial pellicles (biofilms which form on liquid-air interfaces). Curli fibres are secreted into the ECM and like fimbriae facilitate the attachment of planktonic cells to solid surfaces. As discussed by Serra & Hengge, cellulose and curli are produced by stationary-phase bacteria within the biofilm where they contribute to the formation of macroscopic wrinkles/crenulations, ridges and rings<sup>169,170</sup>. The spatial organisation of biofilms has been elucidated using electron microscopy and localisation of specific components using confocal laser scanning microscopy on thin sections of a biofilm and show that cellulose and curli appear to have different localisations within the biofilm<sup>169,170</sup>. These studies show that cellulose forms long filaments which pass between cells to provide structural support, while curli forms lattice networks around individual cells. Not only do they form different structures, their localisation also differs with curli being found nearer the surface and cellulose deeper within the biofilm<sup>169</sup>. Serra *et al.* go on to show the spatial organisation of different cell types within a macrocolony biofilm<sup>171</sup>. Correlative light-electron microscopy (CLEM) was used to show that dividing flagellate cells are localised at the base of the colony and around the periphery, while ovoid non-dividing cells are found in the upper regions and on the surface layers of the biofilm<sup>171</sup>.

It has also been shown that localised cell death within a biofilm focuses mechanical forces and results in the formation of macroscopic structures such as wrinkles and crenulations, particularly in *Bacillus subtilis*<sup>172</sup>. Flagella, along with fimbriae, are important in the initial stages of biofilm attachment<sup>173</sup>. These extracellular appendages facilitate swimming motility in *E. coli* and depending on their location on the outside of the cell control how well the cell is able to swim (i.e. unipolar, bipolar or peritrichous flagella). Flagellar biosynthesis is a complex and highly regulated process which will not be discussed here, however an informative overview is provided by Liu & Ochman

and Belas<sup>150,174</sup>. The cumulative effect of the above extracellular components ensures attachment to surfaces and promotion of biofilm formation. Additionally, in a mature biofilm they confer resistance to mechanical and environmental factors to preserve the structure of the biofilm and the survival of the constituent cells.

### 1.6.2 Spatial patterning in bacterial biofilms

Spatial structure and organisation give rise to the phenomenon of complex spatial patterning within many structures in nature from the scale of whole systems down to single cells. Typical examples of these include the branching networks of neurones in the brain<sup>175</sup>, dorsal closure in the development of *Drosophila melanogaster*<sup>176</sup>, and fractal patterns in the vasculature system<sup>177</sup>. However, these spatial patterns are also displayed by microbial communities<sup>178</sup>. Examples include phenomena such as the cooperative growth dynamics of *Bacillus spp.*<sup>179,180</sup>, the branching networks of *Streptomyces spp.*<sup>181</sup> and the fractal patterns in mature colony biofilms of *E. coli*<sup>182</sup>. Recent studies have demonstrated dynamic spatial patterning of cells within bacterial colonies as a result of environmental factors and cell-cell interactions within the colony. To this end, the emergent properties of biofilms have been studied extensively to explore the social interactions and spatial heterogeneity in bacterial communities<sup>183</sup>. These emergent properties manifest in various ways; for example, macro-colony folds<sup>172,184,185</sup>, population differentiation<sup>158,169,170,183</sup>, and sectoring of founder populations in multi-strain systems<sup>186</sup>. The findings of an intra-colony channel network presented in Chapter 3 visually resemble some of the previous strain sectoring work which has been performed over the last decade, and so it is important to note how these patterning phenomena relate to the channel structures identified here.

Rudge *et al.* discussed the fractal patterns generated by colonies which correlated with predicted computational biofilm structures produced by CellModeller<sup>182</sup>. They

suggested that patterns arise between cells which express different markers (i.e. between different founder populations). They observed cells at the edge of the fractal boundaries were arranged parallel to the course of the fractal pattern and this resulted from an amplification of the mechanical instability caused by cell growth and viscous drag of dividing cells<sup>182</sup> (Figure 1.18). Cell shape has also been noted as an important factor in determining the spatial distribution of cells within a mature colony biofilm (Figure 1.19a). In the environment biofilms are often heterogeneous, in that they can be composed of different species of bacteria which occupy the same niche. This can result in a mixture of different morphologies within biofilms such as spherical cocci and rod-shaped cells. Smith *et al.* showed that when a mixture of spherical and rod-

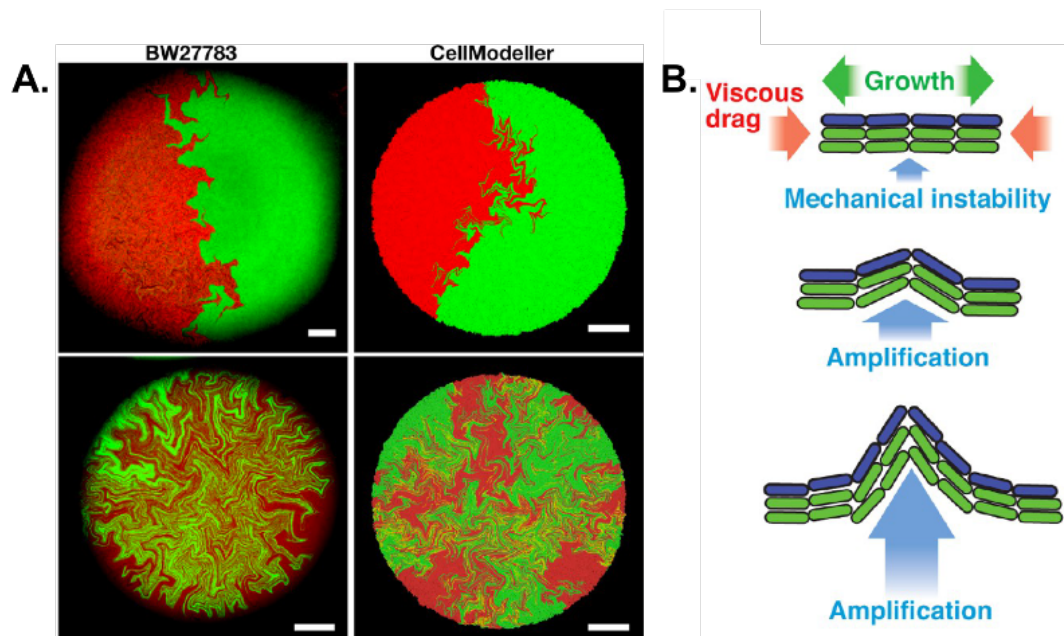


**Figure 1.18. Population sectoring in mature bacterial biofilms.** a) Left: CLSM images of colony biofilms composed of a GFP and RFP expressing strains of *E. coli*, depending on the number of cells in the starting inoculum, the degree of spatial patterning will be altered. Right: *in silico* models of experimental colony biofilms match the CLSM images presented on the left panels. b) Fractal distributions are generated by a combination of growth and viscous drag created by dividing cells and is amplified by the mechanical instability of the underlying medium. Adapted from <sup>182</sup>.

shaped cells results in a layered distribution of both cell types<sup>187</sup>. When two spherical species of bacteria were mixed, they grew to form columnar distributions of cells depending on where the progenitor cell was positioned at the start of colony growth. When two rod-shaped species were mixed, a fractal pattern arose between each domain which concurred with the earlier work of Rudge *et al.*<sup>187</sup>.

The fractal-like patterns which are shown in literature have been recently proposed to be a result of cell-cell and cell-surface interactions during the formation of the bacterial colony (Figure 1.19b & c). Co-cultures of strains with differing social interactions have been shown to have profound effects on the patterning of bacterial colonies<sup>188–190</sup>. Co-cultures of strains which exhibit positive interactions (such as commensalism, mutualism and neutralism) have been shown to increase genetic variance within the biofilm while decreasing the survival of the original bacterial lineage. Those which exhibit negative social interactions (such as parasitism, amensalism and competition) have shown to decrease genetic variance while increasing the survival of the starting lineage due to less horizontal gene transfer between strains which preserves the lineage of the more successful strain<sup>188</sup>. Cell-surface interactions have also been reported to have an effect on the spatial distribution of bacterial colonies, and this has been shown in relation to chirality<sup>189</sup>. Chirality has been noted in various microbial colonies and is most evident in *Bacillus mycoides* colonies where they can produce clockwise or anti-clockwise spirals<sup>191</sup>. Jauffred *et al.* demonstrated this by systematically removing extracellular components of biofilm-forming strains of *E. coli* to observe the effect on the chirality exhibited when two strains are co-cultured and following deletion of the key extracellular components involved in biofilm formation and altering the components of growth medium<sup>189</sup>. This showed that the spatial distribution of bacteria within colonies and biofilms therefore arises from a

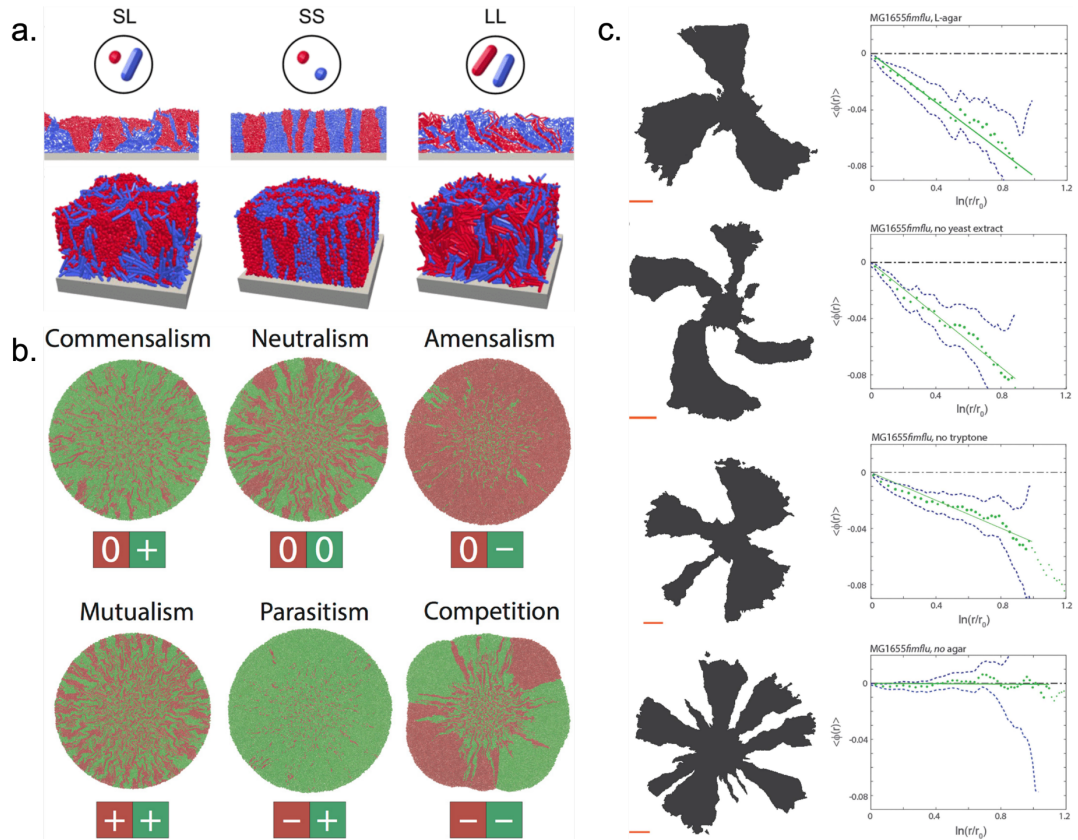


**Figure 1.19. The role of cell-cell and cell-surface interactions in biofilm patterning.**

**a)** *In silico* modelling of the effect of cell shape in biofilm spatial patterning. Short (S) and long (L) cell types are mixed in different combinations, resulting in different spatial organisation throughout the mature biofilm. **b)** Various social interactions which have an effect on the phenotypic heterogeneity in mature biofilms. “0” = baseline fitness, “+” = advantaged, “-” = disadvantaged. **c)** Various cell-surface interactions which have an effect on the phenotypic heterogeneity in mature biofilms. Two strains (black and white) were grown in mixed colonies to produce radial sectors. Colony chirality was altered by changing the surface stiffness and nutrient profiles of the growth medium. Changes in chirality were measured by comparing the average boundary angle ( $\langle\phi(r)\rangle$ ) to the radial vector of the sector boundary ( $\ln(r/r_0)$ ). Scale bars = 1 mm. Adapted from <sup>187-189</sup>.

combination of interactions between growing cells and the interactions of their extracellular matrix components with the underlying substrate.

The patterning in bacterial colonies has been proposed as a method by which bacteria promote genetic diversity and microbial evolution. Goldschmidt *et al.*, suggest that successive range expansion (i.e. seeding a fast-growing and slow-growing strain and having the slow-growing strain grow through the leading edge of the colony created by the fast-growing strain) facilitates horizontal gene transfer between co-cultured strains which form fractal pattern in colonies, thereby increasing the genetic diversity of the colony<sup>190</sup>. A practical application of spatial patterns in bacterial communities is morphogenetic engineering, where one strain can be genetically programmed to instruct patterning cells to produce a product when induced by an exogenous chemical signal is present. This is achieved by culturing an underlying layer of actuation cells which some of the genes necessary for the desired product, while culturing a patterning layer on top which contains at least two strains to form a pattern as noted above, but with one strain expressing the remained of the desired genes<sup>192</sup>. The actuation layer and the patterning layer then produce the desired product by effectively complementing the missing genes in each strain to produce the desired product<sup>192</sup>. Nuñez *et al.* showed that morphogenetic engineering can also be used to inhibit production of proteins in a similar way using a CRISPRi/Cas9 approach<sup>192</sup>. The ability to control the growth of colonies and the substances they produce in this way is limited in practical application as most industrial biotechnology processes use batch or continuous liquid cultures in place of solid cultures. Indeed, many processes actively wish to remove or avoid biofilm formation which would reduce the efficiency of production. Therefore, these applications, although interesting, remain largely inapplicable to the wider field and feature instead as a method for studying the

development and morphogenesis of bacteria in microbial ecology and synthetic biology.

It should be emphasised that the instances of spatial patterning in bacterial colonies mentioned in literature have been observed in colonies composed of multiple strains based on cell-cell and cell-surface interactions. The structures reported in Chapter 3 arose as an emerging property of biofilm formation by a single strain and the fractal-like channels were devoid of cells. Chapter 3 will provide evidence of a previously undocumented functionalised channel system in mature *E. coli* colonies using the Mesolens.

## 1.7 Microbial soil ecology

Bacteria are prolific in terrestrial soils and marine sediments, with high bacterial diversity across a range of soil types and climates<sup>193–198</sup>. The composition of soils is heterogeneous, being composed of clay, silt, sand and pebbles<sup>199</sup>; thus, providing a range of habitats for microorganisms to colonise, either on the surface of particles or the interstitial space. In general, soil bacteria are thought to exist as biofilms associated with plant roots, soil particles or detritus<sup>200</sup>, or as dormant spores during nutrient exhaustion<sup>201</sup>. However, given their hypothesised colonisation phenotypes in the environment, bacteria are not routinely cultured in environments which mimic their natural habitats. This is mainly because soil is difficult to work with as a culture medium for three reasons; due to varying geographical composition<sup>202–204</sup>, the presence of bacteriophage and unwanted contaminants (which can be removed by sterilisation, but may also destroy any nutrients)<sup>205</sup>, and high autofluorescence and intrinsic scattering which prevents study by many microscopical methods. Therefore, most phenotypic observations of soil bacteria are performed on 2D agar surfaces, which are not representative of how they would grow and interact in the environment.



It was thereby hypothesised that culturing bacteria in a tactile 3D environment may provide novel outlooks on how they behave in their native environment. These behaviours could extend to growth dynamics, specialised metabolite production, interspecies and interkingdom interactions, and colonisation phenotypes.

It was recently shown that a synthetic mimetic transparent soil environment can be used to grow and study plant roots, and furthermore, to study bacteria associated with plant roots<sup>206,207</sup>. This 3D environment was designed and optimised to culture plant root systems, but there has been no system developed purely for the purpose of bacterial cell culture. The motivation to develop a synthetic soil system purely for bacterial culture came from observing the work of Downie *et al.*, where EHEC was able to be cultured in the rhizosphere<sup>207</sup>. However, the bacteria depended heavily on the parasitic interaction with the plant roots for survival and would have been unable to grow successfully without nutrients from the plant. Moreover, this study used light sheet microscopy to capture image volumes around individual root hairs, but the global colonisation phenotype was not explored. Therefore, there was an opportunity to refine the transparent soil method specifically for bacterial culture, while incorporating optical mesoscopy with the Mesolens to understand the behaviour of soil bacteria in a mimetic environment over multiple spatial scales. Chapter 4 will outline the fabrication and optimisation of a Nafion™ polymer soil in further detail, which was used to culture soil bacteria in a controlled mimetic environment. This soil could be refractive index matched, where the Nafion™ soil particles were submerged in a solution of equal refractive index to the Nafion™ polymer, thus minimising light refraction and rendering the particles transparent. To this end, the colonisation behaviours of soil bacteria can now be studied in a fully controlled mimetic 3D environment as never before – with the potential to visualise alternative colonisation behaviours *in situ*.

## 1.8 Research aims and objectives

The work described in this thesis centres on the application of advanced optical microscopy to various microbiological questions. Firstly, do bacteria exhibit 3D behaviours as they traverse their environment, and could this be studied using IRM? Additionally, could the 3D orientation of the specimen be made more evident in IRM by adopting a multi-wavelength approach? This was studied using the gliding bacterium, *M. xanthus*, which was hypothesised to glide laterally while adhered firmly upon a solid substrate. A multi-wavelength variant of confocal IRM was optimised and characterised before applying to microbiological specimens for the first time.

Secondly, following the identification of a network of intra-colony channels in mature *E. coli* macro-colonies, there were three main objectives to answer. One, what were these channels composed of? Two, how did the channels form? And three, what function did the channels play in the context of the biofilm and, if beneficial, could this function be exploited? The Mesolens was required to study the spatial organisation of macro-colonies at multiple spatial scales simultaneously and was used to visualise intact multi-millimetre biofilms while resolving over  $1 \times 10^8$  individual bacterial cells. This is a feat which no other optical microscopy method could achieve and provides a new approach for studying the role of individual bacteria at global scales.

Thirdly, could a 3D mimetic culture environment be optimised to study the behaviour of soil bacteria *in situ* by microscopy. Bacterial behaviour has been documented using the same basic 2D culture methods since the time of Koch and Pasteur, over 170 years ago. Given the innumerate range of bacterial behaviours which have been documented by these methods, it was hypothesised that previously unobservable phenotypes could be documented by culturing bacteria in a 3D environment. Not only may this have shown new behaviours, but additionally provides a more representative view of how bacteria grow in their natural environment.

# Chapter 2

## Multi-wavelength confocal interference reflection microscopy reveals novel gliding behaviours in *Myxococcus xanthus*

This chapter describes the development and application of a multi-wavelength confocal variant of interference reflection microscopy to the gliding delta-proteobacterium, *Myxococcus xanthus*. Firstly, the imaging methods were used to characterise a specimen of known geometry to ensure that reliable extraction of 3D information was feasible. Then, for the first time, confocal IRM was applied to bacteriological specimens. Novel gliding behaviours were identified in wild type gliding bacteria, revealing an aperiodic oscillatory behaviour with changes in the position of the basal membrane relative to the substrate on the order of 90 nm *in vitro*. The wild type was then compared with mutants that have reduced motility, which also exhibited the same changes in adhesion profile during gliding. It was then determined that the general gliding behaviour is independent of the proton motive force-generating complex, AgIRQS, and suggested that the novel behaviour we present here may be a result of recoil and force transmission along the length of the cell body following firing of the Type IV pili.

Sections of this Chapter have been adapted from Rooney *et al.* (2020a)<sup>145</sup>.

## 2.1 Introduction

### 2.1.1 Bacterial gliding motility

Bacteria have evolved a number of ways by which they are able to travel through their environment, with the most studied mode of bacterial motility being flagellar-mediated movement. Most bacteria depend on the use of extracellular appendages such as flagella or pili to swim through their environment, or they exist as non-motile planktonic cells which drift in liquid environments due to Brownian motion or attached to surfaces<sup>150</sup>. The ability of bacteria to undergo directed movement in response to chemotactic signals underpins behaviours such as biofilm formation<sup>208,209</sup>, host colonisation<sup>210–212</sup>, and communal swarming and predation<sup>213</sup>. Other modes, such as the twitching motility displayed by *Pseudomonas aeruginosa*, use Type IV pili (T4P) to direct movement based on the extension, adhesion and retraction of polar filaments from the leading pole of the cell<sup>1,2</sup>. However, not all bacteria rely solely on extracellular appendages for motility. The phenomenon of surface-based gliding motility has been identified in a diverse range of bacterial species spanning phylogenetically diverse phyla including *Flavobacterium johnsoniae*, *Cytophaga hutchinsonii*, *Mycobacterium mobile* and *Myxococcus xanthus*<sup>101,140,214,215</sup>.

The Delta-proteobacterium *M. xanthus* displays two different modes of gliding motility - adventurous motility and social motility - to seek out nutrients or prey as part of its complex lifecycle<sup>101,133–135,141,143,216,217</sup>. There are contrasting models proposed to explain the mechanisms underpinning gliding motility<sup>102,139,141,218,219</sup>. The focal adhesion complex (FAC) model proposes that FACs form on the basal surface of the cell and attach to the underlying substrate while coupling to the helical MreB cytoskeleton on the cell's inner-membrane<sup>102,139,220,221</sup>. It has been shown that FACs translocate linearly from the leading pole as the cell moves forwards and is driven by

the force generated by the AgIRQS gliding complex, which is associated with the FAC<sup>139,142</sup>. The FAC model requires the basal layer of the cell to be firmly attached to the underlying substrate, however, it remains unclear how the complex is able to traverse the peptidoglycan cell wall without compromising the structural integrity of the cell<sup>219,222</sup>. A second model has been suggested where proton motive force (PMF) generated by AgIRQS results in a helical rotation of the MreB cytoskeleton in gliding cells which are firmly adhered to a solid substrate<sup>141,142,223–225</sup>. In the helical rotation model, stationary foci of fluorescently-tagged motor complex subunits have been explained as being a build-up of multiple complexes arrayed in “traffic jams” which result from areas of differing resistance in the underlying substrate<sup>141,224</sup>. Both models converge where the gliding cell is adhered firmly to the surface of the underlying substrate to facilitate gliding. However, our observations show that cells are not in fact firmly adhered during gliding motility, but instead exhibit aperiodic fluctuations in surface adhesion as they glide.

### 2.1.2 Background theory for IRM

For the image formation theory in IRM, a simplified three-layer model system is assumed that only consists of the coverglass (*g*), the cell medium (*m*) and the cell (*c*). In this model, the cell medium can be viewed as a thin film with varying height, dependent on how closely the cell is attached to the coverslip. The reflected light beams at the coverglass-medium (*g-m*) and the medium-cell (*m-c*) interface coincide, leading to de-/constructive interference dependent on the optical path length difference between the two beams<sup>226</sup> (Figure 2.1).

Since the refractive index of the cell medium is smaller than the refractive index of the cell, a 180° phase shift occurs upon reflection<sup>106</sup>. Accordingly, deconstructive interference occurs at optical path length differences of  $z = N \frac{\lambda}{2n_m}$  and constructive

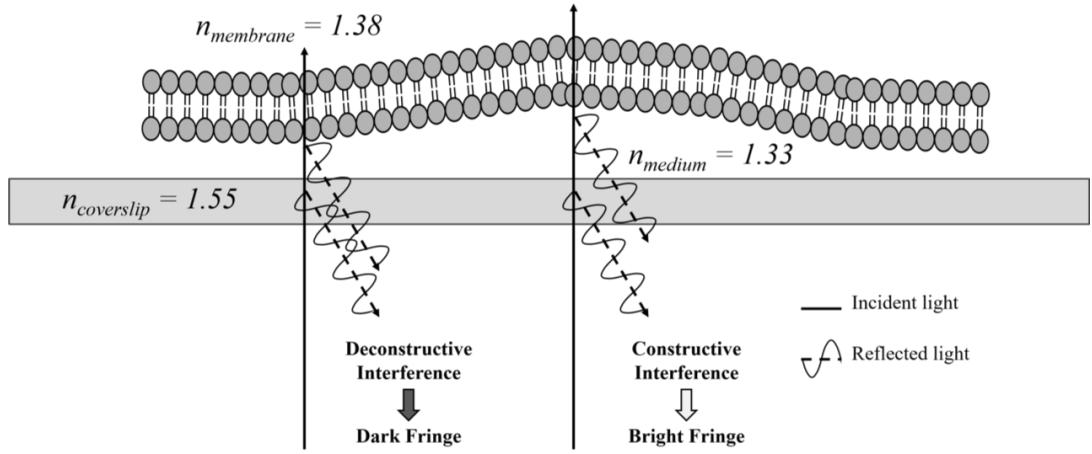


**Figure 2.1. Schematic of the IRM model.** The model system consists of the coverslip, the cell medium and the cell body. Reflections occur at both the coverslip-to-medium and medium-to-cell interfaces. Propagation of direction of the incident and reflected light is perpendicular to the coverslip. The two reflected light beams interfere de-/constructively, dependent on the optical path length difference. This results in the formation of bright and dark fringes which encode 3D information in the final 2D image.

interference occurs at  $z = (N + \frac{1}{2}) \frac{\lambda}{2n_m}$ , with  $N = 0, 1, 2, \dots$  etc. as the interference order,  $n_m$  = refractive index of the medium ( $m$ ) and  $\lambda$  = wavelength of reflected light. This wavelength-dependency can be used to extract the cell topology from IRM images since overlap of the interference fringes of different wavelengths decreases with increasing distance between the cell and the coverslip. The decreasing fringe overlap with increasing separation between the cell and coverslip, as observable in colour-merged IRM images obtained for different wavelengths, results in a clear colour-ordering along the cell body when the cell is lifted up from the coverslip.

There are several assumptions of this IRM model which are taken into account. They are that no other refractive index boundary exists in the cell specimen (i.e. that the refractive index of the cell is constant) and that incident and reflected light are perpendicular to the coverslip<sup>91</sup>. Also, the impact of the NA is neglected which

affects the depth of field that is imaged. In IRM, high NA objectives are used to limit detection of reflection signals to those originating from interfaces close to the coverglass, which establishes an experimental condition that is close to the three-layer system established, here, consisting of the coverglass, the cell medium and the cell body<sup>105</sup>.

### **2.1.3 Interference reflection microscopy for bacterial imaging**

Bacterial gliding motility has mainly been studied using phase contrast and fluorescence microscopy techniques which do not provide 3D information about cell movement<sup>102,141,142,227</sup>. It was hypothesised that axial changes in cell shape during gliding motility may occur due to the complex nature of underlying mechanisms such as FAC translocation and bulk movement of the cytoskeleton. It was reasoned that novel 3D behaviours could be visualised using the label-free microscopy technique interference reflection microscopy (IRM). This technique has previously been used to study focal adhesion sites of eukaryotic cells on glass substrates<sup>90–94,96,97,228</sup> and microtubule dynamics<sup>98–100</sup>. Previous studies have used widefield IRM to observe gliding motility in *Cytophaga spp.*, where rotation and adhesion to glass surfaces were characterised<sup>101</sup>. Twitching motility in *Pseudomonas fluorescens* has also been investigated using widefield IRM, where the attachment profile of twitching cells was found to be dependent on the presence of different electrolytes<sup>104</sup>. However, these previous widefield IRM studies have a low contrast between the orders of interference, arising from the short coherence length of the light source. The contrast of higher order interference fringes can be improved by using IRM in confocal mode where coherent laser light is used and out of focus signal is significantly reduced by incorporating a pinhole before the photodetector<sup>105</sup>.

One modification that decreases the information gap in IRM data is the use of multiple incident wavelengths which, when reflected, separate along the optical axis and the

different constructive orders fill in “gap” of the deconstructive orders. Using multiple wavelengths of incident light also provides directional information based on the colour ordering of IRM fringes. A similar method has been demonstrated using a supercontinuum light source<sup>229</sup> but has yet to be applied to confocal IRM.

The application of IRM to biological specimens has been documented since the 1960s, but the interpretation of IRM data can be difficult<sup>90</sup>. The theoretical axial resolution of IRM can be 15 nm<sup>90</sup>, compared to a few hundred nanometres for confocal microscopy. However in practice, factors such as dense protein aggregates, transport of dry mass to the basal membrane, changes in local membrane density and proximity of intracellular structures to the membrane affect the contrast of the detected IRM image<sup>106,229</sup>. However, in thin specimens such as bacterial cells, where internal shifting of dry mass is unlikely due to the lack of intracellular vesicular transport, IRM remains a viable height-measuring technique<sup>107</sup>. Godwin *et al.* found that separation between the cell and the coverslip on the order of 100 nm can be easily distinguished without the influence from ambiguities introduced by above listed factors<sup>101</sup>. Others have disputed the capability of IRM to accurately measure close contact sites in live cells, for example, by imaging the displacement of a thin layer of fluorescent dye between adherent cells and the coverglass with TIRF microscopy<sup>230</sup>. In the present work it is assumed that the IRM contrast of bacterial specimens is an indication of height of the cell surface above the substrate.

This study is the first application of confocal IRM to bacterial specimens, to reveal key information relating to the biology of the study organism, however, previous studies have used similar techniques as a means of contrast enhancement. One such study used reflection interference contrast microscopy (RICM), where polarising filters and an antireflective objective (where a  $\frac{1}{4}$  lambda plate is included in the objective lens design) are used to filter out reflected light from outside the specimen plane<sup>105,231,232</sup>, to only



image *M. xanthus* surface detachment from the coverglass<sup>102</sup>. Total internal reflection fluorescence (TIRF) microscopy has also shown that FACs which attach to and rotate the MreB cytoskeleton are found in distinct foci on the basal side of the cell<sup>133,141</sup>. These membrane-associated complexes have been suggested to change the surface topology of the gliding cell depending on the cargo load of the molecular motor<sup>141</sup>. More recently, interferometric scattering (iSCAT) microscopy, which detects both the reflected and scattered light, has been used to observe T4P-mediated twitching motility in *P. aeruginosa*. In this work the authors generated 3D illustrations which revealed the role of T4P machinery subunits in extension, attachment and retraction based on the interference pattern in iSCAT images<sup>233</sup>.

#### **2.1.4 Experimental aims**

The primary aim of this chapter is to develop a method for 3D imaging of single bacterial cells to overcome the impracticalities of optically sectioning bacterial specimens. The introduction of a new multi-wavelength confocal approach to IRM will provide more reliable axial directionality to understand the topography of live unlabelled cells and will also provide increased contrast between interference orders to aid in analysis. Additionally, this chapter will aim to describe newly observed gliding motility behaviours in *M. xanthus* and provide a framework for further study to elucidate the underlying mechanism(s) behind the behaviours documented here.

## **2.2 Materials and Methods**

### **2.2.1 Bacterial cell culture**

*Myxococcus xanthus* cultures (see Appendix I for a list of all strains used in this thesis) were maintained as fruiting bodies on clone fruiting agar<sup>234</sup> and prepared for imaging using double casitone yeast extract (DCYE) medium (Appendix II). For imaging, cells were inoculated at high cell densities in liquid DCYE medium and grown for 48 hours

at 30°C while shaking at 250 rpm. Prior to imaging an 800 µL sample of the exponentially growing culture was removed from liquid culture and placed in a 35 mm optical-bottom petri dish with a coverslip thickness of 180 µm (cat. no. 80136; ibidi GmbH, Germany) and incubated at 30°C for 20 minutes to allow cells to adhere.

To inhibit the gliding motility of *M. xanthus* by disrupting ATP production<sup>141</sup>, sodium azide was added to the culture prior to the 20-minute incubation step before imaging at a final concentration of 80 mM.

The refractive index of liquid DCYE medium was measured to be 1.33 using an Abbe Refractometer (Billingham & Stanley Ltd., U.K.).

### **2.2.2 Interference reflection microscopy**

For the characterisation of a model lens specimen, the specimen was placed convex-side down on a 170 µm-thick coverglass measuring 50 mm x 24 mm which bridged the microscope stage insert. An Olympus IX81 inverted microscope coupled to an Fluoview FV1000 confocal scanning unit (Olympus, Japan) was used to image the lens specimen. The microscope was configured for IRM by replacing the emission dichroic by an 80/20 beam splitter. Images were acquired using a 10x/0.3 NA UPlanFI objective lens (Olympus, Japan) and reflection signals were detected using a photomultiplier tube (PMT) for each wavelength, with spectral detection limited to a 10 nm bandwidth over the wavelength of incident light used. A 488 nm line from an Argon laser source (GLG3135; Showa Optronics, Japan) was used for single wavelength acquisition. For multi-wavelength acquisition, 488 nm and 514 nm lines were provided by an Argon laser and 543 nm was provided by a Helium-Neon-Green laser source (GLG3135; Showa Optronics, Japan).

For *M. xanthus* imaging, optical-bottom dishes were placed on the stage of an inverted Olympus IX81 microscope coupled to a Fluoview FV1000 confocal laser

scanning unit (Olympus, Japan). Images were acquired using a 60x/1.35 N.A. UPlanSApo Oil objective lens (Olympus, Japan). The microscope was configured for IRM as described above with incident light of 488 nm from an Argon laser and 635 nm obtained from a 635 nm laser diode (GLG3135; Showa Optronics, Japan) for multi-wavelength acquisitions. These wavelengths were selected based on their large spectral separation, meaning that colour-ordering in the observed IRM images was more distinct. For multi-wavelength images both channels were acquired simultaneously with two separate photomultiplier tube detectors.

For widefield IRM specimens were prepared as above and imaged using a Nikon Eclipse-Ti2 inverted microscope (Nikon Instruments, USA) coupled to a Prime 95B sCMOS detector (Teledyne Photometrics, USA). Images were acquired using a 60x/1.4 NA PlanApo Oil objective lens (Nikon Instruments, USA). The microscope was configured for IRM by placing an 80/20 beam splitter in the detection path and incident light was sourced from 450 nm and 550 nm LEDs (CoolLED, UK). Multi-wavelength images were acquired sequentially.

## **2.2.3 Image processing and analysis**

### **2.2.3.1 Image processing**

Images were initially processed using FIJI<sup>235</sup>. Where specified, kymographs were made of time lapse data using the manual tracking and the Multi-Kymograph plugin (linewidth = 3 pixels). Images were linearly contrast stretched for presentation purposes only.

To illustrate the improvement in axial resolution that can be gained when using three or more wavelengths of incident light in IRM the FIJI difference operation was used to remove overlapping regions of interference fringes. This method is presented in more detail by Tinning *et al.* (2020) (*manuscript in preparation*).

### 2.2.3.2 Background correction for multi- $\lambda$ IRM data

A common problem for the analysis of IRM images is the inhomogeneity of brightness across the image that limits the use of image segmentation tools like thresholding. To correct for changes in image brightness across the field, the moving average of the  $k \times k$  neighbourhood was divided from each pixel using MATLAB 2018b. To rescale the histogram for downstream analysis in FIJI<sup>235</sup> the image intensity was rescaled by dividing by a factor of 2. This background correction workflow was developed for this study by Lisa Kölln (University of Strathclyde).

The length of the neighbourhood,  $k$ , was selected depending on the specimen that was imaged. For the lens specimen, a large  $k$ -value ( $k = 1000$ ) was chosen to prevent lowering the contrast of the lens signal. For IRM images of *M. xanthus*, where the frequency of the observed interference fringes relative to the pixel density is high, a relatively small  $k$ -value ( $k = 30$ ) proved suitable. Line intensity profiles from raw and corrected IRM images were checked to verify that the position and intensity succession of the interference fringes were not altered due to the correction method (Figures 2.11, 13 and 14).

### 2.2.3.3 Lens analysis and reconstruction

To show that multi-wavelength IRM could be used to study the changes in cell topography during gliding, a lens specimen of known geometry was first imaged and compared to the theoretical model (refer to Section 2.1.3). Lens images were analysed using a MATLAB analysis script written by Ross Scrimgeour (University of Strathclyde) for analysis of standing wave microscopy data on lens specimens<sup>85,236</sup>. Images acquired at multiple wavelengths of the lens specimen were linearly contrast adjusted and cropped to create a square image using FIJI<sup>57</sup>. A composite RGB image was created by merging the channels. The data was imported into MATLAB 2018b, and using the same radial analysis method as presented by Tinning *et al.*, the axial

height of interference fringes was calculated from the composite RGB image of the lens specimen<sup>85</sup>. The *findpeaks* function was used to determine the spacing between the experimental intensity maxima of the interference fringes. Each subsequent constructive interference fringe was subtracted from its neighbouring fringe to calculate the experimental spacing.

Lens reconstruction was performed using MATLAB. Firstly, the radial distance for each pixel was extracted from the centre of the RGB IRM image of the lens specimen. By applying *a priori* knowledge of the lens specimen geometry to the radial distance of each pixel (refer to Section 2.1.3), each pixel was assigned an axial height value based on the experimental fringe separation calculated previously. The *x*, *y* and *z* coordinates along with the image intensities were plotted to create a 3D reconstruction of the RGB IRM image.

## 2.3 Results

### 2.3.1 Characterisation of a model plano-convex lens specimen for IRM

To show that topographical information of a given specimen could be extracted from interference fringe data a specimen of known geometry was characterised before applying IRM to biological samples. Single wavelength IRM ( $\lambda = 488 \text{ nm}$ ) was initially used to image an  $f = 72 \text{ mm}$  plano-convex lens specimen in air. The resulting IRM image was compared with a theoretical schematic of a lens specimen where the concentric rings of interference fringes correspond to the topography of the specimen (Figure 2.2a and b). The normalised radial intensity plot (Figure 2.2c) was created using the same analysis script documented by Tinning *et al.* for standing wave microscopy of plano-convex lens specimens and shows the lateral spacing between interference fringes<sup>85,236</sup>. The lateral spacing and can be used to extract 3D information based on the known geometry of the lens specimen. As the axial distance

separating the interference maxima shown in Figure 2.2b follow a  $\lambda/2n$  relationship<sup>107</sup>, the height of each constructive interference order was calculated using the same analysis pipeline developed by Tinning *et al.*<sup>85,236</sup> (Figure 2.2d). For the lens shown, a fringe separation of  $248.7 \pm 1$  nm and fringe FWHM of  $124.3 \pm 1$  nm was measured, compared to a theoretical separation of 244 nm and FWHM of 122 nm (error = 1.9%).

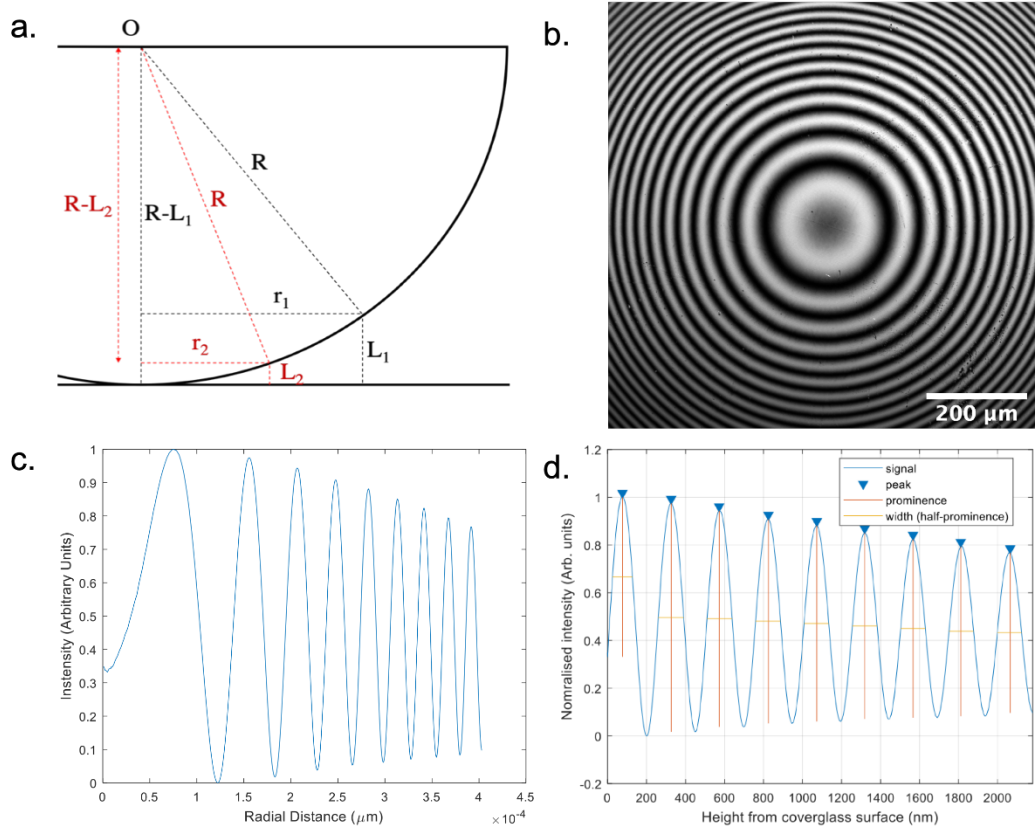


**Figure 2.2. Extracting 3D information from 2D IRM image data.** **a)** A schematic of a plano-convex lens specimen where  $R$  is the lens radius,  $L_1$  and  $L_2$  are the axial position of two constructive interference orders,  $r_1$  and  $r_2$  are the lateral distance from the centre of the lens to the interference orders 1 and 2. Adapted from Amor *et al.*, 2014. **b)** A confocal IRM image of an  $f = 72$  mm plano-convex lens specimen ( $\lambda = 488$  nm). Concentric fringe orders correlate to the topography of the specimen. **c)** A normalised radial intensity profile of the fringe orders in b). **d)** Extracted axial positions of interference fringes from 2D IRM data shown in b).

According to IRM theory, unlike diffraction-limited resolution, the effect of NA on the axial resolution of IRM is negligible. Therefore, interference fringe separation should also remain constant if the same plano-convex lens specimen is imaged under the same conditions with different NA objective lenses. To demonstrate the conservation of axial resolution two plano-convex lens specimens were imaged with two objective lenses. Figure 2.3 shows the resulting IRM images ( $\lambda = 488 \text{ nm}$ ) of a  $f = 48 \text{ mm}$  and  $f = 72 \text{ mm}$  acquired using a 5x/0.1 NA lens (Figure 2.3a) and a 10x/0.3 NA lens (Figure 2.3b). Normalised radial intensity plots were created as before and show that the interference fringe features remain constant despite changing NA. With NA having a negligible effect, the axial resolution of IRM is effectively fixed between different objective lenses given that imaging conditions remain constant. However, due to the relationship between NA and depth of field, having a low NA can result in intensity-based artefacts from self-interference from reflections elsewhere within the samples. This can be observed as inhomogeneous illumination across the image, as in the top panels of Figure 2.3a and b, but it is more apparent when multiple wavelengths are used to acquire IRM images (Figure 2.4). By visualising images acquired at the same focal plane using multiple wavelengths at low NA the intensity differences across the field are apparent, whereas these are much decreased when using a higher NA objective lens. Therefore, the NA should still be taken into account when acquiring IRM data, particularly when imaging specimens where interference is likely to occur within the depth of field of the objective lens (i.e. from the apical membrane of adhered cells or planar side of a plano-convex lens).

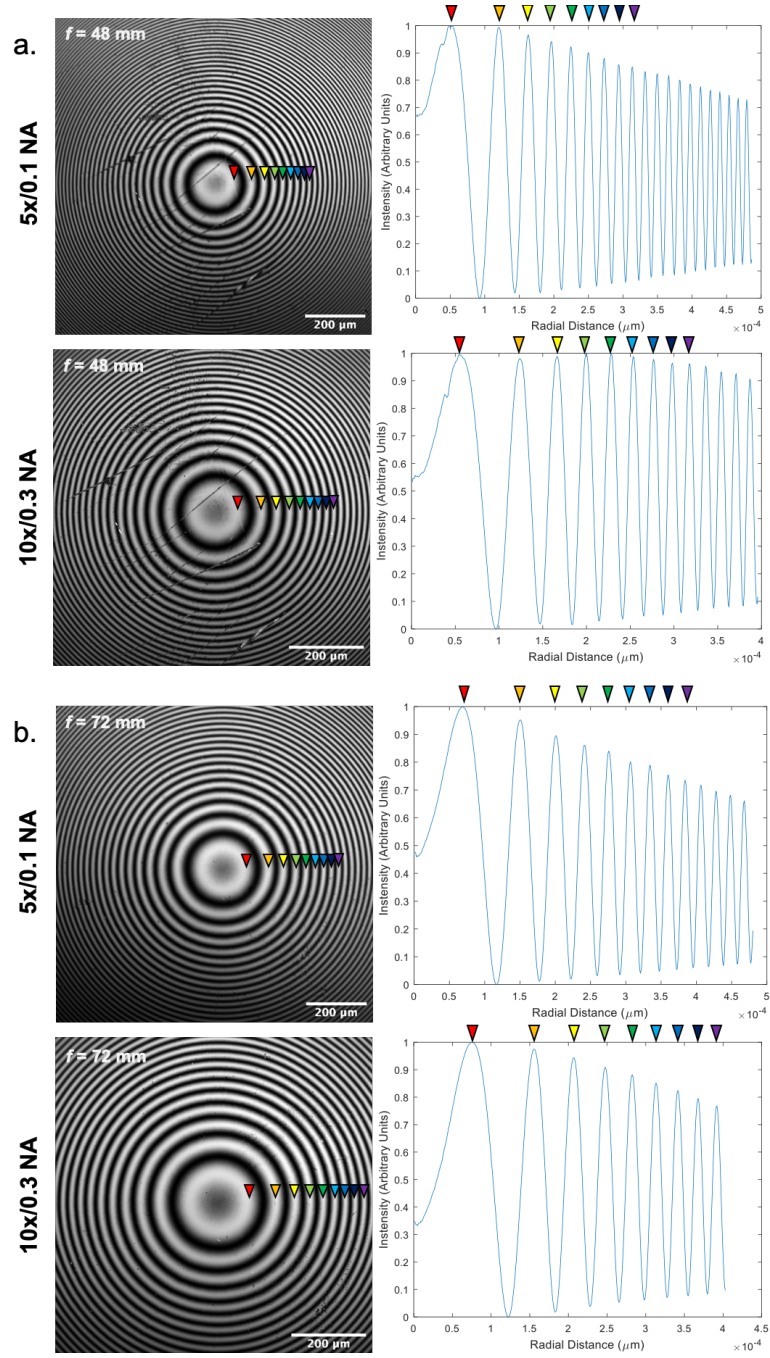


**Figure 2.3. Axial resolution in IRM is independent of numerical aperture. a)** IRM images ( $\lambda = 488$  nm) of an  $f = 48$  mm plano-convex lens specimen acquired using two different objective lenses with different NAs. Associated radial intensity profiles are included. **b)** IRM images ( $\lambda = 488$  nm) of an  $f = 72$  mm plano-convex lens specimen acquired using two different objective lenses with different NAs. Associated radial intensity profiles are included. For both lenses, top panels were acquired using a 5x/0.1 NA lens, and bottom panels were acquired using a 10x/0.3NA lens. Coloured markers indicate the peak intensity of each constructive order for comparison.



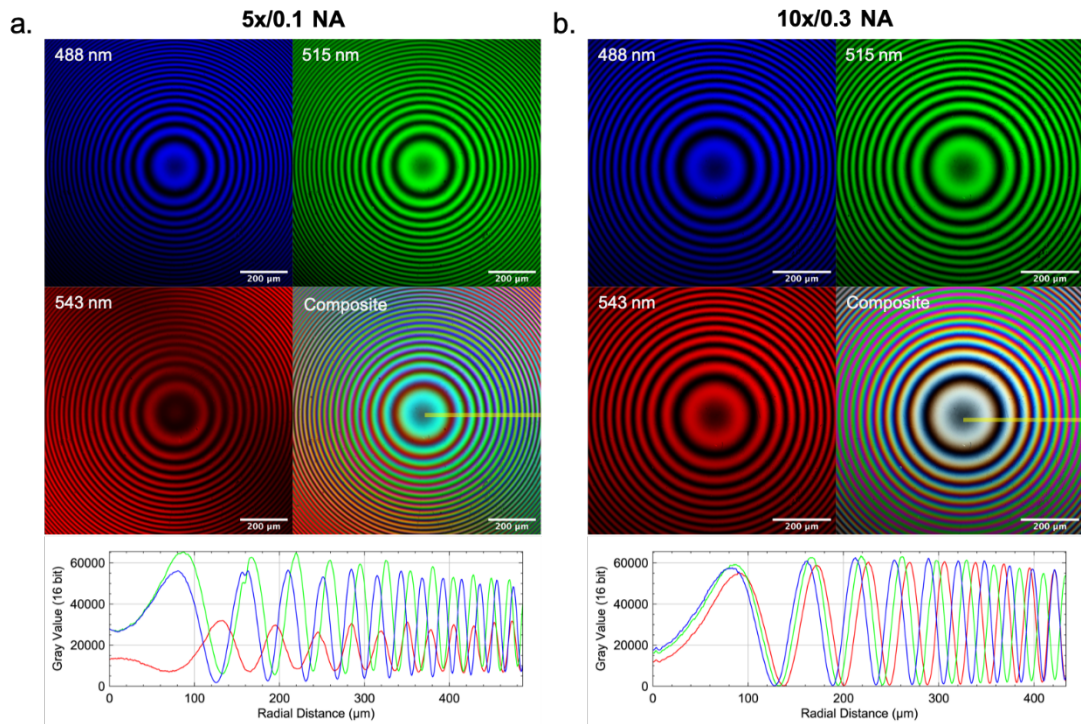


**Figure 2.4. Low NA objective lenses can result in erroneous intensity artefacts. a)** Mutli-wavelength confocal IRM images ( $\lambda = 488$  nm, 515 nm and 543 nm) and a composite merge of an  $f = 72$  mm plano-convex lens specimen acquired using a low NA lens (5x/0.1 NA). Associated intensity plot profile is shown below for each reflected wavelength (red = 543 nm, green = 515 nm, blue = 488 nm). **b)** Mutli-wavelength confocal IRM images ( $\lambda = 488$  nm, 515 nm and 543 nm) and a composite merge of an  $f = 72$  mm plano-convex lens specimen acquired using a high NA lens (10x/0.3 NA). Associated intensity plot profile is shown below for each reflected wavelength (red = 543 nm, green = 515 nm, blue = 488 nm).

### 2.3.2 Application of multi-wavelength confocal IRM to a model specimen

Having characterised a model plano-convex lens specimen using single wavelength IRM and describing the effect of NA on acquiring IRM images the same characterisation methods were applied to multi-wavelength confocal IRM data. As previously introduced, the purpose of using multiple acquisition wavelengths is to rely on the spectral separation of different reflected wavelengths with increasing distance from their reflection boundary. When images are merged post-acquisition, the

constructive orders of each wavelength will occupy some of the deconstructive orders of the others and partially fill in the information gap between fringes, which is most apparent in single-wavelength IRM. This decreases the information gap from 50% in single wavelength IRM to approximately 17% in multi-wavelength IRM (when 3 separate wavelengths are used). A composite of IRM images of a  $f = 72$  mm lens specimen acquired at 488 nm, 514 nm and 543 nm is shown in Figure 2.5a. In Figure 2.5b, a cross-sectional schematic of a plano-convex lens specimen is shown, outlining the axial position of the intensity maxima that are caused by constructive interference for different orders and wavelengths. Additionally, the resulting colour ordering of

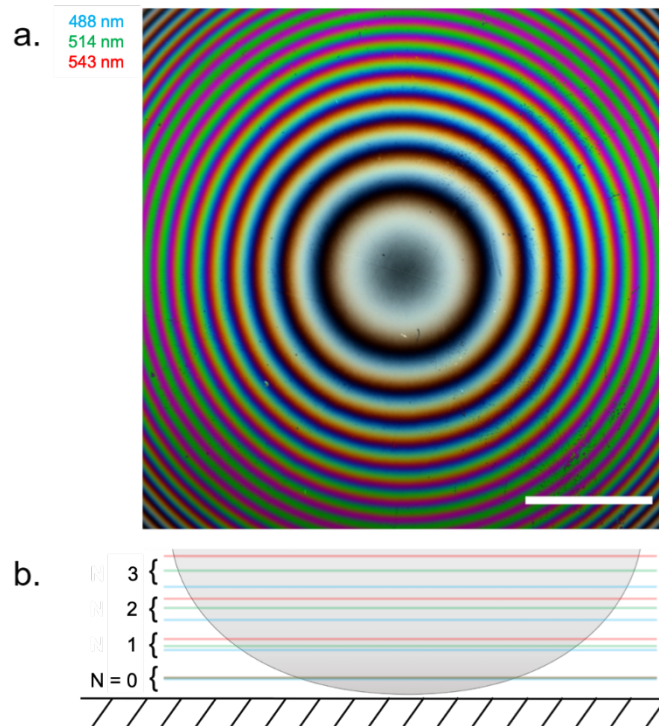


**Figure 2.5. Using multiwavelength IRM to fill the information gap.** a) A composite IRM image acquired using wavelengths at 488 nm, 514 nm and the 543 nm which are false-coloured blue, green and red. The spectral separation of the interference orders can be observed as the concentric fringes propagate away from the coverglass. Scale bar = 200  $\mu\text{m}$  b) A cross-sectional schematic of the lens specimen showing the colour-ordering of each acquisition wavelength as they propagate axially from the coverglass.

multi-wavelength IRM data provides a sense of directionality in the z-dimension, where fringe orders of shorter wavelengths will appear followed by orders of longer wavelengths if the specimen surface is inclined, while the opposite is true if the surface is sloping downward towards the coverglass.

Three-dimensional reconstruction of IRM data is difficult in biological specimens due to, for example, fluctuating refractive indices or changing local environmental conditions. However, to demonstrate that 3D reconstruction of IRM data is possible, the model specimen was reconstructed by assuming constant imaging conditions and applying *a priori* knowledge of specimen geometry. The intensity of the interference orders was analysed by comparing the radial intensity profile (Figure 2.6a) with the theory of IRM regarding fringe separation. The calculated theoretical spacing (i.e.  $\lambda/2n$ ) between the constructive interference maxima for each incident wavelengths were 244 nm, 258 nm and 272 nm ( $n = 1$  (air)). The experimental data resulted in slightly different spacings for between the intensity maxima, with  $249 \pm 1$  nm,  $262 \pm 1$  nm and  $277 \pm 1$  nm (Figure 2.6b). Therefore, experimental and expected values deviated by 2.07%, 1.63% and 1.91% for the different wavelengths. Additionally, the overlap of the intensity maxima of different acquisition wavelengths decreased with lens-to-coverslip distance (Figure 2.6b). These observations provided a sense of directionality regarding specimen topography, where the curvature of the plano-convex lens specimen was clear from the acquired images and allowed for 3D reconstruction of the lens specimen (Figure 2.6c). This means that assumptions outlined in previously in Section 2.1.3 are appropriate to reconstruct the morphology of simple model systems. Furthermore, a multi-wavelength IRM approach provides important additional morphological information over single wavelength IRM.

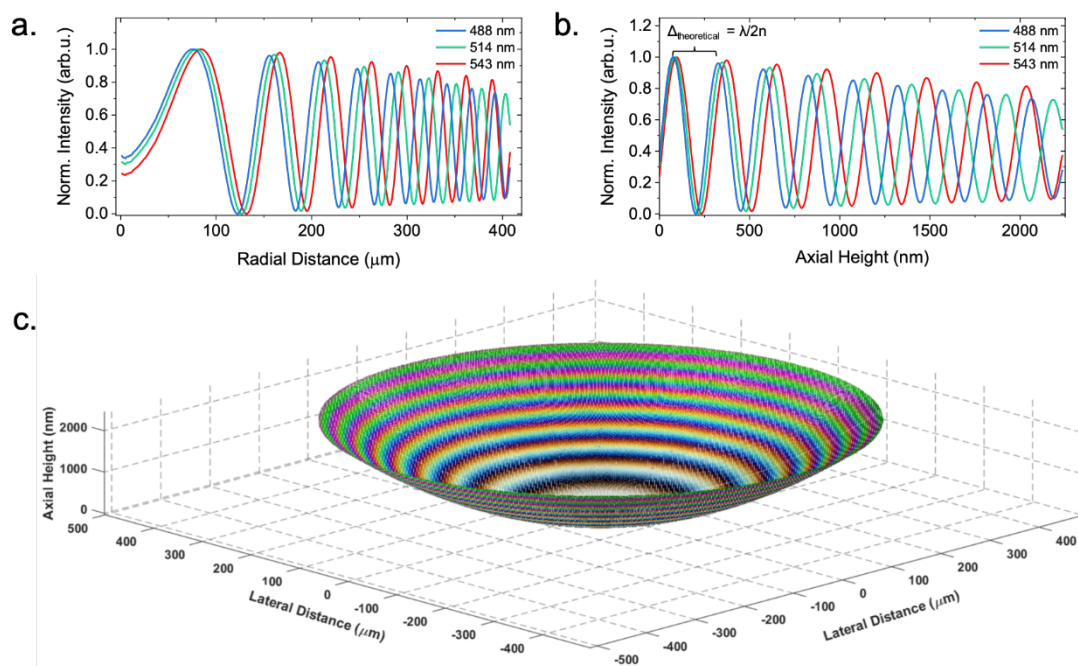


**Figure 2.6. 3D reconstruction of a plano-convex lens specimen.** **a)** The radial intensity profile of the interference fringe pattern shown in Figure 2.5a). We observed the fringe periodicity decrease as observed in the RGB IRM image. **b)** Using *a priori* knowledge of the lens specimen, the axial height was calculated and used to plot the intensity of each pixel as a function of height. **c)** A 3D reconstruction of the lens specimen using the known *x*, *y* and *z* values and intensity extracted from the 2D IRM image.

### 2.3.3 Further improving the axial resolution of IRM using a difference operation

Using multiple wavelengths in IRM results in some overlap of the fringe maxima arising from each reflected wavelength. While providing more information, the overlapping interference orders do not offer any improvement to the axial resolution of IRM. However, it is possible to removing the overlapping intensities using a simple post-acquisition step in FIJI. By applying a difference operation any overlapping regions between two channels can be removed resulting in an overall increase in the number of interference orders obtained compared to a composite of the two images (Figure 2.7). When the difference operation is applied to three-channel data (e.g. 488

nm, 515 nm and 543 nm), an image pair is generated (e.g.  $|543 \text{ nm} - 515 \text{ nm}|$  and  $|515 \text{ nm} - 488 \text{ nm}|$ ) which when merged provides an axial resolution improvement of approximately 50% (Tinning *et al.*, (2020), *manuscript in preparation*).

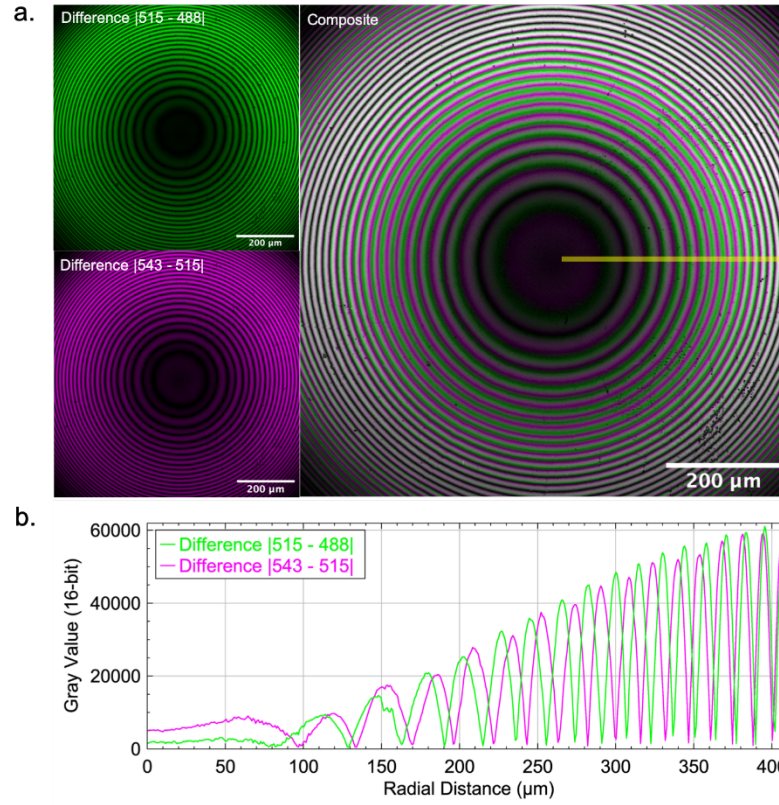


**Figure 2.7. Improving the axial resolution of IRM using a difference operation.** a) Two IRM difference images are presented for wavelengths 488 nm, 515 nm and 543 nm with accompanying composite difference image for a  $f = 72 \text{ mm}$  plano-convex lens specimen. b) A radial intensity profile measured along the yellow ROI presented in a) shows an increased number of interference fringes following the difference operation when compared to multi-wavelength IRM alone (Figure 2.6a). Intensity profile was measured with a line thickness of 10 pixels ( $12.09 \mu\text{m}$ ).

This difference method works optimally with experiments using three or more wavelengths. However, due to instrument limitations it was not possible to acquire three-channel IRM images simultaneously on dynamic biological specimens using the Olympus FV1000 inverted confocal microscope available. Therefore, the difference



method was only applied on model specimen data as a demonstration of its use in improving the axial resolution of multi-wavelength IRM data.

### 2.3.4 Single-wavelength IRM reveals axial gliding behaviours in *M. xanthus*

Having characterised IRM using a specimen of known geometry the technique was applied to the gliding bacterium, *M. xanthus*. When placed on a glass coverglass and imaged using IRM, wild-type *M. xanthus* (DK1622) displayed shifting interference fringe patterns along the length of the cell body (Figure 2.8). This was indicative of changing axial position of the basal membrane of the cell relative to the coverglass. Previous imaging experiments in literature suggested that myxobacterial gliding motility was limited to a flat plane, however using IRM it is clear that cells move in three dimensions while gliding and display a range of topographies while gliding along

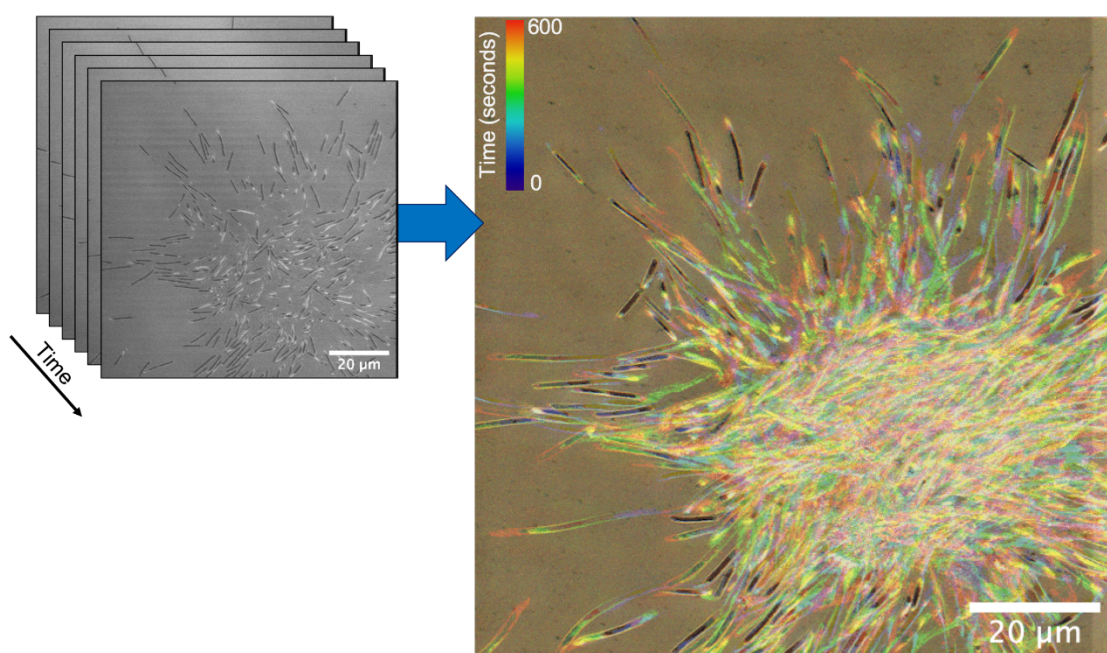


**Figure 2.8. *Myxococcus xanthus* exhibits 3D gliding behaviours.** A temporal hyperstack shows a colour-coded time series of gliding myxobacteria acquired using IRM ( $\lambda = 488$  nm). Changing cell topographies can be identified by observing the changing interference fringe patterns along cell bodies (false coloured according to time).

a solid surface (Figure 2.9). Initially conventional microscopy tracking plugins were used to try and track gliding cells in order to understand their changing shape over time. However, automated tracking algorithms often depend upon the tracked object being spherical, meaning that rod-shaped objects such as *M. xanthus* are more difficult to track<sup>237–239</sup>. This is made more challenging by the reflection interference contrast mechanism which introduces fringe patterns into the image data. Use of conventional tracking tools resulted in multiple fragmented tracks for each cell which would be impractical to use for any analysis (Figure 2.9a). Therefore, manual tracking was used in ImageJ of selected gliding cells within a time series which resulted in tracks lasting the full duration of the gliding path length (Figure 2.9b). Tracks from the manual tracking were used to generate kymographs in FIJI which showed the changing interference fringe patterns along the cell body during gliding (Figure 2.9c). Interestingly, the 3D topography of the leading and lagging poles often changed according to the polarity of the cell (i.e. forward or reverse gliding). Additionally, most cells displayed a behaviour where a centre portion of the cell body was raised by above the surface of the coverglass. Assuming that most of the fringes present along the cell body of the cell shown in Figure 2.9c were first order fringes, these behaviours all involve raising regions of the cell body approximately 90 nm above the surface of the coverglass. However, without the directional information provided by multi-wavelength IRM it is not possible to confirm this.

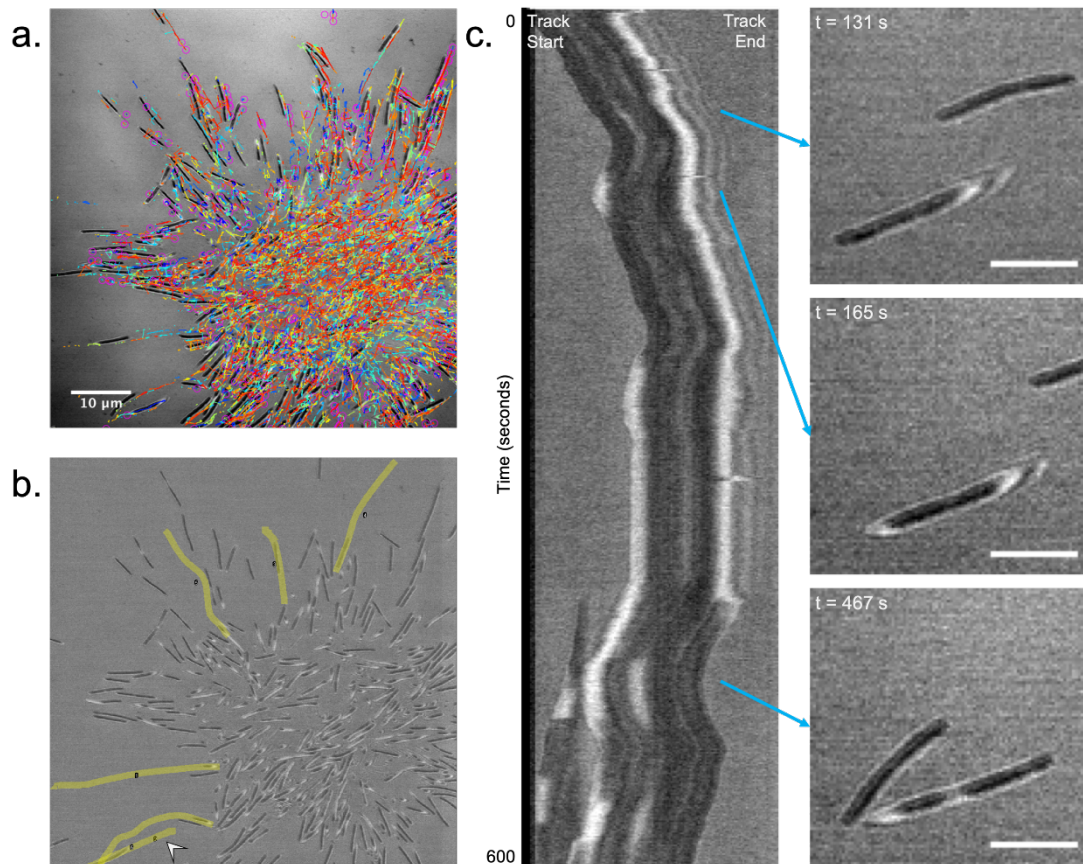


**Figure 2.9. Understanding the 3D behaviour of *M. xanthus* during gliding. a)**

TrackMate output showing calculated tracks for various gliding cells. Multiple tracks are present for every cell which makes kymograph generation impractical. **b)** Manual tracking

using ImageJ allows for more adaptive cell tracking to demonstrate changes in cell behaviour over time. Selected cells were tracked over the course of 600 seconds, or until they moved beyond the edge of the image. **c)** A kymograph of ROI 2 from b) shows the

spatial information collected from a single gliding cell over 600 seconds. As the cell begins gliding the leading pole is inclined, before both poles incline and a polarity shift occurs causing the cell to reverse. During this reversal at approximately 450 seconds a portion of the cell body in the centre of the cell is raised. Three example ROIs of the gliding cell are presented displaying different gliding behaviours. Scale bars = 5 μm.



To ensure that the changing fringe patterns observed in Figure 2.8 were linked solely to gliding motility and not owed to any intensity-based artefacts, cells were treated with 80 mM sodium azide ( $\text{NaN}_3$ ) to inhibit gliding motility. When treated with sodium azide, *M. xanthus* gliding motility was completely inhibited. Cells remained static throughout imaging and any interference fringes present along the cell bodies also remained static (Figure 2.10). This finding determined that the changing fringe patterns observed using IRM was linked to gliding motility, and moreover corresponded to changing topography during gliding.

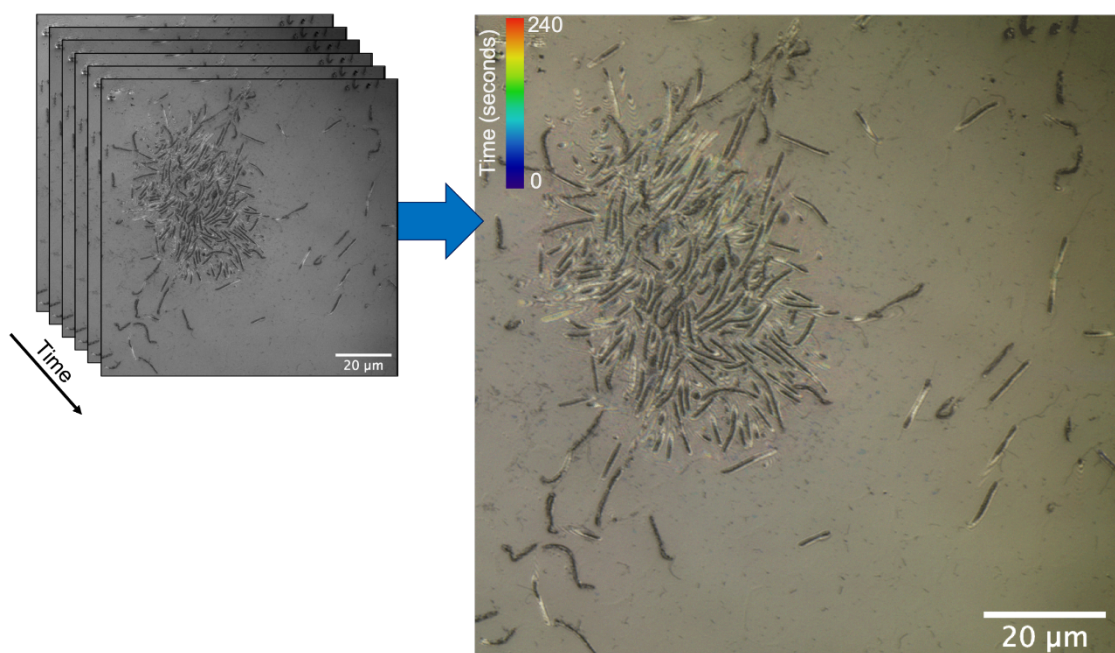


**Figure 2.10. Changing interference fringe patterns are indicative of changing gliding topographies.** A temporal hyperstack shows a colour-coded time series of gliding myxobacteria treated with 80 mM  $\text{NaN}_3$  prior to imaging using IRM ( $\lambda = 488 \text{ nm}$ ). Any interference fringes present remain static while gliding is inhibited.

### **2.3.5 Inhomogeneous background correction for IRM data**

To address the inhomogeneous background intensity present in multi-wavelength IRM data a background correction tool which was developed by Lisa Kölln (University of Strathclyde) was used. Briefly, a moving average (neighbourhood length =  $k$ ) was taken and divided by each pixel in the image which resulted in a homogeneous background signal across the field (Figure 2.11). The  $k$ -value was empirically selected based on having minimal change on the specimen data (Figure 2.12). To demonstrate that the background correction method did not alter the location of the interference order maxima a normalised intensity plot was measured for both model and biological datasets (Figure 2.13). Following background correction, the location of the fringe maxima remained the same whereas the background intensity was more even across the field. The correction method had the additional benefit of increasing contrast between interference orders (Figure 2.14), making image processing more robust.

### **2.3.6 Multi-wavelength IRM reveals 3D behaviours of gliding bacteria**

Following observations of 3D behaviours by gliding cells using IRM with a single acquisition wavelength, multiple wavelengths were used to fill in the information gap between constructive fringe orders. For these experiments two wavelengths were selected that were well separated (e.g. 488 nm and 635 nm) to make colour ordering more apparent and interpreting specimen directionality easier.

To demonstrate the benefit of using confocal approach to multi-wavelength IRM, initially wild-type *M. xanthus* was imaged on a commercial inverted widefield microscope. However, it was clear that due to the contribution from out of focus signal and low coherence length of the light source used by many widefield systems that a widefield approach was impractical. Multi-wavelength IRM in widefield mode resulted

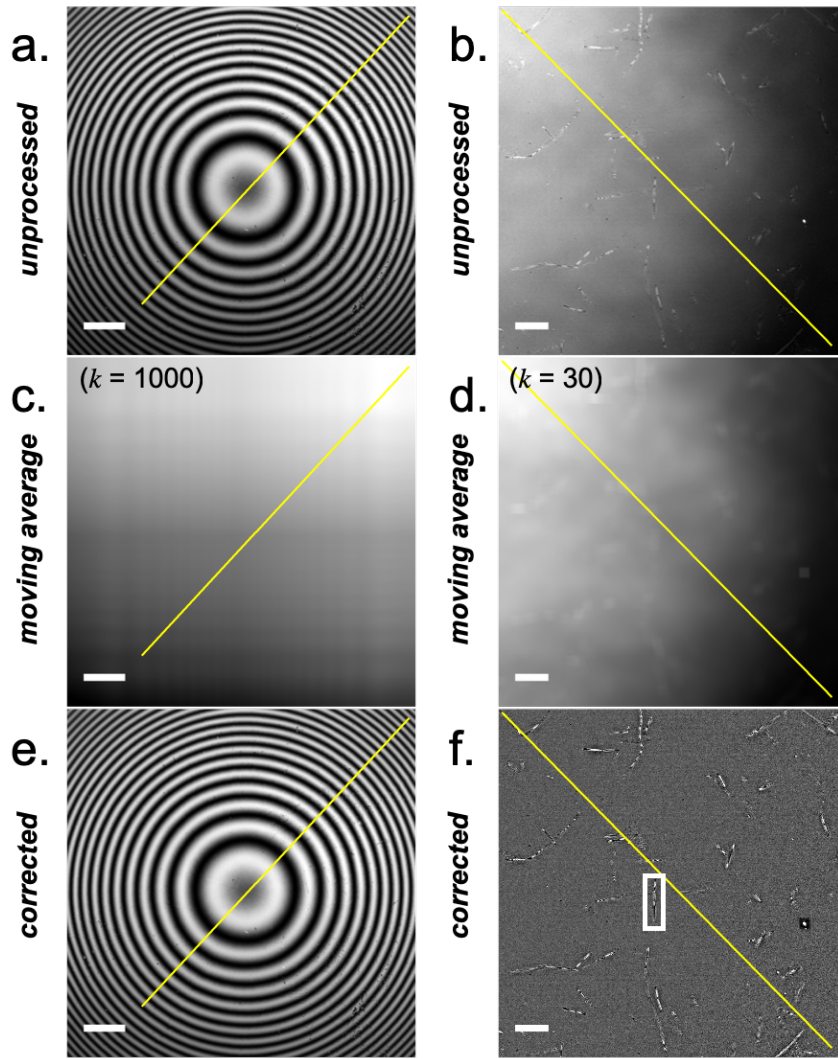


**Figure 2.11. Image correction workflow for IRM data.** **a)** Linearly contrast-adjusted IRM image of a 6 mm diameter lens specimen (focal length = 72 mm) acquired using light at 488 nm. Scale bar = 100  $\mu\text{m}$ . **b)** Linearly contrast adjusted IRM image of *M. xanthus* with inhomogeneous background intensity. Scale bar = 10  $\mu\text{m}$ . **c)** Calculated moving average of **a)** when  $k = 1000$ . The calculated moving average accounts for the inhomogeneous background which is subtracted to correct the raw image. **d)** Calculated moving average of **b)** when  $k = 30$ . **e)** Corrected IRM image resulting from **a)**. **f)** Corrected IRM image resulting from **b)**. The ROI selects a single cell where the intensity profile was measured in Figure 2.13. Selected line plots are shown in each panel where intensity profiles were measured in Figure 2.12.

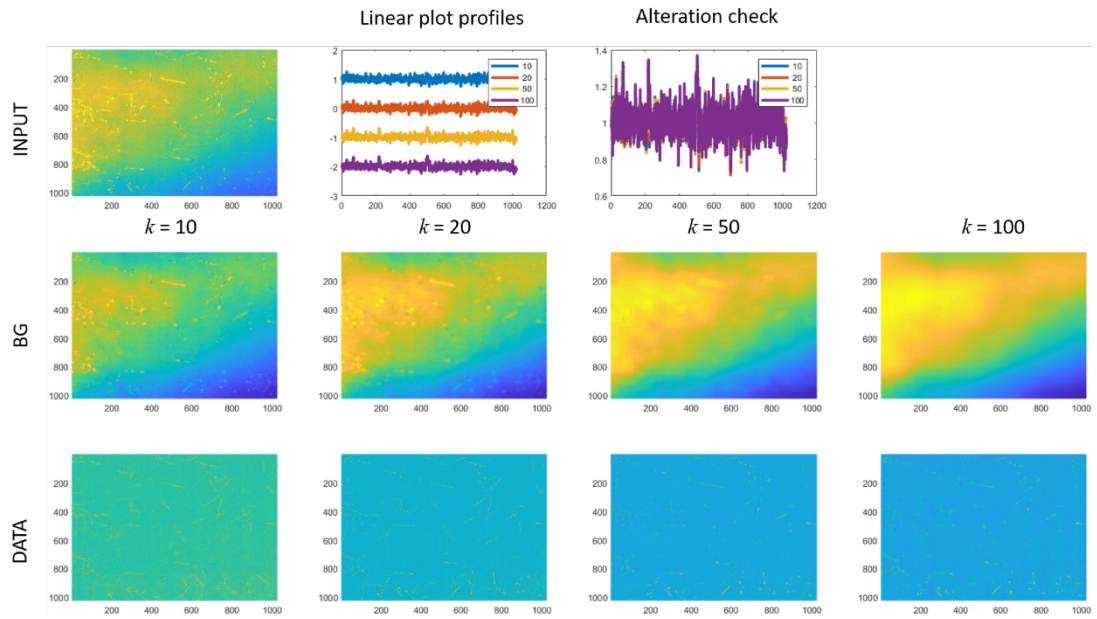


**Figure 2.12. Selecting a  $k$ -value for IRM background correction.** To select the optimum  $k$ -value a series of possible values are presented with accompanying predicted background images (BG) generated by applying the walking average to the input data. The corrected output images are shown for each possible  $k$ -value. The optimum  $k$ -value should have minimal structure in the BG image, and minimal blur in the DATA image. The optimal  $k$ -value for the data shown would be  $k = 50$ . Linear plot profiles are taken through the centre of each  $k$ -value DATA image and merged to perform an alteration check to ensure that the image features are not lost in the correction process.

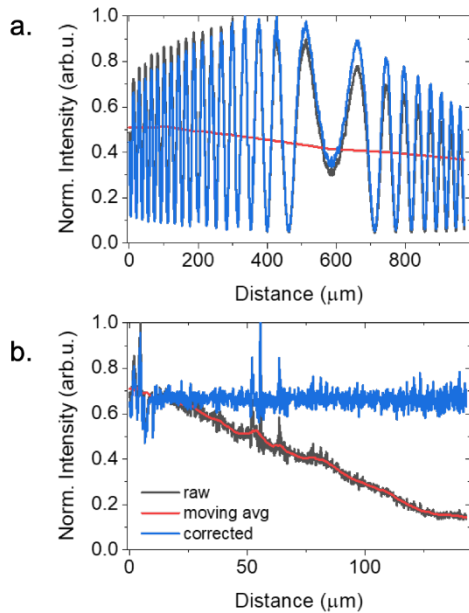


**Figure 2.13. Image correction does not alter the position of fringe maxima and minima.** **a)** Selected line intensity profiles from Figure 2.11 a), c) and e) are shown. Following correction of the raw images using the calculated moving average, there was no change in the peak position of the intensity maxima and minima. **b)** Selected line intensity profiles from Figure 2.11 b), d) and f) are shown. Correction resulted in homogeneity of illumination across the field. Line intensity profiles were averaged using a line width of a) 5 px (4.2  $\mu\text{m}$ ) and b) 5 px (0.5  $\mu\text{m}$ ).

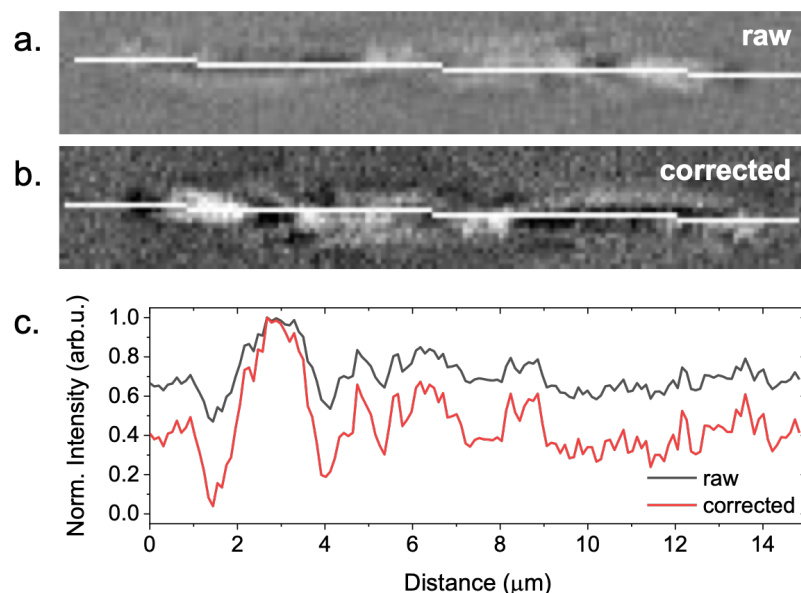


**Figure 2.14. Image correction increases contrast and does not alter the position of intensity peaks.** **a)** Unprocessed ROI from Figure 2.11 f) with a line profile shown for reference. **b)** Corrected ROI shown in a) ( $k = 30$ ). **c)** Selected line intensity profiles of a) and b) show that there are no changes to the position of intensity values along the length of gliding cells. Line intensity profiles were averaged using a line width of 5 px ( $0.5 \mu\text{m}$ ).

in inhomogeneous background intensities, and also provided much lower contrast compared to previous confocal imaging experiments (Figure 2.15a). Raw widefield data was processed using the background correction pipeline above (Figure 2.15b). While the correction pipeline equalised the background intensity across the field, interference orders cannot be clearly resolved in either the raw or corrected data, meaning that a widefield approach is not suitable for studying the changing adhesion profile of gliding bacterial cells.

Given that widefield IRM was not appropriate for bacterial imaging, a confocal multi-wavelength approach was used to image *M. xanthus* gliding motility. Gliding wild type *M. xanthus* (DK1622) cells were imaged on a glass substrate using incident light at 488 nm and 635 nm. Figure 2.16 shows clearly resolved interference fringes along the cell body which indicated that the cell was not completely attached to the



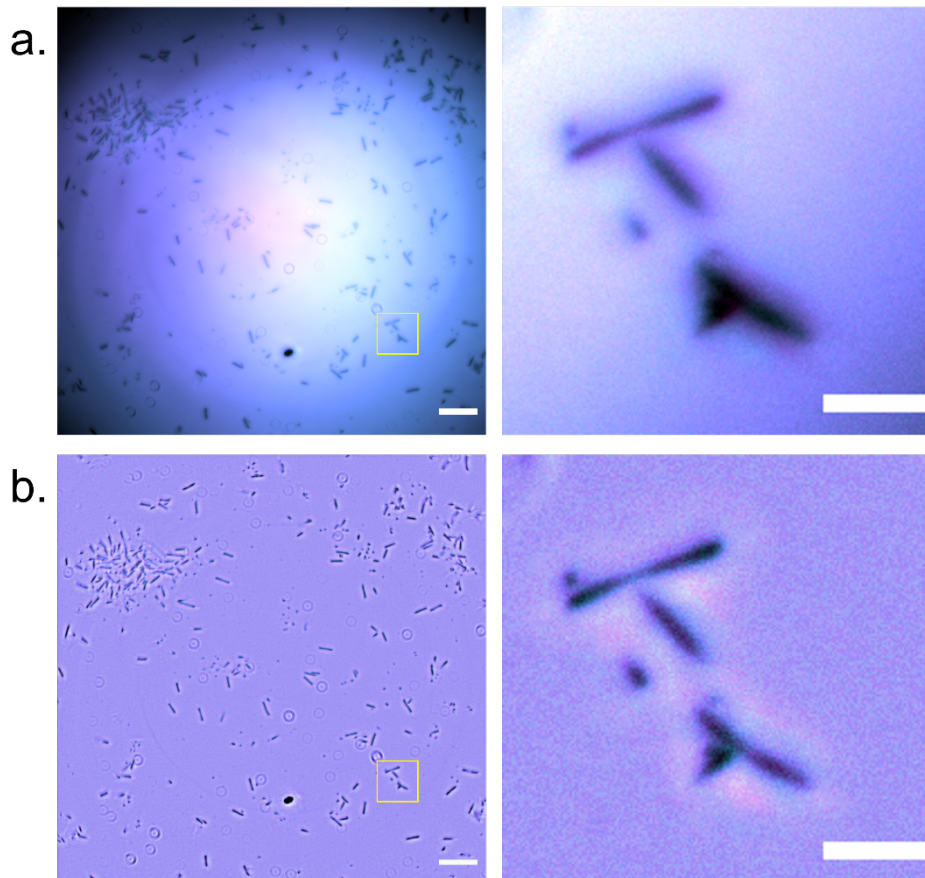


**Figure 2.15. Widefield IRM does not provide sufficient contrast to reveal sub-diffraction limited changes in the adhesion profile of gliding bacteria. a)** Unprocessed and **b)** background corrected ( $k = 30$ ) multi-wavelength widefield IRM composite image of *M. xanthus* (450 nm = cyan, 550 nm = magenta). Magnified ROI of gliding cells shows low contrast between fringe order when images are acquired using widefield modality. Full field scale bars = 20  $\mu\text{m}$ , ROI scale bars = 5  $\mu\text{m}$ .

coverglass, and that the cell-to-coverglass distance varies along the body. There is a clear aperiodic change in the fringe pattern over time which indicates changes in the adhesion profile of the cell body during gliding. Interpreting the colour ordering of these fringes, as with the lens specimen, shows that part of the cell body is lifted up from the glass substrate. There was also no synchronicity in the height changing behaviours between nearby gliding cells. This observed change in adhesion profile

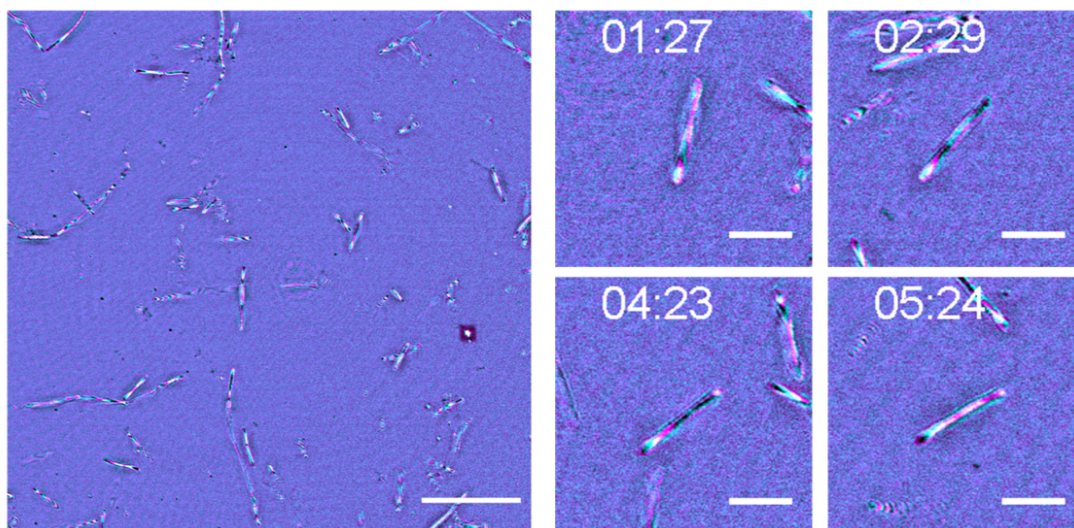


**Figure 2.16. Multi-wavelength confocal IRM reveals axial movements along the cell body during gliding motility.** A single frame from a wild type DK1622 gliding specimen with 4 magnified regions of interest (ROI) of a single representative cell over the course of the time-lapse (from  $t = 1 \text{ min } 27 \text{ s}$  to  $t = 5 \text{ min } 24 \text{ s}$ ). Images were acquired using confocal multi-wavelength IRM, with reflected 488 nm signal false coloured in cyan and reflected 635 nm signal shown in magenta. As the cell glides across the solid substrate the interference fringe pattern changes as the relative position of the cell to the coverglass fluctuates. Full field scale bars =  $20 \mu\text{m}$ , ROI scale bars =  $5 \mu\text{m}$ .

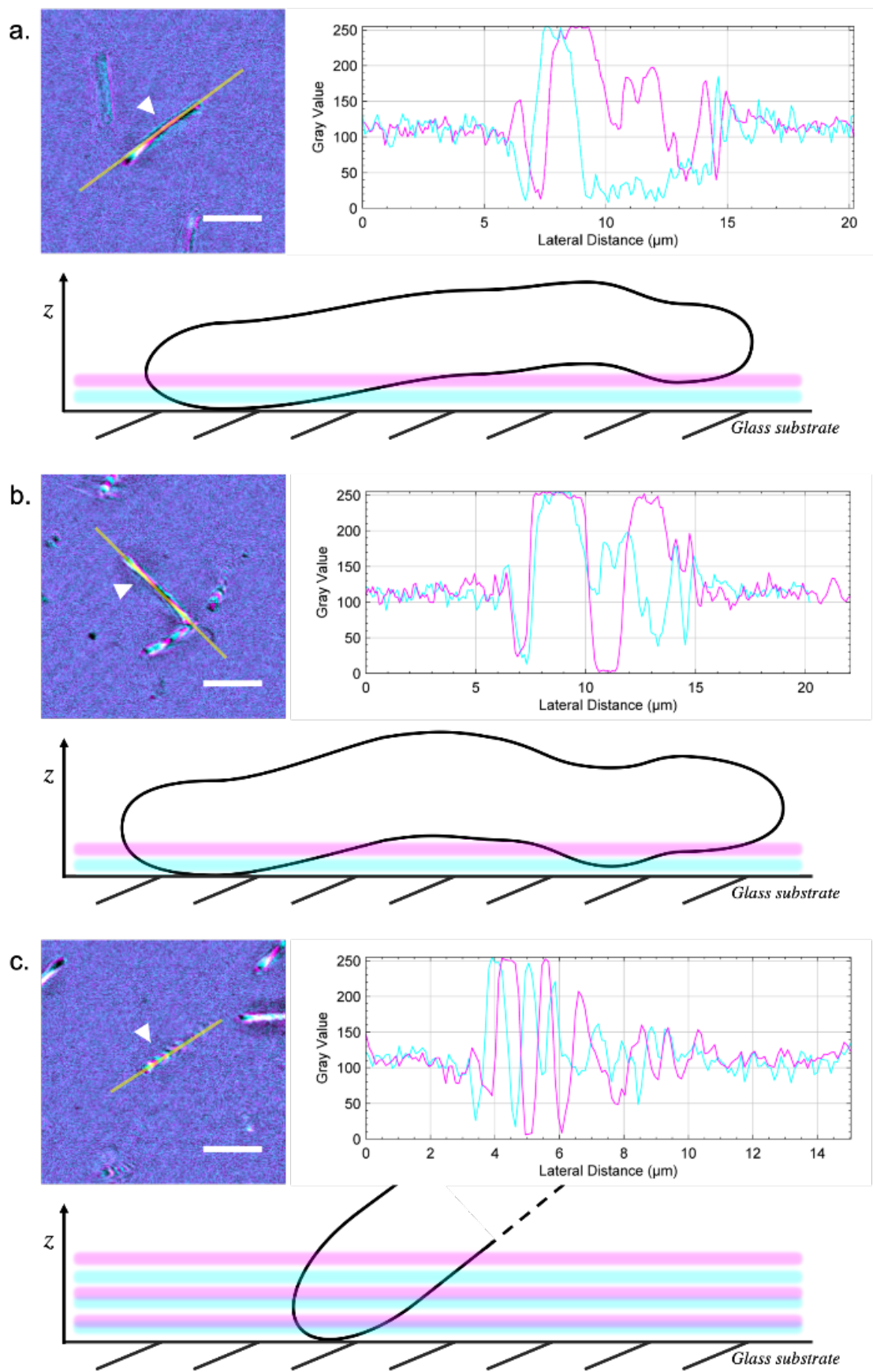
opposes the current theory that gliding cells are firmly adhered along the cell body as they glide.

As discussed previously, the use of multiple acquisition wavelengths allows for a better understanding of the axial directionality of the specimen by observing the colour ordering of fringe orders. This allows for a tentative reconstruction of the cell topography. Figure 2.17a shows a multi-wavelength IRM image of a gliding wild type cell, where the cell is attached to the coverglass at one pole and the body is inclined which is clearly indicated by an alternating fringe pattern along the body. Qualitative topographical information about the cell morphology can be extracted by interpreting the intensity plot profile along the cell body. The cell shown in Figure 2.17a shows a

cyan fringe ( $\lambda = 488$  nm) followed by a magenta fringe ( $\lambda = 635$  nm) and based on this we can conclude that the cell body was attached to the coverglass at the leading pole before the basal surface raised to a height of approximately 180 nm. A cartoon diagram approximating the shape of the cell body is presented to show this. The IRM data indicates a variety of cell orientations and shapes which occur during gliding motility. These include an undulating topology where the cell is attached to the coverglass at the leading pole while the cell body raises to a height of approximately 180 nm before falling to 90 nm, and again raising to 180 nm at the lagging pole (Figure 2.17b). Another cell motility behaviour is depicted at the point of surface attachment prior to the start of gliding where the leading pole of the cell is attached to the coverglass and the cell body projects upwards into the liquid medium at a sharp incline of approximately  $60^\circ$  relative to the coverglass (Figure 2.17c).

**Figure 2.17 (overleaf). Understanding the 3D topography of gliding cells.** Three representative wild type gliding cells are presented from a time series dataset, each with a linear ROI showing where the intensity plot profile was measured along the cell. Interference fringes along the cell body can be observed, with reflected 488 nm signal shown in cyan and 635 nm signal in magenta. Intensity plot profiles are presented for each exemplary gliding morphology which is used to extract axial information. Plots were acquired by averaging the signal over a line width of 3 pixels ( $0.3\ \mu\text{m}$ ). A schematic of the x, z profile of each cell which was generated according to the colour ordering and corresponding intensity profile. The axial position of each interference maxima from each acquisition wavelength was assigned by calculating the height of each maxima relative to the coverglass (using the  $\lambda/2n$  relationship), while directionality along the optical axis of the microscope was deduced from colour ordering of interference maxima along the cell body (i.e. maxima of shorter wavelengths will appear first followed by maxima of longer wavelengths if the cell is inclined – as in (a)). Schematics are not drawn to scale. Scale bars =  $5\ \mu\text{m}$ . Morphologies include **a)** raised, **b)** undulating, and **c)** polar attachment.





### 2.3.7 Understanding the mechanism behind the aperiodic oscillatory 3D gliding motility of *M. xanthus*

One of the main motility mechanisms of *M. xanthus* is PMF-driven focal adhesions and cytoskeletal rotation which propels the cell forward. The PMF which facilitates this mode of motility is provided by the proton pump, AglQ. To determine if PMF-driven motility dynamics were responsible for the behaviours observed using IRM an *aglQ* deletion mutant (DK1622- $\Delta aglQ$ ) was studied using the same imaging conditions as above. Figure 2.18 shows the same oscillating fringe patterns along the length of gliding cells. This conserved behaviour between the wild type and DK1622- $\Delta aglQ$  determines that the novel gliding behaviour observed is independent of PMF-mediated motility mechanisms.

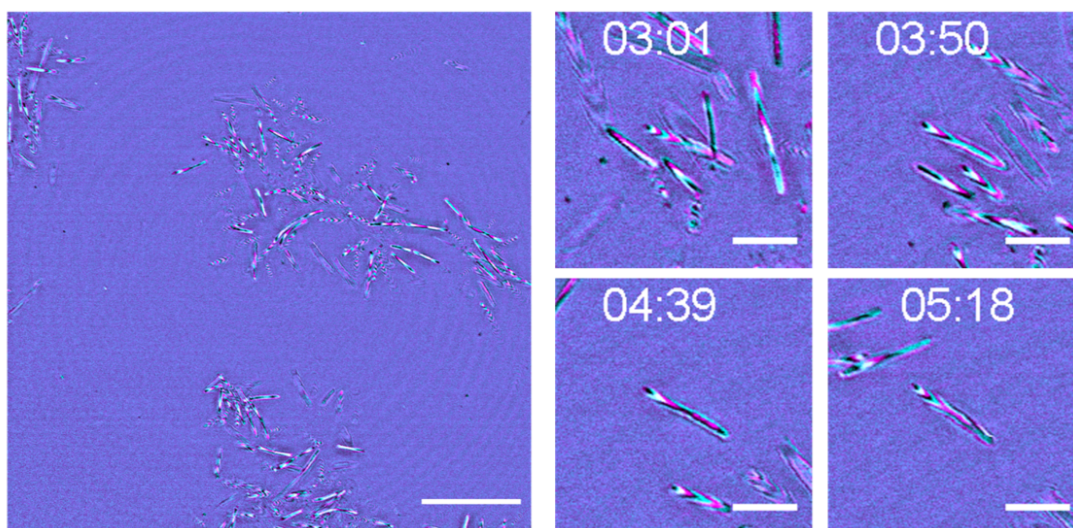


**Figure 2.18. Axial gliding behaviours are independent of PMF-driven motility mechanisms.** A single frame from a DK1622- $\Delta aglQ$  specimen with 4 magnified regions of interest (ROI) of a single representative cell over the course of the time-lapse (from  $t = 3$  min 01 s to  $t = 5$  min 18 s). Images were acquired using confocal multi-wavelength IRM, with reflected 488 nm signal false coloured in cyan and reflected 635 nm signal shown in magenta. As the cell glides across the solid substrate the interference fringe pattern changes as the relative position of the cell to the coverglass fluctuates. Full field scale bars = 20  $\mu\text{m}$ , ROI scale bars = 5  $\mu\text{m}$ .

Despite the conserved 3D behaviour between the wild type and  $\Delta aglQ$  strain, the gliding phenotype was different between the two strains. To assess the difference in gliding ability multiple cells were manually tracked from their time of attachment until they detached from the coverglass. The length of time that cells remained attached to the coverglass and the distance which they travelled while adhered was measured, as well as the mean gliding velocity. Deletion of *aglQ* decreased the length of time which cells remain adhered to the glass substrate compared to the wild type (Figure 2.19a), which implied that *AglQ* is responsible for maintaining adherence to the coverglass during gliding. The mean velocity of gliding cells was determined by measuring the displacement of the cells over time as they glide, selecting cells with an approximately linear trajectory. There was a 41.2% decrease in mean velocity of DK1622- $\Delta aglQ$  (mean velocity =  $9.26 \pm 0.72 \mu\text{m}/\text{min}$ ) when compared with the wild-type (mean velocity =  $15.76 \pm 0.89 \mu\text{m}/\text{min}$ ), which concurs with their altered motility phenotype (Figure 2.19b).

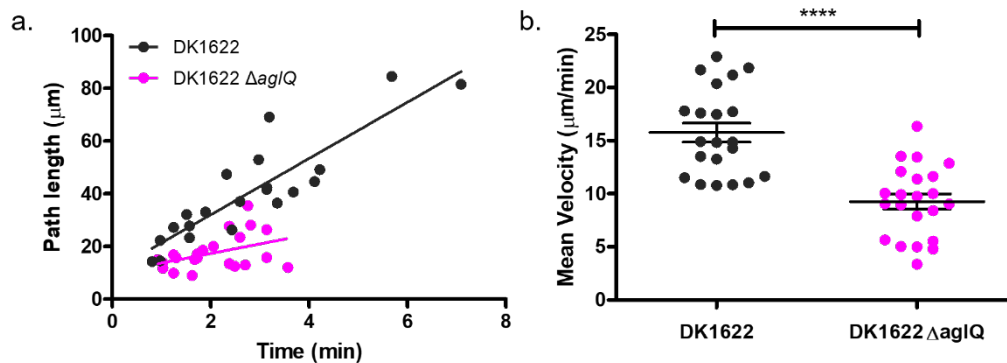


**Figure 2.19. IRM as a method for measuring the velocity of adherent cells. a)** The path length of wild type (DK1622) and DK1622- $\Delta aglQ$  are presented over the course of a time series. Overall DK1622 has an increased mean path length when compared to DK1622- $\Delta aglQ$ , which shows that DK1622- $\Delta aglQ$  has a lower adhesion profile than the wild type. **b)** Deletion of *aglQ* results in a decrease in mean velocity of 41.2% from  $15.76 \pm 0.89 \mu\text{m}/\text{min}$  to  $9.26 \pm 0.72 \mu\text{m}/\text{min}$  when compared with the wild type.  $n_{\text{DK1622}} = 21$ ,  $n_{\text{DK1622-}\Delta aglQ} = 22$ ,  $p < 0.0001$ .

Another canonical gliding mechanism is the use of T4P to propel the cell forward following elongation, attachment and retraction of thin polar filaments from the leading pole of the cell. It was hypothesised that this process could result in force transmission along the cell body and cause some form of mechanical recoil following pili extension. To test this hypothesis, a mutant lacking PilA (the monomer which polymerises to form mature pili) and a mutant lacking both PilA and AglQ were imaged under the same conditions as above. However, due to the lack of attachment apparatus these strains were unable to attach to the coverglass due to a lack of pili, and cells remained out of the depth of focus of the high NA lens used during imaging (Figure 2.20). It remains unclear if T4P dynamics are responsible for the 3D behaviours reported here. A proposed method to determine the involvement of T4P in the oscillatory 3D gliding behaviour reported would be to develop a correlative TIRF/IRM technique. By imaging

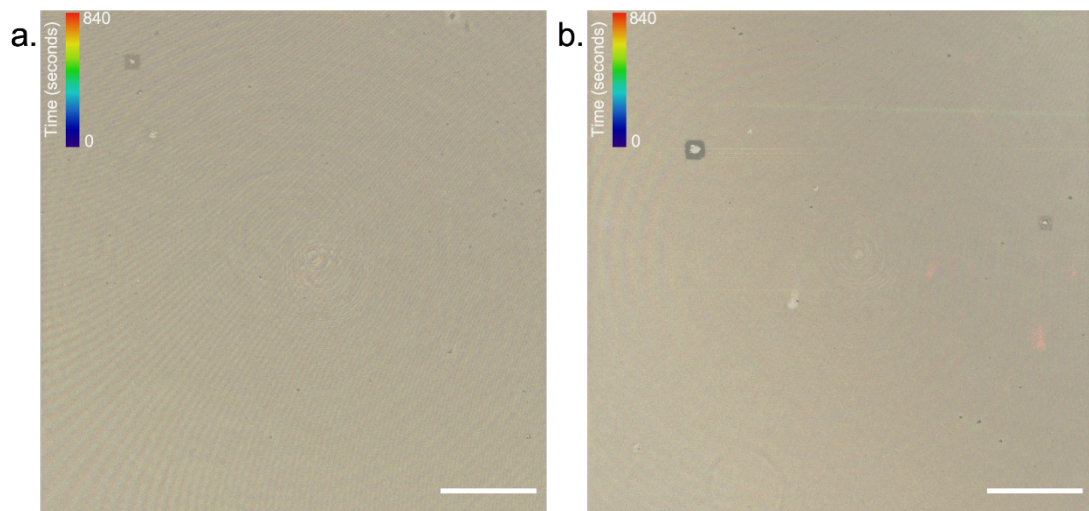


**Figure 2.20. Type IV pili deletions prevent cell attachment and are not applicable for study with IRM.** **a)** A temporal hyperstack of DK1622- $\Delta pilA$  acquired using multi-wavelength IRM ( $\lambda = 488$  nm and 635 nm). Cells remained unattached to the coverglass due to a lack of pili. **b)** A temporal hyperstack of DK1622- $\Delta pilA/\Delta aglQ$  acquired using multi-wavelength IRM ( $\lambda = 488$  nm and 635 nm). Again, cells remained unattached to the coverglass due to a lack of pili. Scale bars = 20  $\mu$ m.

fluorescently labelled pili extension and attachment and correlating any synchronous changes in the adhesion profile of gliding cells by IRM, T4P-mediated effects on cell topography during gliding could be identified.

## 2.4 Discussion

The application of a label-free imaging technique capable of providing topographical 3D information below the diffraction limit in the z-dimension has wide reaching applications in microbiology. Historically, optical sectioning of bacteria has been impossible due to the elongation of the emission PSF along the optical axis of the microscope. Therefore, any live cell observations to date have almost exclusively been limited to 2D studies. This work begins by characterising a novel multi-wavelength confocal variant of IRM for bacterial imaging on a model specimen of known geometry. This approach to validating novel microscopical methods is well documented and has been used for similar interference-based techniques such as standing wave fluorescence microscopy<sup>84,229</sup>. The findings presented in Sections 2.3.1 through Sections 2.3.3 show that multi-wavelength confocal IRM allows for understanding and reliable extraction of 3D data from 2D interference images. A difference method for improving the axial resolution of IRM data is also presented, where an axial resolution improvement of up to 50% can be achieved by a simple post-processing operation in ImageJ. The ease of implementation, minimal specimen preparation and high-contrast label-free imaging make IRM an attractive tool for topographical imaging of individual live bacterial cells.

Aperiodic changes in the adhesion profile of gliding myxobacteria have been observed using the label-free technique, IRM. Given that previous studies had failed to identify any axial behaviours in gliding cells due to the drawbacks with conventional imaging techniques, it was hypothesised that changes in cell height from the substrate

may arise due to the complex mechanisms which govern gliding motility. The data presented in this chapter shows new behaviour in gliding myxobacteria which do not support the current gliding motility models. The behaviours reported suggest that there are additional factors which mediate gliding motility and show the benefit of using IRM to extract 3D information from bacterial specimens by using an easily implemented microscopy technique.

The current consensus is that gliding cells are firmly attached to a solid surface to facilitate gliding, however these data show that this is not the case. The results show that throughout gliding, cells undergo changes in the axial position of their basal surface on the order of 90-180 nm. This new information indicates that the helical rotation and FAC motility models do not fully explain the mechanisms of bacterial gliding. Both of these models converge on constant firm attachment to the substrate for the entirety of the track length of the cell. However, the findings presented in this Chapter show that attachment is transient, and cells display oscillatory attachment and de-attachment of their basal surface to the substrate during gliding. For example, Figure 2.9c, clearly shows aperiodic changes in the axial position of the leading and lagging poles of the cell during gliding, as well as raised portions along the cell body. These motility behaviours cannot be explained by the current FAC or helical rotation models of gliding motility.

One previous study has used RICM to investigate the adhesion profile of myxobacteria during detachment<sup>102</sup>. However, they did not report any fringes along the cell body, or any aperiodic changes in adhesion in gliding cells. This is likely due to the poor contrast of widefield RICM compared to confocal IRM that prohibits the detection of higher interference fringe orders. It is important to also note that some researchers have claimed that the ability of IRM to detect regions of close contact is questionable due to the inhomogeneous refractive index of the cytosol proximal to the



plasma membrane and from self-interference from higher fringe orders within the cell<sup>107,108</sup>. However, these claims are solely based on observations of mammalian cells using widefield IRM. Owing to the lack of vesicular trafficking and much smaller relative size of bacteria compared to mammalian cells, this is not a concern in this bacterial study and confocal IRM remains a valid technique for studying surface adhesion in prokaryotes.

Previous studies which have used conventional optical microscopy methods to image gliding myxobacteria have also failed to observe changes in surface adhesion due to the elongation of the axial point spread function being on the same order as the thickness of a bacterial cell<sup>9,240</sup>. A confocal approach to IRM for bacterial imaging overcomes the inability to optically section thin specimens with standard optical microscopy, while simultaneously visualising the adhesion profile of cells. The drawback of using confocal IRM is a decreased temporal resolution when compared with widefield IRM. However, gliding cells were still able to be tracked manually. While the contrast improvement provided by using a confocal approach over widefield should make image analysis easier<sup>9,241</sup>, the complexity of IRM image data makes image processing and analysis challenging. There are currently no readily available image processing tools that can extract 3D information from a 2D image, such as in IRM. However, with these improved data it may be possible to develop software tools to reconstruct the 3D topography of bacteria using IRM data. The temporal resolution could be improved by using a spinning disk confocal microscope for IRM, however most commercial spinning disk microscopes may not be suitable to incorporate IRM due to hardware limitations<sup>107</sup>. Using confocal IRM also allows us to confirm that the studied cells are in close proximity to the surface of the coverglass and that the gliding behaviours we report are not caused by other factors such as inertia or Brownian motion.

Changes in the relative position of the basal cell membrane above the coverglass could perhaps be explained by proposed distortions in cell wall due to the translocation of FACs along the basal surface of the cell<sup>219</sup>, or because of cell surface unevenness<sup>242</sup>. However, when we compare the axial movements displayed by the wild type with the  $\Delta aglQ$  mutant we see that this novel gilding behaviour remains. The role of AglQ in gliding motility is central to both the helical rotation and FAC models<sup>142,224,225,243</sup>, and having both wild-type and DK1622- $\Delta aglQ$  display the same behaviour highlights that more understanding of the mechanisms of gliding motility is required. It is important to address that the  $\Delta aglQ$  mutant still retains other mechanisms involved in gliding motility (i.e. T4P, slime extrusion etc.), hence why it is still able to traverse its environment by gliding. Moreover, the motility phenotype of the  $\Delta aglQ$  strain does not necessarily subvert its movement to twitching motility. This is evidenced by the lack of a “stop-start” movement in DK1622- $\Delta aglQ$  which is characteristic of twitching motility (in pseudomonads, for example). What the findings show in Figure 2.18, is that the 3D behaviours observed in *M. xanthus* are independent of the central gliding motility complex and of PMF-driven dynamics. Instead, other factors must contribute to the height-changing behaviour of myxobacteria during gliding, and this requires re-evaluation of the current motility models to factor in 3D movement.

A recent study by Tchoufag *et al.* proposed an elasto-hydrodynamic mechanism for bacterial gliding where a sinusoidal basal shape is adopted when myxobacteria glide upon a soft substrate<sup>244</sup>. This was confirmed by observing membrane-stained gliding cells on semi-solid agar pads with TIRF microscopy and revealed distinct foci where the cell membrane was lifted approximately 100 nm above the substrate surface (outside of the TIRF evanescent field). The behaviours described in this chapter are reminiscent of this undulating basal shape, however our observations are



documented on solid glass substrates, and describe a wider variety of behaviours. However, it is possible that slime excretion and accompanying basal membrane deformations could provide an explanation to the behaviours documented here. Additionally, *M. xanthus* is known to produce outer membrane vesicles (OMVs) bearing a host of hydrolytic enzymes and signalling molecules which are used in the predatory stages of its lifecycle<sup>245–247</sup>. The production of OMVs causes membrane distortions along the lateral membranes of predating cells, but according to electron micrographs OMVs are much more pronounced than the topographical changes reported here. Moreover, OMVs are typically produced when *M. xanthus* is either in high cell densities (such as when in biofilms) or when undergoing the predatory phase of its lifecycle<sup>246</sup>, neither of which were conditions tested here.

The mean velocity of wild-type and DK1622- $\Delta$ ag/Q cells was measured. Using  $\Delta$ ag/Q as a control, where it is known from previous work that gliding should be impaired<sup>142</sup>, we have shown that changes in adhesion profile are independent of the gliding velocity or path length where cells remain associated with the coverglass. To determine the gliding velocity, we measured the average time cells glided along approximately linear trajectories. Routine automated tracking algorithms generally have difficulties in tracking bacterial specimen due to their reliance on blob detection of spherical objects<sup>237–239</sup>. Attempting to isolate and track rod-shaped objects, such as *M. xanthus*, has proven difficult and the addition of interference fringes to rod-shaped objects only adds to the complications of automated cell tracking and analysis. We therefore used a manual tracking method to measure the mean velocity of gliding cells. We concluded that the DK1622- $\Delta$ ag/Q moved on average 30% slower than the wild-type. Also, the wild type remains adhered to the surface for longer periods of time, yet the dynamic fluctuations in gliding adhesion we report remain.

The potential role of T4P in the aperiodic oscillations was also investigated. Time lapse data was acquired of DK1622- $\Delta pilA$  and DK1622- $\Delta pilA/\Delta aglQ$  but these cells were unable to adhere to the coverglass and did not display an adherence pattern when imaged using IRM. Therefore, it was not possible to confirm if T4P extension, attachment and retraction were responsible for the 3D behaviours observed. Moving forward it would be interesting to investigate the spatiotemporal dynamics of T4P firing in association with the changing adhesion profile of gliding cells using a correlative TIRF-IRM approach. This would allow for simultaneous imaging of the adhesion profile of gliding cells and fluorescently tagged T4P proximal to the coverglass. The development of an image processing workflow to extract 3D information from confocal IRM images of biological specimens would also provide users with a method to quantify the aperiodic oscillatory behaviour. Additionally, this Chapter has shown that bacteria are ideal candidates for study by IRM, and the new multi-wavelength confocal variant presented here could be easily applied to various other bacteria species and behaviours.

## 2.5 Conclusions

This chapter has provided new insights into the 3D motility of bacteria and identified novel motility behaviours in *M. xanthus* which suggest there are additional mechanisms which do not agree with the current FAC and helical rotation models. A hypothesis is suggested where the fluctuations in height observed could be mediated by T4P and occur due to recoil following firing of pili from the leading pole. Attempts to image T4P mutants using IRM to confirm this hypothesis were unsuccessful as T4P mutants were unable to attach to the glass substrate and therefore unable to glide. Given that IRM was unable to reveal T4P-mediated behaviours due to non-attachment of cells to the coverglass, we suggest that this hypothesis could be

investigated further by means of a correlative TIRF-IRM method to detect synchronicity between pili extension and topographical changes along the cell body.

# Chapter 3

## Characterisation of a novel intra-colony channel system in *Escherichia coli* biofilms using the Mesolens

In this chapter the architecture of mature *E. coli* macro-colony biofilms was explored using a novel mesoscopic imaging approach. The initial aim of this Chapter was to use the Mesolens to investigate the internal architecture of *E. coli* macro-colony biofilms. In doing so a previously undocumented channel system was identified and characterised within *E. coli* biofilms. These emergent proteinaceous channels, which are on the order of 10µm in diameter, allow for nutrient uptake from the external environment, which potentially offers a novel understanding of nutrient delivery in microbial communities beyond passive diffusion. The nutrient uptake hypothesis was also tested to determine if intra-colony channels played a role in the uptake of antimicrobial compounds into the mature biofilm. The findings presented in this chapter provide a novel understanding of how spatial organisation in bacterial biofilms contributes to their ability to transport material from the external environment which, with further study, could be used to develop eradication methods to lower their social and economic burden.

Sections of this chapter have been adapted from Rooney *et al.* (2020b)<sup>248</sup>.

## 3.1 Introduction

### 3.1.1 Spatial organisation in bacterial communities

Biofilms are aggregate communities of microbes held together by a self-secreted extracellular matrix containing extracellular polysaccharides (EPS), lipids, proteins and nucleic acids<sup>178,249</sup>. These microbial communities can be composed of one or more species (mono/poly-microbial) and are found in almost every ecological environment<sup>250</sup>. The protective matrix enveloping the biofilm confers resistance to desiccation and exposure to diffusing agents such as biocides or antibiotics<sup>146,251–254</sup>, in turn promoting the development and spread of antimicrobial resistance<sup>158</sup>. Consequently, the study of biofilm structure is vital to understanding and combatting the development of resistance and lowering the clinical and industrial burden of biofilms. The 3D structure of biofilms can take many forms<sup>147,169,255,256</sup>, for example, mushroom-shaped biofilms grown in liquid flow systems, thin sheet-like biofilms in static liquid systems, pellicle biofilms grown at liquid/air interfaces, and macro-colony biofilms grown on solid surfaces. Although morphologically distinct, what classifies these structurally-different communities as 'biofilms' lies with their shared fundamental biochemical signals and pathways<sup>183</sup>.

The study of biofilm architecture has developed over the past several years and has discussed the role of extracellular components and secreted macromolecules which provide the biofilm with spatial organisation and structural support. Among these surface structures are type I pili (fimbriae), antigen43 (Ag43), colanic acid, cellulose, curli and flagella<sup>165</sup>. The dense extracellular matrix of bacterial biofilms makes transport of substances in and out of the biofilm difficult. For example, oxygen diffusion is often limited in thick biofilms, which requires the emergence of macroscopic folds by some species to increase the surface area and oxygen

permeability of the biofilm<sup>185,257,258</sup>. Diffusion-limited transport has also been linked to the development of persister cells and the emergence of antimicrobial resistance in biofilms. This is caused, for example, when antibiotics are topically applied to a biofilm in effort to clear it, and the limited diffusion due to the matrix results in a concentration gradient of the antibiotic. Cells towards the centre of the biofilm are therefore exposed to sub-optimal concentrations of antibiotics which then fuels the emergence and spread of resistance throughout the biofilm, and possibly beyond if resistant cells become planktonic following mechanical agitation<sup>158</sup>.

The dense spatial organisation of bacterial biofilms also makes imaging them difficult. The abundance of exopolymeric substances results in the scattering of light, particularly in large or thick biofilms, ultimately lowering image quality. Therefore, in effort to shed light on the architecture of large bacterial communities, dynamic computational modelling programmes, such as CellModeller<sup>259,260</sup>, have been routinely used to predict the spatial patterning and arrangement of cells within biofilms<sup>186,259–262</sup>. *In silico* models primarily show growth of polymicrobial communities where cell shape, size, surface properties and cell-cell interactions influence the spatial organisation of the mature biofilm, resulting in sectoring of different strains into distinct populations, which has been validated experimentally<sup>182,187–190</sup>. However, *in silico* modelling has shown little evidence of structural ordering or complex spatial patterning, and a lack of effective multi-scale imaging techniques has presented little experimental evidence of 3D structure within mono-strain biofilms.

### **3.1.2 The Mesolens as a tool for biofilm imaging**

The most common method for studying biofilms is by optical imaging, and often involves routine widefield epifluorescence and confocal laser scanning microscopy. For example, the density-dependent phage sensitivity in *Escherichia coli* colonies has

been studied<sup>263</sup>, the biofilms present on human tooth enamel have been imaged at different pH levels<sup>264</sup>, and synchronies of growth and electrical signalling between adjacent bacterial colonies have been observed<sup>265</sup>. Such studies have exposed a gap in the repertoire of the optical microscope in that either microbes could be individually imaged with a high-power objective lens, or the overall structure could be viewed at low magnification with resolution so poor, particularly in depth, that individual microbial cells could not be seen. Therefore, until this point it has been challenging to image specimens with sufficiently high resolution on a global scale<sup>266</sup>. Alternatively, stitching and tiling has been used routinely to image biofilms<sup>267–269</sup>, however this results in long acquisition times and intensity artefacts over the final image. Without stitching and tiling microscopy, the current size which a biofilm can be imaged while still resolving sub-cellular information is around 2000 cells (or around 100  $\mu\text{m}$  in diameter)<sup>129,131</sup>. Therefore, the Mesolens should provide a vast improvement on the scale at which bacterial communities can be studied.

To address this, the Mesolens was used to image intact live macro-colony biofilms *in situ* with isotropic sub-cellular resolution. As discussed in Chapter 1, along with the lens prescription, the unique ratio between the magnification and NA of the Mesolens provides an imaging volume over 100  $\text{mm}^3$  with sub-cellular resolution throughout<sup>111</sup>. While the Mesolens has proven to be a powerful tool in neuroscience, developmental biology and pathology<sup>111–113</sup>, it also presents an untapped technology for biofilm imaging, where whole live microbial communities can be imaged with unprecedented detail within a single dataset without additional processing or stitching and tiling.

### **3.1.3 The use of antibiotics for biofilm clearance**

To overcome the clinical and industrial impacts that biofilms pose, they are often treated by bombardment of potent antibiotics or by adopting the use of functionalised

surfaces as a preventative measure for bacterial colonisation. Given that up to 80% of chronic infections are linked to biofilms<sup>270</sup>, and that biofilm-related corrosion alone is estimated to cost, according to the BBSRC, anywhere between 1-5% of UK GDP<sup>271</sup> (up to £110 billion as of October 2019), new understanding of bacterial architecture can be of huge benefit. In industry, the most common biofilm clearance methods are physical removal of the biofilm from a surface or by disinfection, often using concentrated solvents or irradiation<sup>272</sup>. The most common clearance method in the clinic involves sustained antibiotic treatment over a number of days, however recently there has been an increase in the development of alternate therapeutic strategies, including nanoparticles, antimicrobial peptides, matrix-degrading enzymes and quorum sensing inhibitors<sup>273,274</sup>. However as discussed previously, these methods all share the problem of diffusion-limited entry into large scale biofilms. As an impasse to this, functionalised surfaces have become a promising alternative to aggressive treatment strategies. Functionalisation involves either adapting the surface of an abiotic material to decrease bacterial attachment and effacement, or using affinity targeting (e.g. with antibodies, glycans etc.) to direct antimicrobial compounds held in vesicles or liposomes into the biofilm<sup>275-279</sup>. Despite these recent advances in clearance and prevention techniques, biofilms remain a huge burden in both clinical and industrial settings and further study is merited to understand the structure of these communities and inform new methods of eradication.

### **3.1.4 Experimental aims**

The initial aim of this chapter was to use the Mesolens to investigate the internal architecture of *E. coli* macro-colony biofilms. Upon visualising these biofilms, a previously undocumented intra-colony channel network was identified. The aim was then to characterise these channel systems with three main questions in mind; what the structural make-up of the intra-colony channels was; how did the intra-colony



channels form; and did the intra-colony channels play a functional role in the wider context of the biofilm. The first of these questions was answered by systematically visualising known components of polymeric biofilm matrices using a combination of reflection confocal microscopy and fluorescent dyes. The formation of the channels was investigated by observing the effect of total mechanical agitation of the biofilm and observing re-growth and reformation of the channels. A functional role in nutrient uptake was suggested following observations using fluorescent microspheres and an arabinose biosensor. The functional role was investigated further by visualising the effect of bactericidal antibiotics on the proportion of non-viable cells in and around the channel structures.

## **3.2 Materials and Methods**

### **3.2.1 Specimen preparation**

#### **3.2.1.1 Designing and 3D-printing an imaging chamber for biofilm mesoscopy**

A custom imaging chamber was designed using AutoCAD (Version no. N.49.M.324, Autodesk, USA) with the purpose of imaging large-scale cultured bacterial communities *in situ* using the Mesolens. The design consisted of a plate with dimensions 90 mm x 80 mm x 12 mm and a central well measuring 60 mm in diameter with a depth of 10 mm (Figure 3.1). The imaging chamber was 3D-printed using black ABS plastic (FlashForge, Hong Kong) with a FlashForge Dreamer 3D printer (FlashForge, Hong Kong). The chamber slide was sterilised prior to use with 70% ethanol and UV irradiation for 15 minutes.

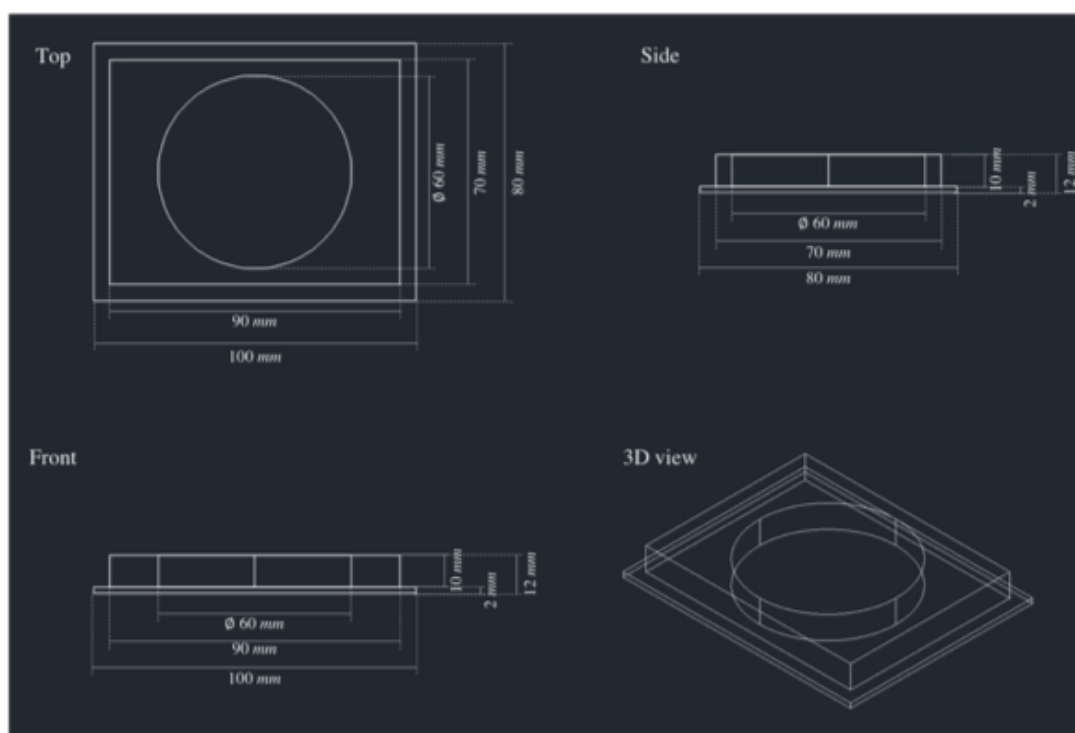


**Figure 3.1. Schematic for bacterial culture and imaging mould.** Technical drawing shows dimensions for the 3D-printed imaging mould used in this study. The design was based on a Petri dish-come-microscope slide with a central well where bacteria can be cultured as required. The top surface could be sealed with a large glass coverslip which was custom-made for the Mesolens, and if required, the design allows the imaging chamber to be incorporated into an immersion bath.

### 3.2.1.2 Bacterial cell culture

All experiments were performed using the *E. coli* (JM105) strains outlined in Appendix I. Colony biofilms were grown by inoculating a lawn of cells at a density of  $1 \times 10^4$  cfu/ml on either solid LB medium or M9 minimal medium<sup>280</sup> to achieve single colonies, and growth medium was supplemented with the appropriate selective antibiotic to maintain the photoprotein. The colonies were grown in the 3D-printed imaging mould at 37°C for 18-24 hours in darkened conditions prior to imaging.

For colony imaging alone, colonies were submerged in sterile LB broth (refractive index ( $n$ ) = 1.338) as a mounting medium following the allocated growth time prior to

imaging. A large coverglass was placed over the central well of the imaging mould (70 mm x 70 mm, Type 1.5, 0107999098 (Marienfeld, Lauda-Koenigshofen, Germany)), and the colonies were then imaged using either the Mesolens or a conventional widefield epifluorescence microscope to compare their performance and to justify using the Mesolens to study biofilm architecture over conventional techniques. All experiments were repeated in triplicate to ensure observations were reliable. A schematic of the experimental setup is presented in Figure 3.2.

The refractive index of the LB mounting medium was measured using an Abbe Refractometer (Billingham & Stanley Ltd., U.K.) which was calibrated using absolute methanol at 21°C ( $\lambda = 589$  nm).

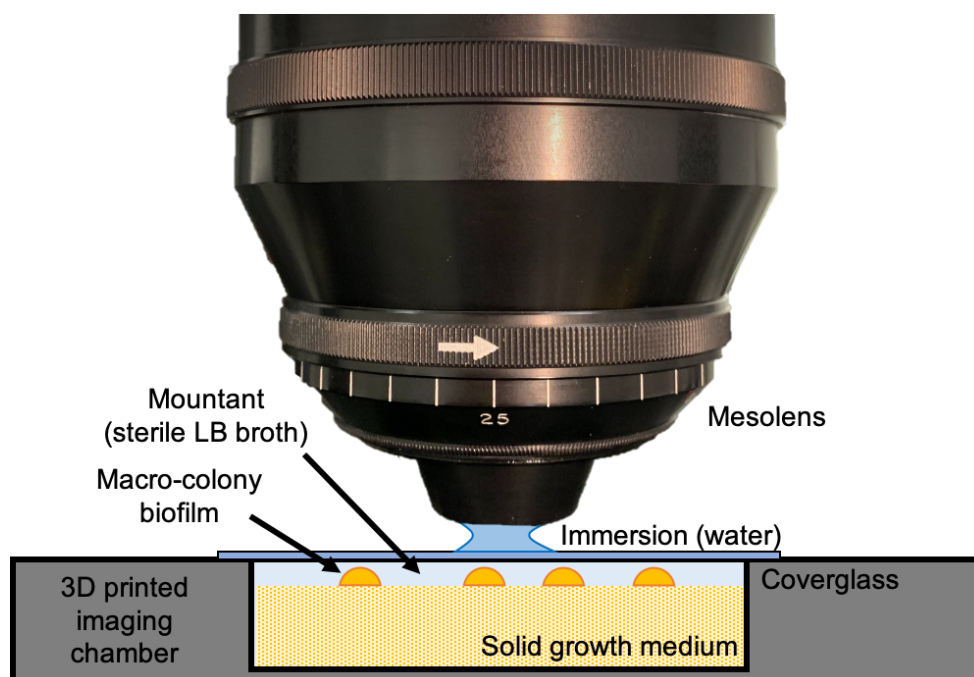


**Figure 3.2. Schematic of specimen preparation for mesoscopic imaging.** A schematic showing the experimental setup for biofilm mesoscopy. The 3D printed imaging chamber is filled with solid bacterial growth medium before biofilms are grown on the surface, mounted in sterile nutrient broth and sealed with a coverglass. The imaging chamber is then placed under the mesolens with water immersion and imaged.

### **3.2.2 Imaging conditions**

#### **3.2.2.1 Stereomicroscopy**

Mature macro-colony biofilms were imaged using an SMZ1500 stereomicroscope coupled with a mercury arc lamp (Nikon, Japan). All stereomicroscope images were acquired at 4x magnification (NA = 0.21). GFP excitation was achieved using the mercury lamp with appropriate excitation and emission filters in place (49002 ET-EGFP (FITC/Cy2), Nikon, Japan). Brightfield transmission and fluorescence images were acquired using a DFK 33UX264 CMOS camera (The Imaging Source Europe GmbH, Germany). Specimens were prepared by growing as single colonies of solid LB medium and imaged in air ( $n = 1.00$ ).

#### **3.2.2.2 Conventional widefield epifluorescence microscopy**

Colony biofilms were also imaged on a conventional an Eclipse E600 upright widefield epifluorescence microscope (Nikon, Japan) equipped with a 4x/0.13 NA PLAN FLUOR objective lens (Nikon, Japan). GFP excitation was provided by a 490 nm LED from a pE-2 illuminator (CoolLED, U.K.), and emission was detected using a bandpass filter (BA 515-555 nm, Nikon, Japan) placed before an ORCA-spark digital CMOS camera (Hamamatsu, Japan). The camera detector was controlled using WinFluor software<sup>281</sup>. Colonies were imaged after 20 hours of growth in an imaging mould as described above.

#### **3.2.2.3 Widefield epifluorescence mesoscopy**

Specifications of the Mesolens have been previously reported<sup>111</sup> and outlined in Chapter 1 (Section 1.4.1). Therefore, only the imaging conditions used in this study will be outlined here. GFP excitation was achieved using a 490 nm LED from a pE-4000 LED illuminator (CoolLED, U.K.). A triple bandpass filter which transmitted light

at  $470 \pm 10$  nm,  $540 \pm 10$  nm and  $645 \pm 50$  nm was placed in the detection pathway. The emission signal was detected using a VNP-29MC CCD camera with chip-shifting modality (Vieworks, South Korea) to capture the full FOV of the Mesolens at high resolution. Widefield mesoscopic imaging was carried out using water immersion ( $n = 1.33$ ) with the Mesolens' correction collars set accordingly to minimise spherical aberration through refractive index mismatch.

#### **3.2.2.4 Confocal laser scanning mesoscopy**

For laser scanning confocal mesoscopy specimens were prepared as outlined above. Fluorescence excitation of GFP was obtained using the 488 nm line set at 5 mW from a multi-line LightHUB-4 laser combiner (Omicron Laserage, Germany). The green emission signal was detected using a PMT (P30-01, Senstech, U.K.) with a 550 nm dichroic mirror (DMLP550R, Thorlabs, USA) placed in the emission path and a 525/39 nm bandpass filter (MF525-39, Thorlabs, USA) placed before the detector.

For reflection confocal mesoscopy incident light was sourced from a 488 nm line set at 1 mW from a multi-line LightHUB-4 laser combiner (Omicron Laserage, Germany). Reflected signal was detected using a PMT (P30-01, Senstech, U.K.) with no source-blocking filter in place.

Confocal laser scanning mesoscopy was carried out using type DF oil immersion ( $n = 1.51$ ) with the Mesolens' correction collars set accordingly to minimise spherical aberration through refractive index mismatch.

#### **3.2.3 Characterising the structure of intra-colony channels**

The distribution of several archetypal biofilm structural components was visualised to characterise the structure of intra-colony channels.

### **3.2.3.1 Assessment of channel composition by reflection**

#### **confocal mesoscopy**

As the biofilms in this study were submerged during imaging in a medium with known refractive index, it was possible to determine if channels were filled with substances of differing refractive index (e.g. air) using reflection confocal mesoscopy as above. Solid LB was cast into a 3D printed imaging chamber and inoculated with JM105 at a density of  $1 \times 10^4$  cfu/ml and incubated for 18-24 hours at 37°C in darkened conditions. Biofilms were mounted in sterile LB medium ( $n = 1.338$ ) prior to imaging.

### **3.2.3.2 Determining the distribution of non-viable cells in *E. coli***

#### **biofilms**

The distribution of non-viable cells in the biofilm was assessed using the approach developed by Asally *et al.*<sup>172</sup>. Briefly, JM105-miniTn7-*HcRed1* colony biofilms were grown for imaging in 3D-printed imaging moulds as outlined previously. LB medium was supplemented with gentamicin (20 µg/ml) (G-3632, Sigma-Aldrich, USA) and 0.5 µM Sytox green dead-cell stain (S7020, Invitrogen, USA). Cells were seeded at a density of  $1 \times 10^4$  cfu/ml and grown for 18-24 hours prior to imaging on the Mesolens in widefield epifluorescence mode as described above. A 490 nm and a 580 nm LED from a pE-4000 LED illuminator (CoolLED, U.K.) were used to excite Sytox Green and HcRed1 respectively. The emission signal was detected using a VNP-29MC CCD detector (Vieworks, South Korea) with 3x3 pixel-shift modality enabled and with a triple band pass filter ( $470 \pm 10$  nm,  $540 \pm 10$  nm and  $645 \pm 50$  nm) in the emission path.

### **3.2.3.3 Determining the distribution of exopolysaccharides in *E. coli* biofilms**

To visualise the distribution of EPS in the biofilm, sialic acid and *N*-acetylglucosaminyl residues were stained by supplementing solid M9 medium (0.2% glucose (w/v))<sup>280</sup> with 20 µg/ml gentamicin and 2 µg/ml Alexa594-wheatgerm agglutinin (WGA) (W11262, Invitrogen, USA) before inoculating with  $1 \times 10^4$  cfu/ml JM105-miniTn7-*gfp* and growing as previously described. EPS-stained specimens were imaged using widefield epifluorescence mesoscopy as before using a 490 nm LED to excite GFP and 580 nm LED to excite Alexa594-WGA.

### **3.2.3.4 Determining the distribution of cellulose in *E. coli* biofilms**

Although *E. coli* K12 isolates do not typically produce cellulose, this is a major constituent of many other biofilm-forming species<sup>171,282</sup>. To effectively exclude this as an option cellulose distribution was tested using the fluorescent dye, Calcofluor-White (CFW), which binds selectively to cellulose and chitin residues. Solid LB medium supplemented with 20 µg/ml gentamicin and 10 µM CFW (18909, Sigma-Aldrich, USA) and inoculated with  $1 \times 10^4$  cfu/ml JM105-miniTn7-*HcRed1* and growing as previously described. CFW-stained specimens were imaged using widefield epifluorescence mesoscopy as before using a 435 nm LED to excite CFW and 580 nm LED to excite HcRed1.

### **3.2.3.5 Determining the distribution of lipids in *E. coli* biofilms**

The lipid localisation throughout the biofilm was determined by staining with Nile Red. Solid LB medium with 20 µg/ml gentamicin was supplemented with 10 µg/ml Nile Red (72485, Sigma-Aldrich, USA) before inoculating with  $1 \times 10^4$  cfu/ml JM105-miniTn7-*gfp* and growing as previously described. The lipid distribution in relation to the intra-

colony channels was observed using widefield epifluorescence mesoscopy as before using a 490 nm LED to excite GFP and 580 nm LED to excite Nile Red.

### **3.2.3.6 Determining the distribution of proteins in *E. coli* biofilms**

The protein distribution was determined by staining the biofilm with FilmTracer SYPRO Ruby biofilm matrix stain (F10318, Fisher Scientific, USA) which binds to a number of different classes of extracellular protein. Solid LB medium was prepared containing 20 µg/ml gentamicin and a final concentration of 2% (v/v) FilmTracer SYPRO Ruby biofilm matrix stain before inoculating with JM105-miniTn7-*gfp* and growing as previously described. Specimens were imaged using widefield epifluorescence mesoscopy. A 490 nm and a 580 nm LED from a pE-4000 illuminator (CoolLED, UK) were used for GFP and SYPRO Ruby excitation, respectively. Fluorescence emission from GFP and SYPRO Ruby were detected as outlined above. Both channels were acquired sequentially.

### **3.2.3.7 Viability screening with structural dyes**

To ensure that the addition of structural stains did not impact the viability of strains used in this chapter the end-point viability was determined by growing each strain in the presence and absence of each dye noted above and recording the number of cfu/ml after growing in the presence of the dye. Overnight cultures of JM105, JM105-miniTn7-*gfp* and JM105-miniTn7-*HcRed1* were prepared in LB broth and the miniTn7 strains were supplemented with 20 µg/ml gentamicin. Following 12 hours of incubation shaking at 250 rpm at 37°C, each overnight culture was subcultured into sterile LB broth at a dilution ratio of 1:100 and grown for 3-4 hours shaking at 250 rpm at 37°C. The OD of each culture was then equalised to OD<sub>600</sub> = 0.5 and then serially diluted to 1x10<sup>-5</sup> before spreading 100 µl on solid LB medium supplemented with the working concentration of each structural dye (described above) and 20 µg/ml



gentamicin for the miniTn7 strains. The inoculated plates were then incubated at 37°C for 20 hours before counting the number of colony-forming units (CFUs).

Statistical analysis (unpaired T-test) was carried out using Prism (v6.0e) to determine if growth in the presence of structural dyes had affected the growth of each strain.

### **3.2.4 Disruption and recovery of intra-colony channel structures**

To assess if intra-colony were able to recover following disruption, single colonies of JM105-miniTn7-*gfp* were grown on solid LB medium supplemented with 20 µg/ml gentamicin and allowed to grow for 10 hours at 37°C in darkened conditions. Following the initial growth step colonies were removed from the incubator and gently mixed with a sterile 10 µl pipette tip to disrupt the channel structures in the growing biofilm. Care was taken to prevent disruption to the underlying solid medium on which the colony was supported. Following disaggregation, the colonies were grown for a further 10 hours at 37°C in darkened conditions prior to imaging. Colonies were then mounted in sterile LB medium and imaged using widefield epifluorescence mesoscopy as described above.

### **3.2.5 Strain mixing**

The phenomenon of strain sectoring has been previously documented and occurs by mechanical buckling as adjacent colonies expand into each other during radial growth<sup>182,186</sup>. Lineage sectoring has also been observed to control interactions between adjacent strains, and so it was investigated if intra-colony channels were able to cross the strain boundary between sectors. A low-density mixed culture of JM105-miniTn7-*gfp* and JM105-miniTn7-*HcRed1* at a 1:1 ratio was inoculated as lawn onto solid LB medium containing 20 µg/ml gentamicin. Colonies of each strain were allowed to stochastically collide into adjacent clonal populations during colony

expansion and then imaged using widefield mesoscopy after incubation for 20 hours at 37°C in darkened conditions as described above.

### 3.2.6 Verification of mini-Tn7 insertion by colony PCR

Colony PCR was used to confirm that the miniTn7 insertion, which contained the photoprotein gene (Figure 3.3), occurred at the same chromosomal location in both strains. The miniTn7 insertion site is believed to be close to the gene encoding the glutamate-fructose-6-phosphate aminotransferase (*glmS*)<sup>283</sup>. Forward and reverse primers were designed using IDT's PrimerQuest tool for the *glmS* gene situated approximately 25 bp upstream of the Tn7 insertion site and the right flanking region of the miniTn7 insert (*glmS* Fwd. – 5'-AAC CTG GCA AAT CGG TTA C-3'; *tn7R109* Rev. – 5'-CAG CAT AAC TGG ACT GAT TTC AG-3'). Colony PCR was carried out using a mastermix containing 1X Green GoTaq® Reaction Buffer (M791A, Promega, USA), 800 µM PCR nucleotide mix (U144A, Promega, USA) (200 µM of each dNTP), 59 pM *glmS* forward primer and 68 pM *tn7R109* reverse primer in a 50 µl reaction. Single colonies of JM105, JM105-miniTn7-*gfp* and JM105-miniTn7-*HcRed1* which were grown on solid LB (miniTn7 cultures supplemented with 20 µg/ml gentamicin) were suspended in the mastermix which was supplemented with 1.25 units of ice cold GoTaq® DNA polymerase (M3005, Promega, USA) and mixed thoroughly immediately prior to cycling. A no template control (NTC) was included by adding 1 µl of nuclease-free water to a mastermix solution and supplemented with polymerase. The cycling conditions involved an initial denaturation at 94°C for 2 minutes followed by 34 cycles of denaturation (94°C for 30 seconds), annealing (49°C for 30 seconds) and extension (72°C for 1 minute), with a final extension at 72°C for 5 minutes.

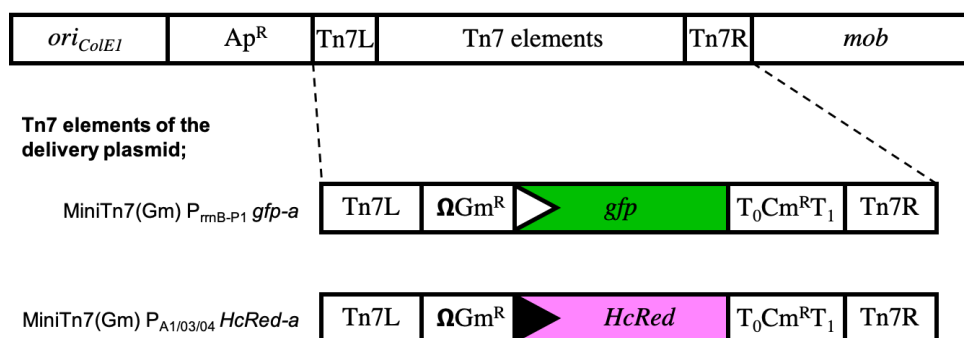


**Figure 3.3. An overview of the miniTn7 photoprotein system.** A schematic of the delivery plasmid containing the miniTn7 insertion element. The insertion element confers gentamicin resistance ( $Gm^R$ ) provided by *aacC1* which encodes for an acetyltransferase-3-1 enzyme, chloramphenicol resistance ( $Cm^R$ ) from *cat* which encodes for a chloramphenicol-acetyltransferase.  $\Omega$  denotes that the  $Gm^R$  gene is flanked by a transcriptional and translational terminator sequence. Each photoprotein is under the control of its own promotor; white triangles represent the growth dependent promotor,  $P_{rmb-P1}$ , and black triangle represent the constitutive promotor,  $P_{A1/04/03}$  (a  $P_{lac}$ -derivative). Figure adapted from <sup>283</sup> to outline only the Tn7 elements used in this study.

Following amplification, PCR products were analysed by gel electrophoresis. Products were run on a 1.5% agarose gel prepared with 1X tris:acetate:ethylenediaminetetraacetic acid (TAE) buffer (40 mM tris, 20 mM glacial acetic acid and 1 mM disodium EDTA) and ethidium bromide. Four microlitres of each product was ran along with 8  $\mu$ l of a 50 bp hyperladder (BIO-33054, Bioline, USA) at 70 volts for 1 hour and 45 minutes in 1X TAE. Gels were then imaged using an inGenius gel imaging system (Syngene, Synoptics Ltd., UK) with UV excitation.

### 3.2.7 Determining the function of intra-colony channels

#### 3.2.7.1 Fluorescein uptake assay

To test if intra-colony channels were able to transport small molecules (e.g. signalling molecules, nutrients etc.) from their external environment, mature colonies of JM105

were prepared as described above. Prior to imaging, fluorescein sodium salt (F6377, Sigma-Aldrich, USA) was added to sterile LB broth at a final concentration of 10  $\mu\text{g/ml}$  (26.6  $\mu\text{M}$ ). The fluorescein-spiked LB broth was used to mount the colony for imaging as before, and colonies were incubated with the mountant at 37°C for 30 minutes to allow fluorescein to diffuse into the colony. Colonies were imaged by confocal mesoscopy, as outlined above, to ensure that detected fluorescein emission was limited to the focal plane.

### **3.2.7.2 Fluorescent microsphere uptake assay**

To further test the function of intra-colony channels a confluent lawn of fluorescent microspheres was seeded along with the bacterial inoculum at the culturing stage. Two-hundred nanometre Fluoresbrite® Multifluorescent microspheres (24050, Polysciences Inc., USA) were seeded at a density of  $1 \times 10^{10}$  microspheres/ml and plated along with  $1 \times 10^4$  cfu/ml JM105-miniTn7-*gfp* in a mixed-inoculum. Microsphere translocation was assessed by widefield epifluorescence mesoscopy as above with two-channel detection for both the GFP and microsphere fluorescence emission. A triple bandpass emission filter which transmitted light at  $470 \pm 10$  nm,  $540 \pm 10$  nm and  $645 \pm 50$  nm was placed in the detection path. Sequential excitation of GFP and the fluorescent microspheres was achieved using a 490 nm and 580 nm LED, respectively, from a pE-4000 LED illuminator (CoolLED, U.K.) Each channel was acquired sequentially using a CCD camera detector (Stemmer Imaging, U.K.). All imaging was carried out using water immersion.

### **3.2.7.3 Assessing channel-mediated nutrient uptake**

The functional role of intra-colony channels was further tested using an arabinose biosensor. The biosensor strain contained the *araBAD* operon with *gfp* inserted downstream on the promoter and *araBAD* functional genes (Figure 3.4), where *gfp*

expression was controlled by the presence or absence of L-arabinose<sup>284</sup> (Figure 3.5).

The biosensor strain was a gift from colleagues at the James Hutton Institute.

JM105 transformed with the arabinose biosensor plasmid, pJM058, were grown overnight at 37°C while shaking at 250 rpm in liquid LB medium supplemented with 25 µg/ml chloramphenicol (C0378, Sigma-Aldrich, USA). Overnight cultures were then diluted in fresh LB and grown until OD<sub>600</sub> = 0.5. Cells were then pelleted and washed three times with 1x M9 salts. Washed cells were inoculated on to solid M9 minimal medium<sup>280</sup> with L-arabinose as the sole carbon source (0.2%) at a density of  $1 \times 10^4$  cfu/ml and grown for 42-48 hours in darkened conditions at 37°C. Specimens were then prepared for imaging as outlined above.

After establishing a role for intra-colony channels in nutrient acquisition, a method for time-delayed induction of P<sub>BAD</sub> was tested so that nutrient uptake might be visualised by time-lapse microscopy. It was initially thought that injecting an L-arabinose suspension directly under a mature colony would allow for induction of *gfp* expression along the intra-colony channels to be visualised. To determine if an injection method was viable a 25 µM solution of fluorescein was prepared and injected directly under the surface of solid M9 medium which had been cast into an imaging chamber, mounted in sterile 1x M9 salts with a Mesolens coverglass on top. Time-lapse widefield mesoscopy was then carried out as described above to observe the diffusion of fluorescein from the injection site.

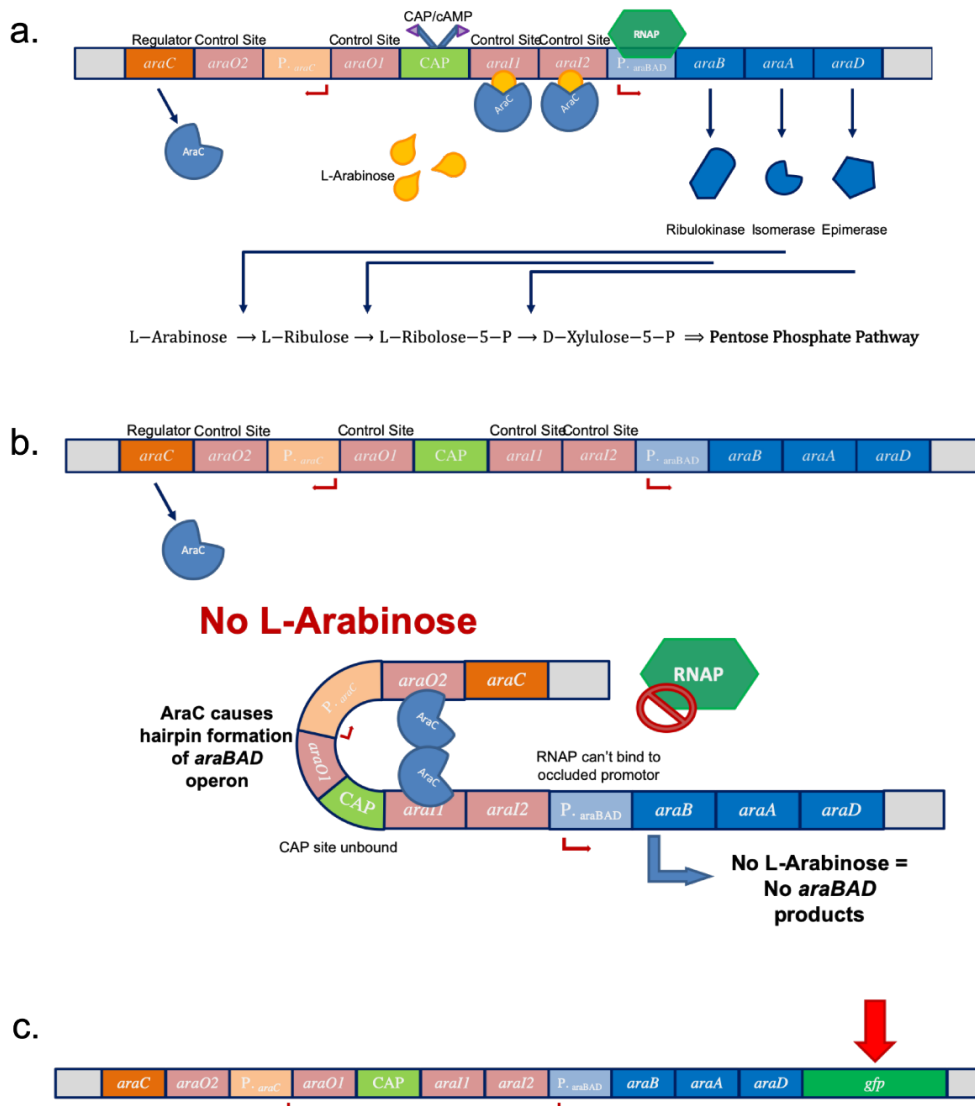


**Figure 3.4. Induction of the arabinose operon.** **a)** When L-arabinose is present positive regulation of the *araBAD* operon occurs, where AraC is able to bind to control sites on *araI1* and *araI2*, which allows RNA polymerase (RNAP) to bind to the *araBAD* promoter sequence and transcribe the functional genes *araB*, *araA* and *araD*, which catalyse steps in the pentose phosphate pathway. **b)** When L-arabinose is not present AraC binds to control sites on *araO2* and *araI1* which results in formation of a hairpin loop and subsequent occlusion of  $P_{BAD}$ . Therefore, in the absence of L-arabinose the downstream functional products AraB, AraA and AraD are not produced. **c)** The biosensor strain used in this work relies on the positive regulation of the *araBAD* operon, meaning that in the presence of L-arabinose all genes under the control of  $P_{BAD}$  will be transcribed, including any inserted gene (e.g. *gfp*). Adapted from <sup>284</sup>.

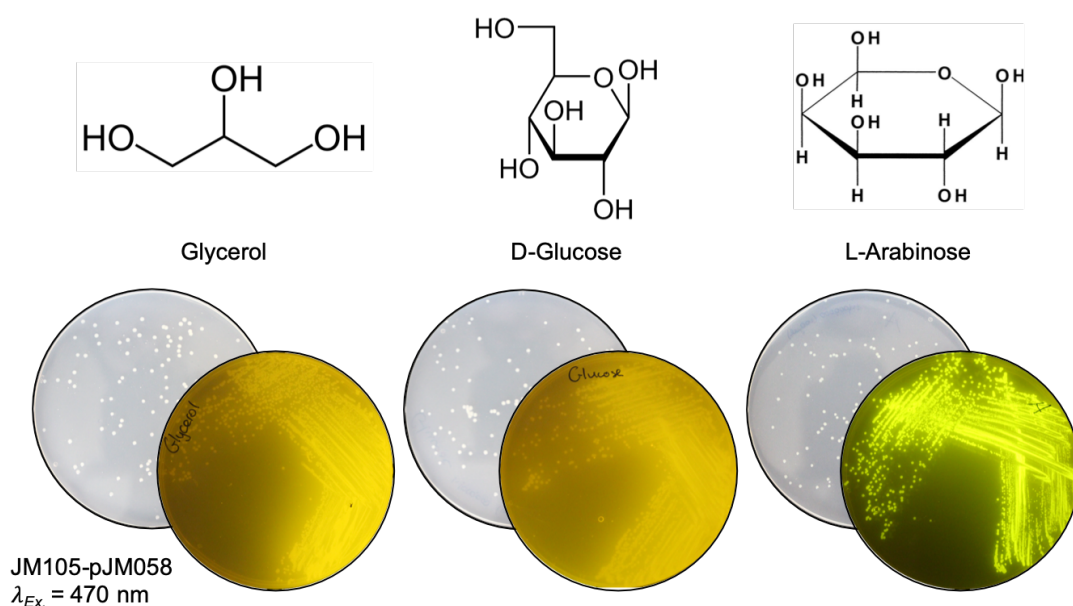


**Figure 3.5. GFP production by JM105-pJM058 is dependent on the presence of L-arabinose.** Three culture of JM105-pJM058 ( $P_{BAD-gfp}$ ) grown on solid M9 minimal medium with various carbon source. Images of plates were acquired in ambient lighting (top) and on a blue lightbox ( $\lambda_{Ex.} = 470 \text{ nm}$ ) (bottom). JM105-pJM058 only expresses *gfp* in the presence of L-arabinose as a carbon source.

Injection of fluorescein was found to result in rapid diffusion, and so a perfusion system which provided more control over the delivery of liquid to the solid medium was investigated. A perfusion system was built using a 20 ml syringe and tubing coupled to an automatic valve controller (VC-6, Warner Instruments, USA), and with a 120 mm long 21-gauge hypodermic needle (4665643, B. Braun Melsungen AG, Germany) inserted into the side wall of the imaging chamber with the tip directly under the surface of the solid medium. A 25  $\mu\text{M}$  solution of fluorescein was then perfused into the solid medium and time-lapse widefield mesoscopy was used to monitor the diffusion of fluorescein in the medium. The perfusion method proved more robust than the injection method, and so the same perfusion method was used to introduce a 0.5% (w/v) L-arabinose solution (33 mM) directly underneath a mature JM105-

pJM058 macro-colony biofilm which had been grown on solid M9 medium supplemented with 25 µg/ml chloramphenicol as above, but with 0.5% (v/v) glycerol (54 mM) as the sole carbon source. The colony was then imaged using the previous acquisition settings over the course of 20 hours after perfusion with L-arabinose, however  $P_{BAD}$  was not induced.

As the colonies were grown initially on glycerol as a carbon source before the introduction of L-arabinose, it was thought that carbon catabolite repression (CCR) may be preventing the induction of  $P_{BAD}$  if the biofilm was under diauxic conditions. To test this theory, GFP emission was used as a proxy measurement for  $P_{BAD}$  induction. A range of diauxic conditions were prepared in a black optical-bottom 96-well plate (265300, ThermoFisher Scientific, USA). M9 minimal medium supplemented with 25 µg/ml chloramphenicol was used as a base medium for all wells. Varying ratios of glycerol and L-arabinose (0.15%:0.05%, 0.1%:0.1%, 0.05%:0.15%) or D-glucose and L-arabinose (0.15%:0.05%, 0.1%:0.1%, 0.05%:0.15%) were tested. JM105-pJM058 was grown in overnight cultures which were then diluted in fresh LB and grown until  $OD_{600} = 0.5$ . Cells were then pelleted and washed three times with 1x M9 salts and used to inoculate the 96-well plate (inoculum volume = 1%). Blanks of each condition containing no cells were also included and used as a baseline for all test wells. The loaded plate was then placed into a Synergy™ HTX multi-mode plate reader (BioTek Instruments Inc., US) with GFP emission selected (490/520 nm). The plate reader was set to medium orbital shaking at 37°C while measuring GFP emission every hour for a period of 36 hours.

#### **3.2.7.4 Testing intra-colony channel-mediated antibiotic transport**

As intra-colony channels were found to transport nutrients into the colony from the external environment it was hypothesised that this function could be exploited to



promote the uptake of antimicrobial compounds. To test this hypothesis antibiotics would have to be introduced to the mature colony once it had already grown, as any antibiotics supplemented into the medium at the start of the experiment would prevent colony formation. To achieve this a modified disk diffusion assay was developed where, instead of filter disks, sterile filter rings with a central bore diameter larger than that of the colony (approx. 3 mm) were placed around the colony for a set time period prior to imaging. Following this a viability staining approach revealed the distribution of non-viable cells throughout the biofilm, including along the intra-colony channels. Three bactericidal antibiotics were selected from a panel of clinically relevant compounds routinely used in antimicrobial disk diffusion and bioactivity assays (as outlined by the European Committee on Antibiotic Susceptibility Testing (EUCAST) and the British Society for Antimicrobial Chemotherapy (BSAC)). Streptomycin (S-6501, Sigma-Aldrich, USA), colistin (C-4461, Sigma-Aldrich, USA) and kanamycin (K-1876, Sigma-Aldrich, USA) were selected.

To narrow down which antibiotic should be tested against mature macro-colony biofilms, each compound was screened in a disk diffusion assay against JM105 and JM105-miniTn7-*HcRed1*. To ensure that the clearance diameter was large enough to effect the whole colony, three different dose concentrations of each antibiotic were tested in triplicate to generate a standard curve of dose concentration versus clearance diameter which was used to determine the optimal dosage for a 6 mm filter ring with a 3 mm diameter bore. Briefly, an overnight culture of each strain was subcultured into fresh LB broth (with 20 µg/ml gentamicin supplemented into the miniTn7 cultures) and grown for 3-4 hours shaking at 250 rpm at 37°C until OD<sub>600</sub> = 0.5. Cultures were then serial diluted to 10<sup>-4</sup> before spreading 100 µl on solid LB medium (again, with 20 µg/ml gentamicin supplemented into the miniTn7 cultures). Four sterile 6 mm filter disks were placed over the lawn and three were saturated by

pipetting 10  $\mu$ l of antibiotics at each dose concentration (streptomycin = 1  $\mu$ g, 5  $\mu$ g and 10  $\mu$ g; colistin = 5  $\mu$ g, 10  $\mu$ g and 25  $\mu$ g; kanamycin = 10  $\mu$ g, 25  $\mu$ g and 50  $\mu$ g). The final filter disk on each plate was saturated with 10  $\mu$ l of sterile distilled water as a negative control. Plates were incubated for 20 hours at 37°C and clearance zones were measured from the centre of each disk. From this, colistin was selected as the appropriate test antibiotic due to its increased potency and clinical relevance.

Having established colistin as the test compound, the clearance diameter of filter rings was compared to that of filter disks. This ensured that filter rings could produce comparable clearance zones despite their lower area when compared to disks. The area of the filter disks was calculated to be 28.26 mm<sup>2</sup>, whereas the area of the filter rings was 25% lower at 21.20 mm<sup>2</sup>. This was taken into account when loading the test dosage onto the rings to ensure that both rings and disks had a proportional mass of test antibiotic. Filter rings were prepared by pressing out 6 mm disks from Whatman 3MM Chr paper (3030-917, GE Healthcare UK Ltd., UK) and using a pair of revolving punch pliers to punch out a 3 mm diameter central bore. Rings were sterilised by autoclaving at 121°C for 15 minutes. As before, lawns of JM105-miniTn7-*HcRed1* were inoculated onto solid LB medium supplemented with 20  $\mu$ g/ml gentamicin. Sterile filter disks and rings were placed evenly spaced on each plate. Disks were loaded with 5  $\mu$ g of colistin and rings were loaded with 3.75  $\mu$ g of colistin (25% less to accommodate for lower surface area) in triplicate as before. Sterile distilled water was loaded as a negative control. Plates were incubated for 20 hours at 37°C and clearance zones were measured from the centre of each disk.

To establish if it was possible for the nutrient acquisition function of the intra-colony channels could be exploited for antibiotic uptake, biofilms were imaged in the presence of a cell viability dye following treatment with colistin for different time periods. JM105-miniTn7-*HcRed1* biofilms were prepared for imaging as in Section

3.2.3.2 by inoculating solid LB medium supplemented with gentamicin (20 µg/ml) and 0.5 µM Sytox green dead-cell stain (S7020, Invitrogen, USA). Plates were then incubated for 20 hours at 37°C in darkened conditions. Following growth, sterile filter rings were carefully placed around several colonies and loaded with 3.75 µg of colistin before incubating specimens for 8, 6, 4 and 2-hour periods at 37°C in darkened conditions to allow diffusion of the antibiotics. Sterile distilled water was used as a negative control. Following antibiotic treatment, the filter rings were carefully removed using sterile forceps as to not disrupt the colony. The specimens were then mounted in sterile LB broth and imaged by widefield epifluorescence mesoscopy as described in Section 3.2.3.2.

To quantify the effect of colistin treatment on the mature biofilms the intensity of the Sytox Green signal was measured each time point. An ROI around the colony was generated using FIJI. Colony segmentation was achieved by automatically thresholding (Huang) raw widefield images and creating a binary mask before selecting as an ROI and measuring the mean fluorescence intensity of Sytox Green emission within the ROI. The mean intensities were then normalised to rescale all datapoints between 0 and 1 using Equation 3.1 (where  $x'$  is the normalised value for datapoint,  $x$ , and  $x_{min}$  and  $x_{max}$  are the minimum and maximum datapoints in the dataset) and plotted using Plots of Data (developed by Joachim Goedhart, University of Amsterdam, Netherlands). Each timepoint was then compared using an unpaired t-test in Prism (v6.0e).

$$x' = \frac{x - x_{min}}{x_{max} - x_{min}} \quad [3.1]$$

### 3.2.8 Image processing and analysis

Widefield epifluorescence mesoscopy z-stacks were deconvolved where specified using with Huygens Professional version 19.04 (Scientific Volume Imaging, The

Netherlands, <http://svi.nl>) using a Classic Maximum Likelihood Estimation algorithm. Hot and cold pixels were removed prior to deconvolution by the Huygens Professional software. A theoretical point spread function was generated using Huygens Professional with parameters adjusted to suit the experimental setup. Deconvolution was performed using a server with a 64-bit Windows Server 2016 Standard operating system (v.1607), two Intel® Xeon® Silver 4114 CPU processors at 2.20 GHz and 2.19 GHz and 1.0 TB installed RAM. Image analysis was performed using FIJI<sup>60</sup>. Figures presented here were linearly contrast adjusted for presentation purposes where required using FIJI<sup>235</sup>.

BiofilmQ<sup>285</sup> was used to quantitatively analyse confocal mesoscopy data. This MATLAB image analysis tool was developed specifically for analysing image data of whole biofilm specimens and uses segmentation to quantify biofilm properties such as density and number of cells. Fluorescence intensity statistics can also be extracted for each individual cell within a multi-millimetre biofilm, however until this work, the programme had only been shown using biofilms on the order of  $1 \times 10^3$  cells<sup>130</sup>. Confocal data was used due to the increased SNR which makes computational analysis easier. A custom MATLAB script was provided by Hannah Jekel (Max-Planck-Institut für terrestrische Mikrobiologie, Marburg, Germany) to overcome the time-out limits included in the published BiofilmQ script. Images were first aligned in the  $z$ -dimension by the programme to account for any drift present in the imaging system. Automated thresholding (Otsu) and segmentation was used to identify and provide spatial and fluorescence information for all cells within a mature colonial biofilm.

## 3.3 Results

### 3.3.1 Identification of a network of intra-colony channels in *E. coli* biofilms

#### 3.3.1.1 Intra-colony channels discovered in mature *E. coli* biofilms

Firstly, GFP-expressing *E. coli* (JM105) macro-colony biofilms were imaged using widefield mesoscopy to reveal a network of previously undocumented channel-like structures which permeated the superstructure of the biofilm (Figure 3.6). These channels measure, on average, 15-20  $\mu\text{m}$  in width and spanned from the centre of the colony to the periphery. The intra-colony channels possessed fractal patterning features, with sharp boundaries consisting of individual cells arranged pole-to-pole. The raw data stack was deconvolved using a Classical Maximum Likelihood Estimation (CMLE) algorithm to improve the image quality and reveal the arrangement of individual cells in the mature biofilm. A colour-coded look-up table (LUT) was then assigned according to the axial position of each image within the 36  $\mu\text{m}$ -thick z-stack. From the axial coded LUT shown in Figure 3.6, the intra-colony channels were determined not to be a 2D lateral arrangements of cells, but instead channels exhibited a 3D topography within the context of the biofilm, resembling canyons and ravines rather than enclosed capillaries. It is difficult to quantitatively analyse these features of the biofilm using conventional image processing tools due to the complex geometry of the channel structures and the sheer size of Mesolens datasets. Similarly, it is difficult to trace these channels in 3D through the biofilm as conventional thresholding does not allow for segmentation of the channels due to the intensity difference between cells at the periphery and centre of the biofilm.

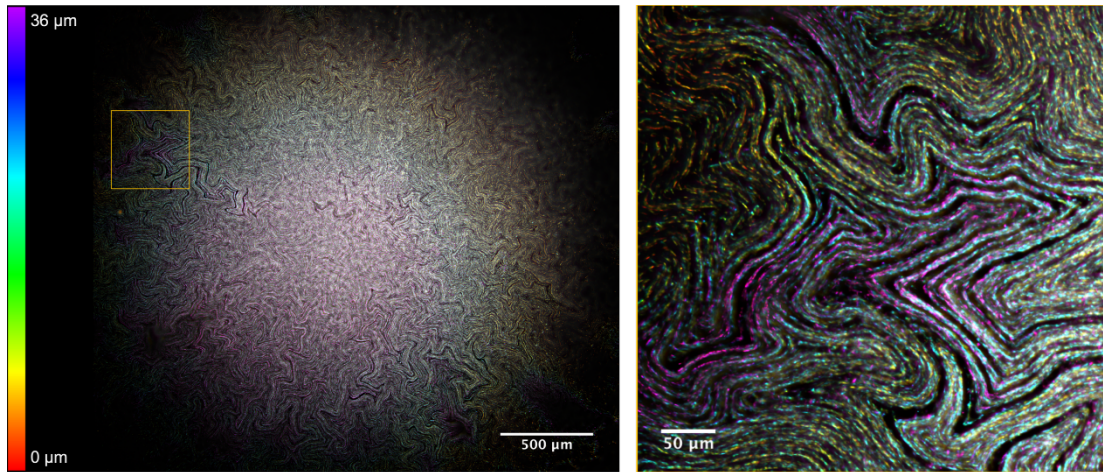


**Figure 3.6. Identification of an intra-colony channel system in *E. coli* macro-colony biofilms.** A deconvolved 36  $\mu\text{m}$ -thick central transverse hyperstack of a mature *E. coli* macro-colony biofilm acquired using widefield mesoscopy. An axial colour coded LUT has been applied which indicates the relative position of each cell within the context of the biofilm. A magnified ROI is presented where individual cells can be clearly resolved. Channel structures are seen to permeate throughout the biofilm and present a 3D topography within the context of the biofilm.

The benefits of deconvolution of widefield Mesolens data include increased resolution and contrast, particularly with thick specimens, as well as decreased acquisition time and light exposure when compared to confocal laser scanning methods. To illustrate the improvement that was achieved by deconvolving widefield data, Figure 3.7 shows a comparison of raw and deconvolved data.

Colonies were also imaged using the Mesolens in confocal laser scanning mode to verify that the post-acquisition processing, such as deconvolution, did not introduce erroneous structural artefacts with similar fractal-like patterns to the intra-colony channels (Figure 3.8). A confocal approach was used because of the marked improvement in signal-to-noise ratio compared to widefield techniques, particularly with thick specimens, resulting in a similar image quality to a deconvolved widefield dataset. Confocal mesoscopy revealed the same channel structures that were

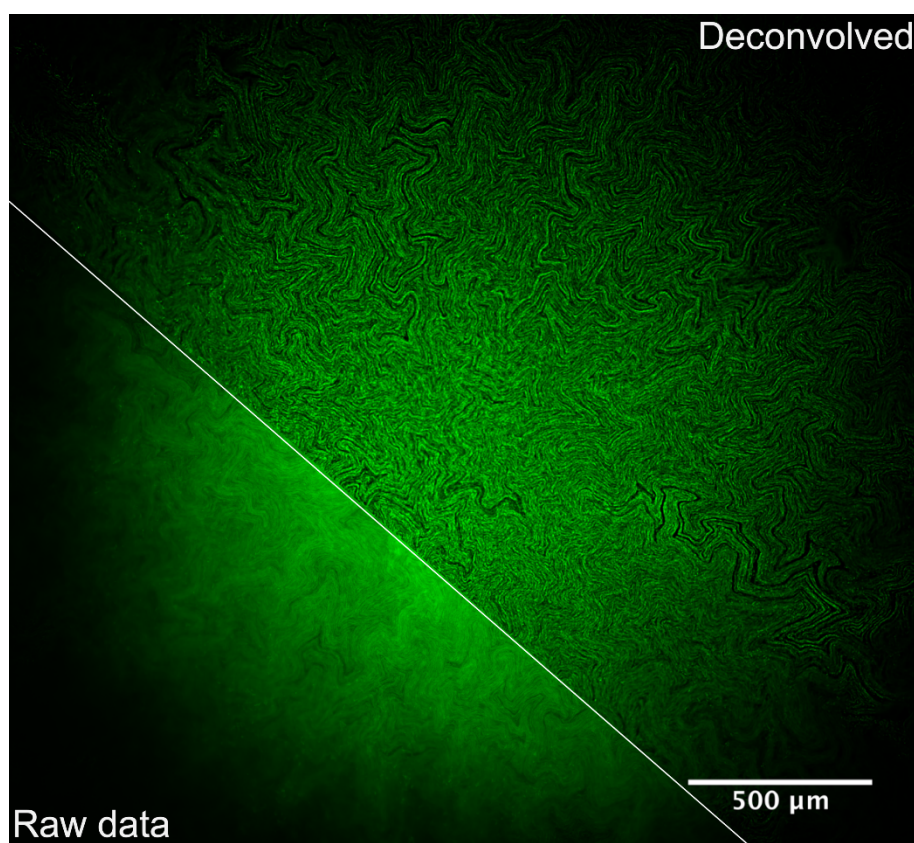


**Figure 3.7. Increasing the quality of widefield mesolens data with deconvolution.** A widefield mesoscopy image of a GFP-expressing JM105 macro-colony biofilm before and after deconvolution. Raw data is presented on the left and deconvolved data is shown on the right. Following deconvolution, intra-colony channels and individual *E. coli* cells are more clearly resolved.

identified by widefield imaging experiments presented in Figure 3.6. This concludes that the structures observed were not introduced as an artefact of image processing. Using the recently published MATLAB analysis tool, BiofilmQ<sup>285</sup>, multi-scale structural analyses were performed to further investigate the channel structures. Parameters such as local cell density and distance from the substrate were able to be extracted from the BiofilmQ programme. Where most analysis tools are unable to process large datasets (such as those generated by the Mesolens), BiofilmQ was capable of handling large file sizes where the only limitation was the processing speed and available RAM of the computer used. This meant that, with Mesolens datasets,



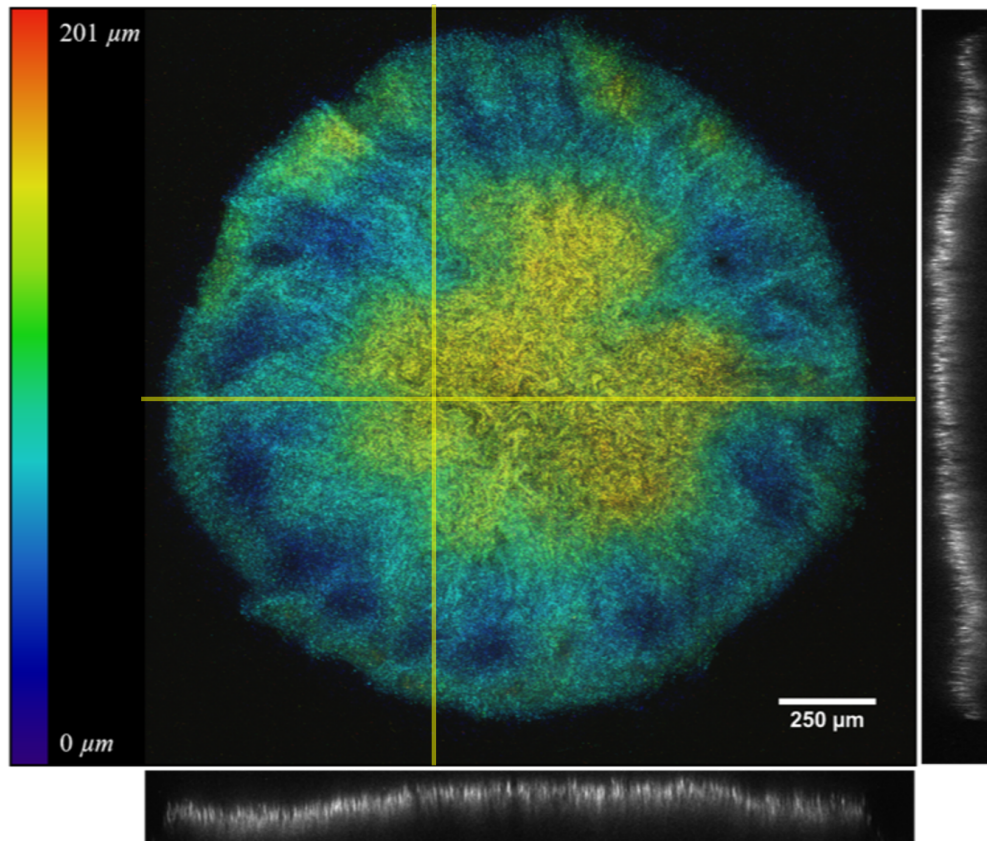


**Figure 3.8. Confocal laser scanning mesoscopy revealed that intra-colony spatial patterns are not an artefact of the deconvolution process.** A maximum intensity projection of a single JM105-miniTn7-*gfp* colony measuring 201  $\mu\text{m}$  thick is shown with a colour coded LUT applied to each optical section depending on its axial position within the dataset. Intra-colony channels could be observed throughout the colony and converged towards the apex of the biofilm. Accompanying orthogonal sections are presented from a cross-section at the centre of the colony. Channels were observed to pass through the majority of the colony from the base to the apex suggesting that they originate at the base of the biofilm. Yellow lines indicate the  $x, z$  and  $y, z$  planes of the orthogonal views.

biofilms containing more than  $1 \times 10^9$  individual cells could be analysed, whereas most image analysis tools are capable of only analysing up to a maximum of approximately  $1 \times 10^4$  cells in any given biofilm. Therefore, until now this has limited the scope of biofilm research to quantitative study of microcolonies. Following thresholding and segmentation, the distance of each cell in the biofilm was determined in relation to the



position of the underlying substrate (Figure 3.9). The number of cells within a mature *E. coli* macro-colony biofilm was extracted and calculated to be 126,308,734 in the case of the confocal dataset presented in Figure 3.8. This number of cells was consistent with what would be expected of culture-based numeration of a single *E. coli* macro-colony of this size. The local density of cells was also extracted from confocal data and cells were found to be more closely packed along the edges of intra-colony channels throughout the colony (Figure 3.10).

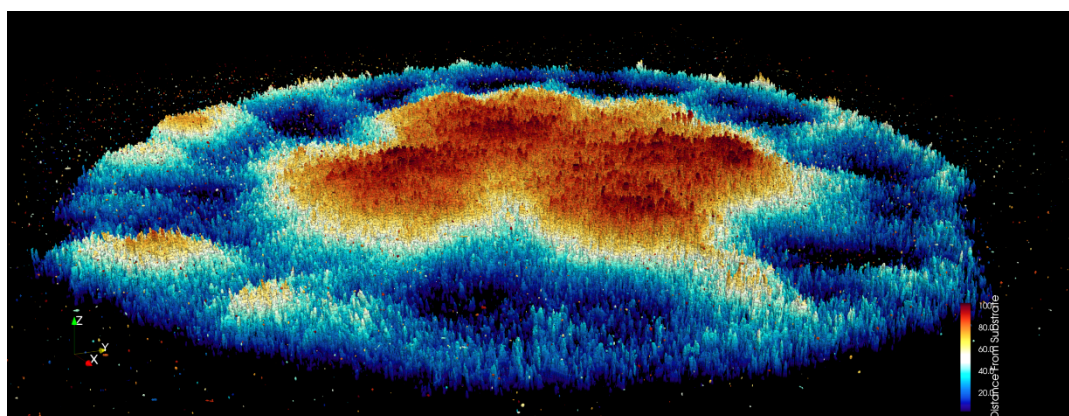


**Figure 3.9. A mature *E. coli* biofilm analysed by BiofilmQ.** A JM105-miniTn7-*gfp* biofilm imaged by confocal mesoscopy and analysed using BiofilmQ. Cell-to-substrate distance is colour coded for each individual cell. BiofilmQ calculated  $1.26 \times 10^8$  cells were present in the biofilm. Input data was of the same colony presented in Figure 3.8.

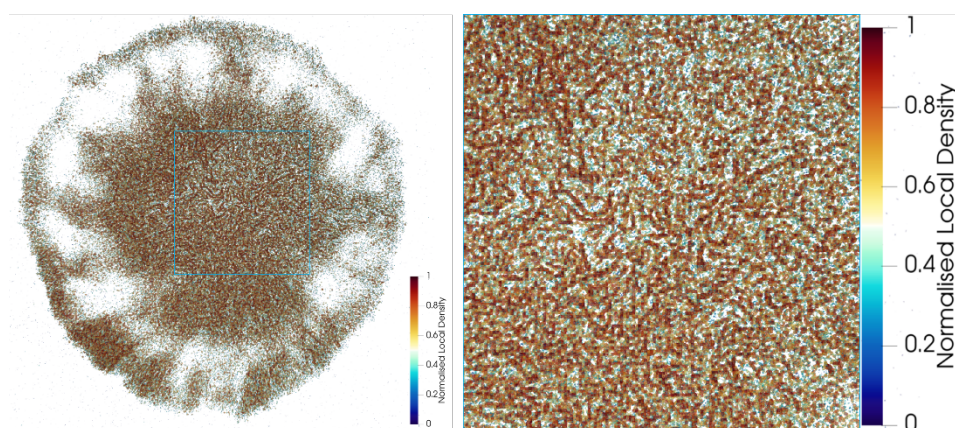


**Figure 3.10. Cells are densely packed along the borders of intra-colony channels.** BiofilmQ analysis reveals that local density is increased along the border of intra-colony channels. Local-density sensitivity = 5 voxels ( $2.5 \mu\text{m} \times 2.5 \mu\text{m} \times 15 \mu\text{m}$ ).

### 3.3.1.2 Demonstrating the benefits of mesoscopy for studying

#### biofilm architecture

Having discovered an intra-colony channels system using the Mesolens, mature colonies were also imaged using conventional optical microscopy methods to demonstrate the benefits of using the Mesolens for biofilm imaging. The internal architecture of *E. coli* macro-colony biofilms was imaged using conventional widefield epifluorescence microscopy and stereomicroscopy (Figure 3.11). Fluorescence stereomicroscopy was able to show some indication of internal structure within the biofilm; however, these features were too poorly resolved to merit using stereomicroscopy to study biofilm architecture beyond macroscopic structures.

The performance of the Mesolens was also compared to that of a conventional upright widefield imaging system to show the benefits of optical mesoscopy. Macro-colonies

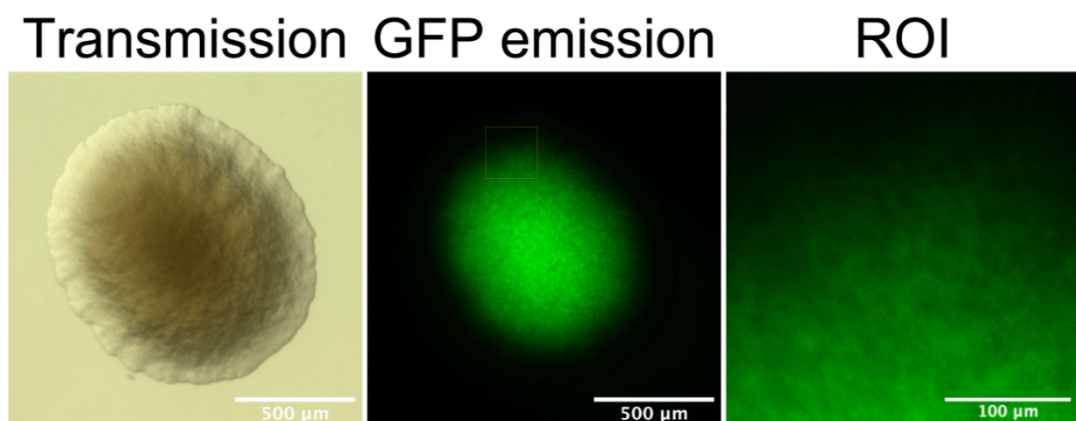


**Figure 3.11. Spatial resolution is too low to sufficiently resolve intra-colony channels**

**by stereomicroscopy.** A JM105-miniTn7-*gfp* macro-colony biofilm imaged by stereomicroscopy. A transmission image, GFP fluorescence image and an ROI of the highlighted region are presented. The transmission image of the colony shows the surface topology of the colony, but no intra-colony channels are evident. Fluorescence mode reveals some indication of intra-colony channels. However, these are poorly resolved and stereomicroscopy does not have optical sectioning capabilities, so 3D imaging is not possible.

of JM105-miniTn7-*gfp* were prepared and imaged using a Nikon Eclipse E600 system with a low magnification objective lens with approximately the same FOV as the Mesolens. Conventional widefield microscopy was able to resolve the intra-colony channel structures that were identified using widefield mesoscopy, however the spatial resolution was once again too low to adequately resolve the fine structure of the channels (Figure 3.12). This was particularly true along the *z*-dimension due to the elongation of the axial PSF along the optical axis of the microscope which scales in relation to the objective NA. Moving forward, these findings confirm that the Mesolens is an appropriate method for imaging large 3D microbial communities with sub-micron spatial resolution.

### **3.3.2 A structural assessment of intra-colony channels**

The channel structures identified in *E. coli* macro-colonies appear as dark regions within the biofilm, and so it was hypothesised that they contained some form of structural matrix. A number of structural candidates were tested by reflection and fluorescence microscopy methods.

#### **3.3.2.1 Intra-colony channels are not composed of solid growth medium or air**

The structural makeup of the channels was initially investigated to determine if they were filled with materials of differing refractive index compared to that of the biomass. Two candidates were solid growth medium which was forced upward during biofilm growth, or air which was trapped in the biofilm. Reflection confocal mesoscopy, where signal is detected from reflections of incident light at refractive index boundaries such as those between bacterial cells and the surrounding growth medium, was used. A

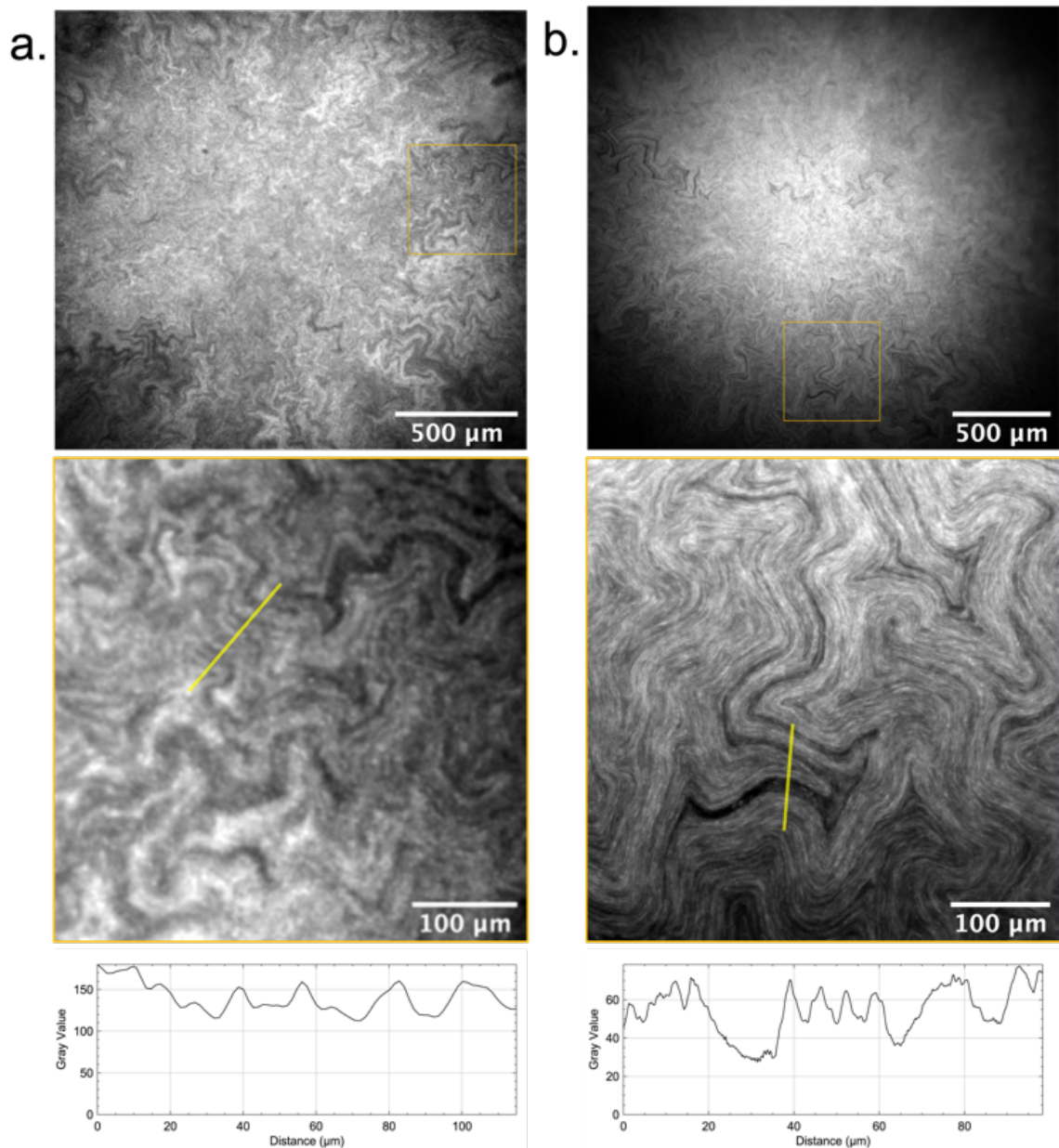


**Figure 3.12. Comparison of conventional low-NA widefield epifluorescence microscopy and high-NA mesoscopy.** **a)** Image of a *JM105-miniTn7-gfp* macro-colony biofilm acquired using a conventional low-magnification, low-NA objective lens on an upright widefield epifluorescence microscope. **b)** A mature *JM105-miniTn7-gfp* colony biofilm imaged using widefield epifluorescence mesoscopy. Intracolony spatial patterns are evident in both a) and b). Magnified regions have comparable FOVs, and line ROIs, shown in yellow, indicate that the increased NA of the Mesolens results in spatial higher resolution than a low-magnification, low numerical aperture lens.

maximum intensity projection of an unlabelled *E. coli* JM105 biofilm acquired in reflection confocal mode showed no reflection signal resembling the intra-colony channels throughout the colony (Figure 3.13a). Instead the surface layers of the colony were visible, where the biomass-medium interface occurs. This finding determined that the channels must be of a similar refractive index to the surrounding biomass and biofilm matrix and are not occupied by solid growth medium or air.

### **3.3.2.2 Biofilm channels are not composed of non-viable cells, EPS, cellulose or lipids**

To determine if the channel structures we observe were occupied by non-viable/non-fluorescing cells, biofilms were grown in the presence of the viability dye, Sytox Green. This dye has an emission peak at 523 nm enabling the use of HcRed1 ( $\lambda_{em}$  618 nm) expressing JM105 *E. coli* cells for two-colour imaging. Figure 3.13b shows a false-coloured composite maximum intensity projection of a JM105-miniTn7-*HcRed1* biofilm stained with Sytox Green acquired using widefield mesoscopy, where live cells are presented in green and non-viable cells are shown in magenta. Here, non-viable cells cluster in the centre of the biofilm while intra-colony channels are not occupied by non-viable/non-fluorescent cells.

To investigate whether intra-colony channels were filled with exopolysaccharides (EPS) secreted by bacteria within the biofilm, JM105 biofilms were grown in the presence of the lectin binding dye conjugate Alexa594-WGA. Figure 3.13c shows a deconvolved composite image of a JM105-miniTn7-*gfp* biofilm (green) and associated EPS (magenta). Exopolysaccharides are distributed throughout the entire biofilm and are not strictly localised within the channel structures.

The distribution of cellulose was determined by growing JM105-miniTn7-*HcRed1* in the presence of CFW. Figure 3.13d shows that intra-colony channels were not filled



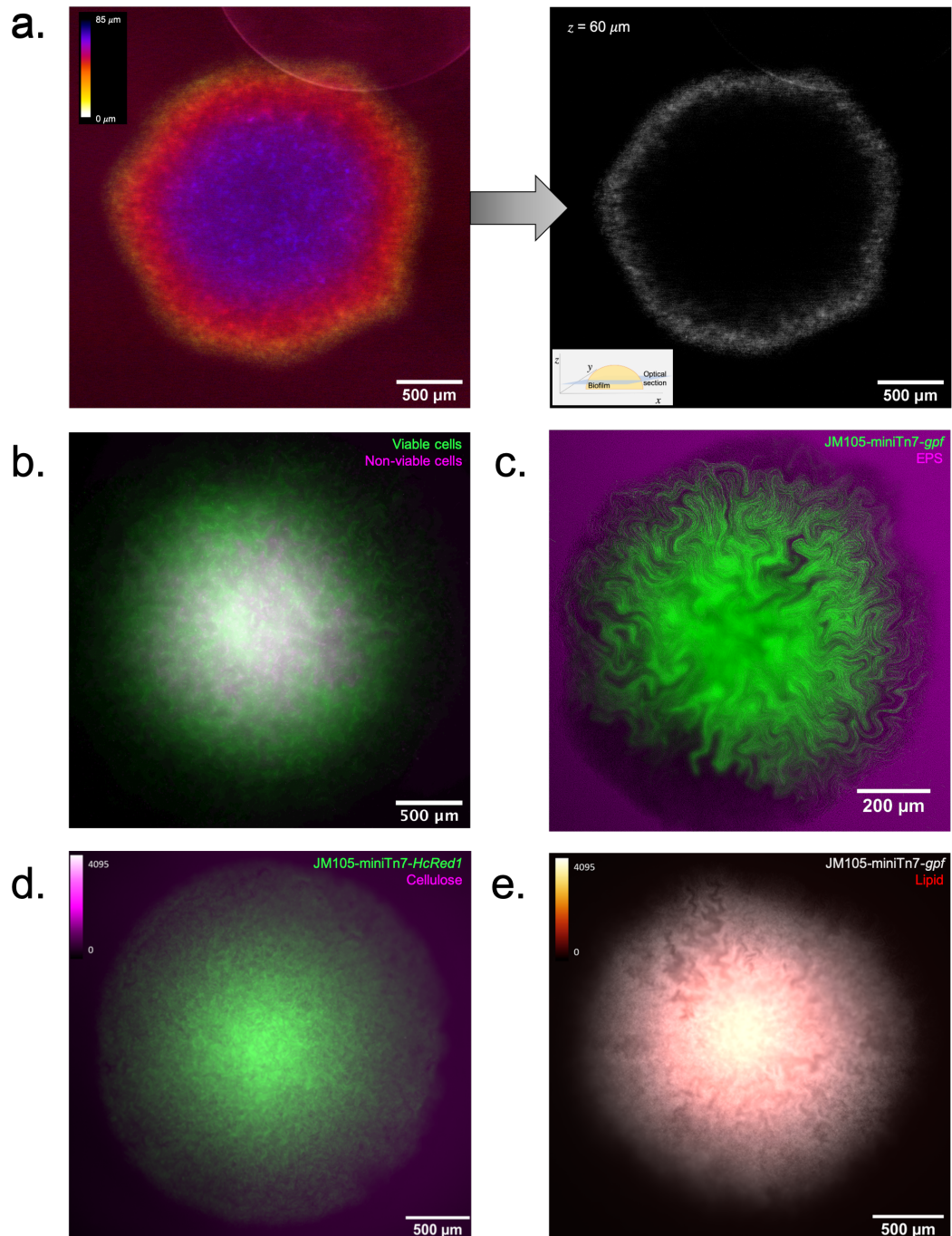


**Figure 3.13. Structural assessment of intra-colony channels.** **a)** Maximum intensity projection of an unlabelled JM105 colony acquired using reflection confocal mesoscopy, with a single isolated optical section shown. Reflection imaging determined that intra-colony channels were not occupied by material of differing refractive index to the biomass. Widefield mesoscopy revealed that channels were not filled with **(b)** non-viable/non-fluorescing cells, **(c)** EPS, **(d)** cellulose or **(e)** lipid matrices.

with a cellulose-based matrix. In fact, the JM105 strain produced little cellulose, as expected due to it being a K12 derivative.

The lipid distribution within macro-colonies was assessed using the lipid-binding dye Nile Red. Staining showed that intra-colony channels are not composed of a lipid matrix, and lipids were mainly distributed throughout the centre of the biofilm (Figure 3.13e).

### **3.3.2.3 Intra-colony channels contain protein**

Extracellular proteins were stained using the protein-specific fluorescent dye, SYPRO Ruby. The interstitial space of the intra-colony channels was found to contain extracellular protein (Figure 3.14). Due to the broad affinity of the SYPRO dye, it is not possible to tell from this data what the specific protein(s) occupying the channels may be. The finding that the channels are filled by a protein matrix suggests that they arise not due to some stochastic process and eludes that the channels have some function in the broader context of the biofilm.

### **3.3.2.4 Fluorescent probes used for structural staining have minimal impact on cell viability**

To ensure that the use of chemical dyes to stain the structural components of biofilms did not drastically affect the viability of the constituent cells, the end-point viability of each strain used in this study was assessed after having grown in the presence of each dye. Strains were only assayed against dyes which they were used with in experiments detailed in Section 3.3.2. Figure 3.15 shows that JM105-miniTn7-*gfp* and JM105-miniTn7-*HcRed1* had lower overall CFUs than the parent strain, and although statistical significance was found between cells grown in the presence of every dye

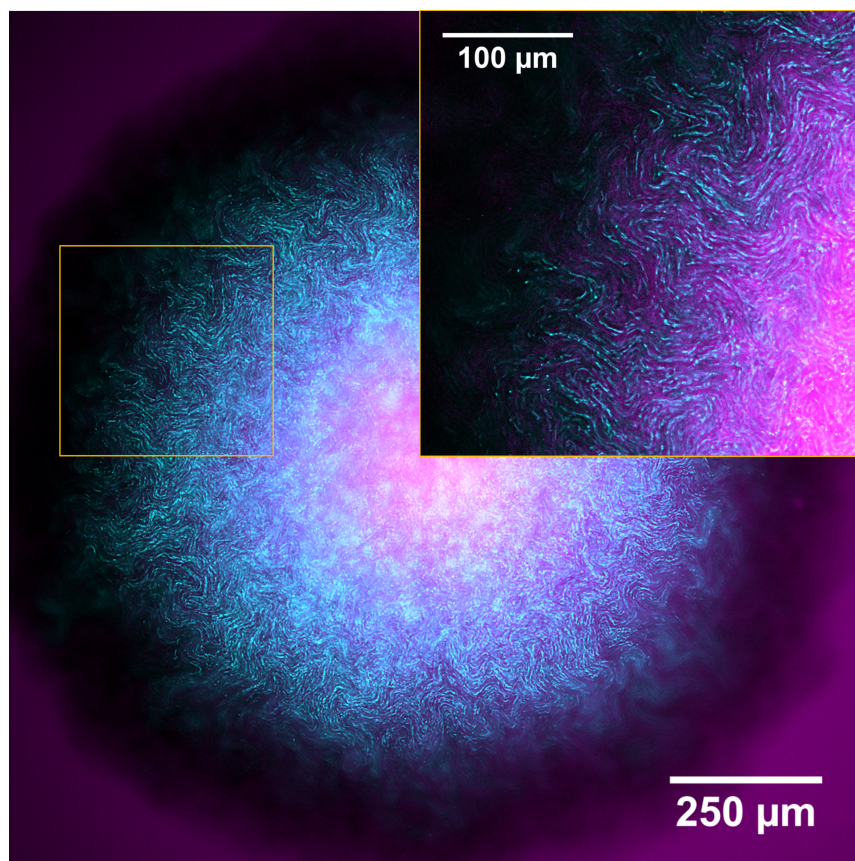


**Figure 3.14. Intra-colony channels are occupied by a protein-based structural matrix.**

A deconvolved widefield Mesolens image of a JM105-miniTn7-*gfp* biofilm stained using SYPRO Ruby. Emission of SYPRO Ruby-stained extracellular proteins (magenta) mimicked the spatial patterns of intra-colony channels, showing that channels were filled by a protein-based matrix. An ROI is shown of a representative region of the biofilm and has been locally contrast adjusted for presentation purposes.

tested, the overall viability did not change drastically stained and unstained samples (i.e. remained within one order of magnitude). The lower overall CFUs between the parental strain and the miniTn7 strains was likely due to the increased metabolic burden of expressing the inserted resistance cassettes and photoprotein genes.



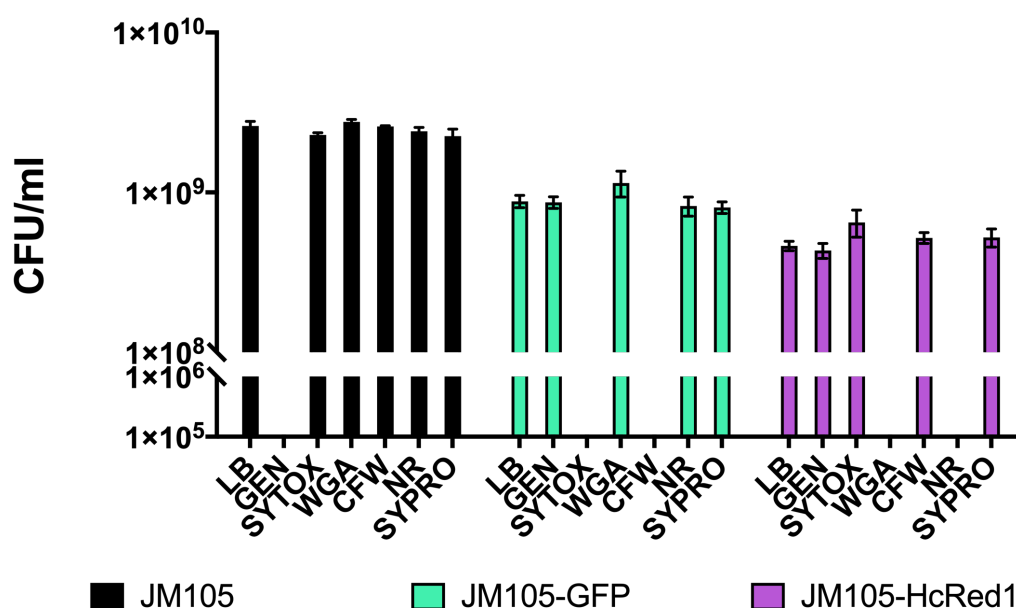


**Figure 3.15. Structural fluorescent dyes do not drastically alter the viability of JM105 strains.** The viability of JM105, JM105-miniTn7-*gfp* and JM105-miniTn7-*HcRed1* grown in the presence of various structural dyes used in this study. Colony-forming units (CFUs) were measured following growth of biofilms on solid LB media containing gentamicin (GEN), Sytox Green (SYTOX), Alexa594-WGA (WGA), calcofluor white (CFW), Nile red (NR) and SYPRO Ruby (SYPRO). All assays were carried out at the working concentration used during imaging experiments in Section 3.3.2. Only the strain/dye combinations noted in Section 3.3.2 were assessed (e.g. JM105-miniTn7-*gfp* viability was not tested against Sytox Green or CFW because these combinations were not used in imaging experiments). Error bars show standard error of the mean ( $n = 3$ ).

### 3.3.3 Understanding the formation of intra-colony channels

#### 3.3.3.1 Channel formation is an emergent property of biofilm formation

To determine whether the formation of intra-colony channels arose as an emergent property of biofilm formation, the ability of the structures to re-form following total mechanical disaggregation was investigated. The biofilm was established to allow the

formation of channels (Figure 3.16a) and then the colony was disrupted by mixing to create a uniform mass of cells. Following a recovery period of 10 hours, the channels reformed in the regrowing regions of the biofilm (Figure 3.16b). The ability of the channels to form in the same way as a naïve colony suggests that they form as an emergent property of *E. coli* colonial growth on a solid surface.

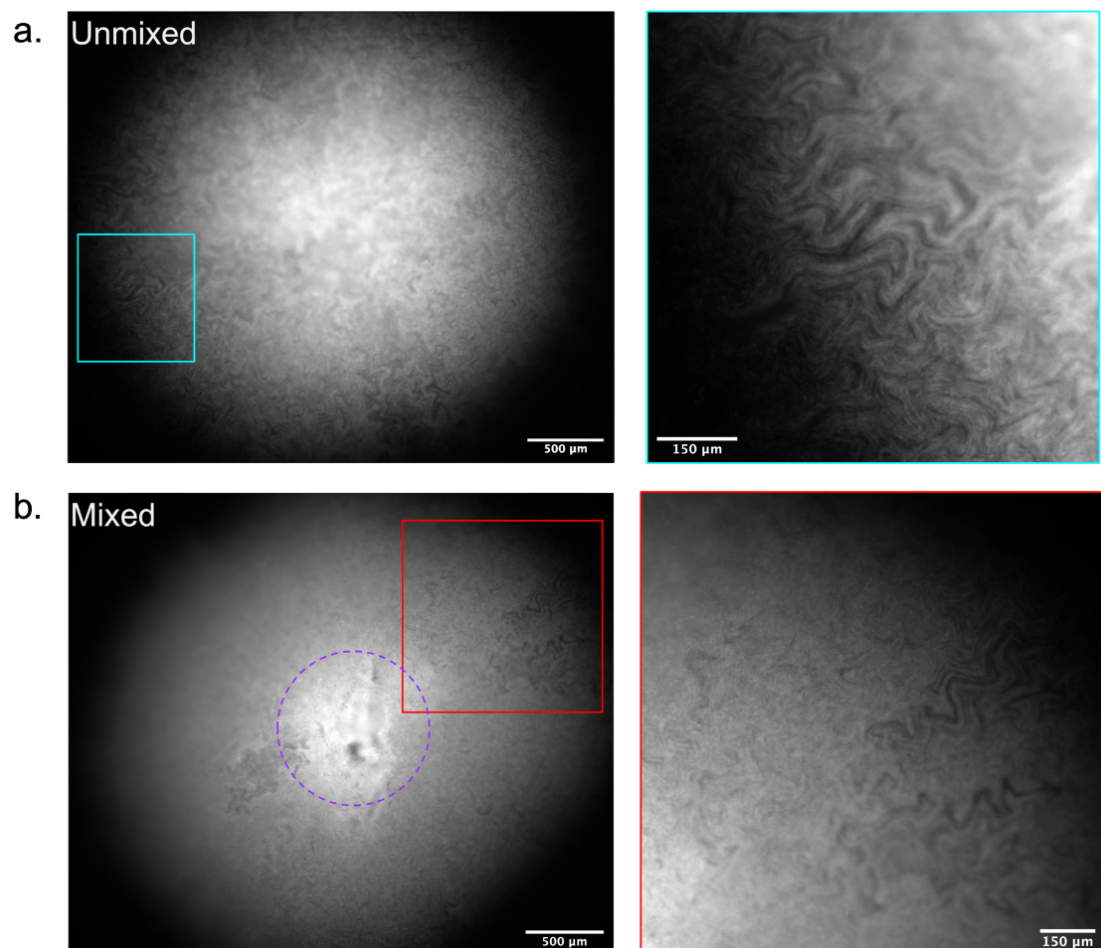


**Figure 3.16. Intra-colony channels form as an emergent property of biofilm formation. (a)** An unmixed, naïve control biofilm of JM105-miniTn7-*gfp* with established intra-colony channels. **(b)** A macro-colony JM105-miniTn7-*gfp* biofilm which was initially grown for 10 hours before mechanical disruption and subsequent recovery and regrowth at 37°C for a further 10 hours (purple outline shows original colony boundary). Regrowth was accompanied with the re-emergence of intra-colony channels in the outgrown region of the disrupted colony, showing that channel formation is an emergent property of macro-colony biofilm development.

### 3.3.3.2 Channels are unable to cross strain boundaries in mixed cultures

Growth of two isogenic strains in co-culture, each expressing a different photoprotein, resulted in the two strains forming sectors, which has been previously described<sup>182,186–190</sup>. The sectoring property was then explored in the context of intra-colony channel formation to determine if the channels were shared between the strains. When the two isogenic strains sector, the channels were found to not intersect the boundary between the strains and were retained within their own sector (Figure 3.17). The confinement of channels was more evident between different populations (i.e. HcRed1 and GFP-expressing), whereas the boundaries between sectors of cells expressing the same photoprotein were less ordered.

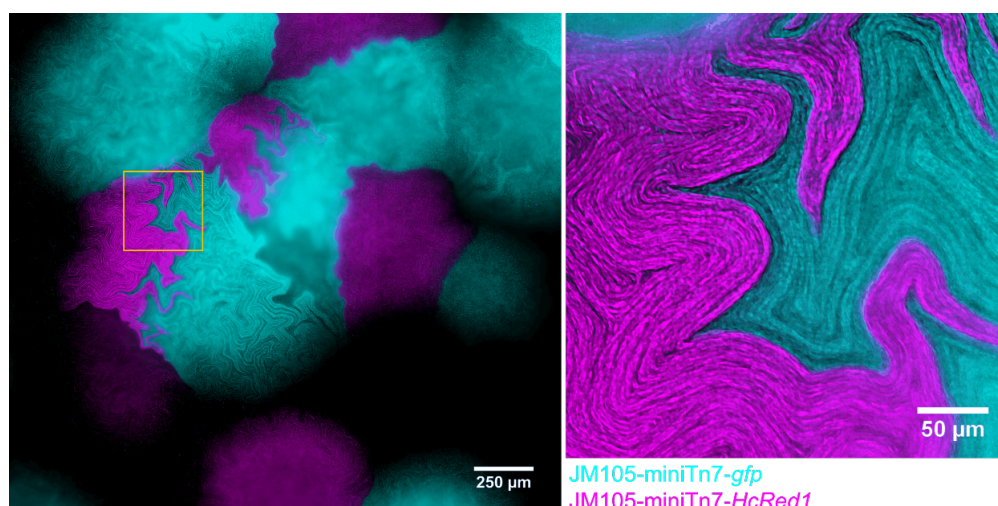


**Figure 3.17. Intra-colony channels are confined within clonal populations and unable to cross strain boundaries.** A mixed culture of isogenic JM105 strains which express either GFP (cyan) or HcRed1 (magenta). Each strain sectored into segregated clonal populations which have propagated from a single colony forming unit, and cells from each sector were unable to cross the strain boundary. The intra-colony channels present within each sector were also unable to cross the strain boundary and were therefore not shared by opposing isogenic colonies.

To ensure that both strains were truly isogenic and that the insertion of the miniTn7 sequence had inserted into the predicted chromosomal location, both miniTn7 strains were verified using colony PCR. The miniTn7 transposon should insert at only one *attTn7* site in the chromosome, downstream of *glmS*<sup>283</sup>. Primers were designed for the *glmS* gene and right flank of the miniTn7 insert. Colony PCR confirmed that the miniTn7 sequence was inserted approximately 25 base pairs downstream of *glmS* in both JM105-miniTn7-*gfp* and JM105-miniTn7-*HcRed1* (Figure 3.18). Therefore, the strains were truly isogenic except for the inserted photoprotein gene, meaning segregation was an emergent property of how founder populations gave rise to the colonies, and not because of any genotypic differences.

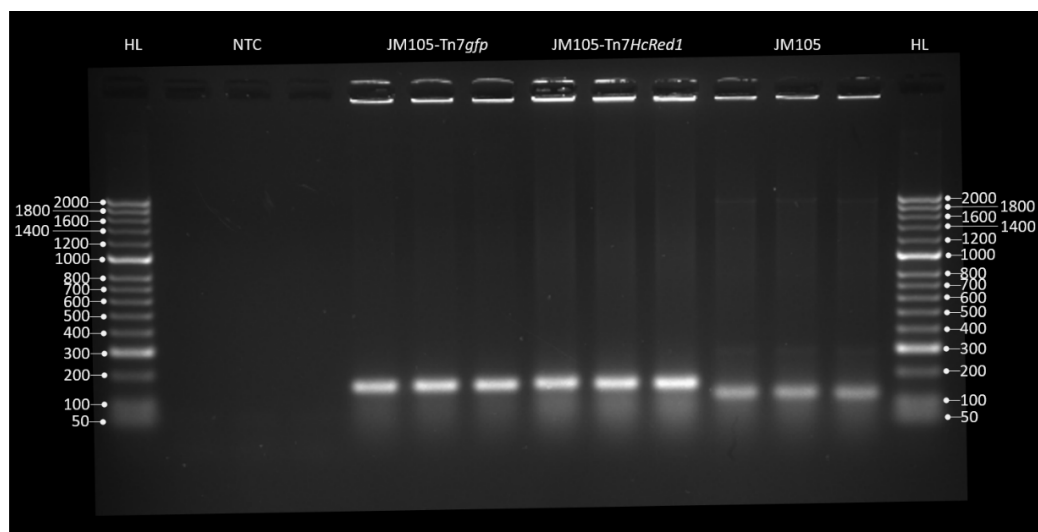


**Figure 3.18. The miniTn7 insert location is conserved between JM105-miniTn7-*gfp* and JM105-miniTn7-*HcRed1*.** A colony PCR gel showing a product of approximately 150 bp in JM105-miniTn7-*gfp* and JM105-miniTn7-*HcRed1*, confirming that the miniTn7 sequence is inserted approximately 25 bp downstream of the *glmS* gene in both strains. The lower molecular weight bands in the JM105 samples is likely due to primer dimerisation. A no template control and two 50 bp hyperladders (HL) are also presented.

### **3.3.4 Determining a functional role for intra-colony channels**

#### **3.3.4.1 Intra-colony channels do not facilitate fluorescein transport when submerged in a fluorescein solution**

To investigate whether the intra-colony channels were able to facilitate the uptake of substances from the external environment, their ability to promote diffusion was tested using a dilute fluorescein solution as a mounting medium. Fluorescein was dissolved in sterile LB broth and used to mount macro-colonies prior to imaging. Initial attempts used widefield mesoscopy, however there was a large contribution of out-of-focus signal which blurred the images. Therefore, confocal laser scanning mesoscopy was used to limit this. Following mounting in a 10 µg/ml fluorescein LB solution, unlabelled JM105 colonies were imaged after a 30-minute incubation period. Figure 3.19 shows the shadow of the unlabelled colony mounted in the fluorescein solution. There is little evidence of diffusion of fluorescein into the colony which follows the same spatial patterning as the intra-colony channels. However, it may be that the low signal present in the centre of the colony is due to limited diffusion of fluorescein molecules but, as they are so small, they may not necessarily need to follow the path of the channels present in the colony. Therefore, a more robust means of testing the function of intra-colony channels was required.

#### **3.3.4.2 Intra-colony channels create a capillary effect and act as uptake systems for fluorescent microspheres**

To further investigate whether the intra-colony channels play a role in the transport of substances into the biofilm, the functional role of the channel system was tested by introducing 200 nm diameter fluorescent microspheres to the extracellular medium when preparing the specimen for widefield mesoscopy. The fluorescent microspheres

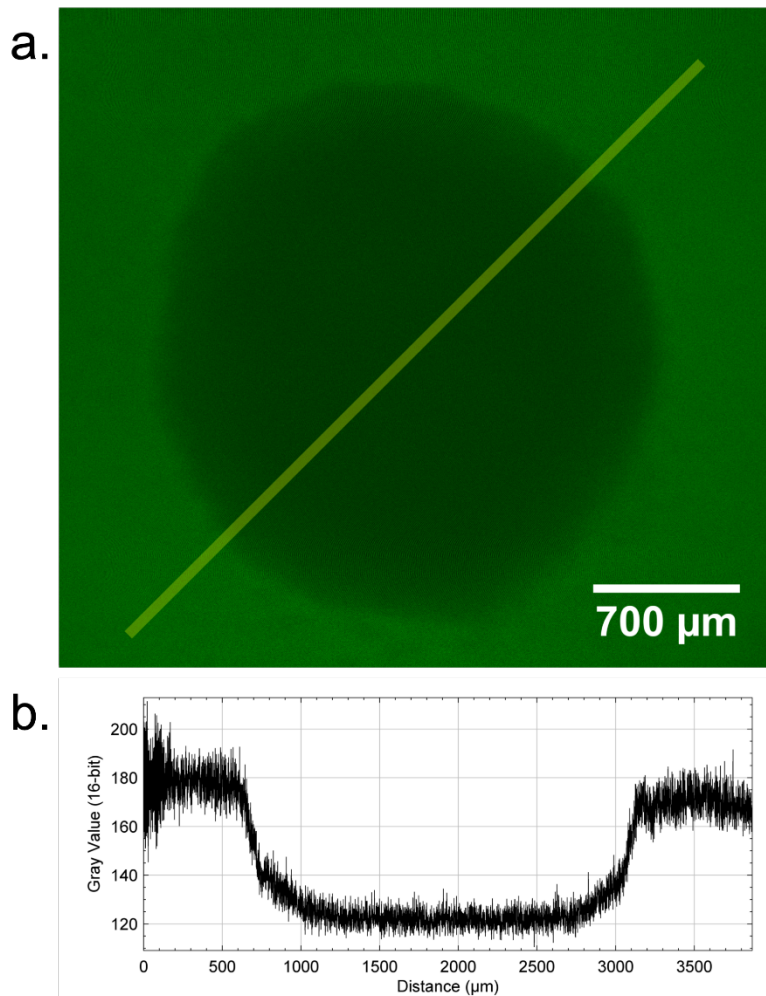


**Figure 3.19. Fluorescein does not enter macro-colonies via intra-colony channels. a)**

A single confocal optical section of a JM105 colony mounted in a 10 µg/ml fluorescein LB solution. The shadow of the colony can be seen surrounded by fluorescein solution. There is no obvious diffusion of fluorescein into the colony through the intra-colony channels. **b)**

An intensity profile measured along the yellow ROI shown in a) shows increased fluorescent signal outside of the colony and confirms no diffusion of fluorescein into the colony via intra-colony channels. Intensity profile was averaged over a line thickness of 100 pixels (50 µm).

were spread as a dense lawn along with a dilute mid-log JM105-miniTn7-*gfp* culture.

A single optical section, 25 µm above the base of the colony, allows the outline of the



colony to be observed at the edges of the image, with the untouched lawn of microspheres outside the colony (Figure 3.20).

The distribution of beads in these areas are homogenous, whereas within the colony the transport of the fluorescent microspheres through the channels reflects the spatial structure of the biofilm. Magnified ROIs of intra-colony channels show that the channels are acting as conduits for the transport of microspheres into the biofilm. The transport of microspheres into the channels suggests that these intra-colony

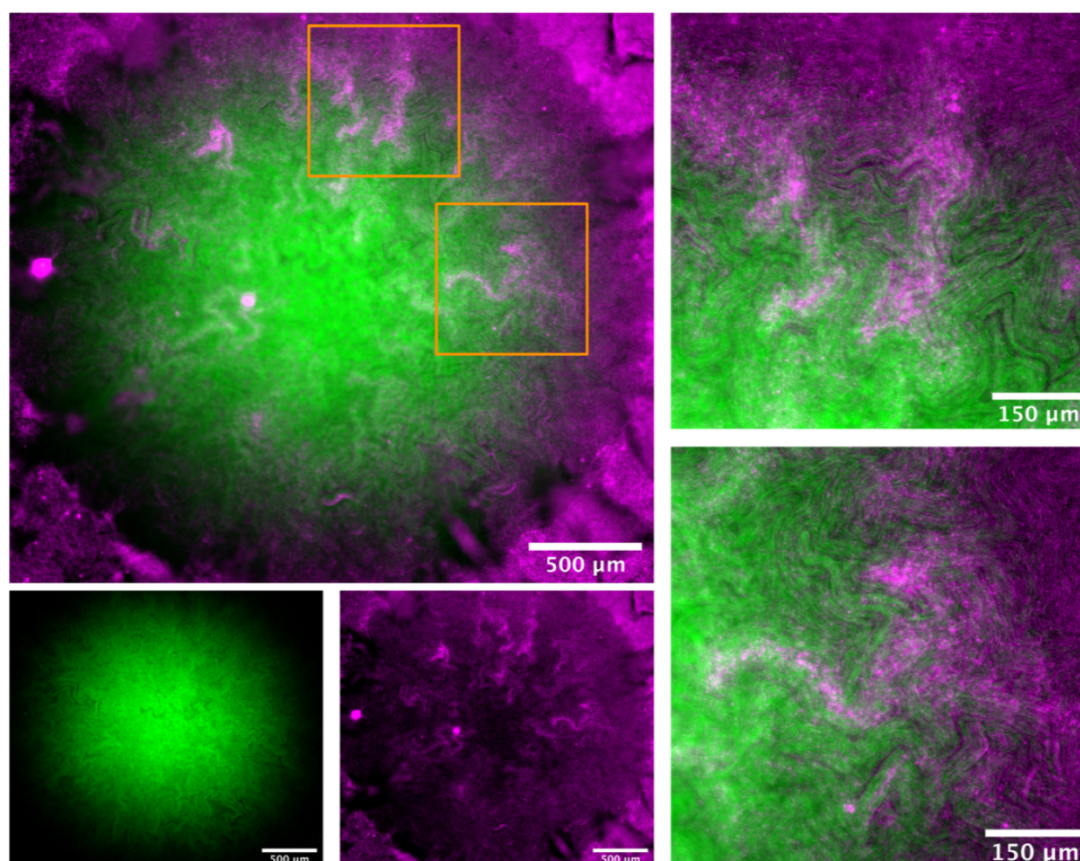


**Figure 3.20. Intra-colony channels facilitate transport of nanoscopic particles.** A single optical section approximately 25  $\mu\text{m}$  above the base of the colony shows a mature JM105-miniTn7-*gfp* biofilm (green) and a lawn of 200 nm fluorescent microspheres (magenta). The fluorescent microspheres were transported from a confluent lawn at the base of the colony into the intra-colony channels and directed towards the centre of the colony. Two ROIs are presented from different regions of the colony where fluorescent microspheres were transported into the colony via intra-colony channels.

structures are involved in the acquisition of substances from the external environment. From these data, was hypothesised that the ability of the channels to transport small fluorescent particles could be extended to facilitate uptake of smaller particles into the colony, such as nutrients.

#### **3.3.4.3 Intra-colony channels facilitate nutrient transport in mature *E. coli* macro-colonies**

To further investigate the role of intra-colony channels in biofilm nutrient acquisition, an arabinose inducible GFP strain (*E. coli* JM105  $P_{BAD}$ -*gfp* (JM105-pJM058)) was used. Growth of the arabinose-inducible GFP strain on solid minimal medium with L-arabinose as the sole carbon source revealed that biofilm fluoresced most intensely in regions which bordered the intra-colony channels (Figure 3.21). This suggested that the concentration of L-arabinose was highest in the channel system compared to the remainder of the biofilm and demonstrates that these structures play a role in nutrient acquisition and transport within the colony. This outcome challenges the long-held belief that bacterial colony nutrient uptake occurs through simple diffusion through the extracellular matrix of the biofilm, and concurs with previous work which showed that large biofilms must develop transport mechanisms to direct nutrients to their centre<sup>249</sup>.

Following from the initial observation of nutrient uptake, a method which would allow for time-lapse imaging of nutrient uptake was trialled. This method required growing the JM105-pJM058 biofilm to maturity on an alternate carbon source and introducing L-arabinose before or during mesoscopic imaging. First a 25  $\mu$ M fluorescein solution was injected directly under the surface of solid M9 medium and time-lapse data was acquired using the Mesolens in widefield mode. There was a rapid diffusion of the fluorescein solution shortly after injection, meaning that the injection method would likely result in rapid diffusion of L-arabinose from underneath the colony (Figure 3.22).



To achieve greater control over the diffusion of the fluorescein solution a perfusion system was used to inject a 25  $\mu$ M fluorescein solution under the surface of solid M9

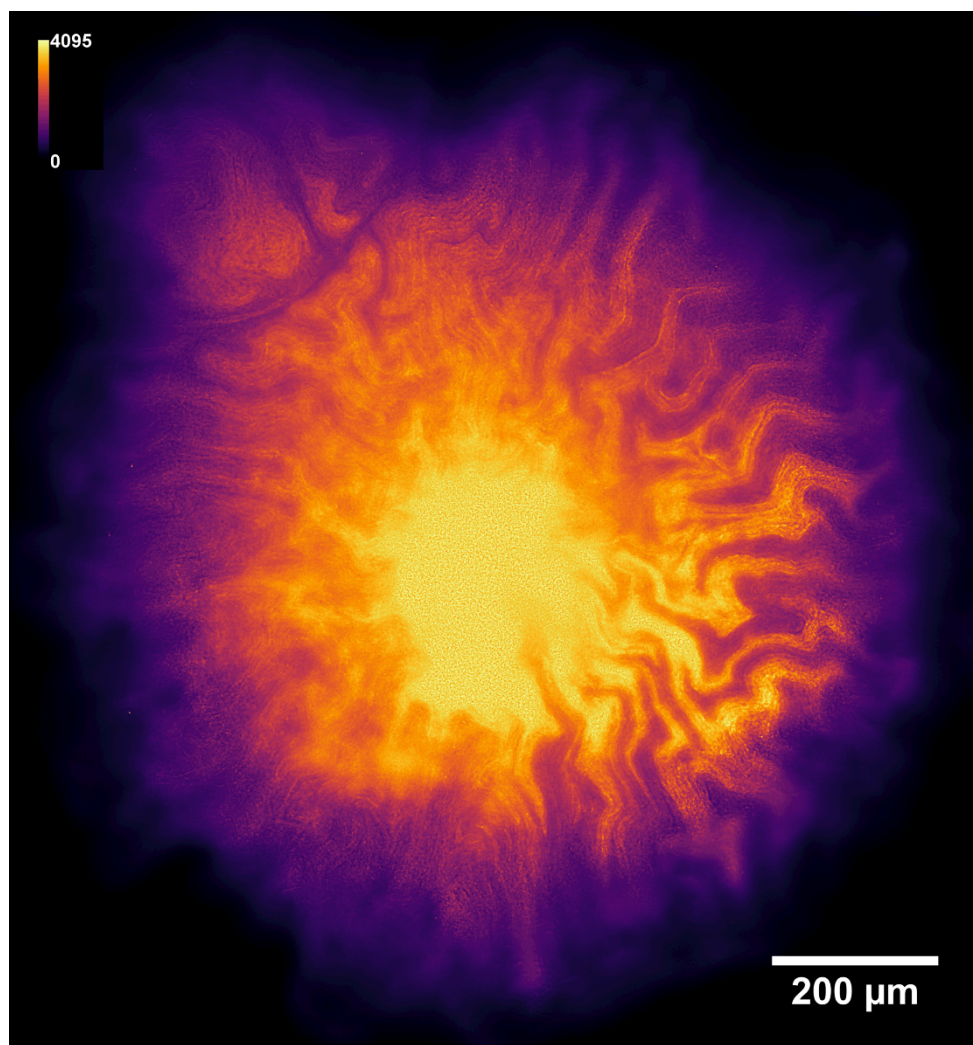


**Figure 3.21. Intra-colony channels play a functional role in nutrient acquisition and transport to the centre of bacterial biofilms.** A deconvolved image of a JM105-pJM058 macro-colony biofilm grown on M9 minimal medium with L-arabinose as the sole carbon source. This arabinose biosensor expresses GFP only in the presence of L-arabinose. GFP emission intensity was higher in cells which line the intra-colony channels compared to cells elsewhere within the biofilm, which shows that the channel structures have a higher concentration of L-arabinose compared to elsewhere within the biofilm. This provides evidence of a functional role in nutrient acquisition and transport for the intracolony channel system.

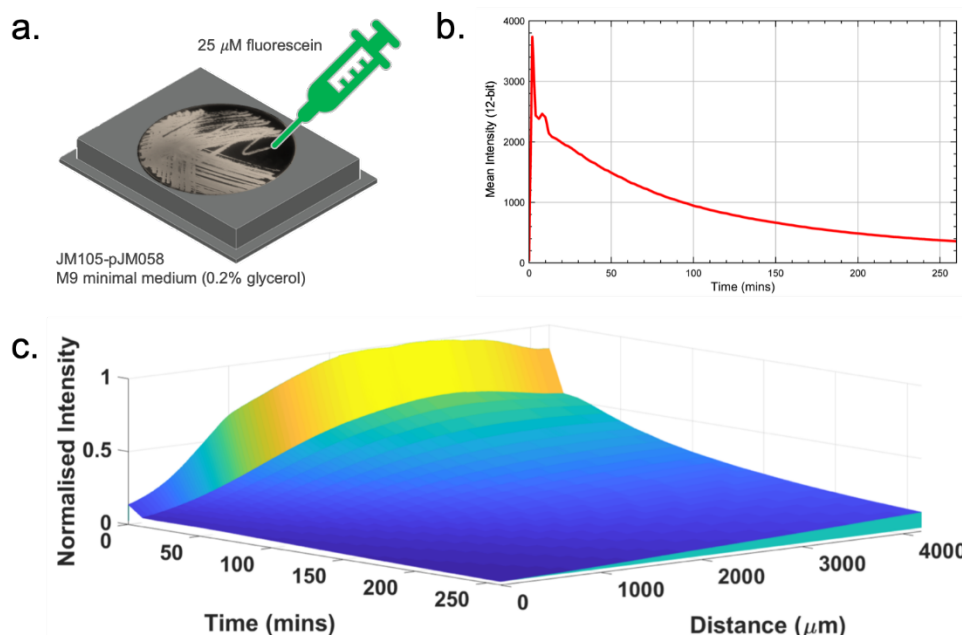


**Figure 3.22. Injection of fluorescein into solid medium resulted in rapid diffusion. a)**

A schematic of the experimental setup prior to imaging. A fluorescein solution was injected directly under the surface of solid M9 medium. **b)** A mean intensity plot profile across the field of view of the injected region over time (line width = 50 pixels (11.30  $\mu\text{m}$ )). There is a sharp decrease in fluorescence over time correlating to rapid diffusion of fluorescein after injection. **c)** A waterfall chart showing the rapid decrease in mean fluorescence intensity over the injection site over time.

medium during time-lapse imaging (Figure 3.23). Perfusion of fluorescein resulted in a more stable signal over time compared to the injection method, meaning that should L-arabinose be perfused into the M9 medium it is more likely to remain at inducible concentrations. A final concentration of 0.5% L-arabinose (33.30 mM) was perfused under the colony, which was approximately 3-fold higher than the concentration required to induce  $P_{\text{BAD}}^{286}$ . However, no GFP emission from the induction of  $P_{\text{BAD}}$  was observed in the resulting time-lapse images acquired over a 20-hour period post-perfusion. Therefore, it was not possible to visualise the uptake of nutrients into the colony over time by these methods.

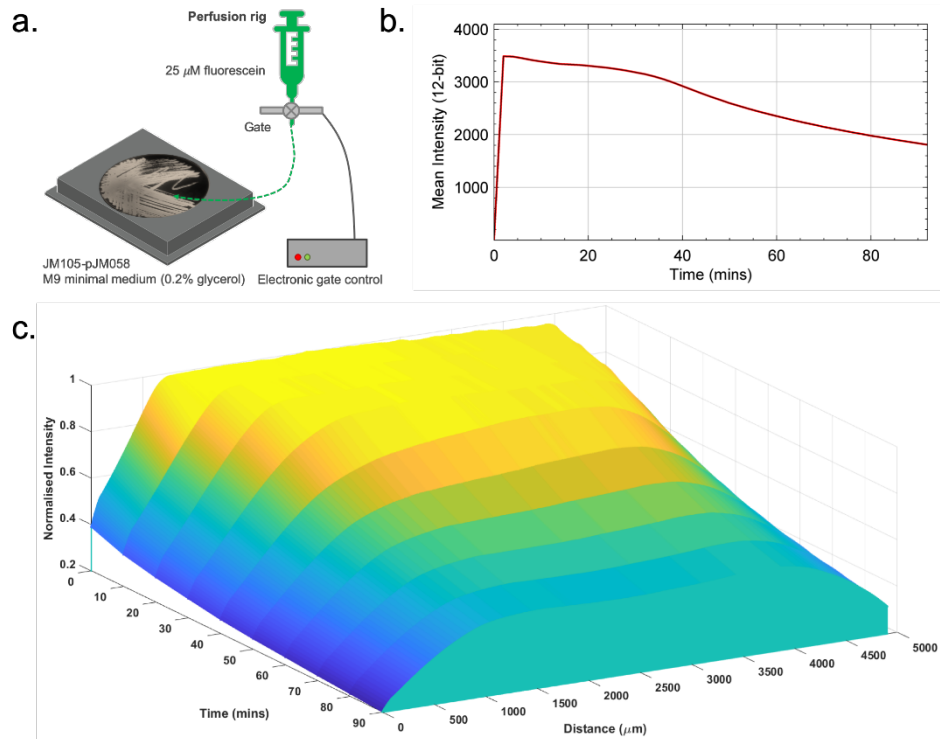


**Figure 3.23. Perfusion of fluorescein into solid medium maintains a higher concentration over time compared to injection. a)** A schematic of the experimental setup prior to imaging. A fluorescein solution was perfused directly under the surface of solid M9 medium using a gated perfusion rig. **b)** A mean intensity plot profile across the field of view of the injected region over time (line width = 50 pixels (11.30 µm)). There is a steady decrease in fluorescence over time, meaning that fluorescein concentration remains relatively high over time. **c)** A waterfall chart showing the decrease in mean fluorescence intensity over the field of view following perfusion of fluorescein.

It was then hypothesised that the lack of GFP emission could be a result of CCR as the strain was growing in the presence of two carbon sources. To test this, JM105-pJM058 was grown under diauxic conditions with varying ratios of glycerol, glucose and L-arabinose as carbon sources and GFP emission was measured over a 36-hour period to determine when  $P_{BAD}$  had been induced. JM105-pJM058 was found to metabolise glycerol and glucose initially before using arabinose as carbon source (Figure 3.24).  $P_{BAD}$  induction was determined to occur more quickly when grown on a

combination of glycerol and L-arabinose compared with glucose and L-arabinose, with an increase in GFP emission after 5 hours. The increased standard error over time shown in Figure 3.24 was due to the build-up of condensation on the lid of the 96-well plate which results in scattering of the incident light from the plate reader; however, even with this the trend is still clear. These data showed that when grown on glycerol, colonies should exhibit some fluorescence after approximately 5 hours, but this did not translate to Mesolens imaging experiments on M9 medium. Therefore, although CCR was likely affecting the induction of  $P_{BAD}$ , it was not possible to account for this by these methods to optimise time-lapse imaging of nutrient acquisition by intra-colony channels.

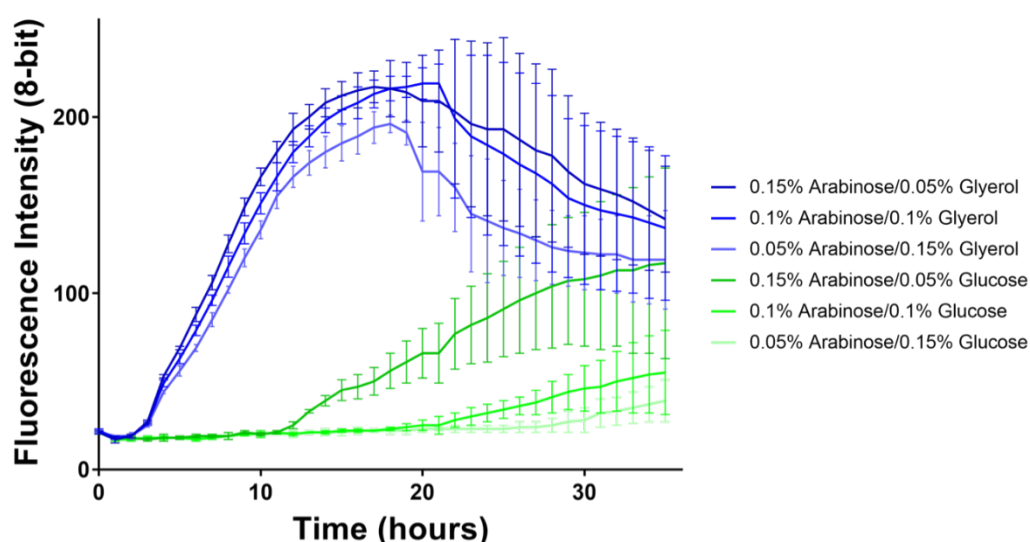


**Figure 3.24. Fluorescence emission of JM105-pJM058 during diauxic growth conditions.** Following exhaustion of a preferred carbon source, L-arabinose metabolism begins and  $P_{BAD}$  induction occurs resulting in the expression of *gfp* and an increase in fluorescence intensity over time. GFP production begins after approximately 5 hours when JM105-pJM058 is grown under diauxic conditions on a mix of L-arabinose and glycerol. When grown with under diauxic condition with glucose,  $P_{BAD}$  induction takes longer depending on the concentration of glucose available.

Despite not being able to show uptake of nutrients over time, the discovery of channel-mediated nutrient uptake in a prokaryote system remains novel. It was hypothesised that the role of intra-colony channels may not solely be limited to nutrient acquisition, and that this beneficial function could be exploited to promote the uptake of antimicrobial compounds or dispersal agents through the channel structures.

### **3.3.5 Exploiting the role of intra-colony channels for antibiotic uptake**

Given the putative role of intra-colony channels in nutrient acquisition, it was hypothesised that this function could be exploited to promote the uptake of biocides. To test this a modified disk diffusion assay was used, where filter rings were loaded with a known concentration of a bactericidal antibiotic.

#### **3.3.5.1 Selecting the appropriate test antibiotic**

The guidelines on antibiotic susceptibility testing by EUCAST and the BSAC were consulted choose appropriate biocide compounds that could be tested for these experiments. Streptomycin, colistin and kanamycin were selected based on their clinical profiles and bactericidal properties. The dose concentration was first optimised by carrying out a standard disk diffusion assay with various concentrations of each antibiotic. A curve of concentration vs. clearance diameter was plotted for each antibiotic (Figure 3.25). Disk diffusion assays revealed that colistin and kanamycin had a bactericidal effect on JM105 strains, with colistin having an increased overall potency. Streptomycin was found to be ineffective against JM105 strains and after consulting published literature it was found that JM105 is intrinsically resistant to streptomycin and it was therefore removed as a potential candidate for imaging experiments. Colistin was selected as the test antibiotic moving forward due to an increased potency compared to kanamycin and its clinical relevance to *E. coli*.

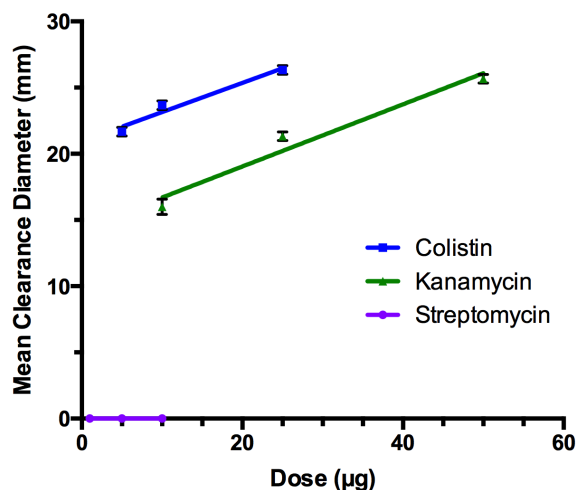


**Figure 3.25. Colistin was selected as the appropriate test antibiotic.** The mean clearance diameter of candidate bactericidal compounds in a disk diffusion assay. Streptomycin had no effect on the viability of JM105 strains. Colistin was more potent than kanamycin and produced sufficiently large clearance diameters (21.67 mm) even at low doses.  $n = 3$  for each test antibiotic, at each concentration.

### 3.3.5.2 Comparison of filter disks and filter rings for antimicrobial susceptibility assays

As the test antibiotic had to be introduced to a mature colony a modified diffusion assay was used with filter disks which could be placed around a mature colony for a set period of time. As the filter rings had a lower surface area compared to the disks used above (25% decrease), the dose of test antibiotic had to be altered for use with the rings. Therefore, 75% of the dose of colistin was added to the filter rings compared to the filter disks (3.75 µg) before the clearance diameters were measured between the filter disks and filter rings. Filter rings loaded with 3.75 µg colistin resulted in a mean clearance diameter of 14 mm, which was an 84.85% decrease in the clearance diameter of 6 mm filter rings loaded with 5 µg colistin (mean clearance diameter = 16.5 mm) (Figure 3.26). Therefore, the efficacy of colistin on filter rings was comparable to the conventional antimicrobial susceptibility method using filter disks.

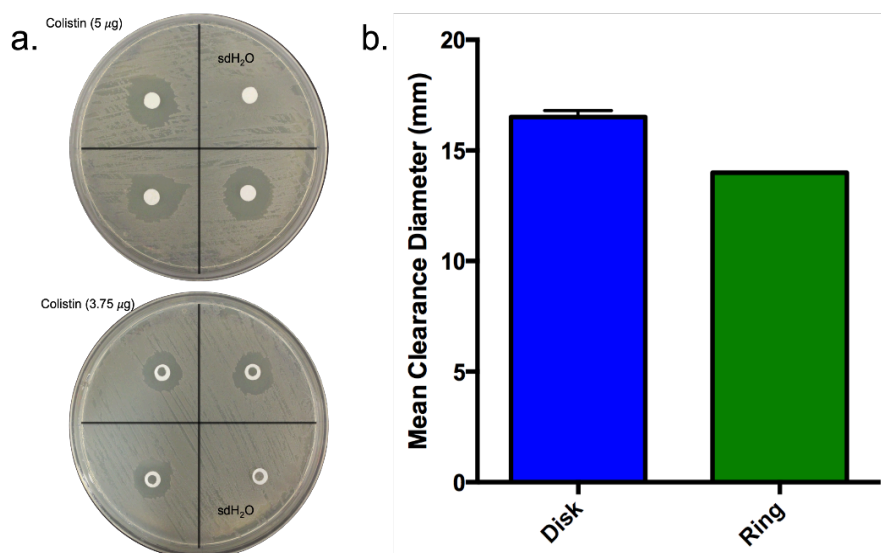


**Figure 3.26. Filter rings have comparable antibiotic diffusion properties to filter disks.** **a)** Images of a colistin diffusion assay (disks = 5  $\mu$ g, rings = 3.75  $\mu$ g) against JM105-miniTn7-*HcRed1* with a negative sdH<sub>2</sub>O control. **b)** The mean clearance diameter of colistin-loaded filter disks and rings shows a decrease from 16.5 mm to 14.0 mm (n = 4). Error bars show standard error of the mean.

### 3.3.5.3 Non-viable cells accumulate within intra-colony channels following antibiotic treatment

The findings involving nutrient transport into mature colonies led to the hypothesis that intra-colony channels could also be used to facilitate antibiotic uptake. Mature JM105-miniTn7-*HcRed1* macro-colonies grown with Sytox Green were treated with antibiotics for set time periods by placing a filter ring loaded with 3.75  $\mu$ g colistin around the colony and removing immediately prior to imaging by widefield mesoscopy (Figure 3.27a). The distribution of non-viable cells was higher in the colistin-treated specimens than the negative control, with the intra-colony channels throughout the colony being filled with Sytox Green-labelled cells in some cases. The mean intensity of Sytox Green in the colony was measured and compared to a negative control



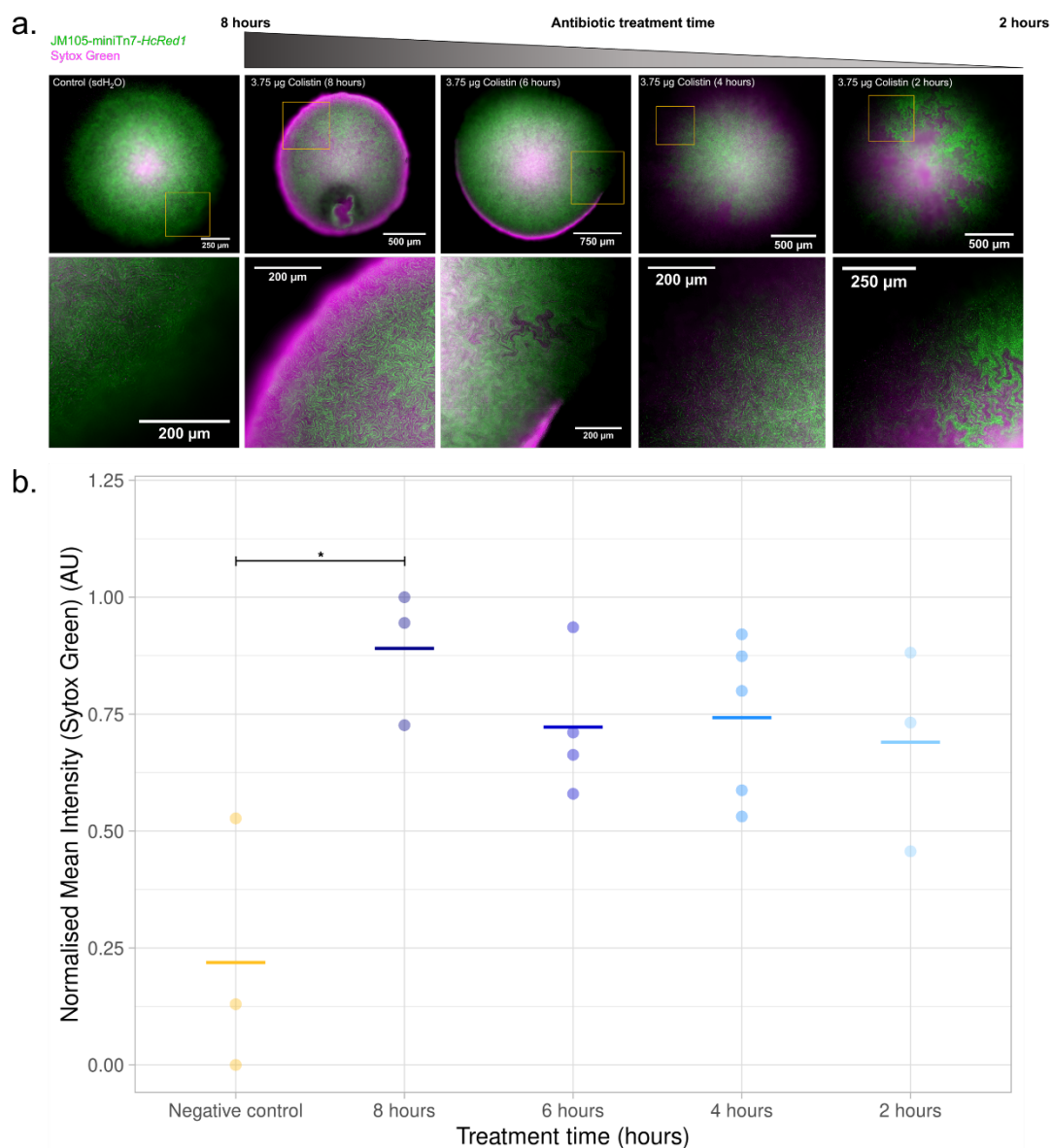


**Figure 3.27. Intra-colony channels can be exploited to facilitate antimicrobial uptake.**

**a)** Deconvolved widefield Mesolens images of Sytox Green-stained JM105-miniTn7-*HcRed1* macro-colony biofilms following exposure to 3.75 µg colistin for 2-8 hours. A negative control is also shown which was treated with sterile distilled water (sdH<sub>2</sub>O). Designated regions of interest are included for each timepoint showing a build-up of non-viable cells within the intra-colony channels. HcRed1 = green, Sytox Green = magenta. **b)** A plot of normalised mean intensity of Sytox Green emission in macro-colony biofilms which were exposed to colistin. An unpaired t-test showed a significant increase in the mean intensity of Sytox Green in biofilms which had been treated with colistin for 8 hours compared to the control ( $p < 0.05$ ).



(sdH<sub>2</sub>O) (Figure 3.27b). The mean fluorescence intensity of Sytox Green was found to be significantly higher when biofilms were treated for 8 hours ( $p < 0.05$ ) compared to the negative control.

### 3.4 Discussion

The internal structure of mature bacterial communities is largely considered to be a uniformly distributed mass of cells with little evidence in literature of internal structure. The reason for this is due to the lack of high-performance imaging systems which are able to image multi-millimetre specimens with sufficiently high spatial resolution to resolve individual bacterial cells. This study was the first application of the Mesolens to microbiology and has offered a new approach for imaging large microbial specimens, enabling the characterisation of a novel structural aspect of *E. coli* macro-colony biofilms. The channel structures reported are formed as an emergent property of biofilm growth and are confined within founder cell boundaries in mixed isogenic cultures. This chapter has also established a functional role for intra-colony channels in nutrient acquisition and transport. Moreover, the role of intra-colony channels was further explored to investigate their role in antimicrobial uptake where accumulation of non-viable cells was visualised in the lumen of channels. The identification and characterisation of this previously undocumented channel network offers a novel outlook for microbial community biology and provides a novel mechanism for transport and delivery in bacterial biofilms.

The structures identified in mature *E. coli* macro-colonies bear similarities to some other aspects of bacterial community architecture, however it is important to note that intra-colony channels are fundamentally different to structures such as the water irrigation channels discovered in mushroom-shaped *Pseudomonas* and *Klebsiella* spp. biofilms<sup>287,288</sup>. There have also been channel-like structures identified in mature

bacterial colonies, such as the crenulations of *B. subtilis* macro-colonies<sup>172,184</sup> or the macroscopic folds of *P. aeruginosa* biofilms<sup>185,289</sup>, which have been extensively described in literature. It is important to note, that crenulations and folds are all visible as surface structures of the colony and resolvable using photography techniques, whereas the intra-colony channels identified here are present within the main body of the biofilm and are not observable by viewing the surface of the colony. A similar phenomenon was recently reported in colonies of *Proteus mirabilis* where 100 nm diameter fluorescent microspheres were observed to penetrate the boundary of the colony through “crack-like conduits” present at the colony edge<sup>290</sup>. However, the authors were unable to show any spatial evidence of the conduits themselves.

The spatial arrangement of the intra-colony channels is fractal in nature, with repeating patterns and complex topographies. Upon first glance, channels resemble fractal features found in multi-strain colonies which form as a result of the mechanical instability between growth and viscous drag of dividing cells<sup>182</sup>. However, these features have only been reported in multi-strain colonies where the fractal dendrites have been composed of live, fluorescing cells<sup>187–190,192</sup>. Similarly, a recent phenomenon has been recorded in polymicrobial macro-colonies where striking flower-like patterns emerge on soft-agar surfaces between motile and non-motile co-cultured strains<sup>291</sup>, where pattern formation occurs in this case by a combination of mechanical instability from non-motile cells, “hitchhiking” motility behaviours and friction-mediated crenulation formation. Again, these patterns only occur in multi-strain systems which is inherently different from the experiments described in this chapter. This study demonstrated that the spatial patterns and channels observed are different to those outlined previously. Firstly, the patterns of intra-colony channels documented here arose in a single population of cells where there are no strain-to-strain interactions to result in the formation of fractal patterns. Given that the intra-

colony channels are not occupied by dead non-fluorescing cells (Figure 3.13b) it is clear that the bacterial colonies used in this work are not composed of two pseudo-domains (i.e. viable and non-viable cells) which could interact to form complex 3D fractal patterning. The finding that non-viable cells localise in the centre of the biofilm agrees with previous studies showing that dense microbial aggregates often have dense hypoxic, acidic centres which have diminished access to nutrients<sup>169,255,264,292–296</sup>.

All of the observations noted in this chapter are of mature *E. coli* (K12) communities, and so it remains unclear if these structures are conserved in biofilms formed by other species. *In silico* modelling of biofilm patterning in two strain systems has shown that cell shape can influence the final structure of the mature colony, where the growth dynamics of rod-shaped and coccoid cells resulted in columnar striations which contained only one species per column<sup>187</sup>. The emergence of intra-colony channels could be owed to the perpendicular division axis of *E. coli*, where cells will divide and can arrange themselves in long chains of cells arranged pole-to-pole. If this were true it may be that bacteria which possess different division mechanisms, such as the alternating orthogonal division planes in *Staphylococcus aureus*<sup>297</sup>, could possess a different intra-colony architecture than *E. coli*. Moving forward it would be interesting to assess the role of cell shape in the formation of intra-colony channels. This could be performed by observing biofilms formed by other species or could be directly compared to the ability of *E. coli* to form channels by altering the natural shape of *E. coli*. This could be achieved, for example, by using a *tatC* mutant which affects amidase (AmiA) expression resulting in long filamentous cells<sup>298</sup>; by mutating *rodZ*<sup>299</sup>, using a strains with truncated MreB cytoskeletons<sup>300</sup> or using *min* system mutants<sup>301</sup> to form short rod-shaped or spherical cells. These experiments would establish if cell shape was a determining factor in the formation of intra-colony channels.

Following a systematic structural assessment of the biofilm, the intra-colony channels were found to be filled with a proteinaceous matrix. The exact composition of this matrix remains unclear, and the SYPRO-Ruby staining method does not allow for specific labelling of any one class of protein. However, it may be possible to determine the make-up of the channels by comparing transcriptomic data from cells adjacent to the intra-colony channels and cells elsewhere in the biofilm, or by comparing RNA sequencing (RNA-seq) data from mature biofilms where intra-colony channels have formed and juvenile biofilms where they have not. Moving forward, if the protein matrix composition was identified then it could lead to the development of targeted drug delivery approaches, such as has been achieved in other therapeutic strategies using functionalised non-ionic surfactant vesicles or liposomes<sup>275–279</sup>.

The intra-colony channels form as an inherent property of biofilm formation, leading to fractal-like patterns which exhibit plasticity which is reminiscent of the results of a classical eukaryotic developmental biology experiment by Moscona, where reformation of the channel architecture in marine sponges occurred after disaggregation by passage through a fine silk mesh<sup>302,303</sup>. The ability of the channels to reform also suggests that they fulfil a functional role in the context of the biofilm, which was further tested using a combination of uptake assays.

The findings presented in this chapter establish a role for intra-colony channels in nutrient acquisition, which provide a new mechanism for transport in large bacterial communities. Moreover, this finding offers some explanation to the BiofilmQ analysis presented in Figure 3.10, where cells lining the borders of intra-colony channels were more densely packed. Given their role in nutrient transport, it would make sense that the area surrounding the nutrient-rich channel networks were more densely packed with actively growing viable cells. To further test the nutrient acquisition role a series of nutrient reporters could be observed to provide further evidence for nutrient uptake.

For example, nutrient-responsive promoters linked to fluorescent protein reporters such as those responding to nitrogen (e.g. the ammonium transporter, AmtB<sup>304</sup>, and glutamine synthetase, GS<sup>305</sup>) and phosphate (e.g. phosphate periplasmic binding protein, PstS<sup>306</sup>).

The long-held understanding of biofilm nutrient acquisition is based on passive diffusion of nutrients from the external environment<sup>259–261</sup>, and the same diffusion-limited mechanism is also thought to be responsible for entry of antimicrobial compounds and dispersal agents during biofilm clearance. Current treatment regimens for biofilm eradication lead to a concentration gradient of the antimicrobial, causing the emergence of persister cells and development of antimicrobial resistance where antimicrobial concentrations become sub-optimal<sup>158</sup>. Viability staining revealed, following treatment with colistin, a significant increase in the signal of non-viable cells within the lumen of intra-colony channels. There was some degree of variability between the replicate biofilms for each timepoint in the experiment, which is likely due to the variability in structure from biofilm to biofilm, but may also be due to variability in viability staining which is common in bacterial live/dead staining protocols<sup>307–310</sup>. It is currently unclear if the intra-colony channels were directly involved in the uptake of antimicrobials into the biomass of the colony, or if the increased number of non-viable cells present in the channels was a result of global cell death and sequestering of non-viable cells into the channels. Additionally, and in relation to experiments which show uptake of fluorescent microspheres and nutrients, it is also unclear if transport is one-directional or if they can also function to expel waste material from the biofilm. To establish if intra-colony channels are directly involved in the uptake of antimicrobials, time-lapse imaging with viability dyes in combination with recently developed fluorescent antibiotic conjugates<sup>311</sup>, such as polymyxin B-Cy3<sup>312</sup> or the BODIPY-based BOCILLIN™-FL penicillin<sup>313,314</sup>, could be

used. If high concentrations of fluorescent antibiotics were found in the lumen of intra-colony channels it would provide further support for this hypothesis. Alternatively, time-lapse imaging of viability-stained antibiotic-treated biofilms may show movement of non-viable cells through the intra-colony channel network, which would suggest that the channels were being used as a method for removing dead cells from the colony. For example, a similar system has been shown in *Bacillus spp.* colonies, where dead cells are found in discrete pockets at the base of macro-colonies which nucleate the formation of macroscopic folds and crenulations<sup>172</sup>. These time-lapse experiments would be difficult to achieve using the current methods outlined in this Chapter, as any attempts to perform time-lapse imaging resulted in either stasis of the biofilm, or conversion to planktonic cells and shedding of the biofilm when mounted in a liquid medium.

Previous biofilm imaging studies have mainly used conventional widefield and laser scanning microscopy to study biofilm architecture, which are inherently limited by sacrificing spatial resolution and imaging volume. For example, automated tile-scanning microscopes which change the location of the FOV or focal plane have been used to image growing colonies from  $1 \times 10^1$ - $1 \times 10^4$  cells<sup>129-131</sup>; however, this method often requires long acquisition periods and results in tiling artefacts. With the Mesolens the need for stitching and tiling is negated when imaging multi-millimetre specimens. This means that images can be acquired of much more than just small bacterial aggregates and live bacterial macro-colonies in excess of  $1 \times 10^9$  cells can be imaged while maintaining sub-micron resolution throughout the entire  $36 \text{ mm}^2$  field. Therefore, in comparison with other conventional large specimen imaging techniques, the Mesolens stands as a novel and improved method for *in situ* imaging of live bacterial communities. Additionally, recent advances in light sheet microscopy<sup>315</sup> and mutli-photon microscopy<sup>264,316</sup> have been applied to biofilm imaging. However, these

methods currently cannot resolve sub-micron information over multi-millimetre scales, as with the Mesolens. The same problem accompanies ultrasound<sup>124,124,125</sup>, optical coherence tomography and photoacoustic tomography<sup>126–128</sup> methods used for mesoscale biofilm imaging, where they cannot properly resolve structures on the order of which are reported in this work.

### **3.5 Conclusions**

In summary, a previously undocumented nutrient uptake system in colonial biofilms has been identified which challenges the current belief where cells that are out with the reach of underlying nutrient-rich medium are able to gain nutrients beyond passive diffusion through the base of the biofilm<sup>259–262</sup>. The presence of these channels may represent a route to circumvent the chemical protection and resistance phenotype of bacterial biofilms<sup>159</sup>, such that rather than applying drugs to the apical surface of the biofilm it may be possible to exploit the intra-colony channels for delivery of antimicrobial agents. The identification and characterisation of an intra-colony channel network could therefore have far-reaching applications to public health and disease prevention, while providing another understanding on the delivery of nutrients to the centre of densely packed microbial communities.

# Chapter 4

## Visualising the growth behaviours of soil bacteria using a transparent soil environment

Bacteria have been historically isolated from soil and aquatic sediments and studied under laboratory conditions which do not reflect the natural habitats in which they are found. Therefore, although interesting and novel behaviours have been documented under these conditions, there may be unknown behaviours that can only be understood by observing bacteria in a structured culture environment. However, soil is difficult to work with as a growth medium as it must be sterilised by a process which removes nutrients, and also cannot be effectively studied by microscopical methods to gain a spatial overview of how bacteria behave in the environment due to the high autofluorescence, absorption and scattering which soil displays. This chapter outlines the development and characterisation of a Nafion™-based transparent soil system specifically designed for bacterial culture. Two species which represent prominent soil bacteria genera were selected (*S. coelicolor* and *B. subtilis*) and cultured in specifically designed, refractive index matched soil systems and imaged using the Mesolens to gain sub-micron resolution over multiple transparent soil particles. In this work it was observed that *S. coelicolor* and *B. subtilis* colonise soil particles by different manners compared to conventional culture techniques, and bacteria were found to be viable in this new system over a number of days. This approach to bacterial culture stands as a platform that could be taken forward to further study the behaviour of bacteria in their native environment and could be expanded to study interactions with other organisms, such as bacterial competition and warfare.



## 4.1 Introduction

Bacteria colonise almost every environment on Earth and can exist as either free-living planktonic cells or as part of microbial communities and biofilms. The colonisation of abiotic and biotic surfaces has long been studied to understand how bacteria establish and grow in their native environment. These processes are crucial in comprehending the development of bacterial disease<sup>317–319</sup>, formation of commensal relationships<sup>320–324</sup> and how bacteria produce novel specialised metabolites which we can exploit for clinical purposes<sup>325–328</sup>. The most common methods of studying these behaviours typically involve culturing bacteria in synthetic lab-based conditions which are not representative of how bacteria would grow in the environment. This problem was addressed by the mammalian cell biology field in the early 2000s by using 3D culture methods<sup>329–337</sup>, however the technology was not readily taken up by the microbiology community. Therefore, although the phenotypes which were observed of bacteria in a lab-based environment to date have been vital to our knowledge, certain behaviours may be overlooked without studying bacteria in a more natural culture system.

The two strains used in this chapter, *Bacillus subtilis* and *Streptomyces coelicolor*, belong to two different phyla of soil bacteria (Firmicutes and Actinobacteria, respectively). Interestingly, the relative abundance of these two genera in terrestrial soils is low compared to the overall bacterial titre, with *Bacillus spp.* only representing 1.6% and Actinobacteria as a whole representing 4.7%<sup>338</sup>. Moreover, studies have shown that *Streptomyces spp.* are the dominant genus of Actinobacteria in soil (accounting for over 95%)<sup>339</sup>, and are typically found in densities of  $1 \times 10^6$ – $1 \times 10^9$  colony forming units per gram of soil<sup>340</sup>. Despite their low comparative abundance, both of these phyla are renowned producers of specialised secondary metabolites, which have been adopted for clinical use as anti-tumour medicines<sup>341–344</sup>, anti-

helminthic treatments<sup>345</sup> and antimicrobial drugs<sup>346–352</sup>. The biosynthetic potential and growth behaviours of these organisms has only been explored by conventional culture methods; however, novel specialised metabolites may be elicited by mimicking the natural conditions in which these bacteria are found.

#### **4.1.1 *Streptomyces* spp. in the environment**

Streptomycetes are found in a variety of soil habitats and their biosynthetic potential has led to huge strides in drug discovery and antimicrobial therapies. Almost all studies which focus on Streptomyces development use an agar-based culture method, and so most observations of these bacteria are based on growth by traditional non-mimetic culture methods. This genus is morphologically distinct from other bacteria and have a complex life cycle which is tightly regulated in relation of production of specialised metabolites<sup>353–356</sup> (Figure 4.1). The Streptomyces life cycle begins with germination of a spore during favourable environmental conditions and a single hypha emerges and begins to branch to form a vegetative mycelium.

Following germination, germ tubes grow by extension of the hyphal tips and begin to branch along the lateral walls, which is controlled by polar growth and division machinery consisting of FilP, Scy and DivIVA proteins (the so-called polarisome)<sup>357,358</sup>. The process of tip elongation and branching is regulated by a Serine/Threonine kinase which phosphorylates DivIVA and initiate branching<sup>359</sup>. Control of aerial hyphae erection and sporulation are governed by Bald (Bld) and White (Whi) proteins, respectively. First, rodlin and chaplin proteins are recruited to the polarisome to create a hydrophobic coating which protects the aerial mycelium from desiccation<sup>360</sup>, and the surfactant SapB is produced to break surface tension to allow aerial hyphae to emerge from below the medium/air interface<sup>361–363</sup>. Septation then occurs, which separates nucleoids into separate cellular compartments before thickening to form individual exospores which are disseminated in the environment<sup>364</sup>.

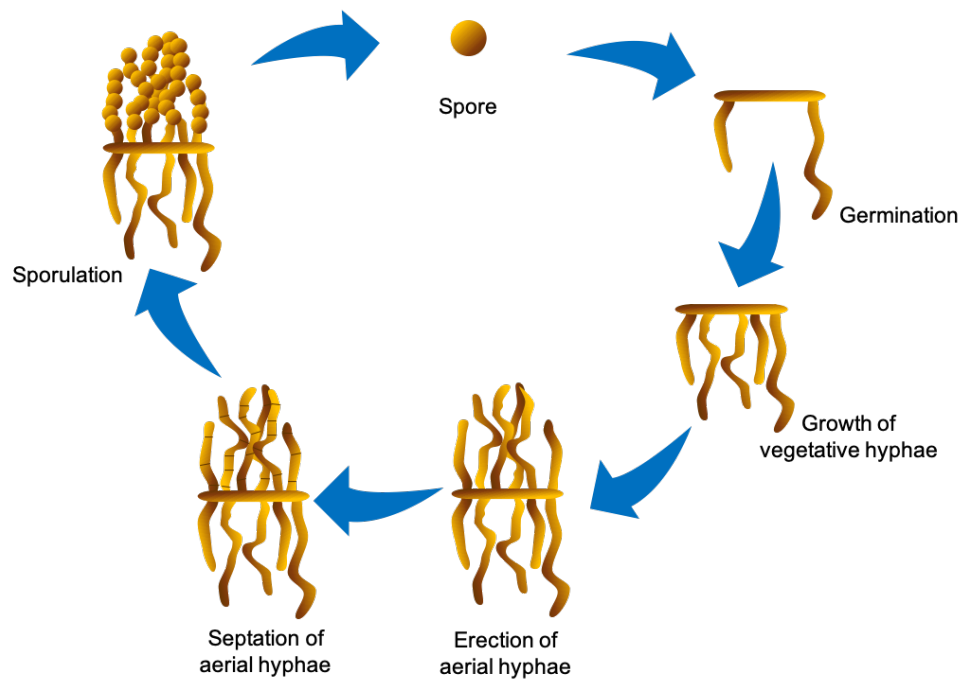


**Figure 4.1 The developmental lifecycle of *Streptomyces*.** A diagram showing the lifecycle of *Streptomyces*, where a spore initially germinates to form a mycelium which grows down into the nutrient-rich substrate before erecting aerial hyphae. During starvation the aerial hyphae septate and form spores which are then disseminated in the environment to restart the cycle. Adapted from <sup>353</sup>.

This complex developmental cycle resembles that of saprophytic fungi and is controlled by a complex cascade of signalling molecules which trigger the next phase of the lifecycle <sup>353,365</sup>.

The regulation of these processes is tightly controlled by a signalling cascade of Bld and Whi proteins. Briefly, the master regulator of aerial hyphae formation, BldD, binds with cyclic-di-GMP and represses a suite of *bld* genes, the sigma factor  $\sigma^{\text{BldN}}$  and *whi* genes <sup>366–371</sup>. Aerial hyphae are erected once nutrients are depleted or environmental response genes are activated <sup>372</sup>. BldD-c-di-GMP repression is removed which activates  $\sigma^{\text{BldN}}$ , in turn activating a BldM homodimer which then goes on to trigger the master regulator of sporulation,  $\sigma^{\text{WhiG}}$ , resulting in a transition from aerial growth to

sporulation<sup>373</sup>. Activation of  $\sigma^{\text{WhiG}}$  results in upregulation of *whiI* and *whiH* which are involved in the latter stages of sporulation<sup>374</sup>. The link between  $\sigma^{\text{WhiG}}$  and WhiA is poorly understood, but it is hypothesised that WhiA and WhiB regulate the expression of the other in a negative feedback loop, while WhiB goes on to direct transcription of two components of the divisome, ParAB and FtsZ<sup>367,373</sup>. The sum of these events leads to a differentiated mycelium, where non-motile Streptomyces are able to be spread throughout the environment and survive for long periods in unfavourable conditions.

The morphology of *Streptomyces spp.* is inherently linked to how they colonise and interact with other species in their environment. Laboratory-based observations routinely document Streptomyces growth as large “fluffy” colonies on agar plates, or as a dispersed or pelleted growth in liquid depending on the strain<sup>375</sup>. The growth of *Streptomyces spp.* in lab-based environments has been compared to those extracted directly from soil samples, which showed that the biomass forms smaller microcolonies<sup>376</sup>, however no *in situ* observations of Streptomyces in soil has been reported. Furthermore, the abundance of Streptomyces has been reported to be unchanged between vegetated and non-vegetated soils<sup>377</sup>, suggesting that some *Streptomyces spp.* are not so dependent on plant roots for soil colonisation as some studies have suggested<sup>378–381</sup>. Recent observations have also documented the phenomenon of “exploratory growth” where the mycelia will traverse a greater distance over a given time, even overcoming physical barriers, in the presence of exogenous signalling molecules such as trimethylamine<sup>382,383</sup>. Despite the many ways which Streptomyces can grow, all of these colonisation phenotypes are adopted to make the most of the nutrients present in the surrounding environment, and by altering their metabolism they are also able to ward off nearby competing microbes.

While the biosynthetic potential of Actinobacteria has been exploited for clinical use, the biocides produced by these bacteria have evolved over millennia to wage an ongoing ecological war in the soil<sup>384–387</sup>. A plethora of antimicrobial compounds are produced by Actinobacteria to subdue nearby competitors, and since the 1940s they have accounted for up to 70% of all clinical and agricultural drugs<sup>387–389</sup>. However, some studies have suggested that the concentration of bioactive metabolites in the environment is too low to have any bactericidal effects, and instead may facilitate inter-species signalling between adjacent strains in a soil microcosm<sup>390–392</sup>. Many strains were known to produce one or two specialised metabolites, however a much larger number of cryptic biosynthetic gene clusters (BGCs) were revealed with the use of whole genome sequencing (many of which cannot be produced under conventional culture conditions)<sup>393,394</sup>. The most common method of activating these silent BGCs is by elicitation; achieved by mimicking the chemical or environmental pressures which require these bioactive metabolites to be produced<sup>395</sup>. As mentioned, most approaches use chemical elicitation, or extremes of temperature, pH, salinity or nutrient concentration to trigger the production of novel metabolites. However, some studies have shown that more could be done to explore the role of a 3D environment on the observation of new behaviours, as behavioural changes in Streptomyces and Bacilli have been documented in changing from static solid to agitated liquid culture conditions<sup>396–400</sup>. Moreover, the co-culture with various plant species has also been documented to elicit specialised metabolite production<sup>401,402</sup>.

#### **4.1.2 *Bacillus* spp. in the environment**

*Bacillus* spp. are also found in a variety of soil habitats around the world and have been noted to produce bioactive metabolites. *Bacillus subtilis* has been a model organism for bacterial genetics and molecular biology for the past 70 years and is perhaps the most well-known *Bacillus* species. The colonisation and growth of

*Bacillus spp.* in the environment has almost exclusively been related to commensal plant relationships and growth in the rhizosphere. The role of *B. subtilis* as an endophyte of plant roots has been well documented and correlated with increased plant growth, increased plant salt tolerance and protection from pathogenic fungi<sup>403–409</sup>. However, there are few spatial observations of how *Bacillus spp.* grow in soil outside of a rhizospheric context.

Again, this genus of bacteria has been found to produce a number of specialised metabolites, similar to Streptomycetes in the environment<sup>410–413</sup>. However, it remains unclear how these bacteria grow in their native habitat, and moreover if viable cells growing in a mimetic environment produce novel metabolites or display previously undocumented behaviours.

#### **4.1.3 Transparent soil as an imaging tool for soil microbes**

A lack of microscopical methods for studying soil bacteria *in situ* has prevented understanding of bacteria in complex structured environments, and as such the colonisation behaviours of soil bacteria in the environment have remained elusive. Most studies currently investigate bacterial colonisation phenotypes using conventional cultivation and culture methods; however, this only provides a view of how bacteria grow in a laboratory environment. While these methods have obviously resulted in successful characterisation of bacterial species, their metabolic profiles and biosynthetic potential, there may be undiscovered behaviours which only occur in the bacteria's native environment.

Current culture methods in microbiology rely on century-old techniques and are largely unsuitable for *in situ* optical imaging. Therefore, spatial understanding of bacterial behaviour has been limited to studying laboratory-based phenomena that may not be representative of environmental behaviours. Taking inspiration from the mammalian cell biology community<sup>329–337</sup>, it was hypothesised that a 3D structural

matrix which mimics the natural habitat of the test organism could result in observation of new behaviours. In order for this new culture technique to be compatible with existing microscopy methods the substrate would have to be optically transparent, and also would have to have a low refractive index (i.e.  $\leq 1.34$ ). Therefore, a range of transparent materials were considered for construction of a transparent soil environment to culture soil-dwelling bacteria.

Cryolite was one contender for transparent soil. This white/transparent mineral ( $\text{Na}_3\text{AlF}_6$ ) has a refractive index of 1.339<sup>414</sup>, making it easy to refractive index match in aqueous solution. However, cryolite is rare and costly, often only available through jewellers and gemstone dealers, and commonly found with siderite, fluorite, and quartz impurities<sup>415</sup>. Synthetic cryolite is commercially available, however is often found with aluminium oxide impurities which result in clouding of the particles and an inconsistent refractive index<sup>414</sup>. Another candidate for transparent soil construction was fluorinated ethylene propylene (FEP); a low-cost synthetic fluoropolymer used as a non-stick coating for Teflon surfaces and has a refractive index of 1.337<sup>416</sup>. The hydrophobicity of FEP polymers makes aqueous suspensions unstable, and traps air bubbles in between the particles when they are submerged, and therefore was not considered for use. GrowDex<sup>®</sup> (UPM Biomedicals, Finland) is a hydrogel product which has recently been developed for use as a 3D culture matrix for mammalian cells. The 3D matrix is composed of a nanofibrillar cellulose mesh and can be mixed with nutrient media to maintain cell viability in a 3D environment<sup>417</sup>. However, the cost of this matrix remains high and has yet to be optimised for bacterial culture. Amorphous silica powder and gel preparations have also been suggested as suitable substrate for transparent soil. However, silica preparations often have a high refractive index (i.e.  $\geq 1.41$ ) and are therefore not suitable for aqueous culture environments<sup>418</sup>. Silica transparent soils have been used mainly for geological studies

to develop geotechnical physical models of soil particles in a controlled environment<sup>419,420</sup>, however they are rarely used with biological specimens.

After eliminating the previous candidate substrates for transparent soil, Nafion™ was considered for construction of transparent soil environments. Nafion™ is a fluorinated co-polymer of tetrafluoroethylene (Teflon) and perfluorosulfonic acid (Figure 4.2) and has been previously used to create transparent soils for observation of plant root growth<sup>206,207</sup>. However, the focus of these studies has involved imaging of root systems or root colonisation by pathogenic bacteria and the culture systems were optimised for plant growth rather than bacterial culture. Nafion™ has a refractive index of 1.34<sup>421</sup> and can be made hydrophilic after chemical processing, meaning Nafion™ soils are able to retain water between particles (similarly to soil)<sup>206</sup>. The Nafion™ polymer was able to undergo processing to imbibe the surface of particles with bacterial growth medium due to the chemical structure of Nafion™. Ionic exchange between growth medium components and perfluorosulfonic acid residues was possible following conversion of Nafion™ precursors to the anionic form, as discussed by Van Nguyen *et al.*<sup>422</sup>. Particles can then be refractive index matched prior to imaging to render them transparent. Nafion™ was chosen as a transparent soil substrate due to its commercial availability, documented use for biological

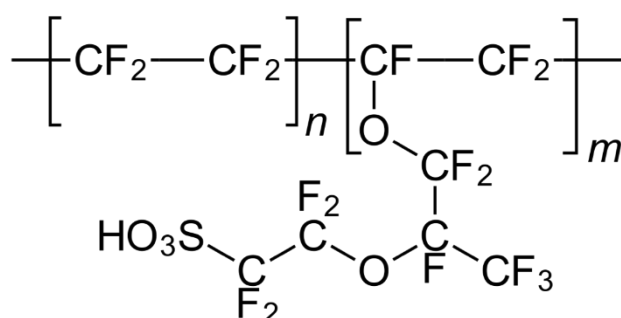


**Figure 4.2 The chemical structure of Nafion™ co-polymers.** Repeating monomers form the bulk material which can be refined and processed to form transparent soil.



imaging<sup>206,207</sup>, ability to be sterilised by autoclave, low refractive index, potential for particle size refinement and ion exchange capacity for nutrient imbibement.

#### **4.1.4 Experimental aims**

3D mimetic environments and 3D culture techniques are now common in eukaryotic cell biology, but have not been so readily taken up by the microbiology community. Some studies have primarily used transparent soil for observing plant root formation and growth, with little optimisation specifically for bacterial culture. The aim of this chapter was to develop and optimise a 3D mimetic environment for soil-dwelling bacteria which could be suitable for study by means of optical microscopy. The hypothesis was that soil-dwelling bacteria would exhibit different colonisation phenotypes and behaviours in a mimetic 3D environment compared to conventional laboratory culture conditions. These methods could then be taken forward to determine if 3D culture could be used to elicit novel behaviour or specialised metabolite production by soil bacteria.

## **4.2 Materials and Methods**

### **4.2.1 Specimen preparation**

#### **4.2.1.1 Bacterial cell culture**

Two representative soil bacteria phyla were selected to characterise a new optically transparent 3D culture system; Actinobacteria and Firmicutes. Well-studied species were selected from both phylum, *Streptomyces coelicolor* and *Bacillus subtilis*, respectively. Transparent soil environments were created, supplemented with nutrients, refractive index matched and optimised for each species with the aim of generating a mimetic 3D culture medium to understand their colonisation phenotypes in the environment. The methods for transparent soil construction were adapted from

Van Nguyen *et al.*<sup>422</sup> and Downie *et al.*<sup>206</sup>, along with helpful guidance from Dr. Lionel Dupuy (James Hutton Institute, Dundee, UK).

*Streptomyces coelicolor* (M145) cultures were maintained on solid Mannitol-Soya Flour (MS) medium<sup>375</sup> and grown in 2x Yeast-Tryptone (2x YT) broth<sup>375</sup> (Appendix II). The GFP-expression strain, *S. coelicolor* M145, containing *idh::gfp* in its native location, integrated on the chromosome and was maintained by supplementing all media with 50 µg/ml apramycin. M145-*idh-gfp*<sup>423</sup> was selected as a test strain for this work as *gfp* was translationally fused to *idh*, which is a highly expressed primary metabolic gene encoding an isocitrate dehydrogenase found throughout the cytosol<sup>424</sup>.

*Bacillus subtilis* cultures were maintained on solid LB medium and grown in LB broth. The plasmids encoding for photoproteins in fluorescent *B. subtilis* strains (JWV042 and CCBS189) were maintained by supplementing growth medium with 5 µg/ml chloramphenicol. JWV042 carried a plasmid which had a translation fusion of *gfp* and *hbs*<sup>423</sup>, a gene encoding for the non-specific DNA-binding protein HBSu, which was under the control of an endogenous promotor (*cat amyE::P<sub>hbs</sub>-hbs-gfp*). CCBS189 carried a plasmid which had a translation fusion of *mRuby2* and *mbl*, a gene encoding for the shape-determining cytoskeletal MreB-homologue protein Mbl, which was under the control of a native promotor (*mbl::mRuby2-mbl, cat*).

#### **4.2.1.2 Schwedock staining for Streptomyces**

To visualise the structure of *S. coelicolor* grown under conventional laboratory condition, specimens were stained using a method known as Schwedock staining<sup>425</sup>. This method uses two fluorescent dyes, fluorescein isothiocyanate-wheatgerm agglutinin (FITC-WGA) and propidium iodide (PI), to label N-acetylglucosamine residues in the peptidoglycan cell wall and nucleic acids, respectively. To prepare

cultures for staining, a 22 mm x 22 mm type 1.5 coverglass (631-0125, VWR International Ltd., UK) was sterilised by immersing in 100% ethanol before passing through a Bunsen flame. Sterile coverglasses were then inserted into solid MS medium at a 45° angle. Five micro-litres of a dilute M145 spore suspension were inoculated at the coverglass-medium interface at the acute angle, and care was taken to ensure that the spores were not injected under the surface of the solid medium. Inoculated plates were then inverted and incubated at 30°C in darkened conditions for 72 hours (when erection of aerial hyphae occurred). Following incubation, coverslips were carefully removed from the agar using sterile forceps and placed with the mycelium facing upwards abridge two sterile wooden toothpicks in a staining dish. The mycelium was fixed by pipetting 500 µl of ice-cold fixative (2.8% (v/v) formaldehyde (344198, Merck Millipore, USA), 0.0045% (v/v) glutaraldehyde (340855, Sigma Aldrich, USA)) onto the coverglass. The coverglasses were then washed twice with ice-cold phosphate-buffered saline (PBS) (BR0014, ThermoFisher Scientific, USA) before being allowed to completely air dry. The mycelia were then re-hydrated by adding 500 µl of ice-cold PBS and incubating for 5 minutes at room temperature (RT). The PBS was then replaced with 500 µl of ice-cold Glucose:Tris:EDTA buffer supplemented with 2 mg/ml lysozyme (L4631, Sigma Aldrich, USA) and incubated for 1 minute at RT before being washed with ice cold PBS. Finally, the mycelia were incubated with a blocking solution of 2% (w/v) bovine serum albumen (BSA) (A8531, Sigma Aldrich, USA) in PBS and incubated for 5 minutes at RT.

All subsequent staining steps were performed in darkened conditions. The 2% BSA solution was removed and replaced with 500 µl of an ice-cold staining solution containing 2 µg/ml FITC-WGA (W834, Invitrogen, USA) and 10 µg/ml PI (P1304MP, Invitrogen, USA) suspended in 2% (w/v) BSA in PBS. The coverglass was then

incubated with the staining solution for 2 hours at RT. Following incubation, the first staining solution was removed and the coverglass was washed eight times with 500  $\mu$ l of a second ice-cold staining solution containing only 10  $\mu$ g/ml PI in PBS. Before imaging, 10  $\mu$ l of 40% (v/v) glycerol was used to mount the stained mycelium, and the coverglass was sealed around the edges using clear nail varnish. Slides were stored at -20°C until required.

#### **4.2.2 Constructing transparent soil for bacterial culture**

Transparent soil has previously been constructed for plant root imaging using Nafion™ co-polymers, which were provided from the manufacturer as approximately 3.5 mm diameter resin pellets. The Nafion™ precursor pellets were initially reduced in size before being taken through a series of chemical treatments to confer a positive charge and purify the surface of the particles, before titrating with bacterial growth medium and refractive index matching prior to inoculation and imaging.

##### **4.2.2.1 Particle size reduction**

The size of naïve Nafion™ NR-50 1100 EW pellets (Ion Power GmbH, Germany) was refined by cryomilling to ensure freeze-fracturing of the particles following submersion in liquid nitrogen. A 10 g sample of Nafion™ NR-50 was placed in a metal sample holder and pre-cooled for 5 minutes in liquid nitrogen before being milled using a cryogenic grinder (6850, SPEX SamplePrep, USA) at the highest frequency (10.0 A.U.) for 2 minutes. Milled particles were then sieved through a series of different pore sizes (500  $\mu$ m, 850  $\mu$ m, 1250  $\mu$ m) (Fisher Scientific, UK) to separate particles of different sizes. Particles larger than 1250  $\mu$ m were re-processed as above until they passed through the 1250  $\mu$ m sieve.

#### **4.2.2.2 Conversion of Nafion™ to an acid form and surface**

##### **purification to ensure cationic exchange**

In order to mimic the water retention profile of soil and to eventually bind nutrient cations, the surface of the milled particles was converted to an anionic form which resulted in a hydrophilic surface and imbibed a negative charge. Milled particles were converted to the acidic form by soaking in a solution of KOH (15% w/v), DMSO (35% v/v) and distilled deionised water (ddH<sub>2</sub>O) (sourced from a Neptune Life water purification and deionisation system (R.2.0/200, Purite Ltd., UK)) and held in an 80°C water bath for 5 hours. The conversion buffer was then replaced with ddH<sub>2</sub>O and left for 30 minutes at RT, before washing the particles three times with fresh ddH<sub>2</sub>O. The particles were then submerged in a 15% (v/v) HNO<sub>3</sub> solution for 1 hour at RT, before washing with ddH<sub>2</sub>O and replacing with fresh 15% (v/v) HNO<sub>3</sub> solution and left overnight at RT.

Inorganic and organic impurities were removed from the protonated particles prior to surface exchange with nutrient cations. Following HNO<sub>3</sub> treatment, inorganic impurities were removed from the particle surfaces by first washing three times with ddH<sub>2</sub>O before replacing with a 1 M H<sub>2</sub>SO<sub>4</sub> solution at RT. The H<sub>2</sub>SO<sub>4</sub> suspension was then heated to 65°C and held in a water bath for 1 hour before cooling down to RT. The H<sub>2</sub>SO<sub>4</sub> was replaced with ddH<sub>2</sub>O and again incubated in a 65°C water bath for 1 hour before allowing to cool to RT. Organic impurities were then removed by H<sub>2</sub>O<sub>2</sub> treatment. Particles were then washed three times with ddH<sub>2</sub>O before being submerged in a 3% (w/v) H<sub>2</sub>O<sub>2</sub> solution and being incubated in a 65°C water bath for 1 hour. The H<sub>2</sub>O<sub>2</sub> suspension was then cooled to RT and rinsed three times with ddH<sub>2</sub>O and stored in ddH<sub>2</sub>O until required for staining or for nutrient titration.

#### **4.2.2.3 Sulphorhodamine-B staining of processed Nafion™**

##### **particles**

Milled and chemically processed Nafion™ particles were fluorescently stained in order to first visualise the size and shape distribution of particles. Sulphorhodamine-B-stained particles were provided by Dr. Lionel Dupuy and colleagues (James Hutton Institute, Dundee, UK), and were created by the following method; 500 µl of 1 µg/ml (1.8 nM) sulphorhodamine-B (S1307, Invitrogen, USA) was added to a sample of milled and chemically processed Nafion™ particles. The dye solution was then removed and placed in a refractive index matching buffer prior to imaging (details below).

#### **4.2.3 Preparing chemically processed Nafion™ particles for bacterial culture**

Following anionic conversion and surface purification, the Nafion™ particles were then titrated with growth medium. The growth medium was selected depending on the test organism (i.e. *S. coelicolor* or *B. subtilis*), and several candidate media were initially screened. Once a growth medium which was suitable for imaging Nafion™ soils was identified (i.e. low autofluorescence, low refractive index etc.), the chemically-processed particles were titrated with nutrient broth and the pH was monitored to determine when the sulphonic acid groups ( $\text{SO}_3\text{H}^+$ ) had been saturated with cations from the growth medium. This meant that ionic exchange was complete and the Nafion™ polymer now mimicked the surface chemistry of a clay-based soil particle, as discussed by Downie *et al.*<sup>206</sup>. Additionally, a range of refractive index matching substances were investigated with the aim of supplementing the growth medium with a non-metabolisable refractive index matching compound which the test bacteria could not break down. Thereby, the refractive index of the surrounding milieu would remain stable over long incubation periods and during imaging.

#### **4.2.3.1 Selecting the appropriate Streptomyces nutrient medium for use with transparent soil**

Initially Yeast Extract Malt Extract (YEME), a rich nutrient medium, was selected for Streptomyces culture in transparent soil. The recipe for YEME medium can be found in Appendix II. The particles were titrated by taking chemically processed transparent soil and submerging in fresh YEME broth and placing in a 30°C shaking incubator set to 225 rpm for 30 minutes. The pH was measured using a ThermoOrion pH meter (0410A0, Thermo Scientific, USA) after 30 minutes, and the spent YEME was replaced with fresh medium before being placed back in the incubator for another 30 minutes. This process was repeated until the pH of the spent medium was equal to that of fresh YEME medium (pH = 6.13). However, it was observed that the first addition of YEME medium resulted in the medium turning transparent and the soil particles were dyed yellow, indicating that the yeast extract in the medium had bound to the surface of the soil particles. Upon imaging, this resulted in high autofluorescence owed to the yeast extract components of the rich medium. Therefore, other media were investigated which did not contain yeast extract as a nutrient source.

The above method of titration was then used with Supplemented Minimal Medium (SMM) with L-arabinose used as the sole carbon source (total [L-arabinose] = 0.2% w/v (13.3 mM)). L-arabinose was chosen as it is a common plant-derived sugar which is found in soil environments<sup>426</sup>. The recipe for SMM can be found in Appendix II. When titrated with SMM<sub>L-arabinose</sub>, there was no observable discolouration of the soil particles and the SO<sub>3</sub>H<sup>+</sup> exchange sites were saturated typically after 6 cycles (3 hours) once the pH stabilised at 7.02. Following nutrient adsorption, the particles could then be refractive index matched prior to inoculation.

#### **4.2.3.2 Selecting the appropriate *Bacillus subtilis* nutrient**

##### **medium for use with transparent soil**

*Bacillus subtilis* 168 was also selected to test the suitability of a mimetic transparent soil culture system. Maintaining the aforementioned criteria of any medium having no yeast extract, a variety of minimal media were considered for nutrient titration for *B. subtilis* growth. Literature suggested either S7<sub>50</sub> defined minimal medium<sup>427</sup> or Spizizen minimal (SM) medium<sup>428</sup> would be logical candidates based on their composition (Appendix II). S7<sub>50</sub> medium was discounted due to a repeated precipitation of the mineral salts from the solution. Spizizen minimal medium provided in a stable solution which could be supplemented with defined carbon and nitrogen sources and had no autofluorescent or pigmented components, and so was used for studying *B. subtilis* colonisation phenotypes in transparent soil. Again, L-arabinose (0.2% w/v (13.3 mM)) was selected as the sole carbon source for imaging experiments. Transparent soil particles were titrated with SM<sub>L-arabinose</sub> as described above and could then be refractive index matched prior to inoculation.

#### **4.2.4 Refractive index matching for transparent soils**

The principle of refractive index matching is to submerge particles in a solution of the same refractive index as the test material to negate refraction of light at the solid-liquid interface, and thereby render the test material transparent. In reference to this work, refractive index matching means that the colonisation of soil environments by bacterial species can be studied by means of optical microscopy with minimal scattering by the 3D culture environment. Refractive index matching is typically achieved using colloidal silica or sugar solutions. However, care must be taken when using sugars to ensure that constituent bacteria are unable to metabolise the correcting sugar, which would alter the refractive index of the imaging medium over time.



#### 4.2.4.1 Refractive index matching for *S. coelicolor* soils

The central carbon metabolism of *S. coelicolor* are well documented<sup>375</sup>, and so finding a refractive index matching substance that would not be metabolised by the bacteria during growth was achieved by consulting a centralised metabolism database, the Kyoto Encyclopaedia of Genes and Genomes (KEGG). No sucrose-degrading pathways were identified in the primary metabolism of the *S. coelicolor* strain used in this chapter (M145), and so it was considered as a suitable candidate for refractive index matching transparent soil for observing M145 growth behaviours.

The refractive index of naïve Nafion™ particles is 1.34<sup>421</sup>, meaning that a refractive index correcting solution must also have a refractive index of 1.34. The refractive index of sucrose at varying concentrations was measured in triplicate using an Abbe refractometer (Billingham & Stanley Ltd., U.K.) which was calibrated using absolute methanol at 21°C ( $\lambda = 589$  nm). A range of sucrose concentrations from 1% to 100% (w/v) were measured in triplicate and plotted. All sucrose solutions were prepared by dissolving in SMM<sub>L-arabinose</sub> medium. A linear fit was applied and the equation of the trendline used to calculate the concentration of sucrose required to effectively refractive index match Nafion™ soils. A concentration of 6.5% (w/v) (190 mM) sucrose was required to refractive index match Nafion™ soil.

#### 4.2.4.2 Refractive index matching for *B. subtilis* soils

*Bacillus subtilis* has been used as a workhorse of molecular microbiology for the past 70 years, and so its central metabolism is also well established. The strains used in this study are able to metabolise many carbon sources commonly found in soil environments, and so a plate-based growth assay was used to determine carbon auxotrophies for potential sugars which could be used for refractive index matching. Logan and Berkley (1984) had previously shown multiple carbon auxotrophies in *B. subtilis*, however it was unclear from their work the genetic background of the strain

they had used<sup>429</sup>. Therefore, an auxotrophy screen was performed with *B. subtilis* 168, JVV042 and CCBS189 to confirm their metabolic profiles. Four sugars were selected from Logan and Berkely's original screening (glucose, D-sorbitol, D-xylose and D-arabinose), and were initially supplemented to SM medium at a final concentration of 0.2% (w/v). A positive control of LB medium was used in all auxotrophy screenings. A preliminary check by growing 5 ml overnight cultures in sterile universals at 37°C shaking at 225 rpm resulted in growth on LB, glucose and D-sorbitol, but none observed on D-xylose or D-arabinose. A 96-well optical bottom dish (265300, ThermoFisher Scientific, USA) was prepared with 198 µl of either SM medium supplemented with a test carbon source, or LB (with selective antibiotics where required). Overnight cultures of each *B. subtilis* strain grown in LB broth before diluting in fresh LB broth and growing to OD<sub>600</sub> = 0.5. To ensure that nutrients from the rich LB medium was not carried over into the plate assay, the cells were washed twice by centrifuging at 12,000 rpm for 3 minutes and replacing supernatant with sterile 1x SM buffer. Two micro-litres of the washed cell suspensions were added to the respective wells of the 96-well plate before being loaded into a Synergy™ HTX multi-mode plate reader (BioTek Instruments Inc., US) set to medium orbital shaking at 37°C while measuring OD<sub>600</sub> emission every 15 minutes for a period of 72 hours. Blanks which contained sterile SM medium with each carbon source and sterile LB were also included.

Following growth over 72 hours, the specific growth rate was calculated to quantify the growth of each strain on different nutrient sources and empirically identify carbon auxotrophies. The growth of microbial cells can be described as an increase in the number of cells over a given time period, which can be expressed as the growth rate ( $\mu$ ) ( $\text{h}^{-1}$ ). The growth rate can be calculated using Equation 4.1d and by understanding

the change in the number of cells ( $N$ ) (which is provided using  $OD_{600}$  as a proxy) between two time points ( $t_1$  and  $t_2$ ).

$$\frac{dN}{dt} = \mu N \quad [4.1a]$$

$$\frac{dN}{N} = \mu \cdot dt \quad [4.1b]$$

$$\int_{N_1}^{N_2} \frac{dN}{N} = \int_{t_1}^{t_2} \mu \cdot dt \quad [4.1c]$$

$$\ln\left(\frac{N_2}{N_1}\right) = \mu(t_2 - t_1) \quad [4.1d]$$

As Equation 4.1d takes the form of  $y = mx + c$ , The growth rate can also be extracted from a growth curve based on knowledge that cells will double over a certain period of time during log phase. Plotting the log phase resulted in a linear response, where the gradient is equal to  $\mu$ . This method was used to compare the specific growth rate of *Bacillus* strains in different nutrient media and found that D-arabinose and D-xylose were not metabolised by any of the test strains.

A curve of refractive index against concentration was created by the same method described in Section 4.2.4.1 for both D-arabinose (1% - 50% w/v) and D-xylose (1% - 50% w/v). All solutions were prepared by dissolving either D-arabinose or D-xylose in  $SM_{L-arabinose}$  medium. A concentration of 5.1% (w/v) (340 mM) D-xylose and 3.8% (w/v) (253 mM) D-arabinose was required to refractive index match Nafion™ soil. D-arabinose was selected as an appropriate refractive index matching material for *B. subtilis* soils moving forward as a lower concentration was required to refractive index match Nafion™ soils.

#### **4.2.4.3 Comparison of refractive index matching sugars to commercial colloid silica solutions**

Refractive index matching is also routinely achieved using commercial colloidal silica suspensions, such as Ludox® (420859, Sigma Aldrich, USA) or Percoll® (P7828,

Sigma Aldrich, USA), which are typically more expensive than sugar correcting solutions. To demonstrate the benefits of using sugar correcting solutions over commercial silica preparations a curve of refractive index against concentration was generated for Percoll® at different concentrations (1% - 100% in dH<sub>2</sub>O) in triplicate. Again, an Abbe refractometer which was calibrated using absolute methanol was used to measure refractive index ( $\lambda = 589 \text{ nm}$ ). The stability of Ludox® was found to be unreliable and became opaque as colloidal silica particles dropped out of solution at room temperature.

#### **4.2.5 Development of an imaging workflow for the Mesolens**

##### **4.2.5.1 Sample preparation for Streptomyces imaging**

For growth in transparent soil, M145-*idh-gfp* spores were pre-germinated by first growing in 10 ml of 2x YT broth for 4-6 hours while shaking at 225 rpm at 30°C. When germ tubes had begun to emerge, the culture was centrifuged at 1000x g for 5 minutes and washed twice with sterile TES buffer (25 mM Tris[hydroxymethyl]methyl-2-aminoethanesulphonic acid (pH 7.2) supplemented with 7.5 mM EDTA). The supernatant was removed and 5 ml of sterile SMM<sub>L-arabinose</sub> medium supplemented with apramycin (50 µg/ml) and sucrose (6.5% w/v) to refractive index match the soil. L-arabinose was chosen as it is a plant-derived sugar which is commonly found in the soil.

Chemically processed and SMM<sub>L-arabinose</sub>-titrated soil was placed in a custom Mesolens imaging chamber slide, with a well depth of 2 mm<sup>112</sup>. The pre-germinated M145-*idh-gfp* culture was then diluted by 1:100 with fresh SMM<sub>L-arabinose</sub> medium supplemented with apramycin (50 µg/ml) and sucrose (6.5% w/v) and 1000 µl was pipetted into the soil so that liquid completely covered the particles. To prevent evaporation of the medium over long incubation times, the lid of a sterile ibidi imaging chamber (cat. no. 80136; ibidi GmbH, Germany) was inverted and placed carefully

over the imaging chamber (Figure 4.3). The entire chamber slide was then placed in a large square Petri dish which contained a paper towel soaked in sterile water to maintain humidity during incubation. The dish was then covered and incubated in darkened conditions for 120 hours at 30°C.

Following incubation, the chamber was removed from the incubator and the ibidi lid was removed before a large coverglass was placed over the well of the imaging chamber (70 mm x 70 mm, Type 1.5, 0107999098 (Marienfeld, Lauda-Koenigshofen, Germany)) and the culture was imaged using widefield mesoscopy.

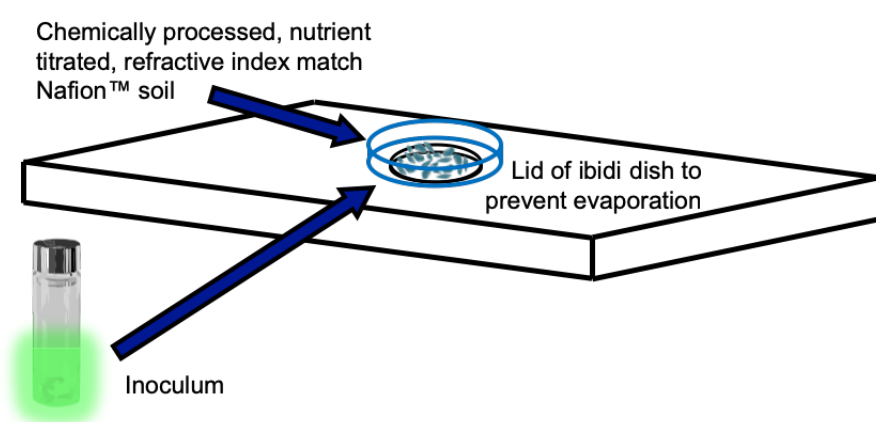


**Figure 4.3 Transparent soil culture method for mesoscopic imaging.** A schematic showing the method used to culture bacteria in a transparent soil environment. A custom imaging chamber is shown which was filled with chemically treated, nutrient-saturated and refractive index match Nafion™ soil and inoculated with a liquid culture. A sterile plastic dish was used to prevent evaporation of liquid medium from the imaging chamber during incubation.

#### 4.2.5.2 Sample preparation for *Bacillus subtilis* imaging

Three different *B. subtilis* strains were originally screened for transparent soil culture (i.e. 169, CCBS189 and JWV042), however, as no phenotypic difference was observed and to simplify the experimental setup, only the *gfp*-expressing strain was selected for mesoscopic imaging as it gave the highest contrast images.

Overnight cultures were prepared by first growing JWV042 in LB broth supplemented with 5 µg/ml chloramphenicol and incubating at 37°C while shaking at 225 rpm. The culture was centrifuged at 1000x g for 5 minutes and washed twice with sterile 1x SM buffer to remove any traces of rich medium from the cells. The chemically processed and SM<sub>L-arabinose</sub>-titrated soil was placed in an imaging chamber as in Section 4.2.5.1. The washed culture was then diluted 1:100 with sterile SM<sub>L-arabinose</sub> medium supplemented with chloramphenicol (5 µg/ml) and D-arabinose (3.8% w/v) to refractive index match the soil. As before, 1000 µl of the culture was pipetted into the soil so that liquid completely covered the particles and the specimen was incubated using the same method as in Section 4.2.5.1, but for 48 hours in darkened conditions at 37°C.

Following incubation, the chamber was removed from the incubator and the ibidi lid was removed before being mounted with a 70 mm x 70 mm, Type 1.5, coverglass and the culture was imaged using widefield and confocal laser scanning mesoscopy.

#### **4.2.5.3 Ensuring specimen viability in transparent soil media**

A phenotypic screening method was used to determine if bacteria remained viable throughout incubation and growth in a transparent soil environment. Following growth and imaging of JWV042 in transparent soil, a 10 µl inoculum was taken from the soil culture and used to inoculate a 5 ml volume of sterile LB broth supplemented with 5 µg/ml chloramphenicol. The culture was then grown overnight at 37°C shaking at 225 rpm before being serially diluted in sterile LB broth to  $1 \times 10^{-8}$  and plated on solid LB medium supplemented with 5 µg/ml chloramphenicol and incubated for 18 hours at 37°C in darkened conditions. A sample was also taken from the overnight liquid culture for visualisation under a conventional widefield epifluorescence microscope to establish if cells recovered from transparent soil remained fluorescent. These cells

were compared to cells which had been grown for 48 hours in liquid SM<sub>L-arabinose</sub> medium. The cellular morphology was compared using the microscopy data, while colonial morphology was compared using the colonies on the serial dilution plates.

#### **4.2.6 Imaging conditions**

##### **4.2.6.1 Widefield microscopy**

Conventional widefield epifluorescence and phase contrast microscopy was used to compare the cellular morphology and GFP expression before and after growth of bacteria in a transparent soil environment. Images were acquired using an Eclipse TE-2000-S microscope with a 100x/1.3 NA CFI PLAN FLUO DLL Oil objective lens (Nikon, Japan) coupled to a digital CCD camera (C4742, Hamamatsu, Japan). Illumination for GFP excitation was sourced from a mercury arc lamp which was coupled into the epi-port of the microscope. A 530 nm  $\pm$  35 nm emission filter was used for fluorescence imaging (1CH81700, Chroma Technology Corporation, USA). Illumination for phase contrast microscopy was provided by a tungsten bulb lightsource.

##### **4.2.6.2 Confocal laser scanning microscopy**

A confocal laser scanning microscope was first used to verify that no reflection signal was detected from soil particles following refractive index matching, and also to assess the autofluorescence profile of the transparent soils. Soil particles were imaged using a Leica TCS-SP5-II confocal laser scanning microscope with a 5x/0.15 NA PL FLUOTAR objective lens (Leica, Germany). Incident light for reflection, autofluorescence excitation and transmission was provided by a 488 nm line from a Kr/Ar laser source (Coherent, USA). Reflection imaging was carried out by placing an 80/20 beamsplitter in the detection path and restricting the PMT detection to 488 nm  $\pm$  5 nm. The autofluorescence signal was acquired by extending the same PMT

detection from 520 nm – 620 nm. Transmission images were acquired by using the TCS-SPT-II in transmission mode and detecting transmitted light using a PMT detector.

#### **4.2.6.3 Widefield mesoscopy**

Brightfield transmission mesoscopy was achieved using a tungsten bulb lightsource and with the condenser position, condenser diaphragm and field iris set for Köhler illumination. Fluorescence excitation was achieved using a 435 nm or 490 nm LED from a pE-4000 LED illuminator (CoolLED, U.K.). A triple bandpass filter which transmitted light at  $470 \pm 10$  nm,  $540 \pm 10$  nm and  $645 \pm 50$  nm was placed in the detection pathway. The emission signal was detected using a VNP-29MC CCD camera with chip-shifting modality (Vieworks, South Korea) to capture the full FOV of the Mesolens at high resolution. Widefield mesoscopic imaging was carried out using water immersion ( $n = 1.33$ ) with the Mesolens' correction collars set accordingly to minimise spherical aberration through refractive index mismatch.

#### **4.2.6.4 Confocal laser scanning mesoscopy**

Fluorescence excitation of GFP was obtained using the 488 nm line set at 8 mW from a multi-line LightHUB-4 laser combiner (Omicron Laserage, Germany). The fluorescence emission signal was detected using a PMT (P30-01, Senstech, U.K.) with a 505 nm longpass dichroic mirror (DMLP505R, Thorlabs, USA) placed in the emission path and a 525/39 nm bandpass filter (MF525-39, Thorlabs, USA) placed before the detector.

Confocal laser scanning mesoscopy was carried out using type DF oil immersion ( $n = 1.51$ ) with the Mesolens' correction collars set accordingly to minimise spherical aberration through refractive index mismatch.



#### **4.2.7 Image processing and analysis**

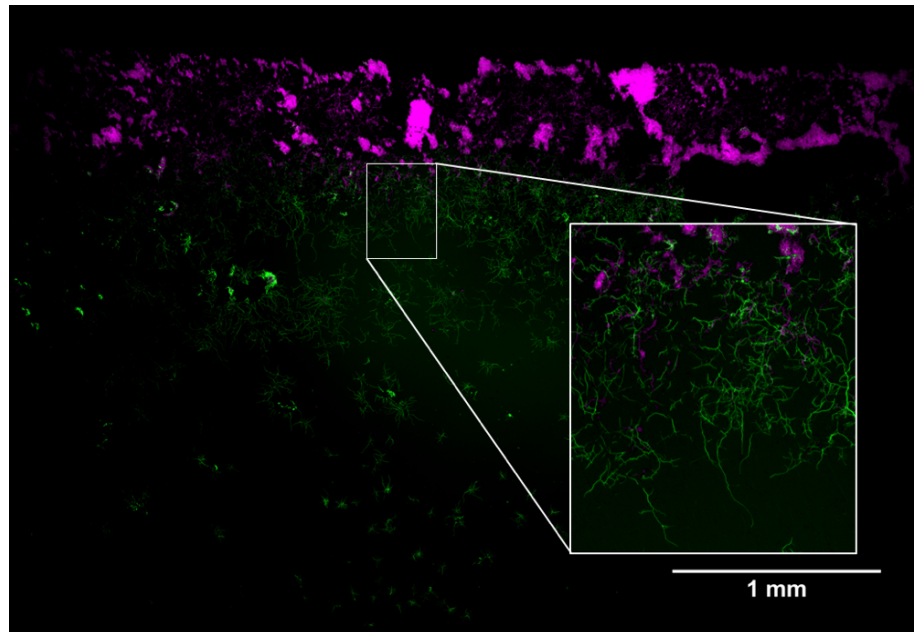
The autofluorescence of Nafion™ particles following different surface treatments was analysed by first acquiring images of soil particles by widefield epifluorescence mesoscopy. As each test strain of bacteria encoded GFP, the autofluorescence intensity was measured in all samples by exciting with 490 nm LED at moderate power and exposure times (35% LED power, 500 ms exposure time). Autofluorescence intensity was quantified by first drawing multiple ROIs randomly over the surface of transparent soil particles. The mean intensity in each ROI was measured and normalised against the dynamic range of the camera sensor (0 – 4095 AU). The mean values for each surface treatment was then compiled in a violin plot using Plots of Data (developed by Joachim Goedhart, University of Amsterdam, Netherlands).

Image analysis was performed using FIJI<sup>60</sup>. Figures presented in this chapter were linearly contrast adjusted for presentation purposes where required using FIJI<sup>60</sup>.

### **4.3 Results**

#### **4.3.1 Morphologies of test species under normal laboratory conditions**

To eventually compare the growth behaviours of soil bacteria in a transparent soil environment, the morphological phenotypes of *S. coelicolor* and *B. subtilis* were first shown following growth under conventional laboratory culture conditions. M145 completes its growth cycle to fully erect aerial hyphae and begin sporulating when grown on solid medium over 72 hours. Tissue differentiation occurs between the vegetative mycelium and the aerial mycelium, where aerial hyphae are the only actively growing part of the mycelium (Figure 4.4).



**Figure 4.4. *Streptomyces* grow as a differentiated mycelium under conventional culture conditions.** A deconvolved widefield image of an M145 mycelium prepared using the Schewdock staining method. Peptidoglycan (FITC-WGA-labelled) is presented in green and nucleoids (PI-labelled) are presented in magenta. An ROI of shows a magnified view of the mycelial architecture, where aerial hyphae are erected from the vegetative mycelium.

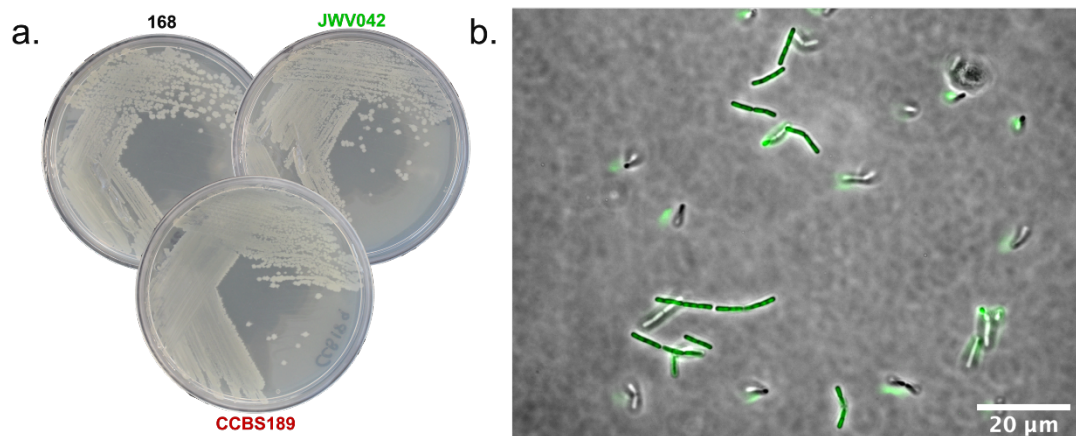


**Figure 4.5. *Bacillus subtilis* strains grown using conventional culture methods.** (a) Macro-colonies of *B. subtilis* strains 168 (WT), JWV042 (*cat amyE::P<sub>hbs</sub>-hbs-gfp*) and CCBS189 (*mbl::(mRuby2-mbl, cat)*) grown on solid LB medium under conventional laboratory conditions. (b) JWV042 grown under conventional conditions in liquid LB broth imaged by widefield epifluorescence and phase contrast microscopy. Cells often appear in short linked chains, or as motile planktonic single cells.

Following routine culture methods for *B. subtilis*, growth on solid media resulted in formation of multi-millimetre sized macro-colonies, whereas growth in liquid broth resulted in either freely motile cells or short chains of cells which remained connected at their poles after mitosis (Figure 4.5). These growth behaviours and colonisation phenotypes have been well documented in literature, but are must be taken into account when comparing to growth of these strains in alternative culture environments.

#### 4.3.2 Optimisation of transparent soil for bacterial culture

To observe the geometry of transparent soil particles after refinement and processing they were stained using sulphorhodamine-B, which electrostatically bound to the surface of the Nafion™ particles. Observations by widefield epifluorescence mesoscopy showed that refined and processed particles were irregularly shaped and ranged from approximately 400  $\mu\text{m}$  – 1200  $\mu\text{m}$  in size (Figure 4.6), which mimics the

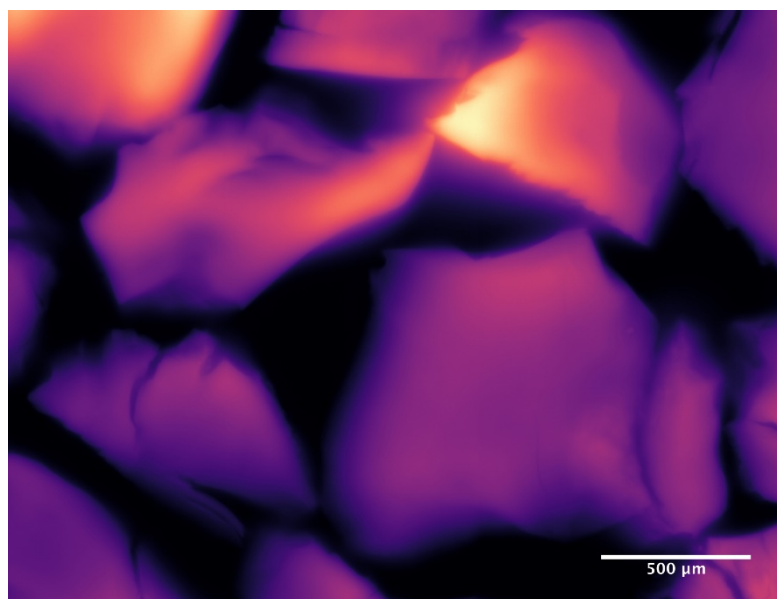


**Figure 4.6. Sulphorhodamine-B labelled transparent soil particles.** Refined, chemically processed and fluorescently labelled Nafion™ soil particles imaged by widefield mesoscopy.

inhomogeneity in soil particle sizes in the environment<sup>430,431</sup>. Some particles also possessed crevasses and cracks along their surface which was likely due to the freeze-fracturing process during cryogenic milling.

#### 4.3.2.1 Refractive index matching soils for Streptomyces culture using sucrose

Sucrose was tested as a refractive index matching solution as M145 was a known sucrose auxotroph. A curve of refractive index against sucrose concentration was generated and compared to the refractive index for Nafion<sup>TM</sup>. The equation of the linear trendline was used to determine the final concentration of sucrose that should be present in the culture medium prior to imaging (Figure 4.7). A final concentration of 6.6% (w/v) sucrose in SMM<sub>L-arabinose</sub> was required to refractive index match Nafion<sup>TM</sup> soils for Streptomyces imaging.

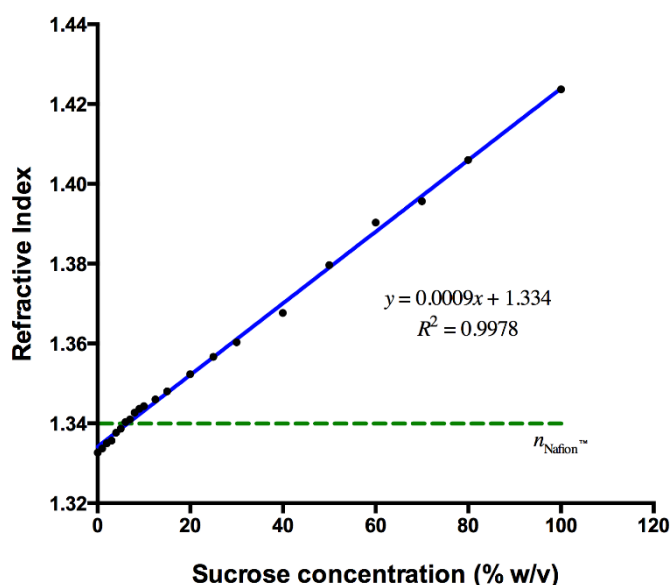


**Figure 4.7. Sucrose refractive index curve for Nafion<sup>TM</sup> refractive index matching.**

The refractive index of SMM medium with a range of sucrose concentrations shows a linear relationship between refractive index and concentration. The refractive index of Nafion<sup>TM</sup> (1.34) is also shown, with a concentration of 6.6% required for refractive index matching. n = 3, error bars show the standard error of the mean.

#### 4.3.2.2 Refractive index matching soils for *B. subtilis* culture

##### using sucrose

The appropriate refractive index matching sugar for *B. subtilis* culture was identified by initially selecting from a range tested by Logan and Berkeley<sup>429</sup>. A plate-based assay was designed to test the ability of *B. subtilis* 168, CCBS189 and JWV042 to break down different carbon sources which could be used for refractive index matching. The aim of this was to identify which carbon source(s) could be supplemented into growth medium and have the concentration (and so refractive index) remain stable throughout incubation and imaging. Measuring growth over three days revealed that *B. subtilis* strains were able to grow in LB, SM<sub>D-glucose</sub> and SM<sub>D-sorbitol</sub>, but not in SM<sub>D-arabinose</sub> or SM<sub>D-xylose</sub> (Figure 4.8), which agreed with the observations of Logan and Berkley. Growth was most rapid and resulted in higher cell densities in rich LB medium, whereas SM medium resulted in lower levels of growth. The shape of the growth curve reveals the growth behaviour of each strain over time, and wells where cells were able to grow produced a canonical growth curve, with a lag, log, stationery and death phase. However, the SM<sub>D-arabinose</sub> or SM<sub>D-xylose</sub> curves resulted in a steady increase in OD<sub>600</sub> over time but did not follow the canonical shape of a bacterial growth curve. The increase in OD<sub>600</sub> was due to the build-up of condensation and resulting scattering of light as it passed through the plate. The specific growth rate ( $\mu$ ) was calculated for each strain under each condition to quantify growth each carbon source. The specific growth rate for each strain verified the trends shown in the growth curve data, and again the small  $\mu$ -value for SM<sub>D-arabinose</sub> and SM<sub>D-xylose</sub> correlated with the presence of condensation around the top of the plate over time (Figure 4.8d). Therefore, it was concluded that either D-arabinose or D-xylose were potential candidates for refractive index matching in *B. subtilis* soils moving forward.

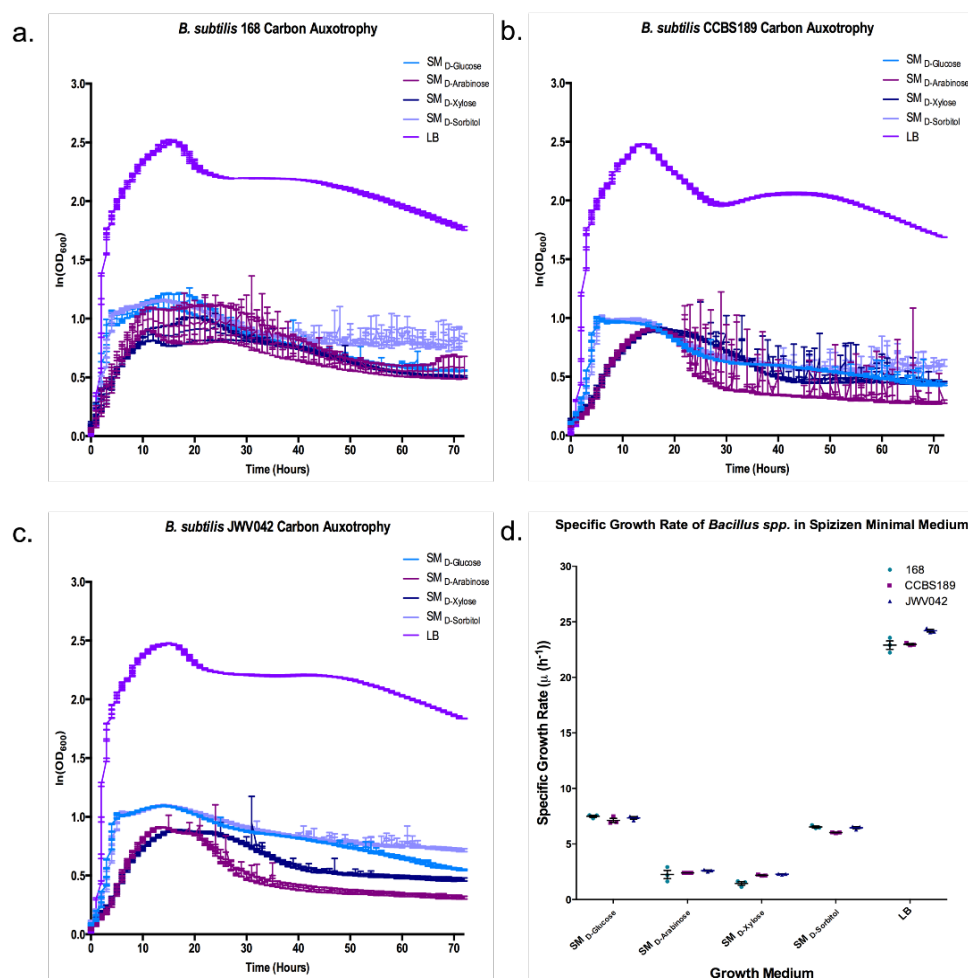


**Figure 4.8. Determining the carbon auxotrophies of *Bacillus* strains for downstream refractive index matching.** The growth of (a) *B. subtilis* 168 (WT), (b) CCBS189 and (c) JWV042 over time under a range of growth conditions. (d) The specific growth rate ( $\mu$ ) for each test strain grown under different nutrient conditions. All strains demonstrated auxotrophy for D-arabinose and D-xylose.  $n = 3$  for each strain in nutrient condition, error bars show the standard error of the mean.

Refractive index curves for D-xylose and D-arabinose were created and compared to the refractive index for Nafion™. Again, the equation of the trendline was used to determine the final concentration of D-arabinose or D-xylose that would be required in the culture medium prior to imaging to refractive index the Nafion™ soil (Figure 4.9). A final concentration of 5.1% (w/v) D-xylose or 3.8% (w/v) D-arabinose supplemented in SM<sub>L-arabinose</sub> was required to refractive index match Nafion™ soils for

*B. subtilis* imaging. The lower concentration and cost resulted in D-arabinose being selected as the most appropriate refractive index matching medium for observing colonisation of *Bacillus spp.* in an optically transparent mimetic soil environment.

#### **4.3.2.3 Comparing commercial colloid silica and sugar refractive index matching preparations**

The refractive index of Percoll<sup>®</sup> was measured at different concentrations to demonstrate the benefits of using sugar-based correcting solutions over commercial silica preparations for refractive index matching. A refractive index curve of Percoll<sup>®</sup> at different concentrations was created and compared to the refractive index for Nafion<sup>™</sup>. Again, the equation of the trendline was used to determine the final concentration of Percoll<sup>®</sup> that was required to match the refractive index of Nafion<sup>™</sup> (Figure 4.10). A final concentration of 35% (v/v) Percoll<sup>®</sup> was required to refractive index match Nafion<sup>™</sup> soils. The lower refractive index of neat Percoll<sup>®</sup> resulted in higher concentrations required, meaning that large quantities would be required compared to less costly sugar solutions.

#### **4.3.3 Assessing the autofluorescence of transparent soils**

The autofluorescence of Nafion<sup>™</sup> soils was assessed using a conventional upright laser scanning confocal microscope and the Mesolens in widefield epifluorescence mode using the same acquisition settings used for bacterial imaging. As the test strains expressed GFP, the autofluorescence of Nafion<sup>™</sup> was measured at an excitation wavelength of 488 nm. Several Nafion<sup>™</sup> treatments were screened, where the soils had been titrated with YEME or SM medium, or sulphorhodamine-B-labelled soils which were reprocessed to recycle the particles and remove the stain from the surface of the soil particle.

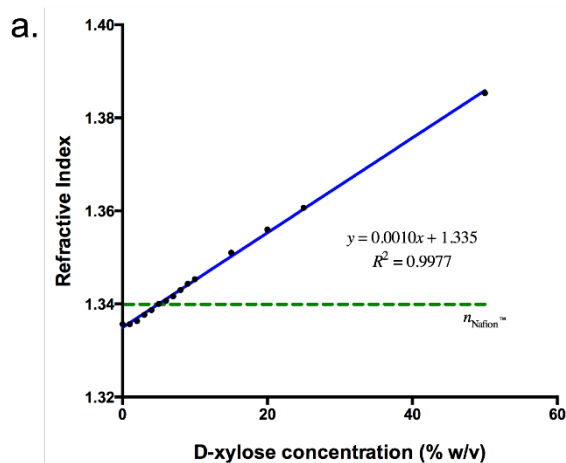
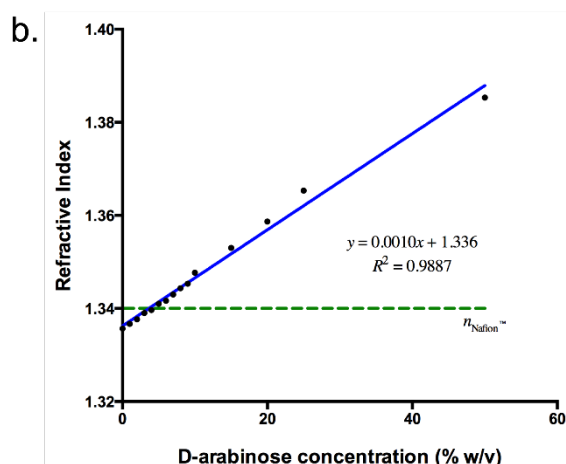


**Figure 4.9. Refractive index curves of D-xylose and D-arabinose for Nafion™ refractive index matching.**

**(a)** The refractive index of a range of D-xylose concentrations in SM medium compared to the refractive index of Nafion™. A concentration of 5.1% was required for refractive index matching.



**(b)** The refractive index of a range of D-arabinose concentrations in SM medium compared to the refractive index of Nafion™. A concentration of 3.8% was required for refractive index matching.

$n = 3$ , error bars show the standard error of the mean.

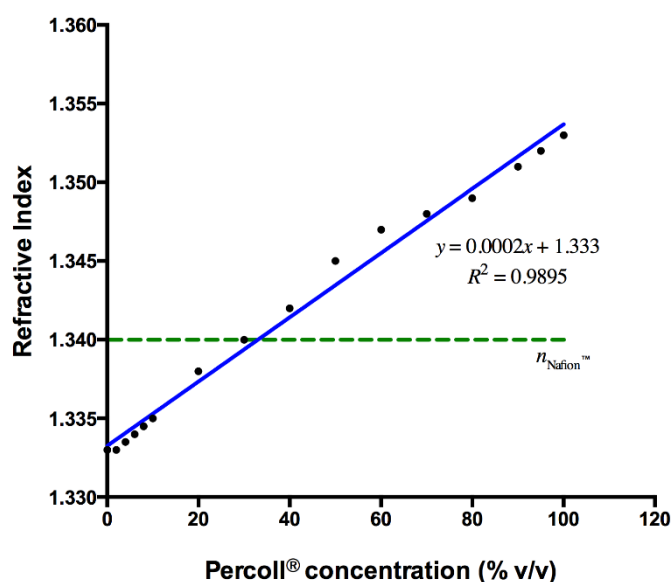


**Figure 4.10. Refractive index curve of Percoll® for Nafion™ refractive index matching.** The refractive index of various concentrations of Percoll®. The refractive index of Nafion™ (1.34) is also shown, with a concentration of 35% Percoll® (v/v) required for refractive index matching.  $n = 3$ , error bars show the standard error of the mean.



The autofluorescence emission of Nafion™ soils were first measured on a conventional confocal laser scanning microscope. Reflection imaging was also carried out to determine the success of refractive index matching, where all soils were matched using 6.6% sucrose (w/v) (Figure 4.11). Fluorescence and reflection imaging of all soil treatments revealed no observable autofluorescence signature or reflection boundaries, indicating that the soil particles had been well refractive index matched

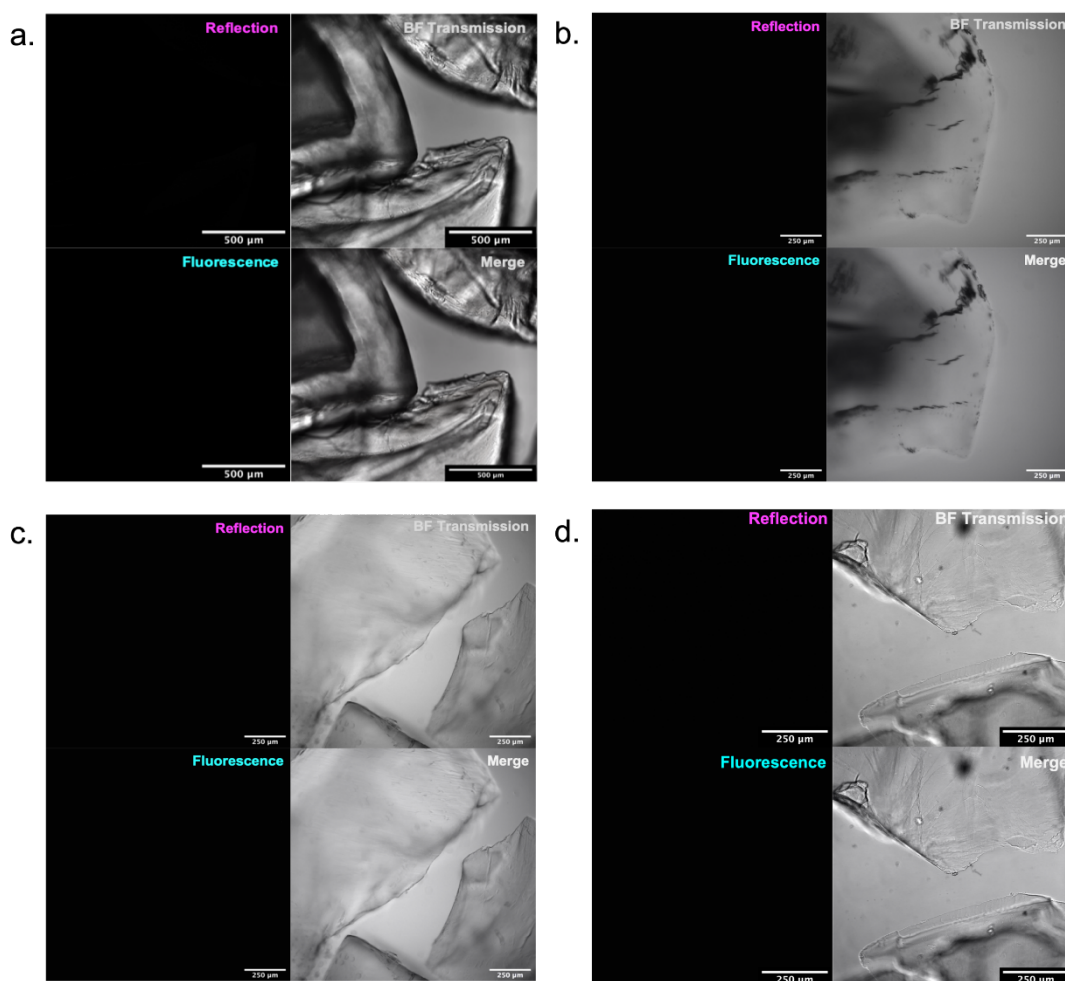


**Figure 4.11. Autofluorescence emission and reflection imaging of Nafion™ soils by confocal laser scanning microscopy.** Reflection (magenta), autofluorescence at  $\lambda_{ex.} = 488$  nm (cyan) and brightfield transmission imaging of Nafion™ soil particles following various treatments. Soils are immersed in a 6.6% sucrose solution. **(a)** naïve milled and chemically processed soil. **(b)** Reprocessed particles which were previously stained with sulphorhodamine-B. **(c)** YEME-titrated soil particles. **(d)** SML-arabinose-titrated soil particles.

and that autofluorescence emission was low when using a conventional confocal microscope at 488 nm excitation. Brightfield transmission images revealed similar features in the soil particles as observed by fluorescent imaging of sulphorhodamine-B stained particles in Figure 4.6.

Autofluorescence emission was also observed using the Mesolens in widefield epifluorescence mode. Autofluorescence emission was observed in all soil treatments when imaged using the Mesolens; however, recycled sulphorhodamine-B-stained and YEME-titrated particles appeared to have the highest autofluorescence intensity of those tested (Figure 4.12). The autofluorescence observed in recycled particles was likely due to left over dye that had bound to the surface of the Nafion™ particles (Figure 4.12b). Autofluorescence of YEME-titrated particles was likely due to the presence of yeast extract in the nutrient medium which fluoresced under 488 nm excitation (Figure 4.12c). To quantify the autofluorescence emission of Nafion™ soils imaged using the Mesolens, the mean intensity was first recorded over multiple ROIs for each sample (Figure 4.13a), before the autofluorescence intensities were normalised to the maximum dynamic range of the camera sensor (0 – 4095 AU) (Figure 4.13b). Quantification of Nafion™ autofluorescence under the Mesolens confirmed that recycling fluorescently labelled particles was not sufficient to remove all fluorescent dye from the particle surface, and that yeast extract-based growth media were not suitable for optical imaging of transparent soils using the Mesolens. Autofluorescence was also detected in naïve and SM-titrated soils, although it was lower than the YEME-titrated soils. The fluorescence from these treatments was not detected using a conventional microscope, and only observed using the Mesolens. This is due to the relationship between numerical aperture and magnification which means that the optical throughput is approximately 25 times higher with the Mesolens compared to a conventional microscope at comparable magnification<sup>111</sup>.

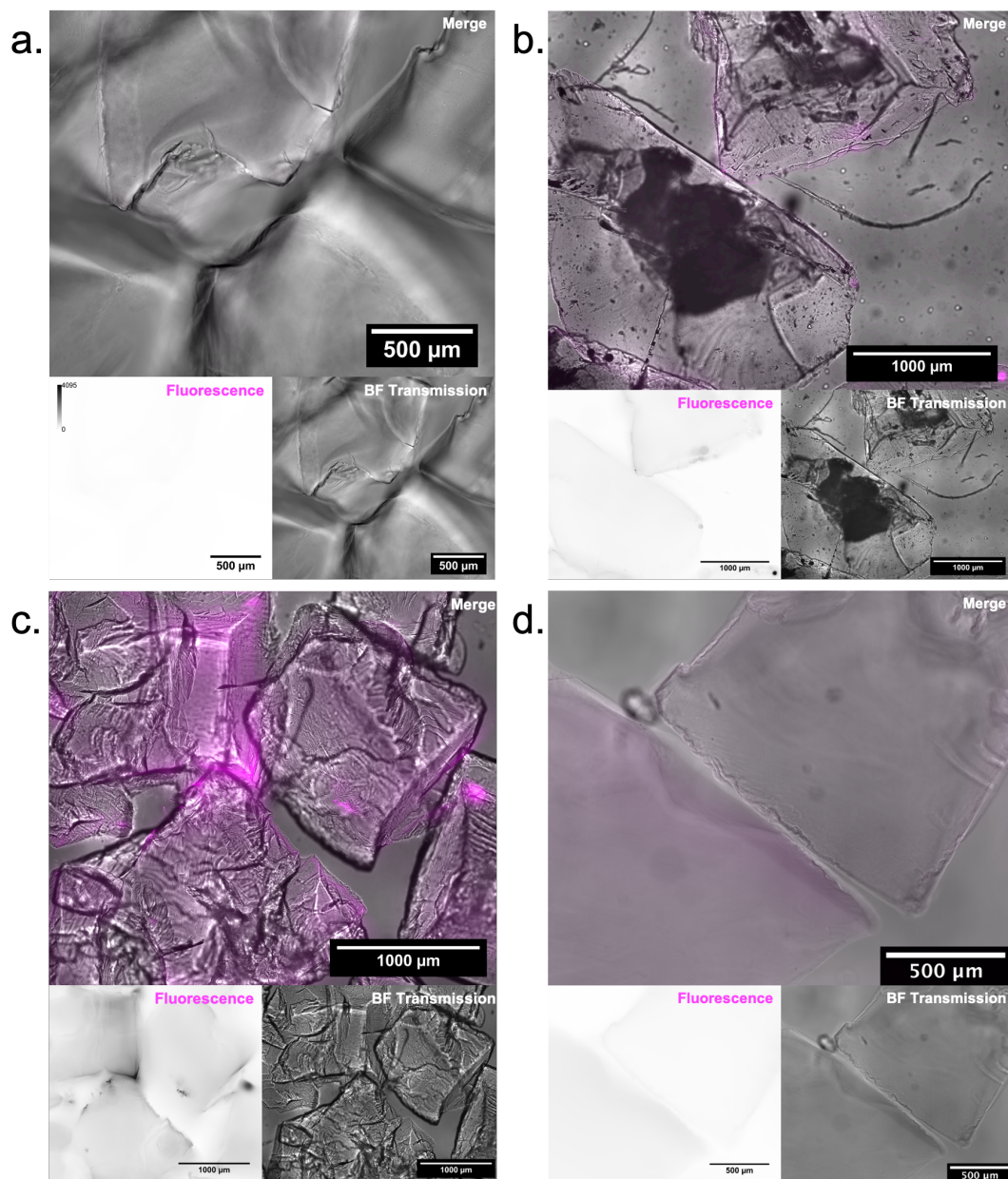


**Figure 4.12. Autofluorescence emission of Nafion™ soils by widefield mesoscopy.**

Autofluorescence at  $\lambda_{\text{ex.}} = 488 \text{ nm}$  (magenta) and brightfield transmission imaging of Nafion™ soil particles following various treatments. Soils are immersed in a 6.6% sucrose solution. Fluorescence images are presented with an inverted LUT due to the low levels of autofluorescence and a corresponding calibration bar is presented in (a). **(a)** naïve milled and chemically processed soil. **(b)** Reprocessed particles which were previously stained with sulphorhodamine-B. **(c)** YEME-titrated soil particles. **(d)** SM<sub>L</sub>-arabinose-titrated soil particles.

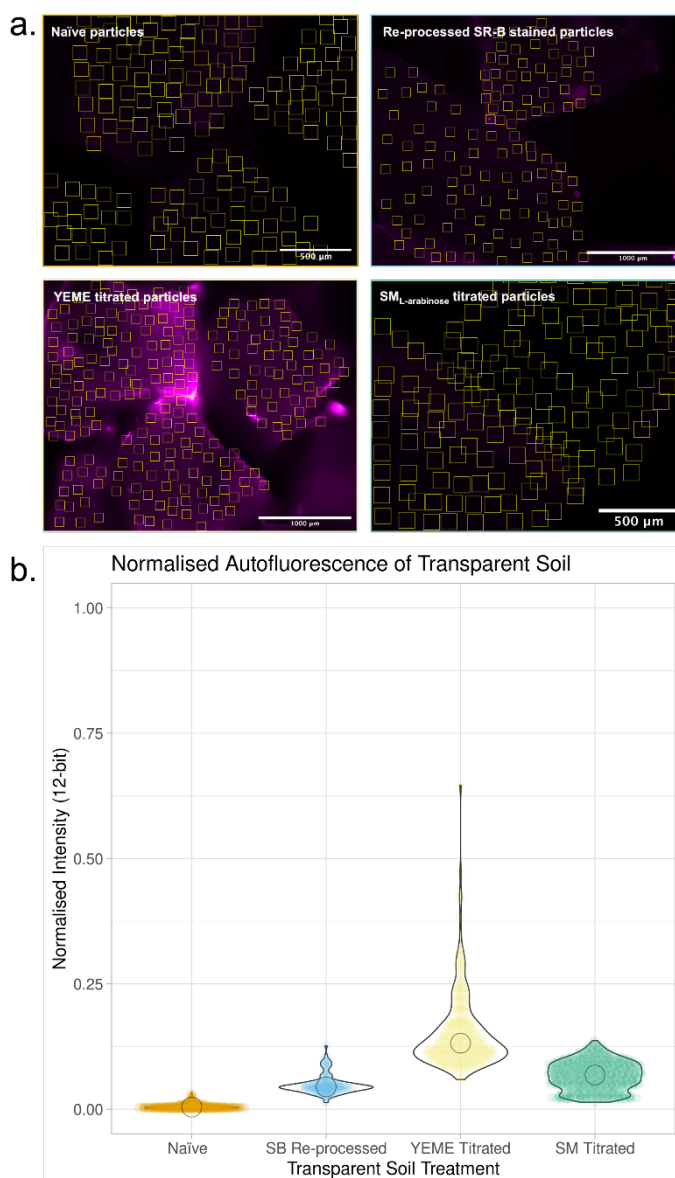


**Figure 4.13. Quantitative analysis of Nafion™ soil autofluorescence using the Mesolens. (a)** Representative ROIs drawn over the surface of soil particles. The mean fluorescence intensity was measured in each ROI and normalised to the dynamic range of the camera. **(b)** The normalised autofluorescence intensity of Nafion™ soils with various treatments. The mean intensity of each ROI is presented and shows that the YEME-treated soils had the highest autofluorescence intensity at  $\lambda_{\text{ex.}} = 488 \text{ nm}$ .  $n_{\text{Naïve}} = 497$ ,  $n_{\text{Reprocessed}} = 122$ ,  $n_{\text{YEME}} = 220$ ,  $n_{\text{SM}} = 420$ . All ROIs were taken over three technical replicates.

#### 4.3.4 Colonisation phenotypes of soil bacteria in a mimetic 3D environment

##### 4.3.4.1 Growth behaviour of Streptomyces in transparent soil

*Streptomyces coelicolor* was grown in a mimetic transparent soil environment after optimising the nutrient titration and refractive index matching methods for



Streptomyces imaging. Following growth in refractive index matched SMM<sub>L-arabinose</sub>-titrated soil, M145-*idh-gfp* was visualised using the Mesolens in widefield mode. The growth behaviour in transparent soil was found to be different compared to conventional growth methods as presented in Figure 4.4. Instead of forming differentiated mycelia, M145 formed microcolonies, measuring approximately 100  $\mu\text{m}$  in diameter, between soil particles or in crevices along the surface of particles (Figure 4.14). Each of these pellets likely formed from a single progenitor spore. The

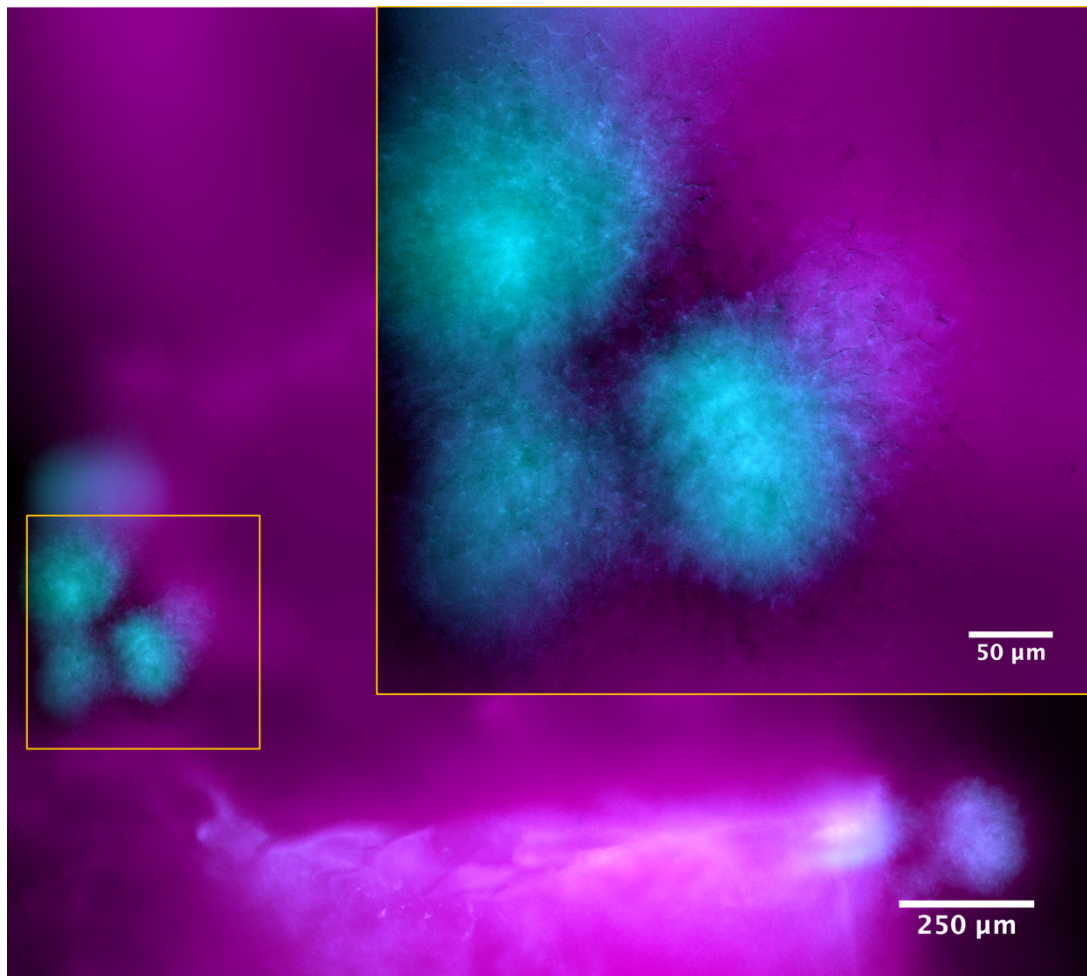


**Figure 4.14. Streptomyces grow as hyphal pellets in a transparent soil environment.** M145-*idh-gfp* does not form a differentiated mycelium when grown in a mimetic soil environment. Instead, colonies of *S. coelicolor* (cyan) grow between or along the edge of soil particles. A magnified ROI is presented showing individual hyphae emerging from dense pellets which have grown at the edge of a soil particle (magenta).

autofluorescence of the soil particles excited at 435 nm was used to show the position of the soil particles in reference to the M145 cells.

#### 4.3.4.2 Growth behaviour of *Bacillus subtilis* in transparent soil

Growth of *B. subtilis* J WV042 in a transparent soil environment after 48 hours was initially visualised by widefield epifluorescence mesoscopy. Widefield mesoscopy revealed that *B. subtilis* exhibited two main colonisation phenotypes (Figure 4.15). *Bacillus subtilis* was observed to either form a mono-dispersed layer of cells which enveloped the entire surface of the soil particle (Figure 4.15a) or would form distinct

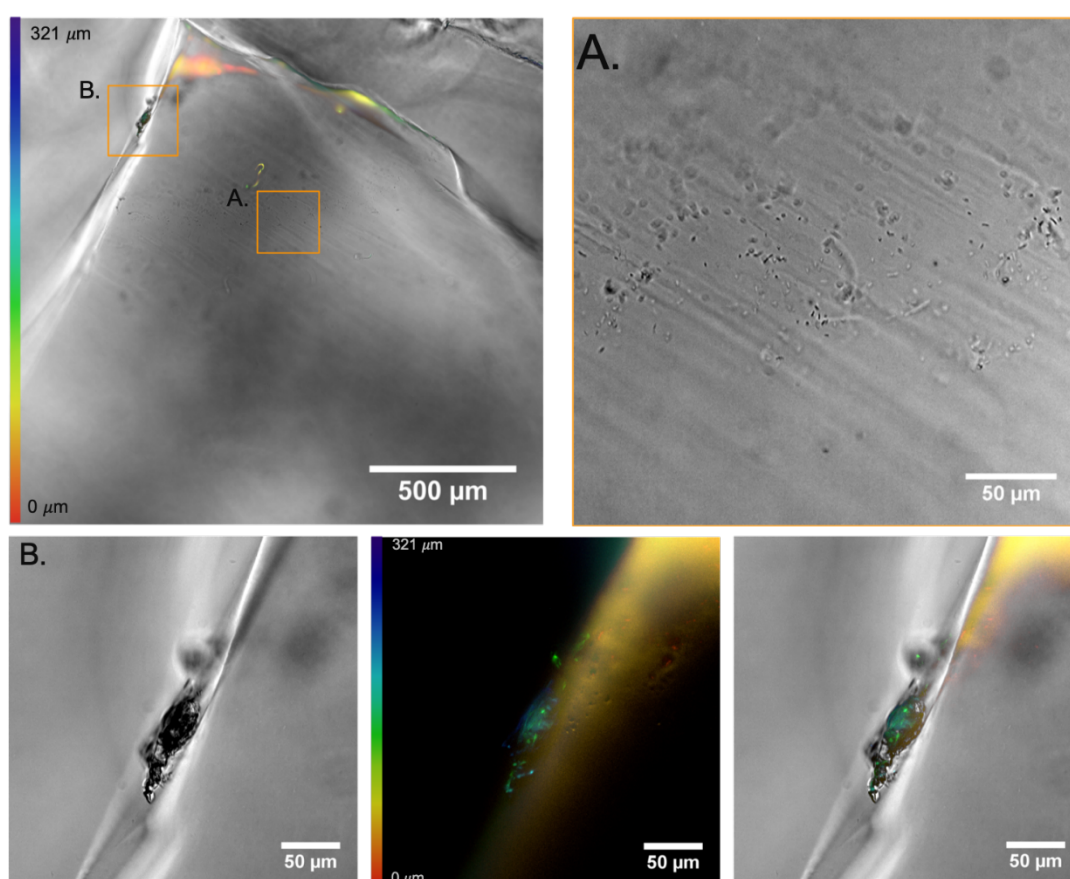


**Figure 4.15. *Bacillus subtilis* colonises mimetic soil environments using two different behaviours.** A maximum intensity z projection of an SM<sub>L</sub>-arabinose-titrated Nafion™ soil particle where GFP emission from J WV042 is merged with brightfield transmission of the soil particle. Cells will colonise the soil particle by one of two methods; **(a)** by forming a layer of individually spaced cells across the surface of the particle, or **(b)** by forming biofilms at the edge or in a crack on the surface of a transparent soil particle.

biofilms around the crevasses and cracks along the surface of soil particles (Figure 4.15b). Few planktonic cells were observed in the interstitial space between soil particles. In either case, individual cells could be resolved using the Mesolens in transmission mode, however detection of GFP was more difficult by widefield epifluorescence. This was especially true of well-spaced single cells, where the GFP signal was so low compared to the background of the rest of the image. Therefore, brightfield transmission images were used to observe the colonisation of individual cells more reliably.

Confocal laser scanning mesoscopy was then used to verify these colonisation phenotypes by acquiring high resolution 3D images of entire soil particles colonised by bacteria. Confocal imaging revealed the same colonisation behaviours by *B. subtilis* in a mimetic transparent soil environment that had been observed by widefield epifluorescence (Figure 4.16). These data confirm that, when grown in a 3D soil-like environment, *B. subtilis* does not form multi-millimetre scale colonial biofilms or exist as free-living planktonic cultures, but instead it colonises the surface of nutrient-imbibed soil particles as a monolayer of cells or in biofilms in cracks along the surface of soil particles.

An inoculum was taken from the transparent soil following 48 hours and used to show that cells were viable while cultured in a transparent soil environment. A phenotypic comparison between JWV042 before and after culture in transparent soil was achieved by assessing morphology, *gfp* expression and the ability of the strain to grow on selective antibiotics (Figure 4.17a). Following growth in transparent soil, *B. subtilis* JWV042 was found to have retained chloramphenicol resistance, *gfp* expression, swimming motility, and possessed the same cellular and colonial morphology (Figure 4.17b). Thereby the bacteria must remain viable in the mimetic soil environment. While the cells remain viable in the transparent soil environment, it remains unclear if

they are actively growing (albeit slowly) or exist in a dormant state. Dormancy in *Bacillus* spp. usually results in spore formation and is triggered by high levels of oxygen. No spore formation was observed in the image data and it is unlikely that sporulation would be triggered since the cultures were immersed and static for long incubation periods. Therefore, this form of dormancy can be excluded. A growth curve could be performed using a fluorescent plate reader in order to determine if the cells were actively growing in the transparent soil.

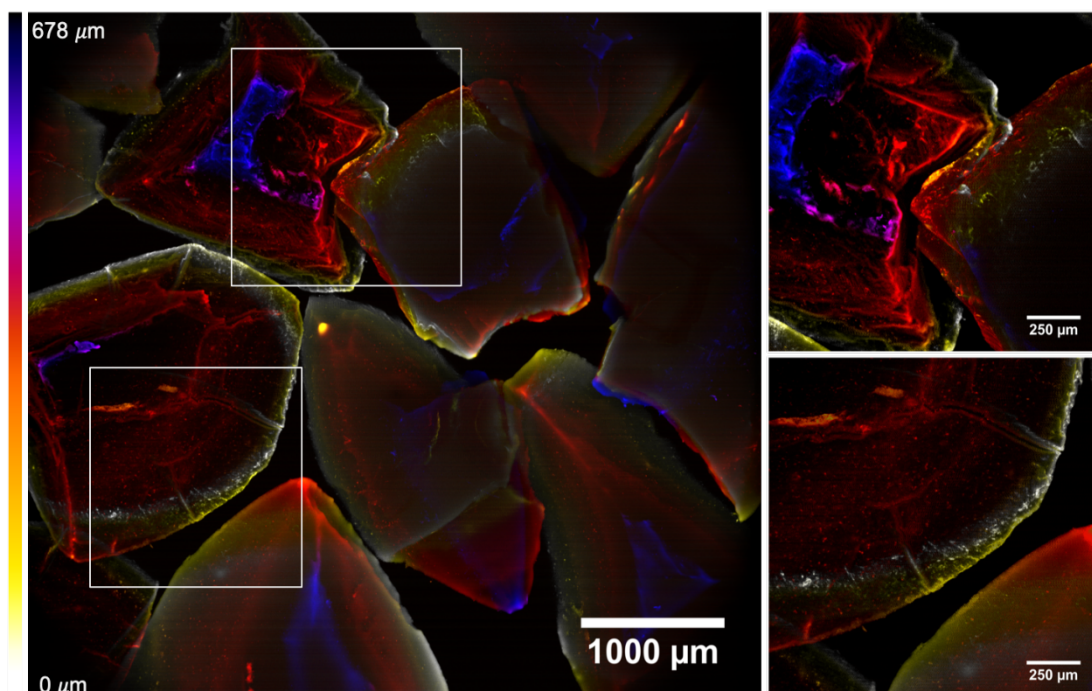


**Figure 4.16. Confocal mesoscopy confirms the two colonisation methods used by *Bacillus subtilis* in a mimetic soil environment.** A maximum intensity projection of a series of transparent soil particles colonised by JWV042. Selected ROIs show that biofilms form at the vertices of soil particles, and individual cells form a monolayer which enveloped whole particles. Low level autofluorescence from the soil particles was also detected which showed the location of the particles, however the individual bacteria are clearly visible on the surface of the particles. The colour coded LUT shows was applied to each optical section depending on its axial position within the dataset.



These data confirm that transparent soil is an effective alternative 3D culture method for studying the behaviour of soil bacteria *in situ*. The colonisation phenotypes of both Actinomycetes and Firmicutes in transparent soils show that bacteria do grow differently compared to conventional laboratory techniques. This work concludes that Nafion™ transparent soils can be taken forward to better understand processes such as competition, antibiotic production and sporulation in a microscope-compatible mimetic environment.

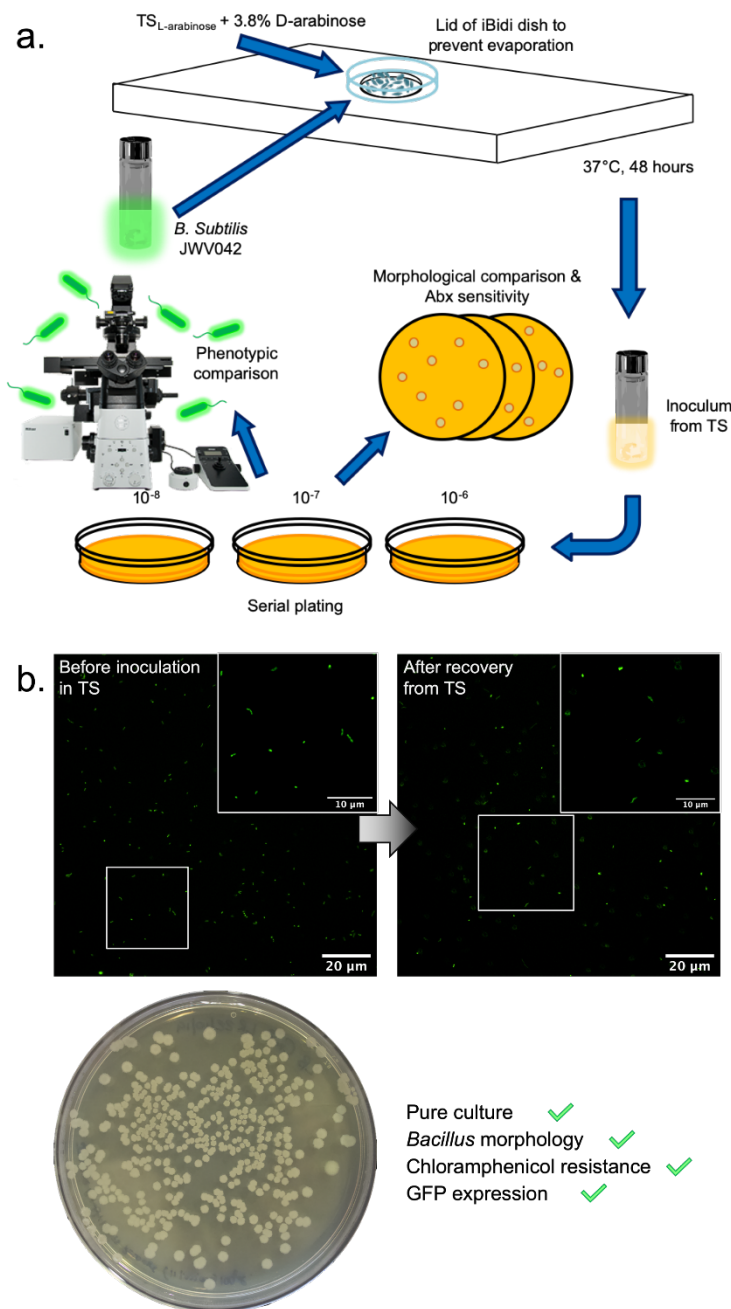


**Figure 4.17. Bacteria remain viable when cultured in a transparent soil environment.** (a) A schematic detailing the methods used to recover bacteria from a transparent soil environment, phenotypic screening and assessment of their viability. (b) *B. subtilis* retained its *gfp* expression and swimming motility in liquid culture following growth in transparent soil. JWV042 was also able to grow on medium supplemented with chloramphenicol and possessed the same colonial and cellular morphology as conventionally cultured *B. subtilis*.

## 4.4 Discussion

*Streptomyces* and *Bacillus* spp. are widely studied Gram-positive microorganisms, and their ability to produce specialised metabolites by environmental and chemical elicitation has been well documented<sup>413,432–438</sup>. The most common way of triggering secondary metabolism and production of specialised metabolites is through chemical elicitation<sup>395</sup>. Previous studies have used a wide range of elicitors from N-acetylglucosamine<sup>439,440</sup>, to solvents and heavy metals<sup>441–444</sup>, to rainwater<sup>445</sup>. The aim of this chapter was to develop and optimise a 3D mimetic culture system for soil bacteria which would be compatible with existing optical microscopy setups. Previous studies have suggested that the triggering of secondary metabolism and production of specialised metabolites can be caused by the culture environment itself. For example, it has been previously shown that Actinobacteria undergo a metabolic switch when cultivated in a liquid environment and produce novel specialised metabolites which are not observed when grown on solid substrates<sup>446</sup>. Furthermore, clumping in liquid media can result in either a positive or negative change in the expression level of antimicrobials, depending on the specific molecule<sup>396–400</sup>, suggesting that the growth behaviour is important for specialised metabolite production. Culture-dependent elicitation of specialised metabolites has also been documented in *B. subtilis* where, for example, cell density and quorum sensing play a part in elicitation of the lanibiotic peptide, subtilin<sup>352,433</sup>.

The mammalian cell biology field have used 3D culture methods for the past 15 years with the aim of creating a more mimetic environment to elicit new behaviours which were previous unreported by conventional culture methods. Biocompatible collagen scaffolds which mimic the basement membrane have been used extensively for tissue engineering<sup>329–331</sup>, and have been developed commercially as Cultrex® (Sigma Aldrich, USA), Matrigel® (Corning Inc., USA) and Geltrex® (ThermoFisher, USA).

Alternative cellulose-based matrices have also been used as 3D culture environments to study the proliferation of mammalian cells in an extracellular matrix-like environment<sup>332</sup>. Various hydrogel substrates have also been used to mimic the structure of mammalian tissue and are typically composed of alginate or polyethylene glycol polymers<sup>333–336</sup>. Microfluidic platforms have also appeared, such as the Lab-on-a-chip<sup>337</sup>, which provide a flow environment for cells to grow in which perfusion of different nutrients and drugs. All of these 3D culture methods have shown novel behaviours of mammalian cells compared to when grown by conventional methods. However, despite the novel behaviours the uptake of 3D culture methods in the field of microbiology has been slow.

To address this knowledge gap, a 3D culture method using transparent soil was created specifically for bacterial culture. Following particle refinement and chemical processing, a Nafion™-based soil was developed which could be visualised by optical microscopy. The chemical processing methods were based on that of Van Nguyen *et al.* (2007) and Downie *et al.* (2012), which have worked well for creating biocompatible Nafion soils for plant growth<sup>206,422</sup>. Therefore, these methods were a logical step for optimising a biocompatible medium specifically for bacterial growth. The importance of processing steps lay in ensuring that nutrients were available on the surface of soil particles and the pH of the soils was stable. The latter is especially important for *S. coelicolor* culture as these bacteria are sensitive to changes in pH and struggle to grow out with pH 6.5 – 8.0<sup>375</sup>. To account for this, the pH of the soil eluent was measured every 30 minutes and between washes during nutrient titration. This allowed monitoring of the pH over time, and also indicated when nutrients were completely adsorbed onto the surface of the Nafion™ particles and the SO<sub>3</sub>H<sup>+</sup>-groups were saturated. In turn, this meant that the pH should remain stable during bacterial growth.

So as to visualise the bacteria on the surface of the particles, they were rendered transparent by refractive index matching with sugar solutions. The concentration of sugars required would not have triggered osmotic stress as many routine growth media recipes up to 5-fold higher concentrations<sup>375</sup>. Aside from the lower cost of using sugars compared to commercial silica preparations, the sugar solutions had a constant refractive index throughout the entire volume, whereas silica preparations will partition overtime resulting in layers of different refractive index according to the particle size distribution of the silica solution<sup>447,448</sup>.

A previous study by Ernebjerg & Kishony discussed that many methods could improve the culturability and widen the variety of behaviours observed by growing bacteria in mimetic, low nutrient, natural environments<sup>449</sup>. Despite this call, very few routine mimetic culture methods are used in microbiology. Sterilised soil has been used to grow viable but non-culturable cells<sup>450–452</sup>, but due to the high autofluorescence and opacity of environmental soil samples they are not applicable for fluorescence microscopy. One recent study used a correlative confocal/MALDI-MSI (Matrix-Assisted Laser Desorption/Ionization-Mass Spectrometry Imaging) approach to investigate the spatial distribution of chitin degrading soil fungi by incubating glass slides in a soil environment; however, the spatial resolution was poor and only *en masse* observations were reported<sup>417</sup>. Other lesser used 3D culture methods in microbiology include the use of fibreglass scaffolding to promote biofilm formation<sup>453,454</sup> and polyethylene glycol-based hydrogels for mimetic chronic wound modelling<sup>156</sup>, however these have not been used routinely. This work provides a platform for understanding the colonisation of bacteria in their natural environment, where new spatiotemporal colonisation behaviours can be studied using available microscopical methods. The work presented here could therefore be easily adopted

by other users to understand if 3D culture environments can elicit novel metabolite production or behaviours, as has been shown in mammalian cells.

The findings documented in this chapter describe the colonisation phenotypes of two different soil-dwelling bacteria and has provided a method which can be taken forward for further study to look for novel behaviours and metabolic elicitation from growth in a 3D environment. Although both *S. coelicolor* and *B. subtilis* are designated as obligate aerobes, both strains have been commonly isolated from anaerobic environments such as marine sediments and stagnated water sources. Therefore, although culturing these strains in a static environment which may be oxygen limited over time, they are clearly able to maintain their viability during incubation (as shown in Figure 4.17). One limitation of this study lies in that aerobic behaviours may be overlooked when grown in a static culture environment. A potential workaround could be the introduction of microfluidics to refresh spent growth medium with oxygen-rich growth medium, mimicking conditions in a riverbed for example. However, it is important to note that, as discussed earlier, elicitation of secondary metabolite production and other interesting processes often happen under stress conditions, and so perhaps partial oxygen limitation would be of benefit for studying these behaviours using the current transparent soil platform.

Previous studies using transparent soil have mainly focused on plant growth and root tip dynamics using conventional confocal laser scanning and lightsheet microscopy<sup>206,455</sup>. Alternatively, when studies have used transparent soil with bacterial specimens, they have used plant roots as colonisation surfaces, while the soil is designed purely to maintain plant viability<sup>206,207</sup>. To this end, the colonisation behaviour of rhizospheric bacteria has been studied extensively in relation to plant root systems, and often with clinical isolates rather than environmental isolates<sup>409,456–</sup>

<sup>461</sup>. Therefore, this work is the first to describe a culture technique consisting of an optically transparent mimetic soil environment specifically designed for bacteria.

While this system has been fabricated and fully optimised for two bacterial phyla, a number of possible future experiments could be carried out to continue this work. The spatial distribution of soil bacteria *in situ* remains unknown, and quantitative image analysis of transparent soil microcosms would provide a more robust overview of how bacteria colonise their ecological niche. This could be achieved using cell segmentation and fluorescence intensity analysis methods to quantify the distribution of cells throughout a 3D transparent soil specimen. Moving forward, it would be interesting to test the viability of other soil dwelling bacteria in this environment. With culture methods for *Streptomyces spp.* and *Bacillus spp.* already optimised, transparent soil environments for other species could be developed. For a new system, the sugar auxotrophies would need to be first determined, and a yeast extract-free minimal medium identified for the test strain. The soil could then be refractive index matched using the auxotrophic sugar and the same growth and imaging methods could be adopted for any optical microscope to study the colonisation behaviours of other bacteria. Phenomena such as biofilm formation, bacterial motility, and inter-kingdom interactions between bacteria and fungi, protists, helminths, or amoebae could all be studied in a mimetic environment. Moreover, it has yet to be established if 3D culture results in any metabolic triggers which elicit the production of specialised metabolites. This could be investigated by assessing the bioactivity of bacteria grown in a transparent soil environment compared to conventional culture methods, or by comparing the transcriptome by RNA-sequencing of bacteria grown under each condition. Additionally, strain-to-strain interactions could be studied in a transparent soil environment to better understand the spatial

distribution of competing bacteria and the role that competition plays in specialised metabolite production.

## 4.5 Conclusions

This chapter has documented the production and optimisation of a mimetic 3D transparent soil culture environment for soil bacteria. This was the first transparent culture platform optimised specifically for bacteria, and the methods presented here could easily be adapted for use with other genera. This chapter has focused on the application of transparent soil for the study of microbial ecology, however, there remains a number of open avenues for which 3D bacterial culture could be used. This culture system was developed by freeze-fracturing and chemically processing Nafion™ precursor particles for culture of Actinobacteria and Firmicutes in a mimetic soil environment. This method showed distinct colonisation phenotypes which were not observed by routine laboratory culture methods while maintaining bacterial viability and was easily adaptable to conventional and custom optical imaging setups. *Bacillus subtilis* was found to envelope soil particles in a mono-dispersed layer of cells and formed discrete biofilms along the vertices of soil particles, while *S. coelicolor* was observed to form small dense pellets in-between soil particles. The system is easily coupled into any optical microscopy setup, and a method is provided to generate transparent soil in large volumes specifically for bacterial culture. This transparent soil platform stands a viable resource which could be taken forward to understand how bacteria behave in the environment, and could be extended to study bacterial interactions, spatiotemporal dynamics and production of specialised metabolites and microbial natural products.

# **Chapter 5**

## **Concluding remarks and recommendations for future work**

This Chapter provides a summary of the work described in Chapters 2, 3 and 4, and provides context to the findings. Several recommendations for future work are also made for the results presented in each Chapter.



## 5.1 Summary

The work presented in this thesis converged on the application of novel microscopical methods to the field of microbiology. This was achieved by the development of a new multi-wavelength confocal variant of IRM which was applied for the first time to live and unlabelled bacterial cells, the application of the Mesolens to understand bacterial community structure, and the development of a transparent soil system to better study the behaviours of bacteria in the natural environment.

In Chapter 2, the long-standing theory that bacterial gliding motility was a purely lateral phenomenon was challenged by means of interference reflection microscopy. A new approach to this underused microscopy method was developed, where multiple wavelengths of incident light were used to fill the information gap between the interference maxima present in IRM images. This had the additional benefit of providing axial directionality due to the spectral separation of the two reflected wavelengths along the optical axis of the microscope. To reliably comment on the gliding behaviours of *M. xanthus*, a model lens specimen was first characterised using multi-wavelength confocal IRM. Analysis of the lens specimen showed that this new IRM method was capable of yielding 3D information about the specimen geometry below the diffraction limit in the  $z$ -dimension. Following characterisation of the model specimen, an image correction workflow to correct inhomogeneous background signal was developed in collaboration with Lisa Kölln (University of Strathclyde). This allowed for more reliable analysis of IRM image data. Bacterial imaging revealed that *M. xanthus* displayed multiple asynchronous oscillatory gliding behaviours, which would have otherwise been undetectable using other methods. The mechanisms behind these behaviours was investigated using deleterious motility mutants. The findings showed that PMF-driven mechanics (via AglQ) were not responsible for the behaviours. The role of Type IV pili was also investigated, however these mutants

were unable to adhere to the solid glass substrate, and so were unobservable by IRM. A correlative TIRF-IRM method was proposed to study pilus-mediated dynamics in gliding motility.

Chapter 3 described the identification and characterisation of a previously undocumented intra-colony channel network in *E. coli* biofilms. These channel networks were investigated using the Mesolens, which was capable of imaging large specimens at sub-cellular resolution without additional processing. Following a structural screening, the biofilm channels were found to be filled with proteins and devoid of any other tested structural component. After disruption of the channels, they were found to reform following subsequent recovery of the colony, which was indicative of intra-colony channels being an emergent property of biofilm formation in *E. coli*. These channels were also found not to cross between founder populations, despite the use of isogenic strains. The functional role of the channels was first explored by attempting to direct the flow of soluble fluorescein into the channels. However, fluorescein was found to be an unreliable method to assess this. Fluorescent microspheres were observed in the channels of mature colonies, indicating that they may be responsible for directing the flow of substances into and out of the colony. Their hypothesised role in nutrient uptake was tested using a fluorescent arabinose biosensor, which showed that a higher concentration of arabinose was found within the channel system compared to elsewhere in the biofilm. The uptake mechanism was further tested to determine if antimicrobial agents could penetrate macro-colonies via intra-colony channels. After identifying a suitable candidate compound (colistin), the channels were found to have a higher proportion of non-viable cells surrounding them compared to a vehicle control. The culmination of these findings presented intra-colony channels as a conduit for the uptake of

substances from the external environment, which has been completely undocumented until now.

Finally, in Chapter 4, the technological gap of 3D cell culture methods in microbiology was addressed by the production and optimisation of a transparent soil environment specifically designed for bacterial culture. Two representative soil genera were selected for this study, and transparent soils were tailored for each. The soil was manufactured from freeze fractured Nafion™ polymer resins and chemically processed to infer a negative charge onto the surface of the particles. This allowed binding of cations from bacterial growth media onto the surface of the milled Nafion™ particles. The soils were then rendered transparent by refractive index matching with a determined concentration of an un-metabolisable sugar prior to inoculation, incubation and subsequent imaging. Again, the Mesolens was selected to image bacteria in this synthetic soil system to take advantage of the large field of view and high spatial resolution. The findings presented in Chapter 4 showed that *S. coelicolor* and *B. subtilis* both colonised soil particles by different manners compared to when grown by conventional laboratory culture methods. Cell viability was found to be maintained even after long incubation periods in the synthetic soil environment. As it stands, this proposed new method of culturing bacteria exists as a platform which has been shown to facilitate growth of two distinct bacterial species and could be taken forward to study various aspects of soil ecology.

## **5.2 Recommendations for future work**

The findings presented in Chapters 2, 3 and 4 describe three bacterial phenomena revealed by novel imaging approaches. By their nature, the novelty of these findings presents a number of yet-unanswered questions and possibilities for future research.

The mechanism(s) which govern the previously unobserved 3D motility behaviours in *M. xanthus* are yet to be elucidated. Chapter 2 attempted to study potential mechanisms; however, the gliding behaviours were not found to be linked to one of the major drivers of *Myxococcus* motility, AglQ-mediated PMF. Type IV pili mutants were unable to adhere to the coverglass, and so were unobservable by IRM. Therefore, one cannot rule out T4P extension, attachment and retraction as the cause of the observed behaviours. A novel TIRF-IRM setup was proposed to circumvent this limitation. Wild-type *M. xanthus* could be imaged using this setup, where the T4P machinery is fluorescently labelled. Should any synchronicity be observed between a changing adhesion profile (detected by IRM) and T4P firing (detected by TIRF microscopy), then it would show that the 3D oscillations documented in Chapter 2 are a result of T4P activity. It would also be interesting to image various other bacterial species which are thought to display 3D behaviours using multi-wavelength confocal IRM. For example, the erection of aerial hyphae by *Streptomyces spp.*, or the effects on prey membrane integrity following predation by *Bdellovibrio bacteriovorus*.

The discovery of an intra-colony channel system in *E. coli* opens many possibilities for further study. In addition to those points made in Chapter 3 (Section 3.4), it would be interesting to study a wider range of genera to determine if these structures are conserved between different species. This would also permit investigation into the effect of cell shape on channel formation (for example by imaging coccoid cells). Time-lapse imaging would allow visualisation of channel formation over time but was not achieved by this study. Attempts to image over time resulted in shedding of the colony due to it being submerged in a liquid environment. For time-lapse imaging to be successful the biofilms would likely have to be imaged in air, however at the times of investigation this was not feasible using the Mesolens.

The development of novel culture methods is applicable to almost any microbiological question. Having this technology also compatible with any optical microscope allows for *in situ* visualisation of bacterial behaviours in a 3D environment. Various suggestions of future applications for transparent soil were discussed in Chapter 4 (refer to Section 4.4). These included applying image analysis methods to Mesolens datasets to quantify the colonisation of soil environments by bacteria. Additionally, tailoring the soil environment for culture of different bacterial species was suggested. This would allow for study of a wide range of bacterial behaviours beyond colonisation. Phenomena such as biofilm formation, motility, predation and signalling could all be studied in a mimetic 3D culture medium. Moreover, the use of co-culture assays could be used to study bacterial interactions. These include interactions such competition and mutualism in the natural environment. Interkingdom interactions could also be observed; for example, predation of Streptomyces spores by the amoeboid, *Dictyostelium discoideum*, or recently identified fungal-specific Type VI-mediated killing by *Serratia marcescens*.

The behaviours documented in this thesis span a range of areas in microbiology. However, one commonality which links them is the application of novel imaging methods. The methods used to investigate these phenomena have wide-reaching implications for the microbiology community and also promote the development and use of novel or underused methods to study bacterial behaviour.

*“Right! That’s quite enough of that.”*

Miss Isabelle Gourley

# References

1. Hooke, R., Allestry, J. & Martyn, J. Micrographia: Some physiological descriptions of minute bodies made by magnifying glasses with observations and inquiries thereupon. (Printed by Jo. Martyn and Ja. Allestry, printers to the Royal Society, 1665).
2. Koch, R. The etiology of anthrax, based on the life history of *Bacillus anthracis*. Beiträge zur Biologie der Pflanzen, 2 (2), 277-310.
3. van Leeuwenhoek, A. Part of a letter from Mr Antony van Leeuwenhoek, F. R. S. concerning green weeds growing in water, and some animalcula found about them. Philosophical Transactions of the Royal Society of London **23**, 1304–1311 (1703).
4. Cremer, C. & Masters, B. R. Resolution enhancement techniques in microscopy. The European Physical Journal H **38**, 281–344 (2013).
5. Abbe, E. Beiträge zur Theorie des Mikroskops und der mikroskopischen Wahrnehmung. Archiv f. mikrosk. anatomie **5**, 413–468 (1873).
6. Airy, G. B. On the Diffraction of an Object-glass with Circular Aperture. Transactions of the Cambridge Philosophical Society **5**, 283–291 (1835).
7. Cole, R. W., Jinadasa, T. & Brown, C. M. Measuring and interpreting point spread functions to determine confocal microscope resolution and ensure quality control. Nature Protocols **6**, 1929–1941 (2011).
8. Abbe, E. On the Estimation of Aperture in the Microscope. Journal of the Royal Microscopical Society **1**, 388–423 (1881).
9. Handbook of Biological Confocal Microscopy. (Springer Science & Business Media, LLC, 2006).
10. Nikon Instruments Ltd. The Diffraction Barrier in Optical Microscopy. <https://www.microscopyu.com/techniques/super-resolution/the-diffraction-barrier-in-optical-microscopy>.
11. Webb, R. H. Confocal optical microscopy. Reports on Progress in Physics **59**, 427–471 (1996).
12. Ernst Keller, H. Objective Lenses for Confocal Microscopy. in The Handbook of Biological Confocal Microscopy (ed. Pawley, J. B.) 145–161 (Springer Science & Business Media, LLC, 2006).
13. Sheppard, C. J., Gu, M., Brain, K. & Zhou, H. Influence of spherical aberration on axial imaging of confocal reflection microscopy. Applied Optics **33**, 616–624 (1994).
14. Lang, W. Nomarski Differential Interference-Contrast Microscopy. 8 (1969).
15. Zernike, F. How I Discovered Phase Contrast. Science **121**, 345–349 (1955).
16. Davidson, M. W. Configuring a microscope for koeller illumination. <http://zeiss-campus.magnet.fsu.edu/articles/basics/kohler.html>.
17. Murphy, D. B. Phase contrast microscopy and dark-field microscopy. in Fundamentals of light microscopy and electronic imaging 97–116 (John Wiley & Sons, 2002).

18. Johnson, S. A. Phase Contrast Microscopy. in Biomedical Optical Phase Microscopy and Nanoscopy 3–18 (Elsevier Inc., 2012).
19. Allen, R. D., David, G. B. & Nomarski, G. The zeiss-Nomarski differential interference equipment for transmitted-light microscopy. *eitschrift fur wissenschaftliche Mikroskopie und mikroskopische Technik* **69**, 193–221 (1969).
20. Murphy, D. B. Differential interference contrast (DIC) microscopy and modulation contrast microscopy. in Fundamentals of light microscopy and electronic imaging 153–168 (John Wiley & Sons, 2002).
21. Heimstädt, O. Das Fluoreszenzmikroskop. *Zeitschrift fur wissenschaftliche Mikroskopie und mikroskopische Technik* **28**, 330–337 (1911).
22. Haitinger, M. Die Fluoreszenzanalyse in der Mikrochemie. (E. Haim, 1937).
23. Coons, A. H., Creech, H. J., Jones, R. N. & Berliner, E. The demonstration of pneumococcal antigen in tissues by the use of fluorescent antibody. *Journal of Immunology* **45**, 159–170 (1942).
24. Coons, A. H. & Kaplan, M. H. Localisation of antigen in tissue cells II. Improvements in a method for the detection of antigen by means of fluorescent antibody. *Journal of Experimental Medicine* **91**, 1–13 (1950).
25. Vogelsang, J. et al. A Reducing and Oxidizing System Minimizes Photobleaching and Blinking of Fluorescent Dyes. *Angewandte Chemie International Edition* **47**, 5465–5469 (2008).
26. Ishikawa-Ankerhold, H. C., Ankerhold, R. & Drummen, G. P. C. Advanced Fluorescence Microscopy Techniques—FRAP, FLIP, FLAP, FRET and FLIM. *Molecules* **17**, 4047–4132 (2012).
27. Tsien, R. Y., Ernst, L. & Waggoner, A. S. Fluorophores for Confocal Microscopy: photophysics and Photochemistry. in *The Handbook of Biological Confocal Microscopy* (ed. Pawley, J. B.) 338–352 (Springer Science & Business Media, LLC, 2006).
28. Shimomura, O., Johnson, F. H. & Saiga, Y. Extraction, Purification and Properties of Aequorin, a Bioluminescent Protein from the Luminous Hydromedusan, Aequorea. *Journal of Cellular and Comparative Physiology* **59**, 223–239 (1962).
29. Chalfie, M., Tu, Y., Euskirchen, G., Ward, W. W. & Prasher, D. C. Green fluorescent protein as a marker for gene expression. *Science* **263**, 802–805 (1994).
30. Giepmans, B. N. G. The Fluorescent Toolbox for Assessing Protein Location and Function. *Science* **312**, 217–224 (2006).
31. Maekawa, M. & Fairn, G. D. Molecular probes to visualize the location, organization and dynamics of lipids. *Journal of Cell Science* **127**, 4801–4812 (2014).
32. Shaner, N. C., Steinbach, P. A. & Tsien, R. Y. A guide to choosing fluorescent proteins. *Nature Methods* **2**, 905–909 (2005).
33. Heim, R., Prasher, D. C. & Tsien, R. Y. Wavelength mutations and posttranslational autooxidation of green fluorescent protein. *Proceedings of the National Academy of Sciences* **91**, 12501–12504 (1994).



34. Heim, R., Cubitt, A. B. & Tsien, R. Y. Improved green fluorescence. *Nature* **373**, 663–664 (1995).
35. Tsien, R. Y. The green fluorescent protein. *Annual Review of Biochemistry* **67**, 509–544 (1998).
36. Zhang, J., Campbell, R. E., Ting, A. Y. & Tsien, R. Y. Creating new fluorescent probes for cell biology. *Nature Reviews Molecular Cell Biology* **3**, 906–918 (2002).
37. Goldstein, G., Slizys, I. S. & Chase, M. W. Studies on fluorescent antibody staining. *The Journal of Experimental Medicine* **114**, 89–110 (1961).
38. Carpentier, P., Violot, S., Blanchoin, L. & Bourgeois, D. Structural basis for the phototoxicity of the fluorescent protein KillerRed. *FEBS Letters* **583**, 2839–2842 (2009).
39. Vegh, R. B. et al. Chromophore Photoreduction in Red Fluorescent Proteins Is Responsible for Bleaching and Phototoxicity. *The Journal of Physical Chemistry B* **118**, 4527–4534 (2014).
40. Shemiakina, I. I. et al. A monomeric red fluorescent protein with low cytotoxicity. *Nature Communications* **3**, 1204 (2012).
41. Aitken, C. E., Marshall, R. A. & Puglisi, J. D. An Oxygen Scavenging System for Improvement of Dye Stability in Single-Molecule Fluorescence Experiments. *Biophysical Journal* **94**, 1826–1835 (2008).
42. Hoebe, R. A. et al. Controlled light-exposure microscopy reduces photobleaching and phototoxicity in fluorescence live-cell imaging. *Nature Biotechnology* **25**, 249–253 (2007).
43. Axelrod, D., Koppel, D. E., Schlessinger, J., Elson, E. & Webb, W. W. Mobility measurement by analysis of fluorescence photobleaching recovery kinetics. *Biophysical Journal* **16**, 1055–1069 (1976).
44. Koppel, D. E., Axelrod, D., Schlessinger, J., Elson, E. L. & Webb, W. W. Dynamics of fluorescence marker concentration as a probe of mobility. *Biophysical Journal* **16**, 1315–1329 (1976).
45. Webb, D. J. & Brown, C. M. Epi-fluorescence microscopy. *Methods Mol. Biol.* **931**, 29–59 (2013).
46. Ploem, J. S. The use of a vertical illuminator with interchangeable dichroic mirrors for fluorescence microscopy with incidental light. *Z Wiss Mikrosk.* **68**, 129–142 (1967).
47. White, J. G., Amos, W. B. & Fordham, M. An Evaluation of Confocal Versus Conventional Imaging of Biological Structures by Fluorescence Light Microscopy. *Cell* **105**, 41–48 (1987).
48. Huiskens, J., Swoger, J., Del Bene, F., Wittbrodt, J. & Stelzer, E. H. K. Optical Sectioning Deep Inside Live Embryos by Selective Plane Illumination Microscopy. *Science* **305**, 1007 (2004).
49. Weber, M., Mickoleit, M. & Huiskens, J. Light sheet microscopy. in *Methods in Cell Biology* vol. 123 193–215 (Elsevier, 2014).

50. Axelrod, D. Cell-substrate contacts illuminated by total internal reflection fluorescence. *The Journal of Cell Biology* **89**, 141–145 (1981).
51. Axelrod, D., Thompson, N. L. & Burghardt, T. P. Total internal reflection fluorescent microscopy. *Journal of Microscopy* **129**, 19–28 (1983).
52. Axelrod, D. Total Internal Reflection Fluorescence Microscopy in Cell Biology: Total Internal Reflection Fluorescence. *Traffic* **2**, 764–774 (2001).
53. Rust, M. J., Bates, M. & Zhuang, X. Sub-diffraction-limit imaging by stochastic optical reconstruction microscopy (STORM). *Nature Methods* **3**, 793–796 (2006).
54. Betzig, E. et al. Imaging Intracellular Fluorescent Proteins at Nanometer Resolution. *Science* **313**, 1642–1645 (2006).
55. van de Linde, S. et al. Direct stochastic optical reconstruction microscopy with standard fluorescent probes. *Nature Protocols* **6**, 991–1009 (2011).
56. Gustafsson, M. G. L. Surpassing the lateral resolution limit by a factor of two using structured illumination microscopy. *Journal of Microscopy* **198**, 82–87 (2000).
57. Minsky, M. *Microscopy Apparatus*. (1961).
58. Minsky, M. Memoir on inventing the confocal scanning microscope. *Scanning* **10**, 128–138 (1988).
59. Amos, W. B. Results obtained with a sensitive confocal scanning system designed for epifluorescence. *Cytoskeleton* **10**, 54–61 (1988).
60. Wilhelm, S., Gröbner, B., Gluch, M. & Heinz, H. Confocal Laser Scanning Microscopy: Optical Image Formation and Electronic Signal Processing. Zeiss Campus <http://zeiss-campus.magnet.fsu.edu/referencelibrary/pdfs/ZeissConfocalPrinciples.pdf> (2017).
61. Jonkman, J. & Brown, C. M. Any Way You Slice It—A Comparison of Confocal Microscopy Techniques. *Journal of Biomolecular Techniques* **26**, 54–65 (2015).
62. Nakano, A. Spinning-disk Confocal Microscopy — A Cutting-Edge Tool for Imaging of Membrane Traffic. *Cell Structure and Function* **27**, 349–355 (2002).
63. Helmchen, F. & Denk, W. Deep tissue two-photon microscopy. *Nature Methods* **2**, 932–940 (2005).
64. Rowlands, C. J. et al. Wide-field three-photon excitation in biological samples. *Light: Science & Applications* **6**, e16255 (2016).
65. Paddock, S. Confocal Reflection Microscopy: The “Other” Confocal Mode. **32**, 4 (2002).
66. Burghardt, T. P. Measuring incidence angle for through-the-objective total internal reflection fluorescence microscopy. *Journal of Biomedical Optics* **17**, 126007 (2012).
67. Hell, S. W. & Stelzer, E. H. K. Fundamental improvement of resolution with a 4Pi-confocal fluorescence microscope using two-photon excitation. *Opt. Commun.* **93**, 277–282 (1992).
68. Hell, S. W. & Stelzer, E. H. K. Properties of a 4Pi confocal fluorescence microscope. *J. Opt. Soc. Am. A* **9**, 2159 (1992).

69. Hell, S. W. Far-field optical nanoscopy. *Science* **316**, 1153–1158 (2007).
70. Hell, S. W., Schrader, M. & van der Voort, H. T. Far-field fluorescence microscopy with three-dimensional resolution in the 100-nm range. *J. Microsc.* **187**, 1–7 (1997).
71. Schrader, M., Bahlmann, K., Giese, G. & Hell, S. W. 4Pi-confocal imaging in fixed biological specimens. *Biophysical Journal* **75**, 1659–1668 (1998).
72. Bahlmann, K., Jakobs, S. & Hell, S. W. 4Pi-confocal microscopy of live cells. *Ultramicroscopy* **87**, 155–164 (2001).
73. Bewersdorf, J., Schmidt, R. & Hell, S. W. Comparison of I5M and 4Pi-microscopy. *J. Microsc.* **222**, 105–117 (2006).
74. Lang, M. C., Staudt, T., Engelhardt, J. & Hell, S. W. 4Pi microscopy with negligible sidelobes. *New Journal of Physics* **10**, 043041 (2008).
75. Nagorni, M. & Hell, S. W. Coherent use of opposing lenses for axial resolution increase in fluorescence microscopy. I. Comparative study of concepts. *Journal of the Optical Society of America* **18**, (2001).
76. Bewersdorf, J., Egner, A. & Hell, S. W. 4Pi-Confocal Microscopy Is coming of Age. *G.I.T. Imaging & Microscop* 24–25 (2004).
77. Gustafsson, M. G. L. G. Extended resolution fluorescence microscopy. *Current Opinion in Structural Biology* **9**, 627–634 (1999).
78. Gustafsson, Agard & Sedat. I<sup>5</sup>M: 3D widefield light microscopy with better than 100 nm axial resolution. *Journal of Microscopy* **195**, 10–16 (1999).
79. Born, M. & Wolf, E. *Principle of Optics: Electromagnetic Theory of Propagation Interference and Diffraction of Light.* (Pergamon Press, 1980).
80. Lanni, F., Taylor, D. L. & Waggoner, A. S. *Standing Wave Luminescence Microscopy.* (1986).
81. Lanni, F. & Bailey, B. Standing-Wave Excitation for Fluorescence Microscopy. *Trends in Cell Biology* **4**, 262–265 (1994).
82. Hell, S. W., Stelzer, E. H. K., Lindek, S. & Cremer, C. Confocal microscopy with an increased detection aperture: type-B 4Pi confocal microscopy. *Optics Letters* **19**, 222 (1994).
83. Bailey, B., Farkas, D. L. & Lanni, F. Enhancement of Axial Resolution in Fluorescence Microscopy by Standing-Wave Excitation. *Nature* **366**, 44–48 (1993).
84. Amor, R., Mahajan, S., Amos, W. B. & McConnell, G. Standing-wave-excited multiplanar fluorescence in a laser scanning microscope reveals 3D information on red blood cells. *Scientific Reports* **4**, (2014).
85. Tinning, P. W., Scrimgeour, R. & McConnell, G. Widefield standing wave microscopy of red blood cell membrane morphology with high temporal resolution. *Biomedical Optics Express* **9**, 1745 (2018).
86. Hell, S. W. & Wichmann, J. Breaking the diffraction resolution limit by stimulated emission: stimulated-emission-depletion fluorescence microscopy. *Optics Letters* **19**, 780–782 (1994).

87. Yang, X. et al. Mirror-enhanced super-resolution microscopy. *Light: Science & Applications* **5**, e16134–e16134 (2016).
88. Heilemann, M. et al. Subdiffraction-Resolution Fluorescence Imaging with Conventional Fluorescent Probes. *Angewandte Chemie International Edition* **47**, 6172–6176 (2008).
89. Heil, H. S. et al. Sharpening emitter localization in front of a tuned mirror. *Light: Science & Applications* **7**, (2018).
90. Curtis, A. S. G. The mechanism of adhesion of cells to glass. *The Journal of cell biology* **20**, 199–215 (1964).
91. Gingell, D. & Todd, I. Interference reflection microscopy. A quantitative theory for image interpretation and its application to cell-substratum separation measurement. *Biophysical Journal* **26**, 507–526 (1979).
92. Bereiter-Hahn, J. Quantitative reflection contrast microscopy of living cells. *The Journal of Cell Biology* **82**, 767–779 (1979).
93. Bailey, J. & Gingell, D. Contacts of chick fibroblasts on glass: results and limitations of quantitative interferometry. *Journal of cell science* **90**, 215–224 (1988).
94. Schindl, M. et al. Cell-substrate interactions and locomotion of *Dictyostelium* wild-type and mutants defective in three cytoskeletal proteins: a study using quantitative reflection interference contrast microscopy. *Biophysical journal* **68**, 1177–1190 (1995).
95. Saunders, R. M. et al. Role of vinculin in regulating focal adhesion turnover. *European journal of cell biology* **85**, 487–500 (2006).
96. Sugiyama, N. et al. Label-free characterization of living human induced pluripotent stem cells by subcellular topographic imaging technique using full-field quantitative phase microscopy coupled with interference reflection microscopy. *Biomedical Optics Express* **3**, 2175 (2012).
97. Saraiva, N. et al. hGAAP promotes cell adhesion and migration via the stimulation of store-operated  $\text{Ca}^{2+}$  entry and calpain 2. *JCB* **202**, 699–713 (2013).
98. Amos, L. A. & Amos, W. B. The bending of sliding microtubules imaged by confocal light microscopy and negative stain electron microscopy. *J Cell Sci* **1991**, 95–101 (1991).
99. Simmert, S., Abdosamadi, M. K., Hermsdorf, G. & Schäffer, E. LED-based interference-reflection microscopy combined with optical tweezers for quantitative three-dimensional microtubule imaging. *Optics express* **26**, 14499–14513 (2018).
100. Mahamdeh, M., Simmert, S., Luchniak, A., Schäffer, E. & Howard, J. Label-free high-speed wide-field imaging of single microtubules using interference reflection microscopy. *Journal of Microscopy* **272**, 60–66 (2018).
101. Godwin, S. L., Fletcher, M. & Burchard, R. P. Interference reflection microscopic study of sites of association between gliding bacteria and glass substrata. *Journal of bacteriology* **171**, 4589–4594 (1989).
102. Faure, L. M. et al. The mechanism of force transmission at bacterial focal adhesion complexes. *Nature* **539**, 530–535 (2016).

103. Fletcher, M. The application of interference reflection microscopy to the study of bacterial adhesion to solid surfaces. in *Biodeterioration* (eds. Houghton, D. R., Smith, R. N. & Eggins, H. O. W.) (Elsevier Science Publishing Co., 1988).
104. Fletcher, M. Attachment of *Pseudomonas fluorescens* to glass and influence of electrolytes on bacterium-substratum separation distance. *Journal of Bacteriology* **170**, 2027–2030 (1988).
105. Weber, I. Reflection interference contrast microscopy. in *Methods in enzymology* vol. 361 34–47 (Elsevier, 2003).
106. Izzard, C. S. & Lochner, L. R. Cell-to-substrate contacts in living fibroblasts: An interference reflexion study with an evaluation of the technique. *J Cell Sci* **21**, 129–159 (1976).
107. Barr, V. A. & Bunnell, S. C. Interference Reflection Microscopy. *Current Protocols in Cell Biology* (2009) doi:10.1002/0471143030.cb0423s45.
108. Verschueren, H. Interference reflection microscopy in cell biology: methodology and applications. *Journal of cell science* **75**, 279–301 (1985).
109. Ortega-Arroyo, J. & Kukura, P. Interferometric scattering microscopy (iSCAT): new frontiers in ultrafast and ultrasensitive optical microscopy. *Physical Chemistry Chemical Physics* **14**, 15625 (2012).
110. Legesse, F. B. et al. Seamless stitching of tile scan microscope images: stitching of tile scan images. *Journal of Microscopy* **258**, 223–232 (2015).
111. McConnell, G. et al. A novel optical microscope for imaging large embryos and tissue volumes with sub-cellular resolution throughout. *eLife* **5**, e18659 (2016).
112. McConnell, G. & Amos, W. B. Application of the Mesolens for subcellular resolution imaging of intact larval and whole adult *Drosophila*. *Journal of Microscopy* **270**, 252–258 (2018).
113. Schniete, J. et al. Fast Optical Sectioning for Widefield Fluorescence Mesoscopy with the Mesolens based on HiLo Microscopy. *Scientific Reports* **8**, (2018).
114. Girkin, J. M. & Carvalho, M. T. The light-sheet microscopy revolution. *Journal of Optics* **20**, 053002 (2018).
115. Ovečka, M. et al. Multiscale imaging of plant development by light-sheet fluorescence microscopy. *Nature Plants* **4**, 639–650 (2018).
116. Lemon, W. C. et al. Whole-central nervous system functional imaging in larval *Drosophila*. *Nature Communications* **6**, (2015).
117. Liu, T.-L. et al. Observing the cell in its native state: Imaging subcellular dynamics in multicellular organisms. *Science* **360**, eaaq1392 (2018).
118. Planchon, T. A. et al. Rapid three-dimensional isotropic imaging of living cells using Bessel beam plane illumination. *Nature Methods* **8**, 417–423 (2011).
119. Chen, B. et al. Lattice light-sheet microscopy: Imaging molecules to embryos at high spatiotemporal resolution. *Science* **346**, 1257998 (2014).

120. Vettenburg, T. et al. Light-sheet microscopy using an Airy beam. *Nature Methods* **11**, 541–544 (2014).
121. Gao, L., Shao, L., Chen, B.-C. & Betzig, E. 3D live fluorescence imaging of cellular dynamics using Bessel beam plane illumination microscopy. *Nature Protocols* **9**, 1083–1101 (2014).
122. Yang, Z. et al. A compact Airy beam light sheet microscope with a tilted cylindrical lens. *Biomedical Optics Express* **5**, 3434 (2014).
123. Sofroniew, N. J., Flickinger, D., King, J. & Svoboda, K. A large field of view two-photon mesoscope with subcellular resolution for in vivo imaging. *eLife* **5**, e14472 (2016).
124. Shemesh, H. et al. High frequency ultrasound imaging of a single-species biofilm. *Journal of Dentistry* **35**, 673–678 (2007).
125. Vaidya, K., Osgood, R., Ren, D., Pichichero, M. E. & Helguera, M. Ultrasound Imaging and Characterization of Biofilms Based on Wavelet De-noised Radiofrequency Data. *Ultrasound in Medicine & Biology* **40**, 583–595 (2014).
126. Xi, C., Marks, D., Schlachter, S., Luo, W. & Boppart, S. A. High-resolution three-dimensional imaging of biofilm development using optical coherence tomography. *Journal of Biomedical Optics* **11**, 034001 (2006).
127. Wagner, M., Taherzadeh, D., Haisch, C. & Horn, H. Investigation of the mesoscale structure and volumetric features of biofilms using optical coherence tomography. *Biotechnology and Bioengineering* **107**, 844–853 (2010).
128. Leite de Andrade, M. C. et al. A new approach by optical coherence tomography for elucidating biofilm formation by emergent *Candida* species. *PLOS ONE* **12**, e0188020 (2017).
129. Drescher, K. et al. Architectural transitions in *Vibrio cholerae* biofilms at single-cell resolution. *Proceedings of the National Academy of Sciences* **113**, E2066–E2072 (2016).
130. Hartmann, R. et al. Emergence of three-dimensional order and structure in growing biofilms. *Nature Physics* **15**, 251–256 (2019).
131. Yan, J., Sharo, A. G., Stone, H. A., Wingreen, N. S. & Bassler, B. L. *Vibrio cholerae* biofilm growth program and architecture revealed by single-cell live imaging. *Proceedings of the National Academy of Sciences* **113**, E5337–E5343 (2016).
132. Wolgemuth, C., Hoiczyk, E., Kaiser, D. & Oster, G. How Myxobacteria glide. *Current Biology* **12**, 369–377 (2002).
133. Mignot, T. The elusive engine in *Myxococcus xanthus* gliding motility. *Cellular and Molecular Life Sciences* **64**, 2733–2745 (2007).
134. Nan, B. & Zusman, D. R. Uncovering the Mystery of Gliding Motility in the Myxobacteria. *Annual Review of Genetics* **45**, 21–39 (2011).
135. Muñoz-Dorado, J., Marcos-Torres, F. J., García-Bravo, E., Moraleda-Muñoz, A. & Pérez, J. Myxobacteria: Moving, Killing, Feeding, and Surviving Together. *Frontiers in Microbiology* **7**, (2016).

136. Blackhart, B. D. & Zusman, D. R. 'Frizzy' genes of *Myxococcus xanthus* are involved in control of frequency of reversal of gliding motility. *Proceedings of the National Academy of Sciences* **82**, 8767–8770 (1985).
137. Zusman, D. R., Scott, A. E., Yang, Z. & Kirby, J. R. Chemosensory pathways, motility and development in *Myxococcus xanthus*. *Nature Reviews Microbiology* **5**, 862–872 (2007).
138. Li, Y. et al. Extracellular polysaccharides mediate pilus retraction during social motility of *Myxococcus xanthus* vol. 100 (9), pp. 5443–5448. *PNAS* **100**, 5443–5448 (2003).
139. Mignot, T., Shaevitz, J. W., Hartzell, P. L. & Zusman, D. R. Evidence That Focal Adhesion Complexes Power Bacterial Gliding Motility. *Science* **315**, 853–856 (2007).
140. McBride, M. J. & Nakane, D. Flavobacterium gliding motility and the type IX secretion system. *Current Opinion in Microbiology* **28**, 72–77 (2015).
141. Nan, B. et al. Myxobacteria gliding motility requires cytoskeleton rotation powered by proton motive force. *Proceedings of the National Academy of Sciences* **108**, 2498–2503 (2011).
142. Sun, M., Wartel, M., Cascales, E., Shaevitz, J. W. & Mignot, T. Motor-driven intracellular transport powers bacterial gliding motility. *Proceedings of the National Academy of Sciences* **108**, 7559–7564 (2011).
143. Zhang, Y., Ducret, A., Shaevitz, J. & Mignot, T. From individual cell motility to collective behaviors: insights from a prokaryote, *Myxococcus xanthus*. *FEMS Microbiology Reviews* **36**, 149–164 (2012).
144. Berleman, J. E. et al. Exopolysaccharide microchannels direct bacterial motility and organize multicellular behavior. *The ISME journal* **10**, 2620–2632 (2016).
145. Rooney, L. M. et al. Three-Dimensional Observations of an Aperiodic Oscillatory Gliding Behavior in *Myxococcus xanthus* Using Confocal Interference Reflection Microscopy. *mSphere* **5**, (2020).
146. Costerton, J. W. et al. Bacterial biofilms in nature and disease. *Annual Review of Microbiology* **41**, 435–64 (1987).
147. Costerton, J. Introduction to biofilms. *International Journal of Antimicrobial Agents* **11**, 217–221 (1999).
148. Davey, M. E. & O'Toole, G. A. Microbial biofilms: from ecology to molecular genetics. *Microbiology and molecular biology reviews* **64**, 847–867 (2000).
149. Sutherland, I. W. The biofilm matrix - an immobilised but dynamic microbial environment. *Trends in Microbiology* **9**, 222–227 (2001).
150. Belas, R. Biofilms, flagella, and mechanosensing of surfaces by bacteria. *Trends in Microbiology* **22**, 517–527 (2014).
151. Beitelshies, M., Hill, A., Jones, C. & Pfeifer, B. Phenotypic Variation during Biofilm Formation: Implications for Anti-Biofilm Therapeutic Design. *Materials* **11**, 1086 (2018).
152. Ha, D.-G. & O'Toole, G. A. c-di-GMP and its Effects on Biofilm Formation and Dispersion: A *Pseudomonas aeruginosa* Review. *Microbiology Spectrum* **3**, (2015).

153. Chang, C.-Y. Surface Sensing for Biofilm Formation in *Pseudomonas aeruginosa*. *Frontiers in Microbiology* **8**, (2018).
154. Valentini, M. & Filloux, A. Multiple Roles of c-di-GMP Signaling in Bacterial Pathogenesis. *Annual Review of Microbiology* **73**, 387–406 (2019).
155. Peng, X., Zhang, Y., Bai, G., Zhou, X. & Wu, H. Cyclic di-AMP mediates biofilm formation. *Molecular Microbiology* **99**, 945–959 (2016).
156. Townsley, L., Yannarell, S. M., Huynh, T. N., Woodward, J. J. & Shank, E. A. Cyclic di-AMP Acts as an Extracellular Signal That Impacts *Bacillus subtilis* Biofilm Formation and Plant Attachment. *mBio* **9**, (2018).
157. Jamal, M. et al. Bacterial biofilm and associated infections. *Journal of the Chinese Medical Association* **81**, 7–11 (2018).
158. Carvalho, G., Balestrino, D., Forestier, C. & Mathias, J.-D. How do environment-dependent switching rates between susceptible and persister cells affect the dynamics of biofilms faced with antibiotics? *npj Biofilms and Microbiomes* **4**, (2018).
159. Jolivet-Gougeon, A. & Bonnaure-Mallet, M. Biofilms as a mechanism of bacterial resistance. *Drug Discovery Today: Technologies* **11**, 49–56 (2014).
160. Walker, S. L., Fourgialakis, M., Cerezo, B. & Livens, S. Removal of Microbial Biofilms from Dispense Equipment: The Effect of Enzymatic Pre-digestion and Detergent Treatment. *Journal of the Institute of Brewing* **113**, 61–66 (2007).
161. Brooks, J. D. & Flint, S. H. Biofilms in the food industry: problems and potential solutions. *International Journal of Food Science & Technology* **43**, 2163–2176 (2008).
162. Fish, K. E., Osborn, A. M. & Boxall, J. Characterising and understanding the impact of microbial biofilms and the extracellular polymeric substance (EPS) matrix in drinking water distribution systems. *Environ. Sci.: Water Res. Technol.* **2**, 614–630 (2016).
163. McKay, G. & Nguyen, D. Antibiotic Resistance and Tolerance in Bacterial Biofilms. in *Handbook of Antimicrobial Resistance* (eds. Berghuis, A., Matlashewski, G., Wainberg, M. A. & Sheppard, D.) 203–229 (Springer New York, 2017). doi:10.1007/978-1-4939-0694-9\_11.
164. Ramage, G. et al. The epithelial cell response to health and disease associated oral biofilm models. *Journal of Periodontal Research* **52**, 325–333 (2017).
165. Beloin, C., Roux, A. & Ghigo, J. M. *Escherichia coli* biofilms. *Curr Top Microbiol Immunol* **322**, 249–289 (2008).
166. Duncan, M. J. et al. The Distinct Binding Specificities Exhibited by Enterobacterial Type 1 Fimbriae Are Determined by Their Fimbrial Shafts. *Journal of Biological Chemistry* **280**, 37707–37716 (2005).
167. Kjærgaard, K., Schembri, M. A., Hasman, H. & Klemm, P. Antigen 43 from *Escherichia coli* Induces Inter- and Intraspecies Cell Aggregation and Changes in Colony Morphology of *Pseudomonas fluorescens*. *Journal of Bacteriology* **182**, 4789–4796 (2000).
168. Schembri, M. A., Hjerrild, L., Gjermansen, M. & Klemm, P. Differential Expression of the *Escherichiacoli* Autoaggregation Factor Antigen 43. *Journal of Bacteriology* **185**, 2236–2242 (2003).



169. Serra, D. O., Richter, A. M., Klauck, G., Mika, F. & Hengge, R. Microanatomy at Cellular Resolution and Spatial Order of Physiological Differentiation in a Bacterial Biofilm. *mBio* **4**, e00103-13-e00103-13 (2013).
170. Serra, D. O. & Hengge, R. Stress responses go three dimensional - the spatial order of physiological differentiation in bacterial macrocolony biofilms: Stress responses shape biofilm architecture. *Environmental Microbiology* **16**, 1455–1471 (2014).
171. Serra, D. O., Richter, A. M. & Hengge, R. Cellulose as an Architectural Element in Spatially Structured *Escherichia coli* Biofilms. *Journal of Bacteriology* **195**, 5540–5554 (2013).
172. Asally, M. et al. Localized cell death focuses mechanical forces during 3D patterning in a biofilm. *Proceedings of the National Academy of Sciences* **109**, 18891–18896 (2012).
173. Pratt, L. A. & Kolter, R. Genetic analysis of *Escherichia coli* biofilm formation: roles of flagella, motility, chemotaxis and type I pili. *Molecular microbiology* **30**, 285–293 (1998).
174. Liu, R. & Ochman, H. Stepwise formation of the bacterial flagellar system. *Proceedings of the National Academy of Sciences* **104**, 7116–7121 (2007).
175. Meunier, D., Lambiotte, R. & Bullmore, E. T. Modular and Hierarchically Modular Organization of Brain Networks. *Frontiers in Neuroscience* **4**, (2010).
176. Gorfinkiel, N., Blanchard, G. B., Adams, R. J. & Martinez Arias, A. Mechanical control of global cell behaviour during dorsal closure in *Drosophila*. *Development* **136**, 1889–1898 (2009).
177. Spaide, R. F. Optical Coherence Tomography Angiography Signs of Vascular Abnormalization With Antiangiogenic Therapy for Choroidal Neovascularization. *American Journal of Ophthalmology* **160**, 6–16 (2015).
178. Nadell, C. D., Drescher, K. & Foster, K. R. Spatial structure, cooperation and competition in biofilms. *Nature Reviews Microbiology* **14**, 589 (2016).
179. Ben-Jacob, E. et al. Generic modelling of cooperative growth patterns in bacterial colonies. *Nature* **368**, 46–49 (1994).
180. Ben-Jacob, E. et al. Bacterial cooperative organisation under antibiotic stress. *Physica A* **282**, 247–282 (2000).
181. Obert, M., Pfeifer, P. & Sernetz, M. Microbial growth patterns described by fractal geometry. *Journal of Bacteriology* **172**, 1180–1185 (1990).
182. Rudge, T. J., Federici, F., Steiner, P. J., Kan, A. & Haseloff, J. Cell Polarity-Driven Instability Generates Self-Organized, Fractal Patterning of Cell Layers. *ACS Synthetic Biology* **2**, 705–714 (2013).
183. Flemming, H.-C. et al. Biofilms: an emergent form of bacterial life. *Nature Reviews Microbiology* **14**, 563–575 (2016).
184. Wilking, J. N. et al. Liquid transport facilitated by channels in *Bacillus subtilis* biofilms. *Proceedings of the National Academy of Sciences* **110**, 848–852 (2013).

185. Kempes, C. P., Okegbe, C., Mears-Clarke, Z., Follows, M. J. & Dietrich, L. E. P. Morphological optimization for access to dual oxidants in biofilms. *Proceedings of the National Academy of Sciences* **111**, 208–213 (2014).
186. Rudge, T. J., Steiner, P. J., Phillips, A. & Haseloff, J. Computational Modeling of Synthetic Microbial Biofilms. *ACS Synthetic Biology* **1**, 345–352 (2012).
187. Smith, W. P. J. et al. Cell morphology drives spatial patterning in microbial communities. *Proceedings of the National Academy of Sciences* **114**, E280–E286 (2017).
188. Blanchard, A. E. & Lu, T. Bacterial social interactions drive the emergence of differential spatial colony structures. *BMC Systems Biology* **9**, (2015).
189. Jauffred, L., Vejborg, R. M., Korolev, K. S., Brown, S. & Oddershede, L. B. Chirality in microbial biofilms is mediated by close interactions between the cell surface and the substratum. *The ISME journal* **11**, 1688 (2017).
190. Goldschmidt, F., Regoes, R. R. & Johnson, D. R. Successive range expansion promotes diversity and accelerates evolution in spatially structured microbial populations. *The ISME journal* **11**, 2112 (2017).
191. Di Franco, C., Beccari, E., Santini, T., Pisaneschi, G. & Tecce, G. Colony shape as a genetic trait in the pattern-forming *Bacillus mycoides*. *BMC microbiology* **2**, 33 (2002).
192. Nuñez, I. N. et al. Artificial Symmetry-Breaking for Morphogenetic Engineering Bacterial Colonies. *ACS Synthetic Biology* **6**, 256–265 (2017).
193. Kallmeyer, J., Pockalny, R., Adhikari, R. R., Smith, D. C. & D'Hondt, S. Global distribution of microbial abundance and biomass in subseafloor sediment. *Proceedings of the National Academy of Sciences* **109**, 16213–16216 (2012).
194. Carr, S. A. et al. Bacterial abundance and composition in marine sediments beneath the Ross Ice Shelf, Antarctica. *Geobiology* **11**, 377–395 (2013).
195. Xue, P.-P., Carrillo, Y., Pino, V., Minasny, B. & McBratney, Alex. B. Soil Properties Drive Microbial Community Structure in a Large Scale Transect in South Eastern Australia. *Scientific Reports* **8**, (2018).
196. Petro, C. et al. Marine Deep Biosphere Microbial Communities Assemble in Near-Surface Sediments in Aarhus Bay. *Frontiers in Microbiology* **10**, (2019).
197. Zhang, J. et al. Diversity of the microbial community and cultivable protease-producing bacteria in the sediments of the Bohai Sea, Yellow Sea and South China Sea. *PLOS ONE* **14**, e0215328 (2019).
198. Lin, Y.-T. et al. Structure and Diversity of Soil Bacterial Communities in Offshore Islands. *Scientific Reports* **9**, (2019).
199. López, G. I. Grain Size Analysis. in *Encyclopedia of Geoarchaeology* (ed. Gilbert, A. S.) 341–348 (Springer Netherlands, 2017). doi:10.1007/978-1-4020-4409-0\_18.
200. Burmølle, M., Hansen, L. H. & Sørensen, S. J. Establishment and Early Succession of a Multispecies Biofilm Composed of Soil Bacteria. *Microbial Ecology* **54**, 352–362 (2007).

201. Bobek, J., Šmídová, K. & Čihák, M. A Waking Review: Old and Novel Insights into the Spore Germination in *Streptomyces*. *Frontiers in Microbiology* **8**, (2017).
202. Bache, B. W., Chesworth, W. & Chesworth, W. Biomes and their Soils. in *Encyclopedia of Soil Science* (ed. Chesworth, W.) 61–68 (Springer Netherlands, 2008). doi:10.1007/978-1-4020-3995-9\_64.
203. Cianfrani, C., Buri, A., Verrecchia, E. & Guisan, A. Generalizing soil properties in geographic space: Approaches used and ways forward. *PLOS ONE* **13**, e0208823 (2018).
204. Zhao, X., Yang, Y., Shen, H., Geng, X. & Fang, J. Global soil–climate–biome diagram: linking surface soil properties to climate and biota. *Biogeosciences* **16**, 2857–2871 (2019).
205. Ashelford, K. E., Day, M. J. & Fry, J. C. Elevated Abundance of Bacteriophage Infecting Bacteria in Soil. *Applied and Environmental Microbiology* **69**, 285–289 (2003).
206. Downie, H. et al. Transparent Soil for Imaging the Rhizosphere. *PLoS ONE* **7**, e44276 (2012).
207. Downie, H. F., Valentine, T. A., Otten, W., Spiers, A. J. & Dupuy, L. X. Transparent soil microcosms allow 3D spatial quantification of soil microbiological processes in vivo. *Plant Signaling & Behavior* **9**, e970421 (2014).
208. Huang, Z. et al. Cross Talk between Chemosensory Pathways That Modulate Chemotaxis and Biofilm Formation. *mBio* **10**, (2019).
209. Oliveira, N. M., Foster, K. R. & Durham, W. M. Single-cell twitching chemotaxis in developing biofilms. *Proceedings of the National Academy of Sciences* **113**, 6532–6537 (2016).
210. Tamar, E., Koler, M. & Vaknin, A. The role of motility and chemotaxis in the bacterial colonization of protected surfaces. *Scientific Reports* **6**, (2016).
211. Johnson, K. S. & Ottemann, K. M. Colonization, localization, and inflammation: the roles of *H. pylori* chemotaxis in vivo. *Current Opinion in Microbiology* **41**, 51–57 (2018).
212. Collins, K. D., Hu, S., Grasberger, H., Kao, J. Y. & Ottemann, K. M. Chemotaxis Allows Bacteria To Overcome Host-Generated Reactive Oxygen Species That Constrain Gland Colonization. *Infection and Immunity* **86**, e00878-17 (2018).
213. Berleman, J. E., Scott, J., Chumley, T. & Kirby, J. R. Predataxis behavior in *Myxococcus xanthus*. *Proceedings of the National Academy of Sciences* **105**, 17127–17132 (2008).
214. Lapidus, I. R. & Berg, H. C. Gliding motility of *Cytophaga* sp. strain U67. *Journal of bacteriology* **151**, 384–398 (1982).
215. Kasai, T., Hamaguchi, T. & Miyata, M. Gliding Motility of *Mycoplasma mobile* on Uniform Oligosaccharides. *Journal of Bacteriology* **197**, 2952–2957 (2015).
216. Spormann, A. M. & Kaiser, A. D. Gliding movements in *Myxococcus xanthus*. *Journal of bacteriology* **177**, 5846–5852 (1995).
217. Spormann, A. M. Gliding Motility in Bacteria: Insights from Studies of *Myxococcus xanthus*. *Microbiol. Mol. Biol. Rev.* **63**, 621–641 (1999).

218. Pogue, C. B., Zhou, T. & Nan, B. PlpA, a PilZ-like protein, regulates directed motility of the bacterium *Myxococcus xanthus*: A PilZ-like protein regulates *M. xanthus* motility. *Molecular Microbiology* **107**, 214–228 (2018).
219. Balagam, R. et al. *Myxococcus xanthus* Gliding Motors Are Elastically Coupled to the Substrate as Predicted by the Focal Adhesion Model of Gliding Motility. *PLoS Computational Biology* **10**, e1003619 (2014).
220. Islam, S. T. & Mignot, T. The mysterious nature of bacterial surface (gliding) motility: A focal adhesion-based mechanism in *Myxococcus xanthus*. *Seminars in Cell & Developmental Biology* **46**, 143–154 (2015).
221. Islam, S. T. et al. Integrin-Like Tethering of Motility Complexes at Bacterial Focal Adhesions. (2018).
222. Nan, B. & Zusman, D. R. Novel mechanisms power bacterial gliding motility: Novel mechanisms for bacterial surface motilities. *Molecular Microbiology* **101**, 186–193 (2016).
223. Nan, B., Mauriello, E. M. F., Sun, I.-H., Wong, A. & Zusman, D. R. A multi-protein complex from *Myxococcus xanthus* required for bacterial gliding motility. *Molecular Microbiology* **76**, 1539–1554 (2010).
224. Nan, B. et al. Flagella stator homologs function as motors for myxobacterial gliding motility by moving in helical trajectories. *Proceedings of the National Academy of Sciences* **110**, E1508–E1513 (2013).
225. Fu, G. et al. MotAB-like machinery drives the movement of MreB filaments during bacterial gliding motility. *Proceedings of the National Academy of Sciences* **115**, 2484–2489 (2018).
226. Contreras-Naranjo, J. C. & Ugaz, V. M. A nanometre-scale resolution interference-based probe of interfacial phenomena between microscopic objects and surfaces. *Nature Communications* **4**, (2013).
227. Ducret, A., Fleuchot, B., Bergam, P. & Mignot, T. Direct live imaging of cell–cell protein transfer by transient outer membrane fusion in *Myxococcus xanthus*. *eLife* **2**, (2013).
228. Saunders, R. M. et al. Role of vinculin in regulating focal adhesion turnover. *European journal of cell biology* **85**, 487–500 (2006).
229. Chiu, L.-D., Su, L., Reichelt, S. & Amos, W. B. Use of a white light supercontinuum laser for confocal interference-reflection microscopy. *Journal of Microscopy* **246**, 153–159 (2012).
230. Iwanaga, Y., Braun, D. & Fromherz, P. No correlation of focal contacts and close adhesion by comparing GFP-vinculin and fluorescence interference of DiI. *European Biophysics Journal* **30**, 17–26 (2001).
231. Mignot, T. & Shaevitz, J. W. Active and passive mechanisms of intracellular transport and localization in bacteria. *Current Opinion in Microbiology* **11**, 580–585 (2008).
232. Gingell, D., Todd, I. & Bailey, J. Topography of cell-glass apposition revealed by total internal reflection fluorescence of volume markers. *The Journal of Cell Biology* **100**, 1334–1338 (1985).

233. Talà, L., Fineberg, A., Kukura, P. & Persat, A. *Pseudomonas aeruginosa* orchestrates twitching motility by sequential control of type IV pili movements. *Nature Microbiology* (2019) doi:10.1038/s41564-019-0378-9.
234. Hagen, D. C., Bretscher, A. P. & Kaiser, D. Synergism between morphogenetic mutants of *Myxococcus xanthus*. *Developmental Biology* **64**, 284–296 (1978).
235. Schindelin, J. et al. Fiji: an open-source platform for biological-image analysis. *Nature Methods* **9**, 676–682 (2012).
236. Scrimgeour, R. Development of computational methods for standing wave microscopy. (University of Strathclyde, 2019).
237. Chenouard, N. et al. Objective comparison of particle tracking methods. *Nature Methods* **11**, 281–289 (2014).
238. Tinevez, J.-Y. et al. TrackMate: An open and extensible platform for single-particle tracking. *Methods* **115**, 80–90 (2017).
239. Wolff, C. et al. Multi-view light-sheet imaging and tracking with the MaMuT software reveals the cell lineage of a direct developing arthropod limb. *eLife* **7**, (2018).
240. Wilson, T. & Sheppard, C. Theory and practice of scanning optical microscopy. (Academic Press, 1984).
241. Roeder, A. H. K., Cunha, A., Burl, M. C. & Meyerowitz, E. M. A computational image analysis glossary for biologists. *Development* **139**, 3071–3080 (2012).
242. Lünsdorf, H. & Schairer, H. U. Frozen motion of gliding bacteria outlines inherent features of the motility apparatus. *Microbiology* **147**, 939–947 (2001).
243. Jakobczak, B., Keilberg, D., Wuichet, K. & Søgaard-Andersen, L. Contact-and protein transfer-dependent stimulation of assembly of the gliding motility machinery in *Myxococcus xanthus*. *PLoS genetics* **11**, e1005341 (2015).
244. Tchoufag, J., Ghosh, P., Pogue, C. B., Nan, B. & Mandadapu, K. K. Mechanisms for bacterial gliding motility on soft substrates. *Proceedings of the National Academy of Sciences* **116**, 25087–25096 (2019).
245. Evans, A. G. L. et al. Predatory activity of *Myxococcus xanthus* outer-membrane vesicles and properties of their hydrolase cargo. *Microbiology* **158**, 2742–2752 (2012).
246. Berleman, J. E. et al. The lethal cargo of *Myxococcus xanthus* outer membrane vesicles. *Frontiers in Microbiology* **5**, (2014).
247. Wei, X., Vassallo, C. N., Pathak, D. T. & Wall, D. Myxobacteria Produce Outer Membrane-Enclosed Tubes in Unstructured Environments. *Journal of Bacteriology* **196**, 1807–1814 (2014).
248. Rooney, L. M., Amos, W. B., Hoskisson, P. A. & McConnell, G. Intra-colony channels in *E. coli* function as a nutrient uptake system. *The ISME Journal* (2020) doi:10.1038/s41396-020-0700-9.
249. Hobley, L., Harkins, C., MacPhee, C. E. & Stanley-Wall, N. R. Giving structure to the biofilm matrix: an overview of individual strategies and emerging common themes. *FEMS Microbiology Reviews* **39**, 649–669 (2015).

250. Flemming, H.-C. & Wuertz, S. Bacteria and archaea on Earth and their abundance in biofilms. *Nature Reviews Microbiology* **17**, 247–260 (2019).
251. Bixler, G. D. & Bhushan, B. Biofouling: lessons from nature. *Philosophical Transactions of the Royal Society A: Mathematical, Physical and Engineering Sciences* **370**, 2381–2417 (2012).
252. Chaves Simões, L. & Simões, M. Biofilms in drinking water: problems and solutions. *RSC Adv.* **3**, 2520–2533 (2013).
253. Percival, S. L., Suleman, L., Vuotto, C. & Donelli, G. Healthcare-associated infections, medical devices and biofilms: risk, tolerance and control. *Journal of Medical Microbiology* **64**, 323–334 (2015).
254. Roberts, A. E. L., Kragh, K. N., Bjarnsholt, T. & Diggle, S. P. The Limitations of *In Vitro* Experimentation in Understanding Biofilms and Chronic Infection. *Journal of Molecular Biology* **427**, 3646–3661 (2015).
255. Ghanbari, A. et al. Inoculation density and nutrient level determine the formation of mushroom-shaped structures in *Pseudomonas aeruginosa* biofilms. *Scientific Reports* **6**, (2016).
256. Sheraton, M. V. et al. Mesoscopic energy minimization drives *Pseudomonas aeruginosa* biofilm morphologies and consequent stratification of antibiotic activity based on cell metabolism. *Antimicrobial Agents and Chemotherapy* **62**, (2018).
257. Dietrich, L. E. P. et al. Bacterial Community Morphogenesis Is Intimately Linked to the Intracellular Redox State. *Journal of Bacteriology* **195**, 1371–1380 (2013).
258. Karampatzakis, A. et al. Measurement of oxygen concentrations in bacterial biofilms using transient state monitoring by single plane illumination microscopy. *Biomedical Physics & Engineering Express* **3**, 035020 (2017).
259. Libicki, S. B., Salmon, P. M. & Robertson, C. R. The effective diffusive permeability of a nonreacting solute in microbial cell aggregates. *Biotechnology and bioengineering* **32**, 68–85 (1988).
260. Hunt, S. M., Werner, E. M., Huang, B., Hamilton, M. A. & Stewart, P. S. Hypothesis for the Role of Nutrient Starvation in Biofilm Detachment. *Applied and Environmental Microbiology* **70**, 7418–7425 (2004).
261. Stewart, P. S. Diffusion in Biofilms. *Journal of Bacteriology* **185**, 1485–1491 (2003).
262. Guélon, T., Mathias, J.-D. & Deffuant, G. Influence of spatial structure on effective nutrient diffusion in bacterial biofilms. *Journal of Biological Physics* **38**, 573–588 (2012).
263. Eriksen, R. S., Svenningsen, S. L., Sneppen, K. & Mitarai, N. A growing microcolony can survive and support persistent propagation of virulent phages. *Proceedings of the National Academy of Sciences* **115**, 337–342 (2018).
264. Xiao, J. et al. Biofilm three-dimensional architecture influences in situ pH distribution pattern on the human enamel surface. *International Journal of Oral Science* **9**, 74–79 (2017).
265. Liu, J. et al. Coupling between distant biofilms and emergence of nutrient time-sharing. *Science* **356**, 638–642 (2017).

266. Neu, T. R. & Lawrence, J. R. Innovative techniques, sensors, and approaches for imaging biofilms at different scales. *Trends in Microbiology* **23**, 233–242 (2015).
267. Karygianni, L. et al. Microscope-Based Imaging Platform for Large-Scale Analysis of Oral Biofilms. *Applied and Environmental Microbiology* **78**, 8703–8711 (2012).
268. Miquel Guennoc, C. et al. A New Method for Qualitative Multi-scale Analysis of Bacterial Biofilms on Filamentous Fungal Colonies Using Confocal and Electron Microscopy. *Journal of Visualized Experiments* (2017) doi:10.3791/54771.
269. Davies, S. K. et al. Visualizing Antimicrobials in Bacterial Biofilms: Three-Dimensional Biochemical Imaging Using TOF-SIMS. *mSphere* **2**, (2017).
270. Donlan, R. M. & Costerton, J. W. Biofilms: Survival Mechanisms of Clinically Relevant Microorganisms. *Clinical Microbiology Reviews* **15**, 167–193 (2002).
271. BBSRC. Biofilms Strategic Opportunity. <https://bbsrc.ukri.org/documents/biofilms-strategic-opportunity-pdf/> (2016).
272. González-Rivas, F., Ripolles-Avila, C., Fontecha-Umaña, F., Ríos-Castillo, A. G. & Rodríguez-Jerez, J. J. Biofilms in the Spotlight: Detection, Quantification, and Removal Methods. *Comprehensive Reviews in Food Science and Food Safety* **17**, 1261–1276 (2018).
273. Algburi, A., Comito, N., Kashtanov, D., Dicks, L. M. T. & Chikindas, M. L. Control of Biofilm Formation: Antibiotics and Beyond. *Applied and Environmental Microbiology* **83**, (2017).
274. Koo, H., Allan, R. N., Howlin, R. P., Stoodley, P. & Hall-Stoodley, L. Targeting microbial biofilms: current and prospective therapeutic strategies. *Nature Reviews Microbiology* **15**, 740–755 (2017).
275. Jones, M. N. Use of Liposomes to Deliver Bactericides to Bacterial Biofilms. in *Methods in Enzymology* vol. 391 211–228 (Elsevier, 2005).
276. Rukavina, Z. & Vanić, Ž. Current Trends in Development of Liposomes for Targeting Bacterial Biofilms. *Pharmaceutics* **8**, 18 (2016).
277. Li, X. et al. Recent developments in smart antibacterial surfaces to inhibit biofilm formation and bacterial infections. *Journal of Materials Chemistry B* **6**, 4274–4292 (2018).
278. Elsayed, S., Paschke, S., Rau, S. & Lienkamp, K. Surface Structuring Combined with Chemical Surface Functionalization: An Effective Tool to Manipulate Cell Adhesion. *Molecules* **24**, 909 (2019).
279. Ghilini, F., Pissinis, D. E., Miñán, A., Schilardi, P. L. & Diaz, C. How Functionalized Surfaces Can Inhibit Bacterial Adhesion and Viability. *ACS Biomaterials Science & Engineering* **5**, 4920–4936 (2019).
280. Elbing, K. L. & Brent, R. Recipes and Tools for Culture of *Escherichia coli*. *Current Protocols in Molecular Biology* **125**, e83 (2019).
281. Dempster, J., Wokosin, D. L., McCloskey, K. D., Girkin, J. M. & Gurney, A. M. WinFluor: an integrated system for the simultaneous recording of cell fluorescence images and electrophysiological signals on a single computer system. *British Journal of Pharmacology* **137**, 146 (2002).

282. Zogaj, X., Nimtz, M., Rohde, M., Bokranz, W. & Romling, U. The multicellular morphotypes of *Salmonella typhimurium* and *Escherichia coli* produce cellulose as the second component of the extracellular matrix. *Molecular Microbiology* **39**, 1452–1463 (2001).
283. Lambertsen, L., Sternberg, C. & Molin, S. Mini-Tn7 transposons for site-specific tagging of bacteria with fluorescent proteins. *Environmental Microbiology* **6**, 726–732 (2004).
284. Willey, J. M., Sherwood, L. M. & Woolverton, C. J. Microbial genetics: regulation of gene expression. in Prescott's Microbiology 331–362 (McGraw-Hill, 2011).
285. Hartmann, R. et al. BiofilmQ, a software tool for quantitative image analysis of microbial biofilm communities. *bioRxiv* 735423 (2019) doi:10.1101/735423.
286. Siegele, D. A. & Hu, J. C. Gene expression from plasmids containing the *araBAD* promoter at subsaturating inducer concentrations represents mixed populations. *Proc Natl Acad Sci USA* **94**, 8168 (1997).
287. Drury, W. J., Characklis, W. G. & Stewart, P. S. Interactions of 1  $\mu$ m latex particles with *Pseudomonas aeruginosa* biofilms. *Water Research* **27**, 1119–1126 (1993).
288. Stoodley, P., Lewandowski, Z. & others. Liquid flow in biofilm systems. *Applied and environmental microbiology* **60**, 2711–2716 (1994).
289. Jo, J., Cortez, K. L., Cornell, W. C., Price-Whelan, A. & Dietrich, L. E. An orphan cbb3-type cytochrome oxidase subunit supports *Pseudomonas aeruginosa* biofilm growth and virulence. *30* (2017).
290. Xu, H., Dauparas, J., Das, D., Lauga, E. & Wu, Y. Self-organization of swimmers drives long-range fluid transport in bacterial colonies. *Nature Communications* **10**, (2019).
291. Xiong, L. et al. Flower-like patterns in multi-species bacterial colonies. *eLife* **9**, (2020).
292. Wimpenny, J. W. T. & Coombs, J. P. Penetration of oxygen into bacterial colonies. *Microbiology* **129**, 1239–1242 (1983).
293. Peters, A. C., Wimpenny, J. W. T. & Coombs, J. P. Oxygen Profiles in, and in the Agar Beneath, Colonies of *Bacillus cereus*, *Staphylococcus albus* and *Escherichia coli*. *Journal of General Microbiology* **133**, 1257–1263 (1987).
294. Jeanson, S., Flourey, J., Gagnaire, V., Lortal, S. & Thierry, A. Bacterial Colonies in Solid Media and Foods: A Review on Their Growth and Interactions with the Micro-Environment. *Frontiers in Microbiology* **6**, (2015).
295. Hwang, G. et al. Simultaneous spatiotemporal mapping of in situ pH and bacterial activity within an intact 3D microcolony structure. *Scientific Reports* **6**, (2016).
296. Webb, J. S. et al. Cell Death in *Pseudomonas aeruginosa* Biofilm Development. *Journal of Bacteriology* **185**, 4585–4592 (2003).
297. Lund, V. A. et al. Molecular coordination of *Staphylococcus aureus* cell division. *eLife* **7**, (2018).



298. Ize, B., Stanley, N. R., Buchanan, G. & Palmer, T. Role of the *Escherichia coli* Tat pathway in outer membrane integrity: AmiA and AmiC are Tat substrates. *Molecular Microbiology* **48**, 1183–1193 (2003).
299. Shiomi, D. et al. Mutations in cell elongation genes *mreB*, *mrdA* and *mrdB* suppress the shape defect of RodZ-deficient cells: Suppressor mutations that restore rod shape. *Molecular Microbiology* **87**, 1029–1044 (2013).
300. Monds, R. D. et al. Systematic Perturbation of Cytoskeletal Function Reveals a Linear Scaling Relationship between Cell Geometry and Fitness. *Cell Reports* **9**, 1528–1537 (2014).
301. Shiomi, D., Sakai, M. & Niki, H. Determination of bacterial rod shape by a novel cytoskeletal membrane protein. *The EMBO Journal* **27**, 3081–3091 (2008).
302. Moscona, A. A. Aggregation of sponge cells: Cell-linking macromolecules and their role in the formation of multicellular systems. *In Vitro* **3**, 13–21 (1967).
303. Lavrov, A. I. & Kosevich, I. A. Sponge cell reaggregation: Mechanisms and dynamics of the process. *Russian Journal of Developmental Biology* **45**, 205–223 (2014).
304. Javelle, A., Severi, E., Thornton, J. & Merrick, M. Ammonium Sensing in *Escherichia coli*: Role of the ammonium transporter AmtB and AmtB-GlnK complex formation. *Journal of Biological Chemistry* **279**, 8530–8538 (2004).
305. Kim, M. et al. Need-based activation of ammonium uptake in *Escherichia coli*. *Molecular Systems Biology* **8**, 616 (2012).
306. Baek, J. H. & Lee, S. Y. Novel gene members in the Pho regulon of *Escherichia coli*. *FEMS Microbiology Letters* **264**, 104–109 (2006).
307. Kirchhoff, C. & Cypionka, H. Propidium ion enters viable cells with high membrane potential during live-dead staining. *Journal of Microbiological Methods* **142**, 79–82 (2017).
308. Yang, Y., Xiang, Y. & Xu, M. From red to green: the propidium iodide-permeable membrane of *Shewanella decolorationis* S12 is repairable. *Scientific Reports* **5**, (2016).
309. Auty, M. A. E. et al. Direct *in situ* viability assessment of bacteria in probiotic dairy products using viability staining in conjunction with confocal scanning laser microscopy. *Applied and Environmental Microbiology* **67**, 420–425 (2001).
310. Rosenberg, M., Azevedo, N. F. & Ivask, A. Propidium iodide staining underestimates viability of adherent bacterial cells. *Scientific Reports* **9**, (2019).
311. Stone, M. R. L., Butler, M. S., Phetsang, W., Cooper, M. A. & Blaskovich, M. A. T. Fluorescent Antibiotics: New Research Tools to Fight Antibiotic Resistance. *Trends in Biotechnology* **36**, 523–536 (2018).
312. Wang, W. & Chen, X. Antibiotics-based fluorescent probes for selective labeling of Gram-negative and Gram-positive bacteria in living microbiotas. *Science China Chemistry* **61**, 792–796 (2018).
313. Allen, J. P. et al. BODIPY-Based Profluorescent Probes Containing Meso - and  $\beta$ -Substituted Isoindoline Nitroxides: BODIPY-Based Profluorescent Probes Containing Meso - and  $\beta$ -Substituted Isoindoline Nitroxides. *European Journal of Organic Chemistry* **2017**, 476–483 (2017).

314. Verderosa, A. D., Dhouib, R., Fairfull-Smith, K. E. & Totsika, M. Profluorescent Fluoroquinolone-Nitroxides for Investigating Antibiotic–Bacterial Interactions. *Antibiotics* **8**, (2019).
315. Lagree, K., Desai, J. V., Finkel, J. S. & Lanni, F. Microscopy of fungal biofilms. *Current Opinion in Microbiology* **43**, 100–107 (2018).
316. Thomsen, H. et al. Delivery of cyclodextrin polymers to bacterial biofilms — An exploratory study using rhodamine labelled cyclodextrins and multiphoton microscopy. *International Journal of Pharmaceutics* **531**, 650–657 (2017).
317. Dryden, M. S. Skin and soft tissue infection: microbiology and epidemiology. *International Journal of Antimicrobial Agents* **34**, S2–S7 (2009).
318. Percival, S. L., Emanuel, C., Cutting, K. F. & Williams, D. W. Microbiology of the skin and the role of biofilms in infection. *International Wound Journal* **9**, 14–32 (2012).
319. Ribet, D. & Cossart, P. How bacterial pathogens colonize their hosts and invade deeper tissues. *Microbes and Infection* **17**, 173–183 (2015).
320. Backhed, F. Host-Bacterial Mutualism in the Human Intestine. *Science* **307**, 1915–1920 (2005).
321. Eckburg, P. B. Diversity of the Human Intestinal Microbial Flora. *Science* **308**, 1635–1638 (2005).
322. Fung, T. C., Artis, D. & Sonnenberg, G. F. Anatomical localization of commensal bacteria in immune cell homeostasis and disease. *Immunological Reviews* **260**, 35–49 (2014).
323. Koskella, B., Hall, L. J. & Metcalf, C. J. E. The microbiome beyond the horizon of ecological and evolutionary theory. *Nature Ecology & Evolution* **1**, 1606–1615 (2017).
324. Leggett, R. M. et al. Rapid MinION profiling of preterm microbiota and antimicrobial-resistant pathogens. *Nature Microbiology* (2019) doi:10.1038/s41564-019-0626-z.
325. Davies, J. Specialized microbial metabolites: functions and origins. *The Journal of Antibiotics* **66**, 361–364 (2013).
326. Niu, G., Chater, K. F., Tian, Y., Zhang, J. & Tan, H. Specialised metabolites regulating antibiotic biosynthesis in *Streptomyces* spp. *FEMS Microbiology Reviews* **40**, 554–573 (2016).
327. Galey, M. M. & Sanchez, L. M. Spatial Analyses of Specialized Metabolites: The Key to Studying Function in Hosts. *mSystems* **3**, (2018).
328. Tobias, N. J. & Bode, H. B. Heterogeneity in Bacterial Specialized Metabolism. *Journal of Molecular Biology* **431**, 4589–4598 (2019).
329. Yang, X. B., Bhatnagar, R. S., Li, S. & Oreffo, R. O. C. Biomimetic Collagen Scaffolds for Human Bone Cell Growth and Differentiation. **14** (2004).
330. Glowacki, J. & Mizuno, S. Collagen scaffolds for tissue engineering. *Biopolymers* **89**, 338–344 (2008).
331. Kanta, J. Collagen matrix as a tool in studying fibroblastic cell behavior. *Cell Adhesion & Migration* **9**, 308–316 (2015).

332. Modulevsky, D. J., Lefebvre, C., Haase, K., Al-Rekabi, Z. & Pelling, A. E. Apple Derived Cellulose Scaffolds for 3D Mammalian Cell Culture. *PLoS ONE* **9**, e97835 (2014).
333. Tibbitt, M. W. & Anseth, K. S. Hydrogels as extracellular matrix mimics for 3D cell culture. *Biotechnology and Bioengineering* **103**, 655–663 (2009).
334. Frampton, J. P., Hynd, M. R., Shuler, M. L. & Shain, W. Fabrication and optimization of alginate hydrogel constructs for use in 3D neural cell culture. *Biomedical Materials* **6**, 015002 (2011).
335. Hilderbrand, A. M., Ford, E. M., Guo, C., Sloppy, J. D. & Kloxin, A. M. Hierarchically structured hydrogels utilizing multifunctional assembling peptides for 3D cell culture. *Biomaterials Science* (2020) doi:10.1039/C9BM01894H.
336. Andrée, B. et al. Formation of three-dimensional tubular endothelial cell networks under defined serum-free cell culture conditions in human collagen hydrogels. *Scientific Reports* **9**, (2019).
337. Toh, Y.-C. et al. A novel 3D mammalian cell perfusion-culture system in microfluidic channels. *Lab on a Chip* **7**, 302 (2007).
338. Janssen, P. H. Identifying the Dominant Soil Bacterial Taxa in Libraries of 16S rRNA and 16S rRNA Genes. *Applied and Environmental Microbiology* **72**, 1719–1728 (2006).
339. Williams, S. T. & Vickers, J. C. Detection of Actinomycetes in the natural environment: problems and perspectives. in *Biology of actinomycetes* 165–270 (Japan Scientific Societies Press, 1988).
340. Goodfellow, M. & Williams, S. T. Ecology of Actinomycetes. *Annual Review of Microbiology* **37**, 189–216 (1983).
341. Olano, C., Méndez, C. & Salas, J. Antitumor Compounds from Marine Actinomycetes. *Marine Drugs* **7**, 210–248 (2009).
342. Ahmad, M. S. et al. Exploring the Antimicrobial and Antitumor Potentials of *Streptomyces* sp. AGM12-1 Isolated from Egyptian Soil. *Frontiers in Microbiology* **8**, (2017).
343. Zhao, H. et al. Potential of *Bacillus subtilis* lipopeptides in anti-cancer I: induction of apoptosis and paraptosis and inhibition of autophagy in K562 cells. *AMB Express* **8**, (2018).
344. Kronheim, S. et al. A chemical defence against phage infection. *Nature* **564**, 283–286 (2018).
345. Pimentel-Elardo, S. M. et al. Anti-Parasitic Compounds from *Streptomyces* sp. Strains Isolated from Mediterranean Sponges. *Marine Drugs* **8**, 373–380 (2010).
346. Barka, E. A. et al. Taxonomy, Physiology, and Natural Products of Actinobacteria. *Microbiology and Molecular Biology Reviews* **80**, 1–43 (2016).
347. Pawlik, K., Kotowska, M., Chater, K. F., Kuczek, K. & Takano, E. A cryptic type I polyketide synthase (cpk) gene cluster in *Streptomyces coelicolor* A3(2). *Archives of Microbiology* **187**, 87–99 (2007).

348. Ohnishi, Y. et al. Genome Sequence of the Streptomycin-Producing Microorganism *Streptomyces griseus* IFO 13350. *Journal of Bacteriology* **190**, 4050–4060 (2008).
349. Oliynyk, M. et al. Complete genome sequence of the erythromycin-producing bacterium *Saccharopolyspora erythraea* NRRL23338. *Nature Biotechnology* **25**, 447–453 (2007).
350. Udvary, D. W. et al. Genome sequencing reveals complex secondary metabolome in the marine actinomycete *Salinispora tropica*. *Proceedings of the National Academy of Sciences* **104**, 10376–10381 (2007).
351. Santhi, L. S., Vssli, P. T., Sy, N. & Krishna E, R. Bioactive Compounds from Marine Sponge Associates: Antibiotics from *Bacillus* sp.. *Natural Products Chemistry & Research* **05**, (2017).
352. Stein, T. *Bacillus subtilis* antibiotics: structures, syntheses and specific functions. *Molecular Microbiology* **56**, 845–857 (2005).
353. Bush, M. J., Tschowri, N., Schlimpert, S., Flärdh, K. & Buttner, M. J. c-di-GMP signalling and the regulation of developmental transitions in streptomycetes. *Nature Reviews Microbiology* **13**, 749–760 (2015).
354. Liu, G., Chater, K. F., Chandra, G., Niu, G. & Tan, H. Molecular Regulation of Antibiotic Biosynthesis in *Streptomyces*. *Microbiology and Molecular Biology Reviews* **77**, 112–143 (2013).
355. Hoskisson, P. A. & Fernández-Martínez, L. T. Regulation of specialised metabolites in Actinobacteria - expanding the paradigms. *Environmental Microbiology Reports* **10**, 231–238 (2018).
356. Kong, D., Wang, X., Nie, J. & Niu, G. Regulation of Antibiotic Production by Signaling Molecules in *Streptomyces*. *Frontiers in Microbiology* **10**, (2019).
357. Flärdh, K. Essential role of DivIVA in polar growth and morphogenesis in *Streptomyces coelicolor* A3(2). *Molecular Microbiology* **49**, 1523–1536 (2003).
358. Howell, M. & Brown, P. J. Building the bacterial cell wall at the pole. *Current Opinion in Microbiology* **34**, 53–59 (2016).
359. Claessen, D., Rozen, D. E., Kuipers, O. P., Søgaard-Andersen, L. & van Wezel, G. P. Bacterial solutions to multicellularity: a tale of biofilms, filaments and fruiting bodies. *Nature Reviews Microbiology* **12**, 115–124 (2014).
360. Elliot, M. A. The chaplins: a family of hydrophobic cell-surface proteins involved in aerial mycelium formation in *Streptomyces coelicolor*. *Genes & Development* **17**, 1727–1740 (2003).
361. Willey, J. M., Willems, A., Kodani, S. & Nodwell, J. R. Morphogenetic surfactants and their role in the formation of aerial hyphae in *Streptomyces coelicolor*. *Molecular Microbiology* **59**, 731–742 (2006).
362. Capstick, D. S., Willey, J. M., Buttner, M. J. & Elliot, M. A. SapB and the chaplins: connections between morphogenetic proteins in *Streptomyces coelicolor*. *Molecular Microbiology* **64**, 602–613 (2007).

363. Jong, W., Vijgenboom, E., Dijkhuizen, L., Wösten, H. A. B. & Claessen, D. SapB and the rodmins are required for development of *Streptomyces coelicolor* in high osmolarity media. *FEMS Microbiology Letters* **329**, 154–159 (2012).
364. Ohnishi, Y., Seo, J.-W. & Horinouchi, S. Deprogrammed sporulation in *Streptomyces*. *FEMS Microbiology Letters* **216**, 1–7 (2002).
365. Flärdh, K. & Buttner, M. J. *Streptomyces* morphogenetics: dissecting differentiation in a filamentous bacterium. *Nature Reviews Microbiology* **7**, 36–49 (2009).
366. Jones, S. E. & Elliot, M. A. 'Exploring' the regulation of *Streptomyces* growth and development. *Current Opinion in Microbiology* **42**, 25–30 (2018).
367. McCormick, J. R. & Flärdh, K. Signals and regulators that govern *Streptomyces* development. *FEMS Microbiology Reviews* **36**, 206–231 (2012).
368. Den Hengst, C. D. et al. Genes essential for morphological development and antibiotic production in *Streptomyces coelicolor* are targets of BldD during vegetative growth. *Molecular Microbiology* **78**, 361–379 (2010).
369. Claessen, D., de Jong, W., Dijkhuizen, L. & Wösten, H. A. B. Regulation of *Streptomyces* development: reach for the sky! *Trends in Microbiology* **14**, 313–319 (2006).
370. Pope, M. K., Green, B. & Westpheling, J. The *bldB* Gene Encodes a Small Protein Required for Morphogenesis, Antibiotic Production, and Catabolite Control in *Streptomyces coelicolor*. *Journal of Bacteriology* **180**, 1556–1562 (1998).
371. Chater, K. F. & Chandra, G. The evolution of development in *Streptomyces* analysed by genome comparisons. *FEMS Microbiology Reviews* **30**, 651–672 (2006).
372. Elliot, M. A., Bibb, M. J., Buttner, M. J. & Leskiw, B. K. BldD is a direct regulator of key developmental genes in *Streptomyces coelicolor* A3(2). *Molecular Microbiology* **40**, 257–269 (2001).
373. Kaiser, B. K. & Stoddard, B. L. DNA recognition and transcriptional regulation by the WhiA sporulation factor. *Scientific Reports* **1**, (2011).
374. Yagüe, P., López-García, M. T., Rioseras, B., Sánchez, J. & Manteca, Á. Pre-sporulation stages of *Streptomyces* differentiation: state-of-the-art and future perspectives. *FEMS Microbiology Letters* **342**, 79–88 (2013).
375. Kieser, T., Bibb, M. J., Buttner, M. J., Chater, K. F. & Hopwood, D. A. *Practical streptomyces genetics*. (The John Innes Foundation, 2000).
376. Manteca, A. & Sanchez, J. *Streptomyces* Development in Colonies and Soils. *Applied and Environmental Microbiology* **75**, 2920–2924 (2009).
377. Zappelini, C., Alvarez-Lopez, V., Capelli, N., Guyeux, C. & Chalot, M. *Streptomyces* Dominate the Soil Under Betula Trees That Have Naturally Colonized a Red Gypsum Landfill. *Frontiers in Microbiology* **9**, (2018).
378. Kortemaa, H., Rita, H., Haahtela, K. & Smolander, A. Root-colonization ability of antagonistic *Streptomyces griseoviridis*. *Plant and Soil* **163**, 77–83 (1994).
379. Franco, C. et al. Actinobacterial endophytes for improved crop performance. *Australasian Plant Pathology* **36**, 524 (2007).

380. Bonaldi, M. et al. Colonization of lettuce rhizosphere and roots by tagged *Streptomyces*. *Frontiers in Microbiology* **6**, (2015).
381. Viaene, T., Langendries, S., Beirinckx, S., Maes, M. & Goormachtig, S. *Streptomyces* as a plant's best friend? *FEMS Microbiology Ecology* **92**, fiw119 (2016).
382. Jones, S. E. et al. *Streptomyces* exploration is triggered by fungal interactions and volatile signals. *eLife* **6**, (2017).
383. Jones, S. E. et al. *Streptomyces* Volatile Compounds Influence Exploration and Microbial Community Dynamics by Altering Iron Availability. **10**, 18 (2019).
384. Lewin, G. R. et al. Evolution and Ecology of Actinobacteria and Their Bioenergy Applications. *Annual Review of Microbiology* **70**, 235–254 (2016).
385. van der Meij, A., Worsley, S. F., Hutchings, M. I. & van Wezel, G. P. Chemical ecology of antibiotic production by Actinomycetes. *FEMS Microbiology Reviews* **41**, 392–416 (2017).
386. Granato, E. T., Meiller-Legrand, T. A. & Foster, K. R. The Evolution and Ecology of Bacterial Warfare. *Current Biology* **29**, R521–R537 (2019).
387. Choudoir, M., Rossabi, S., Gebert, M., Helmig, D. & Fierer, N. A Phylogenetic and Functional Perspective on Volatile Organic Compound Production by Actinobacteria. *mSystems* **4**, (2019).
388. Miyadoh, S. Research on antibiotic screening in Japan over the last decade: a producing microorganism approach. *Actinomycetologica* **7**, 100–106 (1993).
389. Tanaka, Y. & Omura, S. Agroactive compounds of microbial origin. 31.
390. Yim, G., Huimi Wang, H. & Davies, J. The truth about antibiotics. *International Journal of Medical Microbiology* **296**, 163–170 (2006).
391. Bernier, S. P. & Surette, M. G. Concentration-dependent activity in natural environments. *Frontiers in Microbiology* **4**, (2013).
392. Vaz Jauri, P., Bakker, M. G., Salomon, C. E. & Kinkel, L. L. Subinhibitory antibiotic concentrations mediate nutrient use and competition among soil *Streptomyces*. *PLoS ONE* **8**, e81064 (2013).
393. Ward, A. & Allenby, N. Genome mining for the search and discovery of bioactive compounds: The *Streptomyces* paradigm. *FEMS Microbiology Letters* (2018) doi:10.1093/femsle/fny240.
394. Xu, L. et al. Comparative Genomic Insights into Secondary Metabolism Biosynthetic Gene Cluster Distributions of Marine *Streptomyces*. *Marine Drugs* **17**, 498 (2019).
395. Abdelmohsen, U. R. et al. Elicitation of secondary metabolism in Actinomycetes. *Biotechnology Advances* **33**, 798–811 (2015).
396. Giudici, R., Pamboukian, C. R. D. & Facciotti, M. C. R. Morphologically structured model for antitumoral retamycin production during batch and fed-batch cultivations of *Streptomyces olindensis*. *Biotechnology and Bioengineering* **86**, 414–424 (2004).
397. Vecht-Lifshitz, S. E., Sasson, Y. & Braun, S. Nikkomycin production in pellets of *Streptomyces tendae*. *Journal of Applied Bacteriology* **72**, 195–200 (1992).

398. Sarrà, M., Casas, C. & Gòdia, F. Continuous production of a hybrid antibiotic by *Streptomyces lividans* T K21 pellets in a three-phase fluidized-bed bioreactor. *Biotechnology and Bioengineering* **53**, 601–610 (1997).
399. Jonsbu, E., McIntyre, M. & Nielsen, J. The influence of carbon sources and morphology on nystatin production by *Streptomyces noursei*. *Journal of Biotechnology* **95**, 133–144 (2002).
400. Park, Y., Tamura, S., Koike, Y., Toriyama, M. & Okabe, M. Mycelial pellet intrastucture visualization and viability prediction in a culture of *Streptomyces fradiae* using confocal scanning laser microscopy. *Journal of Fermentation and Bioengineering* **84**, 483–486 (1997).
401. Tokala, R. K. et al. Novel Plant-Microbe Rhizosphere Interaction Involving *Streptomyces lydicus* WYEC108 and the Pea Plant (*Pisum sativum*). *Applied and Environmental Microbiology* **68**, 2161–2171 (2002).
402. Clark, L. C. et al. Mammalian cell entry genes in *Streptomyces* may provide clues to the evolution of bacterial virulence. *Scientific Reports* **3**, (2013).
403. Zhao, Q. et al. Inoculation of soil by *Bacillus subtilis* Y-IVI improves plant growth and colonization of the rhizosphere and interior tissues of muskmelon (*Cucumis melo* L.). *Biology and Fertility of Soils* **47**, 507–514 (2011).
404. Cao, Y. et al. *Bacillus subtilis* SQR 9 can control Fusarium wilt in cucumber by colonizing plant roots. *Biology and Fertility of Soils* **47**, 495–506 (2011).
405. Huang, B., Lv, C., Zhuang, P., Zhang, H. & Fan, L. Endophytic colonisation of *Bacillus subtilis* in the roots of *Robinia pseudoacacia* L. *Plant Biology* **13**, 925–931 (2011).
406. Han, Q.-Q. et al. Beneficial soil bacterium *Bacillus subtilis* (GB03) augments salt tolerance of white clover. *Frontiers in Plant Science* **5**, (2014).
407. Allard-Massicotte, R. et al. *Bacillus subtilis* Early Colonization of *Arabidopsis thaliana* Roots Involves Multiple Chemotaxis Receptors. *mBio* **7**, (2016).
408. Posada, L. F., Álvarez, J. C., Romero-Tabarez, M., de-Bashan, L. & Villegas-Escobar, V. Enhanced molecular visualization of root colonization and growth promotion by *Bacillus subtilis* EA-CB0575 in different growth systems. *Microbiological Research* **217**, 69–80 (2018).
409. Mendis, H. C. et al. Strain-specific quantification of root colonization by plant growth promoting rhizobacteria *Bacillus firmus* I-1582 and *Bacillus amyloliquefaciens* QST713 in non-sterile soil and field conditions. *PLOS ONE* **13**, e0193119 (2018).
410. Wang, T. et al. Natural products from *Bacillus subtilis* with antimicrobial properties. *Chinese Journal of Chemical Engineering* **23**, 744–754 (2015).
411. Andryukov, B., Mikhailov, V. & Besednova, N. The Biotechnological Potential of Secondary Metabolites from Marine Bacteria. **16** (2019).
412. Caulier, S. et al. Overview of the Antimicrobial Compounds Produced by Members of the *Bacillus subtilis* Group. *Frontiers in Microbiology* **10**, (2019).
413. Kaspar, F., Neubauer, P. & Gimpel, M. Bioactive Secondary Metabolites from *Bacillus subtilis*: A Comprehensive Review. *Journal of Natural Products* **82**, 2038–2053 (2019).

414. Josephson, R. K. & Flessa, K. W. Cryolite: a medium for the study of burrowing aquatic organisms. *Limnology and Oceanography* **17**, 134–135 (1972).
415. Pauly, H. & Bailey, J. C. Genesis and evolution of the Ivigtut cryolite deposit, SW Greenland. (Commission for Scientific Research in Greenland, 1999).
416. Fluorotherm. Materials overview: FEP Properties. <https://www.fluorotherm.com/technical-information/materials-overview/fep-properties/> (2020).
417. Bhattacharya, M. et al. Nanofibrillar cellulose hydrogel promotes three-dimensional liver cell culture. *Journal of Controlled Release* **164**, 291–298 (2012).
418. Iskander, M. Modelling with transparent soils: visualizing soil structure interaction and multi phase flow, non-intrusively. (Springer, 2010).
419. Yuan, B. et al. Transparent Synthetic Soil and Its Application in Modeling of Soil-Structure Interaction Using Optical System. *Frontiers in Earth Science* **7**, (2019).
420. Ganiyu, A. A., Rashid, A. S. A. & Osman, M. H. Utilisation of transparent synthetic soil surrogates in geotechnical physical models: A review. *Journal of Rock Mechanics and Geotechnical Engineering* **8**, 568–576 (2016).
421. Leis, A. P., Schlicher, S., Franke, H. & Strathmann, M. Optically Transparent Porous Medium for Nondestructive Studies of Microbial Biofilm Architecture and Transport Dynamics. *Applied and Environmental Microbiology* **71**, 4801–4808 (2005).
422. Van Nguyen, T., Vu Nguyen, M., Nordheden, K. J. & He, W. Effect of Bulk and Surface Treatments on the Surface Ionic Activity of Nafion Membranes. *Journal of The Electrochemical Society* **154**, A1073 (2007).
423. Nieminen, L. Modelling Metabolic Switching in the Differentiating Bacterium *Streptomyces coelicolor*. (University of Strathclyde, 2012).
424. Thomas, L. et al. Metabolic Switches and Adaptations Deduced from the Proteomes of *Streptomyces coelicolor* Wild Type and *phoP* Mutant Grown in Batch Cultures. *Molecular & Cellular Proteomics* **11**, 18 (2012).
425. Schwedock, J., McCormick, J. R., Angert, E. R., Nodwell, J. R. & Losick, R. Assembly of the cell division protein FtsZ into ladder-like structures in the aerial hyphae of *Streptomyces coelicolor*. *Molecular Microbiology* **25**, 847–858 (1997).
426. Kotake, T., Yamanashi, Y., Imaizumi, C. & Tsumuraya, Y. Metabolism of L-arabinose in plants. *Journal of Plant Research* **129**, 781–792 (2016).
427. Hardwood, C. R. & Cutting, S. M. Molecular biological methods for *Bacillus*. (John Wiley & Sons, 1990).
428. Spizizen, J. Transformation of biochemically deficient strains of *Bacillus subtilis* by Deoxyribonucleaten. **7**.
429. Logan, N. A. & Berkeley, R. C. W. Identification of *Bacillus* Strains Using the API System. *Microbiology* **130**, 1871–1882 (1984).
430. Ryżak, M. & Bieganski, A. Methodological aspects of determining soil particle-size distribution using the laser diffraction method. *Journal of Plant Nutrition and Soil Science* **174**, 624–633 (2011).



431. Qi, F. et al. Soil particle size distribution characteristics of different land-use types in the Funiu mountainous region. *Soil and Tillage Research* **184**, 45–51 (2018).
432. Bibb, M. J. Regulation of secondary metabolism in streptomycetes. *Current Opinion in Microbiology* **8**, 208–215 (2005).
433. Sansinenea, E. & Ortiz, A. Secondary metabolites of soil *Bacillus spp.* *Biotechnology Letters* **33**, 1523–1538 (2011).
434. Liu, R., Deng, Z. & Liu, T. *Streptomyces* species: Ideal chassis for natural product discovery and overproduction. *Metabolic Engineering* **50**, 74–84 (2018).
435. Baral, B., Akhgari, A. & Metsä-Ketelä, M. Activation of microbial secondary metabolic pathways: Avenues and challenges. *Synthetic and Systems Biotechnology* **3**, 163–178 (2018).
436. Harwood, C. R., Mouillon, J.-M., Pohl, S. & Arnau, J. Secondary metabolite production and the safety of industrially important members of the *Bacillus subtilis* group. *FEMS Microbiology Reviews* **42**, 721–738 (2018).
437. Chevrete, M. G. et al. The antimicrobial potential of *Streptomyces* from insect microbiomes. *Nature Communications* **10**, (2019).
438. Zhao, Q., Wang, L. & Luo, Y. Recent advances in natural products exploitation in *Streptomyces* via synthetic biology. *Engineering in Life Sciences* **19**, 452–462 (2019).
439. Ochi, K. & Hosaka, T. New strategies for drug discovery: activation of silent or weakly expressed microbial gene clusters. *Applied Microbiology and Biotechnology* **97**, 87–98 (2013).
440. Zhu, H., Sandiford, S. K. & van Wezel, G. P. Triggers and cues that activate antibiotic production by Actinomycetes. *Journal of Industrial Microbiology & Biotechnology* **41**, 371–386 (2014).
441. Doull, J. L., Singh, A. K., Hoare, M. & Ayer, S. W. Conditions for the production of jadomycin-B by *Streptomyces venezuelae* ISP5230: Effects of heat shock, ethanol treatment and phage infection. *Journal of Industrial Microbiology* **13**, 120–125 (1994).
442. Chen, G., Wang, G.-Y.-S., Li, X., Waters, B. & Davies, J. Enhanced Production of Microbial Metabolites in the Presence of Dimethyl Sulfoxide. *The Journal of Antibiotics* **53**, 1145–1153 (2000).
443. Paranagama, P. A., Wijeratne, E. M. K. & Gunatilaka, A. A. L. Uncovering Biosynthetic Potential of Plant-Associated Fungi: Effect of Culture Conditions on Metabolite Production by *Paraphaeosphaeria quadriseptata* and *Chaetomium chiversii*. *Journal of Natural Products* **70**, 1939–1945 (2007).
444. Zheng, W. et al. Oxidative stress response of *Inonotus obliquus* induced by hydrogen peroxide. *Medical Mycology* **47**, 814–823 (2009).
445. Sarmiento-Vizcaíno, A. et al. Atmospheric Precipitations, Hailstone and Rainwater, as a Novel Source of *Streptomyces* Producing Bioactive Natural Products. *Frontiers in Microbiology* **9**, (2018).
446. Manteca, Á. & Yagüe, P. *Streptomyces* Differentiation in Liquid Cultures as a Trigger of Secondary Metabolism. *Antibiotics* **7**, 41 (2018).

447. Vincent, B., Király, Z., Emmett, S. & Beaver, A. The stability of silica dispersions in ethanol/ cyclohexane mixtures. *Colloids and Surfaces* **49**, 121–132 (1990).
448. Snowden, M. J., Williams, P. A., Garvey, M. J. & Robb, I. D. Phase separation of concentrated aqueous silica dispersions in the presence of nonadsorbed polyelectrolytes. *Journal of colloid and interface science* **166**, 160–167 (1994).
449. Ernebjerg, M. & Kishony, R. Distinct Growth Strategies of Soil Bacteria as Revealed by Large-Scale Colony Tracking. *Applied and Environmental Microbiology* **78**, 1345–1352 (2012).
450. Turpin, P. E., Maycroft, K. A., Rowlands, C. L. & Wellington, E. M. H. Viable but non-culturable *Salmonellas* in soil. *Journal of Applied Bacteriology* **74**, 421–427 (1993).
451. Ghezzi, J. I. & Steck, T. R. Induction of the viable but non-culturable condition in *Xanthomonas campestris* pv. *campestris* in liquid microcosms and sterile soil. *FEMS Microbiology Ecology* **30**, 203–208 (1999).
452. Stelting, S. A., Burns, R. G., Sunna, A. & Bunt, C. R. Survival in Sterile Soil and Atrazine Degradation of *Pseudomonas* sp. Strain ADP Immobilized on Zeolite. *Bioremediation Journal* **18**, 309–316 (2014).
453. Benamara, H. et al. Characterization of Membrane Lipidome Changes in *Pseudomonas aeruginosa* during Biofilm Growth on Glass Wool. *PLoS ONE* **9**, e108478 (2014).
454. Balsanelli, E., Baura, V. A. de, Pedrosa, F. de O., Souza, E. M. de & Monteiro, R. A. Exopolysaccharide Biosynthesis Enables Mature Biofilm Formation on Abiotic Surfaces by *Herbaspirillum seropedicae*. *PLoS ONE* **9**, e110392 (2014).
455. Ma, L. et al. Hydrogel-based transparent soils for root phenotyping *in vivo*. *Proceedings of the National Academy of Sciences* **116**, 11063–11068 (2019).
456. Schlöter, M. et al. Root colonization of different plants by plant-growth-promoting *Rhizobium leguminosarum* bv. *trifolii* R39 studied with monospecific polyclonal antisera. *Applied and environmental microbiology* **63**, 2038–2046 (1997).
457. Rodríguez-Navarro, D. N., Dardanelli, M. S. & Ruíz-Sañez, J. E. Attachment of bacteria to the roots of higher plants. *FEMS Microbiology Letters* **272**, 127–136 (2007).
458. Massalha, H., Korenblum, E., Malitsky, S., Shapiro, O. H. & Aharoni, A. Live imaging of root–bacteria interactions in a microfluidics setup. *Proceedings of the National Academy of Sciences* **114**, 4549–4554 (2017).
459. Kandel, S., Joubert, P. & Doty, S. Bacterial Endophyte Colonization and Distribution within Plants. *Microorganisms* **5**, 77 (2017).
460. Olanrewaju, O. S. & Babalola, O. O. *Streptomyces*: implications and interactions in plant growth promotion. *Applied Microbiology and Biotechnology* **103**, 1179–1188 (2019).
461. Yoolong, S. et al. Modulation of salt tolerance in Thai jasmine rice (*Oryza sativa* L. cv. KDML105) by *Streptomyces venezuelae* ATCC 10712 expressing ACC deaminase. *Scientific Reports* **9**, (2019).
462. Kaiser, D. Social gliding is correlated with the presence of pili in *Myxococcus xanthus*. *Proceedings of the National Academy of Sciences* **76**, 5952–5956 (1979).

463. Wu, S. S. & Kaiser, D. Markerless deletions of pil genes in *Myxococcus xanthus* generated by counterselection with the *Bacillus subtilis* sacB gene. *Journal of Bacteriology* **178**, 5817–5821 (1996).
464. Yanisch-Perron, C., Vieira, J. & Messing, J. Improved M13 phage cloning vectors and host strains: nucleotide sequences of the M13mp18 and pUC19 vectors. *Gene* **33**, 103–119 (1985).
465. Nieminen, L., Webb, S., Smith, M. C. M. & Hoskisson, P. A. A Flexible Mathematical Model Platform for Studying Branching Networks: Experimentally Validated Using the Model Actinomycete, *Streptomyces coelicolor*. *PLoS ONE* **8**, e54316 (2013).

# **Appendix I**

## **Bacterial Strains**

Strain ID	Genotype	Source
<i>Myxococcus xanthus</i> DK1622	WT	462
<i>M. xanthus</i> SA5293	DK1622 $\Delta aglQ$	243
<i>M. xanthus</i> DK10410	DK1622 $\Delta pilA$	463
<i>M. xanthus</i> SA7705	DK1622 $\Delta aglQ$ , $\Delta pilA$	Lotte Søgaaard-Andersen (MPI-Institute for Terrestrial Microbiology, Germany)
<i>Escherichia coli</i> JM105	WT, no fluorescent marker K12 derivative <i>thi rpsL endA sbcB15 hspR4</i> $\Delta(lac-proAB)$ (F' <i>traD36 proAB</i> <i>lacI<sup>q</sup> lacZ</i> $\Delta$ M15)	464 DSMZ, Germany
JM105-miniTn7- <i>gfp</i>	miniTn7 (Gm <sup>R</sup> ) <i>P<sub>rmb P1</sub> gfp-a</i>	283
JM105-miniTn7- <i>HcRed1</i>	miniTn7 (Gm <sup>R</sup> ) <i>P<sub>A1/04/03</sub> HcRed-a</i>	283
<i>Streptomyces coelicolor</i> M145	WT Prototrophic derivative of A3(2) lacking SCP1 and SCP2	375
M145- <i>idh-gfp</i>	LN108 M145 SCO7000::EGFP ( <i>idh-egfp</i> ), Apramycin <sup>R</sup>	423,465
<i>Bacillus subtilis</i> 168	WT, no fluorescent marker	Rut Carballido-Lopez, Institut National de la recherche Agronomique (INRA), Paris, France
<i>B. subtilis</i> CCBS189	<i>mbI::(mRuby2-mbl, cat)</i>	Rut Carballido-Lopez, INRA, Paris, France
<i>B. subtilis</i> JWV042	<i>cat, amyE::P<sub>hbs</sub>-hbs-gfp</i>	Rut Carballido-Lopez, INRA, Paris, France

# **Appendix II**

## **Bacterial growth media and buffers**

### **Clone Fruiting (CF) Agar**

Casitone/Casein Hydrolysate	150 mg
Sodium Pyruvate	1.0 g
Sodium Citrate	2.0 g
(NH <sub>4</sub> ) <sub>2</sub> SO <sub>3</sub>	200 mg
TrisHCl (1M) (pH 7.6)	10.0 ml
MgSO <sub>4</sub> •7H <sub>2</sub> O (1M)	8.0 ml
KH <sub>2</sub> PO <sub>4</sub> (1M)	1.0 ml
Agar	15.0 g
dH <sub>2</sub> O	1000 ml

Dissolve reagents in dH<sub>2</sub>O before adding to flask containing agar, then autoclave.

### **Double-Casitone Yeast Extract (DCYE) Medium**

Casitone/Casein Hydrolysate	20.0 g
Yeast Extract	2.0 g
MgSO <sub>4</sub> •7H <sub>2</sub> O (1M)	8.0 ml
TrisHCl (1M)	10.0 ml
Agar*	20.0 g
dH <sub>2</sub> O	1000 ml

\* concentration of agar can be adjusted to promote either A or S motility in

*Myxococcus xanthus*

### **Luria-Bertani (Miller)/Lysogeny Broth (LB) Medium**

Tryptone	10.0 g
Yeast Extract	5.0 g
NaCl	10.0 g
Agar	20.0 g
dH <sub>2</sub> O	1000 ml

### **M9 Minimal Medium**

#### 5x M9 Salts (1 L)

Na <sub>2</sub> HPO <sub>4</sub>	30.0 g
KH <sub>2</sub> PO <sub>4</sub>	15.0 g
NH <sub>4</sub> Cl	5.0 g
NaCl	2.5 g
CaCl <sub>2</sub>	15.0 mg
dH <sub>2</sub> O	1000 ml

Autoclave 5x salts solution.

#### 1.5% agar solution

Agar	15.0 g
dH <sub>2</sub> O	1000 ml

Autoclave 1.5% agar solution.



Cool 5x M9 salts and 1.5% agar solutions to 50°C and dilute 5x M9 salts to 1x with agar solution by mixing 200 ml 5x M9 salts with 800 ml 1.5% agar. Then add the following filter sterilised solutions aseptically per litre of agar.

MgSO <sub>4</sub> •7H <sub>2</sub> O (1 M)	1.0 ml
Carbon source solution (20% w/v)	10.0 ml

For liquid M9 medium, dilute 5x M9 salts in sterile dH<sub>2</sub>O and supplement with MgSO<sub>4</sub>•7H<sub>2</sub>O and the desired carbon source.

### **S7<sub>50</sub> defined minimal medium**

MOPS (pH adjusted to 7.0 with KOH)	50 mM
(NH <sub>4</sub> ) <sub>2</sub> SO <sub>4</sub>	10 mM
KH <sub>2</sub> PO <sub>4</sub> (pH 7.0)	5 mM
MgCl <sub>2</sub>	2 mM
CaCl <sub>2</sub>	0.7 mM
MnCl <sub>2</sub>	50 µM
ZnCl <sub>2</sub>	1 µM
Thiamine-HCl	1 µg/ml
HCl	20 µM
FeCl <sub>3</sub>	5 µM
dH <sub>2</sub> O	974 ml

Autoclave and add the following filter-sterilised solutions;

Carbon source solution (50% w/v)	20.0 ml
Glutamate (50% w/v)	2.0 ml
Casamino acids (1% w/v)	4.0 ml

### **Soya Flour Mannitol Agar (SFM/MS)**

Prepare the following solution;

Agar	20.0g
Mannitol	20.0 g
Soya Flour	20.0 g
Tap Water*	1000 ml

\* dH<sub>2</sub>O will not provide necessary trace elements.

Dissolve mannitol in water before adding to flasks with agar and soya flour.

### **Spizizen minimal (SM) medium**

(NH <sub>4</sub> ) <sub>2</sub> SO <sub>4</sub>	2.0 g
K <sub>2</sub> HPO <sub>4</sub>	14.0 g
KH <sub>2</sub> PO <sub>4</sub>	6.0 g
Na-Citrate•2H <sub>2</sub> O	1.0 g
MgSO <sub>4</sub> •7H <sub>2</sub> O	200 mg
dH <sub>2</sub> O	995 ml

Autoclave Spizizen salt solution before supplementing with filter sterilised carbon source solution;

Carbon source solution (50% w/v)	5.0 ml
----------------------------------	--------

### **Supplemented Minimal Medium, Solid (SMMS)**

Prepare the following solution and adjust pH to 7.2 with 5 N NaOH;

Casaminoacids	2.0 g
TES Buffer	5.73 g (25 mM Final)
dH <sub>2</sub> O	1000 ml

Pour 200ml into flasks containing 3.0g agar and autoclave. At time of use, melt and add each of the following filter sterilised solutions to the flasks;

NaH <sub>2</sub> PO <sub>4</sub> + K <sub>2</sub> HPO <sub>4</sub> (50mM of each)	2.0 ml (1 mM Final)
MgSO <sub>4</sub> (1M)	1.0 ml (5 mM Final)
Glucose (50% w/v)	3.6 ml (50 mM Final)
Trace Elements Solution (as in SMM)	0.2 ml
Required growth factors for auxotrophs*	1.5 ml

\* not required for M145

### **Yeast Extract Malt Extract (YEME) Medium (Modified)**

Agar	15.0 g
Yeast Extract	3.0 g
Peptone	5.0 g
Malt Extract	3.0 g
Glucose	10.0 g
Sucrose*	170.0 g
dH <sub>2</sub> O	1000 ml

\* Sucrose is not metabolised by M145 and therefore is not required.

### **Schwedock staining buffers**

#### Phosphate buffered saline (PBS)

NaCl	8.0 g
KCl	0.2 g
Na <sub>2</sub> HPO <sub>4</sub>	1.44 g
KH <sub>2</sub> PO <sub>4</sub>	240 mg
dH <sub>2</sub> O	800 ml

Adjust pH to 7.4 with HCl. Make up to 1000ml with dH<sub>2</sub>O

#### GTE buffer

Glucose (50% w/v)	180 µl
Tris-HCL (1 M, pH8.0)	200 µl
EDTA (1M, pH8.0)	2.0 ml
dH <sub>2</sub> O	7.62 ml

# Appendix III

## Published works

**Rooney, L.M.**, Kölln, L.S., Scrimgeour, R., Amos, W.B., Hoskisson, P.A., McConnell, G., (2020). Three-Dimensional Observations of an Aperiodic Oscillatory Gliding Behavior in *Myxococcus xanthus* Using Confocal Interference Reflection Microscopy. *mSphere*, 5; e00846-19.

<https://doi.org/10.1128/mSphere.00846-19>

**Rooney, L.M.**, Amos, W.B., Hoskisson, P.A., McConnell, G., (2020). Intra-colony channels in *E. coli* function as a nutrient uptake system. *ISME J.*

<https://doi.org/10.1038/s41396-020-0700-9>.

# Three-Dimensional Observations of an Aperiodic Oscillatory Gliding Behavior in *Myxococcus xanthus* Using Confocal Interference Reflection Microscopy

Liam M. Rooney,<sup>a</sup> Lisa S. Kölln,<sup>b</sup> Ross Scrimgeour,<sup>b</sup> William B. Amos,<sup>b</sup> Paul A. Hoskisson,<sup>a</sup> Gail McConnell<sup>b</sup>

<sup>a</sup>Strathclyde Institute of Pharmacy and Biomedical Sciences, University of Strathclyde, Glasgow, United Kingdom

<sup>b</sup>Department of Physics, SUPA, University of Strathclyde, Glasgow, United Kingdom

**ABSTRACT** The deltaproteobacterium *Myxococcus xanthus* is a model for bacterial motility and has provided unprecedented insights into bacterial swarming behaviors. Fluorescence microscopy techniques have been invaluable in defining the mechanisms that are involved in gliding motility, but these have almost entirely been limited to two-dimensional (2D) studies, and there is currently no understanding of gliding motility in a three-dimensional (3D) context. We present here the first use of confocal interference reflection microscopy (IRM) to study gliding bacteria, revealing aperiodic oscillatory behavior with changes in the position of the basal membrane relative to the substrate on the order of 90 nm *in vitro*. First, we use a model plano-convex lens specimen to show how topological information can be obtained from the wavelength-dependent interference pattern in IRM. We then use IRM to observe gliding *M. xanthus* bacteria and show that cells undergo previously unobserved changes in their adhesion profile as they glide. We compare the wild type with mutants that have reduced motility, which also exhibit the same changes in the adhesion profile during gliding. We find that the general gliding behavior is independent of the proton motive force-generating complex AgIRQS and suggest that the novel behavior that we present here may be a result of recoil and force transmission along the length of the cell body following firing of the type IV pili.

**IMPORTANCE** 3D imaging of live bacteria with optical microscopy techniques is a challenge due to the small size of bacterial cells, meaning that previous studies have been limited to observing motility behavior in 2D. We introduce the application of confocal multiwavelength interference reflection microscopy to bacteria, which enables visualization of 3D motility behaviors in a single 2D image. Using the model organism *Myxococcus xanthus*, we identified novel motility behaviors that are not explained by current motility models, where gliding bacteria exhibit aperiodic changes in their adhesion to an underlying solid surface. We concluded that the 3D behavior was not linked to canonical motility mechanisms and that IRM could be applied to study a range of microbiological specimens with minimal adaptation to a commercial microscope.

**KEYWORDS** 3D imaging, bacterial motility, gliding motility, label free, live-cell imaging, optical microscopy

Bacteria use a number of mechanisms to move through their local environment in response to chemotactic signals, to form communities or to invade their host. The most-studied mode of bacterial motility is flagellar-mediated movement. Other modes, such as the twitching motility displayed by *Pseudomonas aeruginosa*, use type IV pili (T4P) to direct movement based on the extension, adhesion, and retraction of polar filaments from the leading pole of the cell (1, 2). However, not all bacteria rely solely on

**Citation** Rooney LM, Kölln LS, Scrimgeour R, Amos WB, Hoskisson PA, McConnell G. 2020. Three-dimensional observations of an aperiodic oscillatory gliding behavior in *Myxococcus xanthus* using confocal interference reflection microscopy. *mSphere* 5:e00846-19. <https://doi.org/10.1128/mSphere.00846-19>.

**Editor** Katherine McMahon, University of Wisconsin—Madison

**Copyright** © 2020 Rooney et al. This is an open-access article distributed under the terms of the [Creative Commons Attribution 4.0 International license](https://creativecommons.org/licenses/by/4.0/).

Address correspondence to Liam M. Rooney, [liam.rooney@strath.ac.uk](mailto:liam.rooney@strath.ac.uk).

**Twitter** 3D gliding behaviours in *Myxococcus xanthus* identified using a multi-wavelength confocal interference microscopy method.

Reported by @lrmr\_1994, @liskoein, @RCScrimgeour, @WilliamBAmos, @PaulHoskisson & @gailmcconnell (@StrathScience @UniStrathclyde)

**Received** 14 November 2019

**Accepted** 13 January 2020

**Published** 29 January 2020

extracellular appendages for motility. The phenomenon of gliding motility has been identified in a diverse range of bacterial species spanning various phyla (3–8). The deltaproteobacterium *Myxococcus xanthus* displays two different modes of gliding motility, adventurous motility and social motility, to seek out nutrients or prey as part of its complex life cycle (4, 9–15).

There are contrasting models proposed to explain the mechanisms underpinning gliding motility (9, 16–19). The focal adhesion complex (FAC) model proposes that FACs form on the basal surface of the cell and attach to the underlying substrate while coupling to the helical MreB cytoskeleton on the cell's inner membrane (16, 17, 20, 21). It has been shown that FACs translocate linearly from the leading pole as the cell moves forward, which is driven by the force generated by the AglRQS gliding complex, which is associated with the FAC (16, 22). The FAC model requires the basal layer of the cell to be firmly attached to the underlying substrate; however, it remains unclear how the complex is able to traverse the peptidoglycan cell wall without compromising the structural integrity of the cell (8, 19). A second model has been suggested where proton motive force (PMF) generated by AglRQS results in a helical rotation of the MreB cytoskeleton in gliding cells that are firmly adhered to a solid substrate (9, 22–25). In the helical rotation model, stationary foci of fluorescently tagged motor complex subunits have been explained as being a buildup of multiple complexes arrayed in “traffic jams,” which result from areas of differing resistance in the underlying substrate (9, 24). Both models converge where the gliding cell is adhered firmly to the surface of the underlying substrate to facilitate gliding. However, our observations show that cells are not in fact firmly adhered during gliding motility but instead exhibit aperiodic fluctuations in surface adhesion as they glide.

Bacterial gliding motility has mainly been studied using phase-contrast and fluorescence microscopy techniques, which do not provide three-dimensional (3D) information about cell movement (9, 17, 22, 26). We hypothesized that axial changes in cell shape during gliding motility may occur due to the complex nature of underlying mechanisms such as FAC translocation and bulk movement of the cytoskeleton. We reasoned that novel motility behaviors could be visualized using the label-free microscopy technique interference reflection microscopy (IRM) to detect cell shape changes in 3D. This relatively low-cost and easily implemented technique for existing microscope systems has previously been used to study focal adhesion sites of eukaryotic cells on glass substrates (27–34) and microtubule dynamics (35–37). Previous studies have used wide-field IRM to observe gliding motility in *Cytophaga* spp., where rotation and adhesion to glass surfaces were characterized (4). Wide-field IRM has also been used to investigate twitching motility in *Pseudomonas fluorescens*, where the attachment profile of twitching cells was found to be dependent on the presence of different electrolytes (38). However, wide-field IRM images have a low contrast between the orders of interference due to the short coherence length of the light source. The contrast of higher-order interference fringes can be improved by using IRM in confocal mode where coherent laser light is used and the out-of-focus signal is significantly reduced by incorporating a pinhole before the photodetector (39).

In IRM, the specimen is illuminated via the lens objective, and the same objective serves to capture the signal originating from the interference of reflected light at refractive index boundaries within a live-cell specimen that is plated on a glass coverslip. Methods for adjusting the epicondenser were described previously by Izzard and Lochner and by Verschuere, who recommended that contributions to the image from the dorsal side of the cell (i.e., the side most distant from the cover glass) could be reduced in wide-field mode by opening the illumination aperture fully and that glare could be lessened by reducing a field aperture to illuminate only the cell under observation (40, 41). Confocal scanning optical microscopes introduced in the 1980s were mainly used for epifluorescence microscopy but also proved to work well for IRM when a beam splitter was substituted for the chromatic reflector in the beam path. Indeed, it became possible to study individual microtubules gliding over glass substrates in a motility assay, which had not been reported with wide-field IRM, indicating

that the use of confocal optics increases the sensitivity of IRM, perhaps by orders of magnitude (35, 39, 42).

In either wide-field or confocal mode, the IRM image is formed by the same principle. Reflected light originating from the coverslip-medium and the medium-cell interfaces results in constructive and deconstructive interference, dependent on the optical path length difference between both. The resulting fringe pattern can be used to estimate the axial position of the cell surface (see "Background theory," below) (41, 43). Using IRM, a 5-fold axial resolution enhancement is achieved over conventional wide-field or point-scanning microscopy techniques, where 3D information can be extracted from a two-dimensional (2D) image, thus overcoming the limitations in optical sectioning of thin specimens (i.e., bacteria) (27, 41, 43). An additional benefit of IRM in comparison to other similar methods is that it requires almost no adaptation to a standard confocal or wide-field microscope and is compatible with existing lens objectives. Additionally, no fluorescence labeling of the specimen is required.

The application of IRM to biological specimens has been documented since the 1960s, but the interpretation of IRM data can be difficult (27). Theoretically, the axial resolution of IRM can be as high as 15 nm (27), but in practice, factors such as dense protein aggregates, the transport of dry mass to the basal membrane, changes in local membrane density, and the proximity of intracellular structures to the membrane affect the brightness of the detected IRM image (41, 44). However, in thin specimens such as bacterial cells, where internal shifting of dry mass is unlikely due to the lack of intracellular vesicular transport, IRM remains a viable height-measuring technique (45). Godwin et al. found that separation between the cell and the coverslip on the order of 100 nm can be easily distinguished without an influence from ambiguities introduced by the above-listed factors (4). Others have disputed the ability of IRM to accurately measure close-contact sites in live cells, for example, by imaging the displacement of a thin layer of fluorescent dye between adherent cells and the cover glass with total internal reflection fluorescence (TIRF) microscopy (46). In the present work, it is assumed that the IRM contrast of bacterial specimens is an indication of the height of the cell surface above the substrate (see "Background theory," below).

This study is the first application of confocal IRM to bacterial specimens. However, previous studies have used similar techniques as a means of contrast enhancement. One such study used reflection interference contrast microscopy (RICM), where polarizing filters and an antireflective objective are used to filter out reflected light outside the specimen plane and increase the image contrast (39, 47, 48), to image only *M. xanthus* surface detachment from the cover glass (17). TIRF microscopy has also shown that FACs that attach to and rotate the MreB cytoskeleton are found in distinct foci on the basal side of the cell (9, 16). These membrane-associated complexes have been suggested to change the surface topology of the gliding cell depending on the cargo load of the molecular motor (9). More recently, interferometric scattering microscopy (iSCAT), which detects both reflected and scattered light, has been used to observe T4P-mediated twitching motility in *P. aeruginosa*. In that work, the authors generated 3D illustrations that revealed the role of T4P machinery subunits in extension, attachment, and retraction based on the interference pattern in iSCAT images (49).

**Background theory.** For the image formation theory in IRM, a simplified three-layer model system is assumed, which consists of only the cover glass (*g*), the cell medium (*m*), and the cell (*c*). In this model, the cell medium can be viewed as a thin film with varying height, dependent on how closely the cell is attached to the coverslip. The intensity of the reflected light,  $I_{g-m}$ , at an interface, for example, the cover glass-medium interface (*g-m*), follows the Fresnel equations:

$$I_{g-m} = I_0 \left( \frac{n_g - n_m}{n_g + n_m} \right)^2$$

where  $I_0$  is the intensity of the incident light beam and  $n_g$  and  $n_m$  are the respective refractive indices of the adjacent materials.



The reflected light beams at the cover glass-medium (*g-m*) and the medium-cell (*m-c*) interfaces coincide, leading to (de)constructive interference dependent on the optical path length difference, *z*, between the two beams (see Fig. S1 in the supplemental material). The intensity follows *I(z)*:

$$I(z) = I_{g-m} + I_{m-c} + 2\sqrt{I_{g-m}I_{m-c}}\cos\left(\frac{4\pi n_m}{\lambda}z + \delta\right)$$

where *n<sub>m</sub>* is the refractive index of the cell medium, *λ* is the wavelength of the light, and *δ* is the phase difference (50). Since the refractive index of the cell medium is smaller than the refractive index of the cell, a phase shift occurs upon reflection so that *δ* equals *π* (41). Accordingly, deconstructive interference occurs at optical path length differences of *z* = *N*(*λ*/2*n<sub>m</sub>*), and constructive interference occurs at *z* = (*N* + 1/2)(*λ*/2*n<sub>m</sub>*), with *N* = 0, 1, 2, ... as the interference order. This wavelength dependence can be used to extract the cell topology from IRM images since the overlap of the interference fringes of different wavelengths decreases with increasing distance between the cell and the cover glass. The decreasing fringe overlap increasing the separation between the cell and cover glass, as observable in color-merged IRM images obtained for different wavelengths, results in a clear color ordering along the cell body when the cell is lifted up from the cover glass.

Common assumptions of this IRM model are that no other refractive index boundary exists in the cell specimen (i.e., that the refractive index of the cell is constant) and that incident and reflected light are perpendicular to the cover glass (28). Also, the impact of the numerical aperture (NA) is neglected, which affects the depth of the field that is imaged. In IRM, high-NA objectives are used to limit the detection of reflection signals to those originating from interfaces close to the cover glass, which establishes an experimental condition that is close to the three-layer system consisting of the cover glass, the cell medium, and the cell body (39).

## RESULTS

**Characterization of the model specimen.** We characterized the axial height intensity profile of a specimen of known structure to compare with IRM theory by acquiring IRM images at different wavelengths of a planoconvex lens (focal length = 72 mm) that was placed on a cover glass. A composite of IRM images of the lens specimen acquired at 488 nm, 514 nm, and 543 nm is shown in Fig. 1a. In Fig. 1b, a cross-sectional schematic of a planoconvex lens specimen is shown, outlining the axial position of the intensity maxima that are caused by constructive interference for different orders and wavelengths. We analyzed the intensity of the interference fringes by comparing the radial intensity profile with the theory of IRM regarding fringe separation (27). We calculated that the theoretical spacings (*λ*/2*n*) between the intensity maxima caused by constructive interference for the different wavelengths are 244 nm, 258 nm, and 272 nm (*n* = 1). With the experimental data, we obtained slightly different spacings for the intensity maxima, 249 ± 1 nm, 262 ± 1 nm, and 277 ± 1 nm (Fig. 2b). Thus, experimental and expected values deviated by 2.07%, 1.63%, and 1.91% for the different wavelengths. Additionally, the overlap of the intensity maxima of different acquisition wavelengths decreased with lens-to-coverslip distance (Fig. 2). These observations provided a sense of directionality regarding specimen topology, where the curvature of the planoconvex lens specimen was clear from the acquired images and allowed 3D reconstruction of the lens specimen (Fig. 2c). This means that the assumptions outlined above (see "Background theory") are appropriate to reconstruct the morphology of simple model systems. Here, a multiwavelength IRM approach provides important additional morphological information over single-wavelength IRM.

**Axial changes along the cell body during gliding motility are independent of AgIQ.** To demonstrate the benefit of using confocal IRM over wide-field IRM, we first imaged wild-type *M. xanthus* on a commercial wide-field system. We demonstrated that low-contrast images are generated in wide-field IRM where interference fringes along the cell cannot be seen clearly. The raw wide-field data are presented with a

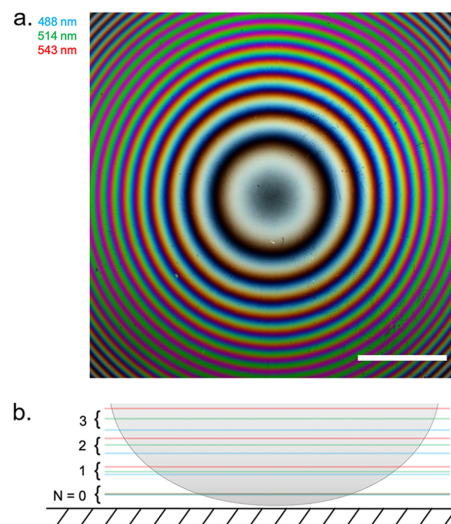


**FIG 1** IRM image and schematic diagram of a planoconvex lens specimen. (a) Composite IRM image acquired using wavelengths at 488 nm, 514 nm, and 543 nm, which are false colored as indicated. As the concentric fringes propagate away from the cover glass, we observed spectral separation of the fringes. Bar = 200  $\mu$ m. (b) Cross-sectional schematic of the lens specimen showing the color ordering of each acquisition wavelength as the fringes propagate axially from the cover glass.

magnified region showing gliding cells (Fig. S2a) accompanied by the background-corrected data (Fig. S2b). Interference fringes cannot be clearly resolved in either the raw or corrected data, meaning that a wide-field approach is not suitable for studying the changing adhesion profile of gliding bacterial cells.

Using confocal IRM, we observed previously undocumented changes in the axial position of *M. xanthus* cells as they glide. Figure 3a shows a single frame from a background-corrected (see the supplemental material) multiwavelength confocal IRM time-lapse recording of wild-type cells with a magnified view of a representative cell at different time points throughout the time series (the full data set is provided in Movie S1). In Fig. 3a, clearly resolved interference fringes along the cell body indicate that the cell is not completely attached to the cover glass but that the cell-to-cover glass distance varies along the cell body. There is a clear aperiodic change in the fringe pattern over time, which indicates changes in the adhesion profile of the cell body during gliding. Interpreting the color ordering of these fringes, as with the lens specimen, shows that part of the cell body is lifted up from the glass substrate. This observed change in the adhesion profile opposes the current theory that gliding cells firmly adhere along the cell body as they glide. Height changes also show no synchronicity between nearby gliding cells.

Figure 3b shows a single frame from a background-corrected multiwavelength confocal IRM time-lapse recording of a DK1622  $\Delta aglQ$  strain with a magnified view of a representative gliding cell (the full data set is provided in Movie S2). The deletion of *aglQ* results in a loss of PMF from the AglRQS complex, which in turn prevents the rotation of the MreB cytoskeleton and transit of the FAC along the cell body (23). Figure 3b shows that the fluctuations in cell topology present in the wild type are also present in DK1622  $\Delta aglQ$ . This conserved motility behavior suggests that axial changes in the cell body during gliding are independent of PMF-driven translocation of FACs along the cell body and are not linked to the proposed membrane protrusions reported in other studies. We then investigated if T4P were responsible for the changes in the

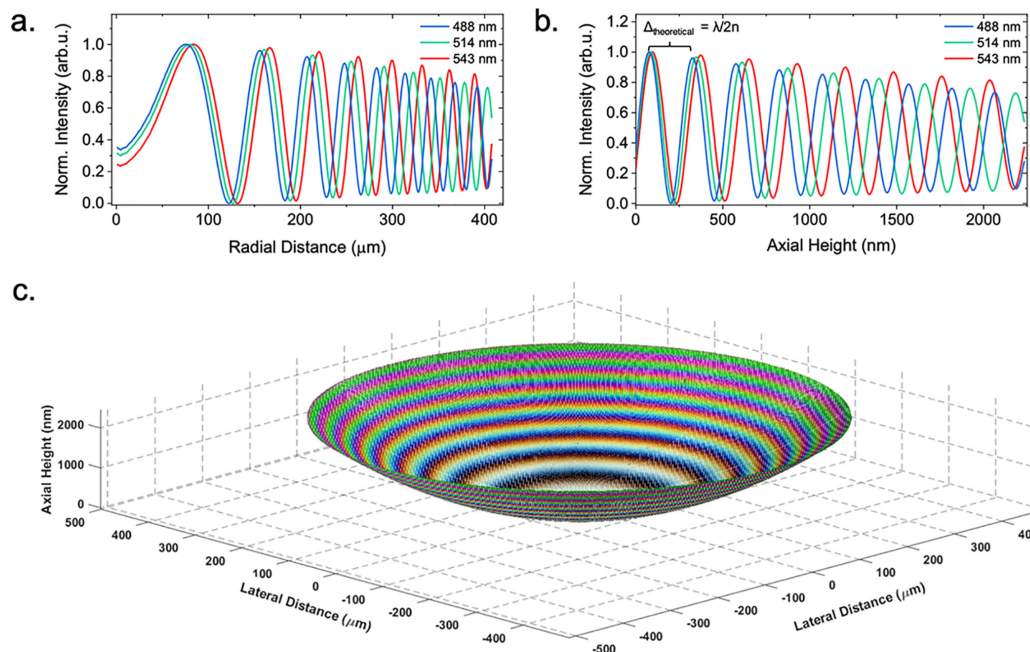


**FIG 2** 3D reconstruction of a planoconvex lens specimen. (a) Radial intensity profile of the interference fringe pattern shown in Fig. 1a. We observed the fringe periodicity decrease as observed in the RGB IRM image. (b) Using *a priori* knowledge of the lens specimen, the axial height was calculated and used to plot the intensity of each pixel as a function of height. arb.u., arbitrary units. (c) 3D reconstruction of the lens specimen using the known *x*, *y*, and *z* values and intensity extracted from the 2D IRM image.

adhesion profile that we report. The deletion of the T4P subunit PilA resulted in cells being unable to adhere to the cover glass and initiate gliding (Movies S3 and S4).

**Using multiwavelength IRM for extracting 3D directionality.** Figure 4 illustrates how multiwavelength IRM data can be assessed qualitatively to understand the geometry of a single gliding *M. xanthus* cell (additional gliding morphologies are presented in Fig. S3). A representative wild-type gliding cell is presented, where multicolor fringes can be observed along the cell body (Fig. 4a). In the IRM image, lifting of the cell body is clearly indicated by an alternating fringe pattern along the body. By interpreting the intensity plot profile along the cell body (Fig. 4b), we can extract qualitative topological information about cell morphology. Figure 4b shows a cyan fringe ( $\lambda = 488$  nm) followed by a magenta fringe ( $\lambda = 635$  nm), and based on this, we can conclude that the cell body was attached to the cover glass at the leading pole before the basal surface raised to a height of approximately 180 nm. A cartoon diagram approximating the shape of the cell body is shown in Fig. 4c. The IRM data indicate a variety of cell orientations and shapes that occur during gliding motility. Examples of additional morphologies are presented in Fig. S3. These include an undulating topology where the cell is attached to the cover glass at the leading pole, while the cell body raises to a height of approximately 180 nm before falling to 90 nm and again raising to 180 nm at the lagging pole (Fig. S3a). Another cell motility behavior is depicted at the point of surface attachment prior to the start of gliding, where the leading pole of the cell is attached to the cover glass and the cell body projects upward into the liquid medium at a sharp incline of approximately  $60^\circ$  relative to the cover glass (Fig. S3b).

**Using IRM to measure the velocity of gliding cells.** We used IRM to determine the mean velocity of motile cells and showed that the deletion of *aglQ* decreased the

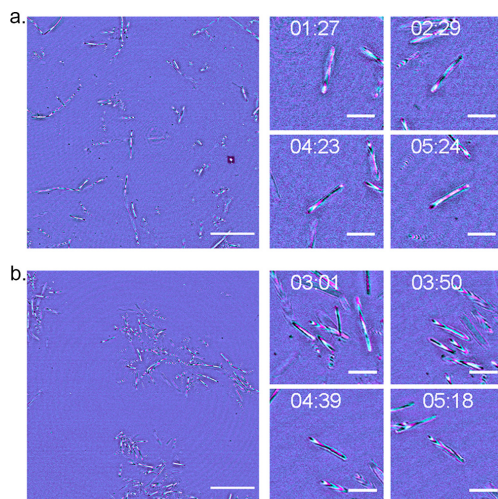


**FIG 3** IRM reveals axial movements along the cell body during gliding motility. (a) A single frame from a wild-type DK1622 gliding specimen with 4 magnified regions of interest (ROI) of a single representative cell over the course of the time-lapse (from  $t = 1 \text{ min } 27 \text{ s}$  to  $t = 5 \text{ min } 24 \text{ s}$ ). Images were acquired using a multiwavelength approach, with the reflected 488-nm signal false colored in cyan and the reflected 635-nm signal shown in magenta. As the cell glides across the solid substrate, the interference fringe pattern changes as the relative position of the cell to the cover glass fluctuates. (b) A single frame of DK1622  $\Delta aglQ$  with magnified ROI from a single representative gliding cell over the course of the time-lapse (from  $t = 3 \text{ min } 1 \text{ s}$  to  $t = 5 \text{ min } 18 \text{ s}$ ). Images were acquired using incident light at 488 nm (cyan) and 635 nm (magenta). DK1622  $\Delta aglQ$  exhibits the same axial movements as the wild type, demonstrated by the presence of interference fringes which fluctuate as the cell glides. Full time series data for DK1622 and DK1622  $\Delta aglQ$  are presented in Movies S1 and S2 in the supplemental material, respectively. Bars =  $20 \mu\text{m}$  (single frame) and  $5 \mu\text{m}$  (ROI).

length of time that cells remain adhered to the glass substrate compared to the wild type (Fig. 5a). This implies that *AgIQ* is responsible for maintaining adherence to the cover glass during gliding. The mean velocity of gliding cells was determined by measuring the displacement of the cells over time as they glide, selecting cells with an approximately linear trajectory. We found a 41.2% decrease in the mean velocity of DK1622  $\Delta aglQ$  (mean velocity =  $9.26 \pm 0.72 \mu\text{m}/\text{min}$ ) compared with the wild type (mean velocity =  $15.76 \pm 0.89 \mu\text{m}/\text{min}$ ), which concurs with their altered motility phenotype (Fig. 5b).

## DISCUSSION

We report aperiodic changes in the adhesion profile of gliding myxobacteria using the label-free technique IRM. Given that previous studies had failed to identify any axial behaviors in gliding cells due to the drawbacks of conventional imaging techniques, we hypothesized that changes in cell height from the substrate may arise due to the complex mechanisms that govern gliding motility. The data presented here show new behavior in gliding myxobacteria that do not support the current gliding motility models. The behaviors that we report suggest that there are additional factors that mediate gliding motility and show the benefit of using IRM to extract 3D information from bacterial specimens by using an easily implemented microscopy technique.

The current consensus is that gliding cells must be firmly attached to a solid surface to facilitate gliding; however, these data show that this is not the case. Our results show that throughout gliding, cells undergo changes in the axial position of their basal surface on the order of 90 to 180 nm. This new information indicates that the helical rotation and FAC motility models do not fully explain the mechanisms of bacterial

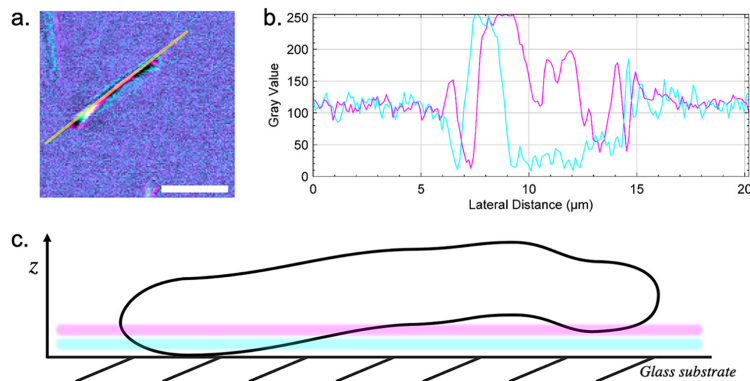


**FIG 4** The interference fringe patterns of a gliding cell reveal the axial profile of the cell. (a) A representative DK1622 cell from a time series data set with the location where the intensity profile in panel b was measured. Interference fringes along the cell body can be observed, with the reflected 488-nm signal shown in cyan and the 635-nm signal in magenta. Bar = 5  $\mu\text{m}$ . (b) Intensity plot profile from the line through the cell presented in panel a. The plot shows the maxima and minima of the interference fringes acquired using both 488-nm (cyan) and 635-nm (magenta) light. The spectral separation of the two interference patterns can also be observed. Axial directionality of the cell can be determined by interpreting the color ordering of the fringes, where fringes arising from the longer wavelength appear after those from the shorter wavelength when the cell is inclined, and the opposite is observed for declining slopes. The plot was acquired by averaging the signal over a line width of 3 pixels (0.3  $\mu\text{m}$ ). (c) Schematic of the  $x, z$  profile of the cell shown in panel a according to the color ordering and intensity profile in panel b. The axial positions of the colored fringes from each acquisition wavelength are also shown. The cell has not adhered to the solid surface during gliding and does not maintain a linear cylindrical profile along the length of the cell body. According to theory, regions that intersect the axial position of the first-order 488-nm maxima are located 91.7 nm above the substratum, and those for the first-order 635-nm maxima are located 119.3 nm above the substratum. The schematic is not drawn to scale.

gliding. One previous study used RICM to investigate the adhesion profile of myxobacteria during detachment (17). However, those authors did not report any fringes along the cell body or any aperiodic changes in adhesion in gliding cells. This is likely due to the poor contrast of wide-field IRM and RICM compared to confocal IRM, which prohibits the detection of higher interference fringe orders. It is important to also note that some researchers have claimed that the ability of IRM to detect regions of close contact is questionable due to the inhomogeneous refractive index of the cytosol proximal to the plasma membrane and from self-interference from higher fringe orders within the cell (44, 46). However, these claims are based solely on observations of mammalian cells using wide-field IRM. Owing to the lack of vesicular trafficking and the

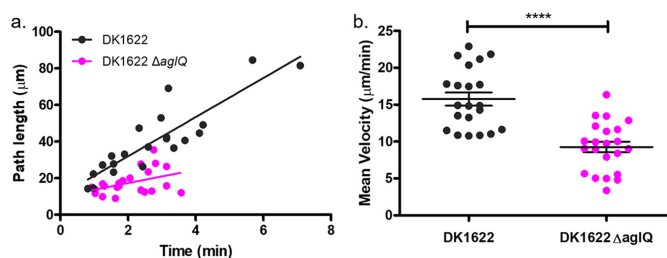


**FIG 5** IRM as a method for measuring the velocity of adherent cells. (a) Path lengths of DK1622 and DK1622  $\Delta\text{aglQ}$  over the course of a time series. Overall, DK1622 has an increased mean path length compared to DK1622  $\Delta\text{aglQ}$ , which shows that DK1622  $\Delta\text{aglQ}$  has a lower adhesion profile than the wild type. (b) Deletion of *aglQ* results in a decrease in the mean velocity of 41.2%, from  $15.76 \pm 0.89 \mu\text{m}/\text{min}$  to  $9.26 \pm 0.72 \mu\text{m}/\text{min}$ , compared with the wild type ( $n_{\text{DK1622}} = 21$ ;  $n_{\text{DK1622 } \Delta\text{aglQ}} = 22$  [\*\*\*\*,  $P < 0.0001$ ]).

much smaller relative size of bacteria than mammalian cells, we maintain that confocal IRM remains a valid technique for studying surface adhesion in prokaryotes.

Previous studies that have used conventional optical microscopy methods to image gliding myxobacteria have also failed to observe changes in surface adhesion due to the elongation of the axial point spread function being on the same order as the thickness of a bacterial cell (51, 52). By adopting a confocal approach to IRM for bacterial imaging, we overcome the limits of optical sectioning of thin specimens in standard optical microscopy while simultaneously visualizing the adhesion profile of cells. The drawback of using confocal IRM is a decreased temporal resolution compared with that of wide-field IRM. However, we were still able to track gliding cells sufficiently. While the contrast improvement provided by using a confocal approach over wide-field microscopy should make image analysis easier (52, 53), the complexity of IRM image data makes image processing and analysis challenging. There are currently no readily available image-processing tools that can extract 3D information from a 2D image, such as in IRM. However, with these improved data, it may be possible to develop software tools to reconstruct the 3D topography of bacteria using IRM data. The temporal resolution could be improved by using a spinning-disk confocal microscope for IRM; however, most commercial spinning-disk microscopes may not be suitable to incorporate IRM due to hardware limitations (43). The use of confocal IRM also allows us to confirm that the studied cells are in close proximity to the surface of the cover glass and that the gliding behaviors that we report are not caused by other factors such as inertia or Brownian motion.

Changes in the relative position of the basal cell membrane above the cover glass could perhaps be explained by proposed distortions in the cell wall due to the translocation of FACs along the basal surface of the cell (19) or because of cell surface unevenness (54). However, when we compare the axial movements displayed by the wild type with those of the  $\Delta aglQ$  mutant, we see that this novel gliding behavior remains. The role of AglQ in gliding motility is central to both the helical rotation and FAC models (22, 24, 25, 55), and having both wild-type and DK1622  $\Delta aglQ$  cells display the same behavior highlights that more understanding of the mechanisms of gliding motility is required. We then investigated the role of T4P in the changes that we observe. Time-lapse images of DK1622  $\Delta pilA$  and DK1622  $\Delta aglQ \Delta pilA$  mutants were acquired to establish if T4P-mediated events altered the adhesion behaviors that we observed, but these cells were not able to adhere to the cover glass and did not display an adherence pattern when imaged using IRM. We were therefore unable to confirm if T4P extension, attachment, and retraction were responsible for the behaviors that we document (see Movies S3 and S4 in the supplemental material).

It could be possible that slime secreted from the gliding cell could be responsible for the behaviors that we observe, where slime with a refractive index so close to that of the culture medium was not detected by IRM. This could perhaps be demonstrated by the use of fine graphite particles, scanning electron microscopy, or atomic force microscopy, which are all effective in revealing the otherwise invisible slime secretions. A recent study by Tchoufag et al. proposed an elastohydrodynamic mechanism for bacterial gliding where a sinusoidal basal shape is adopted when myxobacteria glide upon a soft substrate (56). This was observed using membrane-stained gliding cells on semisolid agar pads with TIRF microscopy and revealed distinct foci where the cell membrane was lifted approximately 100 nm above the substrate surface (outside the TIRF evanescent field). The motility behaviors described here are reminiscent of this undulating basal shape; however, our observations are documented for solid glass substrates and describe a wider variety of 3D behaviors in addition to the sinusoidal oscillatory behavior reported by Tchoufag et al. Moreover, our findings indicate that sinusoidal oscillatory gliding behaviors of *M. xanthus* may be surface independent.

Finally, we measured the mean velocity of wild-type and DK1622  $\Delta aglQ$  cells. Using the  $\Delta aglQ$  mutant as a control, where we know from previous work that gliding should be impaired (22), we have shown that height-changing behaviors are independent of the gliding velocity or path length where cells remain associated with the cover glass.



**TABLE 1** Bacterial strains used in this study

Strain	Characteristic(s)	Reference or source
DK1622	Wild type	59
DK10410	$\Delta pilA$	60
SA5293	$\Delta aglQ$	53
SA7705	$\Delta pilA \Delta aglQ$	Lotte Søgaard-Andersen, MPI-Institute for Terrestrial Microbiology, Germany

To determine the gliding velocity, we measured the average time that cells glided along approximately linear trajectories. Routine automated tracking algorithms generally have difficulties in tracking bacterial specimens due to their reliance on blob detection of spherical objects (57–59). Attempts to isolate and track rod-shaped objects, such as *M. xanthus*, have proven difficult, and the addition of interference fringes to rod-shaped objects only adds to the complications of automated cell tracking and analysis. We therefore used a manual tracking method to measure the mean velocity of gliding cells. We concluded that the DK1622  $\Delta aglQ$  mutant moved on average 30% slower than the wild type. Also, the wild type remains adhered to the surface for longer periods of time, yet the dynamic fluctuations in gliding adhesion that we report remain.

This work has provided new insights into the 3D motility of bacteria and identified novel motility behaviors in *M. xanthus*, which suggests that there are additional mechanisms that do not agree with the current FAC and helical rotation models. We suggest that the fluctuations in height that we observe are mediated by T4P and occur due to recoil following firing of pili from the leading pole. In this work, we attempted to image T4P mutants to confirm this hypothesis (Movies S3 and S4); however, these mutants were unable to attach to the glass substrate and therefore were unable to glide. Given that IRM was unable to reveal T4P-mediated behaviors due to nonattachment of cells to the cover glass, we suggest that this hypothesis could be investigated further by means of a correlative IRM method. Moving forward, it would be interesting to investigate the spatiotemporal dynamics of T4P firing in association with the changing adhesion profile of gliding cells using a correlative TIRF-IRM approach. This would allow the simultaneous imaging of the adhesion profiles of gliding cells and fluorescently tagged T4P proximal to the cover glass. Additionally, the development of an image-processing workflow to extract 3D information from confocal IRM images of myxobacteria would provide users with a method to quantify aperiodic oscillatory behavior. Alternatively, an astigmatic approach to single-molecule localization microscopy could be used to image the basal membrane of cells at nanometer resolution. However, this would require laborious specimen preparation, fixation of cells during gliding, and long acquisition times, which would make observations of such dynamic behaviors impractical compared to the gentler label-free nature of IRM. Furthermore, structured illumination microscopy (SIM), which can provide up to two times the resolution of point-scanning microscopy, could be used to obtain high-resolution 3D images. However, SIM would also require cells to be fluorescently labeled, which could alter the behavior of the specimen, whereas this is of no concern in label-free techniques such as IRM.

## MATERIALS AND METHODS

**Bacterial cell culture.** *Myxococcus xanthus* cultures (Table 1) were maintained on double Casitone yeast extract (DCYE) medium (20 g/liter casein hydrolysate, 2 g/liter yeast extract, 8 mM  $MgSO_4$ , 10 mM Tris-HCl [with 20 g/liter agar for solid medium]). For imaging, cells were inoculated at high cell densities in liquid DCYE medium and grown for 48 h at 30°C with shaking at 250 rpm. Prior to imaging, an 800- $\mu$ l sample of the exponentially growing culture was removed from liquid culture and placed in a 35-mm optical-bottom petri dish with a coverslip thickness of 180  $\mu$ m (catalog no. 80136; ibidi GmbH, Germany) and incubated at 30°C for 20 min to allow cells to adhere.

The refractive index of liquid DCYE medium was measured to be 1.33 using an Abbe refractometer (Billingham & Stanley Ltd., UK).

**Interference reflection microscopy.** For the characterization of a model lens specimen, the specimen was placed convex side down on a 170- $\mu\text{m}$ -thick cover glass measuring 50 by 24 mm, which bridged the microscope stage insert. An Olympus IX81 inverted microscope coupled to a FluoView FV1000 confocal scanning unit (Olympus, Japan) was used to image the lens specimen. The microscope was configured for IRM by replacing the emission dichroic with an 80/20 beam splitter. Images were acquired using a 10 $\times$ /0.3-NA UPlanFl lens objective (Olympus, Japan), and reflection signals were detected using a photomultiplier tube (PMT) for each wavelength, with spectral detection limited to a 10-nm bandwidth over the wavelength of the incident light. A 488-nm line from an argon laser source (model no. GLG3135; Showa Optronics, Japan) was used for single-wavelength acquisition. For multi-wavelength acquisition, 488-nm and 514-nm lines were provided by an argon laser and a 543-nm line was provided by a helium-neon-green laser source (model no. GLG3135; Showa Optronics, Japan).

For *M. xanthus* imaging, optical-bottom dishes were placed on the stage of an inverted Olympus IX81 microscope coupled to a FluoView FV1000 confocal laser scanning unit (Olympus, Japan). Images were acquired using a 60 $\times$ /1.35-NA UPlanSApo oil lens objective (Olympus, Japan). The microscope was configured for IRM as described above, with incident light of 488 nm from an argon laser and 635 nm obtained from a 635-nm laser diode (model no. GLG3135; Showa Optronics, Japan) for multiwavelength acquisitions. These wavelengths were selected based on their large spectral separation, meaning that color ordering in the observed IRM images was more distinct. For multiwavelength images, both channels were acquired simultaneously with two separate photomultiplier tube detectors.

For wide-field IRM, specimens were prepared as described above and imaged using a Nikon Eclipse-Ti2 inverted microscope (Nikon Instruments, USA) coupled to a Prime 95B sCMOS camera (Teledyne Photometrics, USA). Images were acquired using a 60 $\times$ /1.4-NA PlanApo oil objective lens (Nikon Instruments, USA). The microscope was configured for IRM by placing an 80/20 beam splitter into the detection path, and incident light was sourced from 450-nm and 550-nm light-emitting diodes (LEDs) (CoolLED, UK). Multiwavelength images were acquired sequentially.

**Image processing and analysis. (i) Image correction.** A common problem for the analysis of IRM images is the inhomogeneity of brightness across the image, which limits the utility of image segmentation tools like thresholding. To correct for changes in image brightness across the field, the moving average of the  $k \times k$  neighborhood was divided from each pixel using MATLAB 2018b. To rescale the histogram for downstream analysis in Fiji (60), the image intensity was rescaled by dividing by a factor of 2.

The length of the neighborhood,  $k$ , was selected depending on the specimen that was imaged. For the lens specimen, a large  $k$  value ( $k = 1,000$ ) was chosen to prevent lowering the contrast of the lens signal. For IRM images of *M. xanthus*, where the frequency of the observed interference fringes relative to the pixel density is high, a relatively small  $k$  value ( $k = 30$ ) proved suitable. Line intensity profiles from raw and corrected IRM images were checked to verify that the position and intensity succession of the interference fringes were not altered due to the correction method (see Fig. S4 to S6 in the supplemental material).

**(ii) Lens analysis and reconstruction.** In this work, we verified that multiwavelength IRM can be used to study the change in cell topology during gliding by imaging a lens specimen of known geometry and comparing the results with the theoretical model (see "Background theory," above). The one-dimensional height profile of a lens,  $z_{\text{lens}}$  is  $z(x) = R - \sqrt{R^2 - x^2}$ , where  $R$  is the radius of the lens and  $x$  is the distance to the center point of the lens that touches the surface/coverglass ( $x = 0$ ;  $z = 0$ ).

Images acquired at multiple wavelengths of the lens specimen were linearly contrast adjusted and cropped to create a square image using Fiji (60). A composite red/green/blue (RGB) image was created by merging the channels. The data were imported into MATLAB 2018b, and using the same radial analysis method as the one presented by Tinning et al., we calculated the axial height of interference fringes from the composite RGB image of the lens specimen (61). We used a findpeaks function to determine the spacing between the experimental intensity maxima of the interference fringes. Each subsequent constructive interference fringe was subtracted from its neighboring fringe to calculate the experimental spacing.

Lens reconstruction was performed using MATLAB. First, the radial distance for each pixel was extracted from the center of the RGB IRM image of the lens specimen. By applying *a priori* knowledge of the lens specimen geometry to the radial distance of each pixel (see "Background theory," above), we were able to assign each pixel to an axial height value based on the experimental fringe separation calculated previously. The  $x$ ,  $y$ , and  $z$  coordinates along with the image intensities were plotted to create a 3D reconstruction of the RGB IRM image.

## SUPPLEMENTAL MATERIAL

Supplemental material is available online only.

**FIG S1**, TIF file, 1.1 MB.

**FIG S2**, TIF file, 2.6 MB.

**FIG S3**, TIF file, 2.8 MB.

**FIG S4**, TIF file, 2.2 MB.

**FIG S5**, TIF file, 1.8 MB.

**FIG S6**, TIF file, 2.9 MB.

**MOVIE S1**, AVI file, 8.8 MB.

**MOVIE S2**, AVI file, 8.4 MB.



**MOVIE S3**, AVI file, 5 MB.

**MOVIE S4**, AVI file, 9.4 MB.

#### ACKNOWLEDGMENTS

We thank David Whitworth (Aberystwyth University, UK) for helpful discussions and the kind gift of the wild-type DK1622 strain used in this work. We also thank Lotte Søgaard-Andersen, Dobromir Szadkowski, and Anke Treuner-Lange (Max Planck Institute for Terrestrial Microbiology, Germany) for the kind donations of the motility mutants used in this study. We also thank the facility staff at the Beatson Advanced Imaging Resource (Beatson Institute, UK) and especially Margaret O'Prey for her technical assistance.

This work was supported by the Medical Research Council (MR/K015583/1). L.S.K. is supported by the EPSRC and the MRC Centre for Doctoral Training in Optical Medical Imaging (reference no. EP/L016559/1).

L.M.R. and L.S.K. acquired the data. L.M.R., L.S.K., and R.S. analyzed the data. L.S.K. developed the image correction workflow. R.S. developed the lens analysis scripts. L.M.R., W.B.A., P.A.H., and G.M. designed the study. L.M.R., L.S.K., R.S., W.B.A., P.A.H., and G.M. prepared the manuscript.

We declare no competing interests.


#### REFERENCES

1. Skerker JM, Berg HC. 2001. Direct observation of extension and retraction of type IV pili. *Proc Natl Acad Sci U S A* 98:6901–6904. <https://doi.org/10.1073/pnas.121171698>.
2. Merz AJ, So M, Sheetz MP. 2000. Pilus retraction powers bacterial twitching motility. *Nature* 407:98–102. <https://doi.org/10.1038/35024105>.
3. McBride MJ. 2001. Bacterial gliding motility: multiple mechanisms for cell movement over surfaces. *Annu Rev Microbiol* 55:49–75. <https://doi.org/10.1146/annurev.micro.55.1.49>.
4. Godwin SL, Fletcher M, Burchard RP. 1989. Interference reflection microscopic study of sites of association between gliding bacteria and glass substrata. *J Bacteriol* 171:4589–4594. <https://doi.org/10.1128/jb.171.9.4589-4594.1989>.
5. Kasai T, Hamaguchi T, Miyata M. 2015. Gliding motility of *Mycoplasma mobile* on uniform oligosaccharides. *J Bacteriol* 197:2952–2957. <https://doi.org/10.1128/JB.00335-15>.
6. Chang LE, Pate JL, Betzig RJ. 1984. Isolation and characterization of nonspreading mutants of the gliding bacterium *Cytophaga johnsonae*. *J Bacteriol* 159:26–35. <https://doi.org/10.1128/JB.159.1.26-35.1984>.
7. Holcycyk E. 2000. Gliding motility in cyanobacteria: observations and possible explanations. *Arch Microbiol* 174:11–17. <https://doi.org/10.1007/s002030000187>.
8. Nan B, Zusman DR. 2016. Novel mechanisms power bacterial gliding motility. *Mol Microbiol* 101:186–193. <https://doi.org/10.1111/mmi.13389>.
9. Nan B, Chen J, Neu JC, Berry RM, Oster G, Zusman DR. 2011. Myxobacteria gliding motility requires cytoskeleton rotation powered by proton motive force. *Proc Natl Acad Sci U S A* 108:2498–2503. <https://doi.org/10.1073/pnas.1018556108>.
10. Nan B, Zusman DR. 2011. Uncovering the mystery of gliding motility in the myxobacteria. *Annu Rev Genet* 45:21–39. <https://doi.org/10.1146/annurev-genet.110410-132547>.
11. Mignot T. 2007. The elusive engine in *Myxococcus xanthus* gliding motility. *Cell Mol Life Sci* 64:2733–2745. <https://doi.org/10.1007/s00018-007-7176-x>.
12. Spormann AM, Kaiser AD. 1995. Gliding movements in *Myxococcus xanthus*. *J Bacteriol* 177:5846–5852. <https://doi.org/10.1128/jb.177.20.5846-5852.1995>.
13. Spormann AM. 1999. Gliding motility in bacteria: insights from studies of *Myxococcus xanthus*. *Microbiol Mol Biol Rev* 63:621–641. <https://doi.org/10.1128/MMBR.63.3.621-641.1999>.
14. Muñoz-Dorado J, Marcos-Torres FJ, García-Bravo E, Moraleda-Muñoz A, Pérez J. 2016. Myxobacteria: moving, killing, feeding, and surviving together. *Front Microbiol* 7:781. <https://doi.org/10.3389/fmicb.2016.00781>.
15. Zhang Y, Ducret A, Shaevizt J, Mignot T. 2012. From individual cell motility to collective behaviors: insights from a prokaryote, *Myxococcus xanthus*. *FEMS Microbiol Rev* 36:149–164. <https://doi.org/10.1111/j.1574-6976.2011.00307.x>.
16. Mignot T, Shaevizt JW, Hartzell PL, Zusman DR. 2007. Evidence that focal adhesion complexes power bacterial gliding motility. *Science* 315:853–856. <https://doi.org/10.1126/science.1137223>.
17. Faure LM, Fiche J-B, Espinosa L, Ducret A, Anantharaman V, Luciano J, Lhosspice S, Islam ST, Tréguier J, Sotes M, Kuru E, Van Nieuwenhze MS, Brun YV, Théodoly O, Aravind L, Nollmann M, Mignot T. 2016. The mechanism of force transmission at bacterial focal adhesion complexes. *Nature* 539:530–535. <https://doi.org/10.1038/nature20121>.
18. Pogue CB, Zhou T, Nan B. 2018. PilpA, a PilZ-like protein, regulates directed motility of the bacterium *Myxococcus xanthus*. *Mol Microbiol* 107:214–228. <https://doi.org/10.1111/mmi.13878>.
19. Balagam R, Litwin DB, Czerwinski F, Sun M, Kaplan HB, Shaevizt JW, Igoshin OA. 2014. *Myxococcus xanthus* gliding motors are elastically coupled to the substrate as predicted by the focal adhesion model of gliding motility. *PLoS Comput Biol* 10:e1003619. <https://doi.org/10.1371/journal.pcbi.1003619>.
20. Islam ST, Mignot T. 2015. The mysterious nature of bacterial surface (gliding) motility: a focal adhesion-based mechanism in *Myxococcus xanthus*. *Semin Cell Dev Biol* 46:143–154. <https://doi.org/10.1016/j.semcdb.2015.10.033>.
21. Islam ST, Belgrave AM, Fleuchot B, Jolivet NY, My L, Faure LM, Sharma G, Lemon DJ, Fiche J-B, Bratton BT, Singer M, Garza AG, Nollmann M, Shaevizt JW, Mignot T. 7 June 2018. Integrin-like tethering of motility complexes at bacterial focal adhesions. SSRN, Rochester, NY. <https://ssrn.com/abstract=3188409>.
22. Sun M, Wartel M, Cascales E, Shaevizt JW, Mignot T. 2011. Motor-driven intracellular transport powers bacterial gliding motility. *Proc Natl Acad Sci U S A* 108:7559–7564. <https://doi.org/10.1073/pnas.1101101108>.
23. Nan B, Mauriello EMF, Sun I-H, Wong A, Zusman DR. 2010. A multi-protein complex from *Myxococcus xanthus* required for bacterial gliding motility. *Mol Microbiol* 76:1539–1554. <https://doi.org/10.1111/j.1365-2958.2010.07184.x>.
24. Nan B, Bandaria JN, Moghtaderi A, Sun I-H, Yildiz A, Zusman DR. 2013. Flagella stator homologs function as motors for myxobacterial gliding motility by moving in helical trajectories. *Proc Natl Acad Sci U S A* 110:E1508–E1513. <https://doi.org/10.1073/pnas.1219982110>.
25. Fu G, Bandaria JN, Le Gall AV, Fan X, Yildiz A, Mignot T, Zusman DR, Nan B. 2018. MotAB-like machinery drives the movement of MreB filaments during bacterial gliding motility. *Proc Natl Acad Sci U S A* 115:2484–2489. <https://doi.org/10.1073/pnas.1716441115>.
26. Ducret A, Fleuchot B, Bergam P, Mignot T. 2013. Direct live imaging of cell-cell protein transfer by transient outer membrane fusion in *Myxococcus xanthus*. *Elife* 2:e00868. <https://doi.org/10.7554/eLife.00868>.
27. Curtis ASG. 1964. The mechanism of adhesion of cells to glass: a study

- by interference reflection microscopy. *J Cell Biol* 20:199–215. <https://doi.org/10.1083/jcb.20.2.199>.
28. Gingell D, Todd I. 1979. Interference reflection microscopy. A quantitative theory for image interpretation and its application to cell-substratum separation measurement. *Biophys J* 26:507–526. [https://doi.org/10.1016/S0006-3495\(79\)85268-6](https://doi.org/10.1016/S0006-3495(79)85268-6).
  29. Bereiter-Hahn J, Fox CH, Thorell B. 1979. Quantitative reflection contrast microscopy of living cells. *J Cell Biol* 82:767–779. <https://doi.org/10.1083/jcb.82.3.767>.
  30. Bailey J, Gingell D. 1988. Contacts of chick fibroblasts on glass: results and limitations of quantitative interferometry. *J Cell Sci* 90:215–224.
  31. Schindl M, Wallraff E, Deubzer B, Witke W, Gerisch G, Sackmann E. 1995. Cell-substrate interactions and locomotion of Dictyostelium wild-type and mutants defective in three cytoskeletal proteins: a study using quantitative reflection interference contrast microscopy. *Biophys J* 68:1177–1190. [https://doi.org/10.1016/S0006-3495\(95\)80294-8](https://doi.org/10.1016/S0006-3495(95)80294-8).
  32. Saunders RM, Holt MR, Jennings L, Sutton DH, Barsukov IL, Bobkov A, Liddington RC, Adamson EA, Dunn GA, Critchley DR. 2006. Role of vinculin in regulating focal adhesion turnover. *Eur J Cell Biol* 85:487–500. <https://doi.org/10.1016/j.ejcb.2006.01.014>.
  33. Sugiyama N, Asai Y, Yamauchi T, Kataoka T, Ikeda T, Iwai H, Sakurai T, Mizuguchi Y. 2012. Label-free characterization of living human induced pluripotent stem cells by subcellular topographic imaging technique using full-field quantitative phase microscopy coupled with interference reflection microscopy. *Biomed Opt Express* 3:2175–2183. <https://doi.org/10.1364/BOE.3.002175>.
  34. Saraiva N, Prole DL, Carrara G, Johnson BF, Taylor CW, Parsons M, Smith GL. 2013. hGAAP promotes cell adhesion and migration via the stimulation of store-operated  $Ca^{2+}$  entry and calpain 2. *J Cell Biol* 202:699–713. <https://doi.org/10.1083/jcb.201301016>.
  35. Amos LA, Amos WB. 1991. The bending of sliding microtubules imaged by confocal light microscopy and negative stain electron microscopy. *J Cell Sci Suppl* 14:95–101. [https://doi.org/10.1242/jcs.1991.Supplement\\_14.20](https://doi.org/10.1242/jcs.1991.Supplement_14.20).
  36. Simmert S, Abdosamadi MK, Hermsdorf G, Schäffer E. 2018. LED-based interference-reflection microscopy combined with optical tweezers for quantitative three-dimensional microtubule imaging. *Opt Express* 26:14499–14513. <https://doi.org/10.1364/OE.26.014499>.
  37. Mahamdeh M, Simmert S, Luchniak A, Schäffer E, Howard J. 2018. Label-free high-speed wide-field imaging of single microtubules using interference reflection microscopy. *J Microsc* 272:60–66. <https://doi.org/10.1111/jmi.12744>.
  38. Fletcher M. 1988. Attachment of *Pseudomonas fluorescens* to glass and influence of electrolytes on bacterium-substratum separation distance. *J Bacteriol* 170:2027–2030. <https://doi.org/10.1128/jb.170.5.2027-2030.1988>.
  39. Weber I. 2003. Reflection interference contrast microscopy. *Methods Enzymol* 361:34–47. [https://doi.org/10.1016/s0076-6879\(03\)61004-9](https://doi.org/10.1016/s0076-6879(03)61004-9).
  40. Izzard CS, Lochner LR. 1976. Cell-to-substrate contacts in living fibroblasts: an interference reflexion study with an evaluation of the technique. *J Cell Sci* 21:129–159.
  41. Verschuere H. 1985. Interference reflection microscopy in cell biology: methodology and applications. *J Cell Sci* 75:279–301.
  42. Chiu L-D, Su L, Reichelt S, Amos WB. 2012. Use of a white light super-continuum laser for confocal interference-reflection microscopy. *J Microsc* 246:153–159. <https://doi.org/10.1111/j.1365-2818.2012.03603.x>.
  43. Barr VA, Bunnell SC. 2009. Interference reflection microscopy. *Curr Protoc Cell Biol* Chapter 4:Unit 4.23. <https://doi.org/10.1002/0471143030.cb0423s45>.
  44. Iwanaga Y, Braun D, Fromherz P. 2001. No correlation of focal contacts and close adhesion by comparing GFP-vinculin and fluorescence interference of Dil. *Eur Biophys J* 30:17–26. <https://doi.org/10.1007/s002490000119>.
  45. Mignot T, Shaevitz JW. 2008. Active and passive mechanisms of intracellular transport and localization in bacteria. *Curr Opin Microbiol* 11:580–585. <https://doi.org/10.1016/j.mib.2008.10.005>.
  46. Gingell D, Todd I, Bailey J. 1985. Topography of cell-glass apposition revealed by total internal reflection fluorescence of volume markers. *J Cell Biol* 100:1334–1338. <https://doi.org/10.1083/jcb.100.4.1334>.
  47. Limozin L, Sengupta K. 2009. Quantitative reflection interference contrast microscopy (RICM) in soft matter and cell adhesion. *Chemphyschem* 10:2752–2768. <https://doi.org/10.1002/cphc.200900601>.
  48. Contreras-Naranjo JC, Ugaz VM. 2013. A nanometre-scale resolution interference-based probe of interfacial phenomena between microscopic objects and surfaces. *Nat Commun* 4:1919. <https://doi.org/10.1038/ncomms2865>.
  49. Talà L, Fineberg A, Kukura P, Persat A. 2019. *Pseudomonas aeruginosa* orchestrates twitching motility by sequential control of type IV pili movements. *Nat Microbiol* 4:774–780. <https://doi.org/10.1038/s41564-019-0378-9>.
  50. Raedler J, Sackmann E. 1992. On the measurement of weak repulsive and frictional colloidal forces by reflection interference contrast microscopy. *Langmuir* 8:848–853. <https://doi.org/10.1021/la00039a019>.
  51. Wilson T, Sheppard C. 1984. Theory and practice of scanning optical microscopy. Academic Press, London, United Kingdom.
  52. Pawley J (ed). 2006. Handbook of biological confocal microscopy, 3rd ed. Springer Science+Business Media, LLC, New York, NY.
  53. Roeder AHK, Cunha A, Burl MC, Meyerowitz EM. 2012. A computational image analysis glossary for biologists. *Development* 139:3071–3080. <https://doi.org/10.1242/dev.076414>.
  54. Lünsdorf H, Schairer HU. 2001. Frozen motion of gliding bacteria outlines inherent features of the motility apparatus. *Microbiology* 147:939–947. <https://doi.org/10.1099/00221287-147-4-939>.
  55. Jakobczak B, Keilberg D, Wuichet K, Søgaard-Andersen L. 2015. Contact- and protein transfer-dependent stimulation of assembly of the gliding motility machinery in *Myxococcus xanthus*. *PLoS Genet* 11:e1005341. <https://doi.org/10.1371/journal.pgen.1005341>.
  56. Tchoufag J, Ghosh P, Pogue CB, Nan B, Mandadapu KK. 2019. Mechanisms for bacterial gliding motility on soft substrates. *Proc Natl Acad Sci U S A* 116:25087–25096. <https://doi.org/10.1073/pnas.1914678116>.
  57. Chenouard N, Smal I, de Chaumont F, Maška M, Sbalzarini IF, Gong Y, Cardinale J, Carthel C, Coraluppi S, Winter M, Cohen AR, Godínez WJ, Rohr K, Kalaidzidis Y, Liang L, Duncan J, Shen H, Xu Y, Magnusson KEG, Jaldén J, Blau HM, Paul-Gilloteaux P, Roudot P, Kervrann C, Waharte F, Tinevez J-Y, Shorte SL, Willemsse J, Keller K, van Wezel GP, Dan H-W, Tsai Y-S, de Solórzano CO, Olivo-Marín J-C, Meijering E. 2014. Objective comparison of particle tracking methods. *Nat Methods* 11:281–289. <https://doi.org/10.1038/nmeth.2808>.
  58. Tinevez J-Y, Perry N, Schindelin J, Hoopes GM, Reynolds GD, Laplantine E, Bednarek SY, Shorte SL, Eliceiri KW. 2017. TrackMate: an open and extensible platform for single-particle tracking. *Methods* 115:80–90. <https://doi.org/10.1016/j.ymeth.2016.09.016>.
  59. Wolff C, Tinevez J-Y, Pietzsch T, Stamatakis E, Harich B, Guignard L, Preibisch S, Shorte S, Keller PJ, Tomancak P, Pavlopoulos A. 2018. Multi-view light-sheet imaging and tracking with the MaMuT software reveals the cell lineage of a direct developing arthropod limb. *Elife* 7:e34410. <https://doi.org/10.7554/eLife.34410>.
  60. Schindelin J, Arganda-Carreras I, Frise E, Kaynig V, Longair M, Pietzsch T, Preibisch S, Rueden C, Saalfeld S, Schmid B, Tinevez J-Y, White DJ, Hartenstein V, Eliceiri K, Tomancak P, Cardona A. 2012. Fiji: an open-source platform for biological-image analysis. *Nat Methods* 9:676–682. <https://doi.org/10.1038/nmeth.2019>.
  61. Tinning PW, Scrimgeour R, McConnell G. 2018. Widefield standing wave microscopy of red blood cell membrane morphology with high temporal resolution. *Biomed Opt Express* 9:1745–1761. <https://doi.org/10.1364/BOE.9.001745>.



## Intra-colony channels in *E. coli* function as a nutrient uptake system

Liam M. Rooney<sup>1,3</sup> · William B. Amos<sup>2</sup> · Paul A. Hoskisson<sup>1</sup>  · Gail McConnell<sup>2</sup>

Received: 24 January 2020 / Revised: 5 May 2020 / Accepted: 12 May 2020  
© The Author(s) 2020. This article is published with open access

### Abstract

The ability of microorganisms to grow as aggregated assemblages has been known for many years, however their structure has remained largely unexplored across multiple spatial scales. The development of the Mesolens, an optical system which uniquely allows simultaneous imaging of individual bacteria over a 36 mm<sup>2</sup> field of view, has enabled the study of mature *Escherichia coli* macro-colony biofilm architecture like never before. The Mesolens enabled the discovery of intra-colony channels on the order of 10 µm in diameter, that are integral to *E. coli* macro-colony biofilms and form as an emergent property of biofilm growth. These channels have a characteristic structure and re-form after total mechanical disaggregation of the colony. We demonstrate that the channels are able to transport particles and play a role in the acquisition of and distribution of nutrients through the biofilm. These channels potentially offer a new route for the delivery of dispersal agents for antimicrobial drugs to biofilms, ultimately lowering their impact on public health and industry.

### Introduction

Bacteria frequently grow as surface-attached communities within complex extracellular matrices containing extracellular polysaccharides (EPS), lipids, proteins and nucleic acids [1, 2]. These microbial communities may be composed of one or more species (mono/poly-microbial) and are found in almost every ecological niche [3]. The structure and protective matrix enveloping the biofilm confers resistance to unfavourable environmental conditions and deleterious agents such as biocides or antibiotics [4–8]. The ecological benefits of these heterogeneous phenotypic responses are poorly understood, yet there is evidence that suggests that biofilm formation may

promote the development and spread of antimicrobial resistance [9]. Consequently, the study of biofilm structure is vital in understanding how microbial assemblages grow and persist in a range of environments and conditions. The 3D organisation of biofilms may take many forms [10–13]; for example, mushroom-shaped biofilms grown in liquid flow systems, thin sheet-like biofilms in static liquid systems, pellicle biofilms grown at liquid/air interfaces and macro-colony biofilms on solid surfaces. Although morphologically distinct, what classifies these structurally different communities as ‘biofilms’ lies with their shared fundamental biochemical signals and pathways [3].

Dynamic computational modelling programmes, such as CellModeller [14, 15], have been used to predict the spatial patterning and arrangement of cells within bacterial communities [14–18]. In silico models primarily show growth of poly-microbial communities where cell shape, size, surface properties and cell–cell interactions influence the spatial organisation of the mature biofilm, resulting in sectoring of different strains into distinct populations, which has been validated experimentally [19–23]. However, in silico modelling has shown little evidence of structural ordering or complex spatial patterning largely as a result of a lack of effective multi-scale imaging techniques.

The study of living biofilms has been mainly performed by optical imaging, and has shown phenomena such as the density-dependent phage sensitivity in *Escherichia coli* colonies [24], the effect of pH on biofilms present on

**Supplementary information** The online version of this article (<https://doi.org/10.1038/s41396-020-0700-9>) contains supplementary material, which is available to authorized users.

✉ Liam M. Rooney  
l.rooney@hw.ac.uk

<sup>1</sup> Strathclyde Institute of Pharmacy and Biomedical Sciences, University of Strathclyde, 161 Cathedral Street, Glasgow G4 0RE, UK

<sup>2</sup> Department of Physics, SUPA, University of Strathclyde, 107 Rottenrow East, Glasgow G4 0NG, UK

<sup>3</sup> Present address: Institute of Biological Chemistry, Biophysics and Bioengineering, School of Engineering and Physical Sciences, Heriot-Watt University, Edinburgh EH14 4AS, UK

human tooth enamel [25] and the synchronies of growth and electrical signalling between adjacent bacterial colonies [26]. Observation by optical microscopy has also been used to investigate macroscopic channel features in biofilms. For example, the macro-colony folds formed by *Pseudomonas* spp. in response to oxygen stress when the biofilm reaches a critical mass [27, 28], the crenulations formed by *Bacillus* spp. macro-colonies for water transport [29, 30], or the cavernous water channels which are formed at the base of submerged mushroom-shaped biofilms often grown in under shear flow [31]. These studies have exposed a gap in the repertoire of the optical microscope in that either microbes could be imaged individually with a high-power objective lens, or the overall biofilm structure could be viewed at low magnification with poor resolution, particularly in depth, that individual microbial cells could not be seen. To address this shortcoming, we use the Mesolens to image intact live macro-colony biofilms in situ with isotropic sub-cellular resolution. In essence, the Mesolens is a giant objective lens with the unique combination of  $\times 4$  magnification with a numerical aperture (NA) of 0.47; which is approximately five-times greater than that of a conventional  $4\times$  objective lens [32]. The low magnification coupled with a high NA result in a field of view (FOV) measuring  $\sim 6\text{ mm}^2$  with lateral resolution of 700 nm and  $7\text{ }\mu\text{m}$  axially, while the lens prescription provides a working distance of 3 mm. Moreover, the lens is chromatically corrected across the visible spectrum and designed to be compatible with various immersion routines. While the Mesolens has proven to be a powerful tool in neuroscience, developmental biology and pathology [32–34], it remains an untapped technology for biofilm imaging, where we can image whole live microbial communities with unprecedented detail within a single dataset without additional processing or stitching and tiling.

We used the Mesolens to investigate the internal architecture of mature *E. coli* macro-colony biofilms. We identified and characterised a previously undocumented channel system within these biofilms that facilitates nutrient uptake from the external environment and offers novel insight into nutrient delivery in large microbial communities. These findings offer additional support for diffusion dynamics in bacterial biofilms; which is widely accepted as the main route of delivery for any external compounds to enter a biofilm, whether they be nutrients or antimicrobial drugs [14–17]. In addition, we demonstrated that intra-colony channels form as an emergent property of biofilm formation in *E. coli*. These findings provide novel understanding of how spatial organisation in bacterial biofilms contributes to their ability to transport material from the external environment.

## Materials and methods

### Designing and 3D-printing a chamber slide for biofilm imaging

A custom imaging chamber was designed using AutoCAD (Autodesk, USA) with the purpose of imaging large-scale-cultured bacterial communities in situ using the Mesolens. The design consisted of a plate with dimensions  $90\times 80\times 12\text{ mm}$  and a central well measuring 60 mm in diameter with a depth of 10 mm (Supplementary Fig. 1). The imaging chamber was 3D-printed using black acrylonitrile butadiene styrene plastic (FlashForge, Hong Kong) with a FlashForge Dreamer 3D printer (FlashForge, Hong Kong). The chamber slide was sterilised prior to use with 70% ethanol and UV irradiation for 15 min.

### Bacterial strains and growth conditions

All experiments were performed using the *E. coli* strains outlined in Supplementary Table 1. Colony biofilms were grown by inoculating a lawn of cells at a density of  $1\times 10^4\text{ cfu/ml}$  on either solid LB medium or M9 minimal medium [35] to achieve single colonies, and growth medium was supplemented with the appropriate selective antibiotic to maintain the photoprotein. The colonies were grown in the 3D-printed imaging mould at  $37^\circ\text{C}$  for 18–24 h in darkened conditions prior to imaging. All experiments were repeated in triplicate to ensure observations were reliable.

### Specimen preparation

For colony imaging alone, colonies were submerged in sterile LB broth (refractive index ( $n$ ) = 1.338) as a mounting medium following the allocated growth time prior to imaging. A large coverglass was placed over the central well of the imaging mould ( $70\times 70\text{ mm}$ , Type 1.5, 0107999098 (Marienfeld, Lauda-Koenigshofen, Germany)), and the colonies were then imaged using either the Mesolens or a conventional widefield epi-fluorescence microscope to compare their performance and to justify using the Mesolens to study biofilm architecture over conventional techniques.

The refractive index of the LB mounting medium was measured using an Abbe Refractometer (Billingham & Stanley Ltd, UK) which was calibrated using Methanol at  $21^\circ\text{C}$ .

### Conventional widefield epi-fluorescence microscopy

Colony biofilms were imaged on a conventional Eclipse E600 upright widefield epi-fluorescence microscope



(Nikon, Japan) equipped with a 4×/0.13 NA Plan Fluor objective lens (Nikon, Japan). GFP excitation was provided by a 490 nm LED from a pE-2 illuminator (CoolLED, UK), and emission was detected using a bandpass filter (BA 515–555 nm, Nikon, Japan) placed before an ORCA-spark digital CMOS camera (Hamamatsu, Japan). The camera detector was controlled using WinFluor software [36]. Colonies were imaged after 20 h of growth in an imaging mould as described above.

### Widefield epi-fluorescence mesoscopy

Specifications of the Mesolens have been previously reported [32], and therefore only the imaging conditions used in this study will be outlined here. GFP excitation was achieved using a 490 nm LED from a pE-4000 LED illuminator (CoolLED, UK). A triple-bandpass filter which transmitted light at  $470 \pm 10$ ,  $540 \pm 10$  and  $645 \pm 50$  nm was placed in the detection pathway. The emission signal was detected using a VNP-29MC CCD camera with a chip-shifting modality (Vieworks, South Korea) to capture the full FOV of the Mesolens at high resolution. Widefield mesoscopic imaging was carried out using water immersion ( $n = 1.33$ ) with the Mesolens' correction collars set accordingly to minimise spherical aberration through refractive index mismatch.

### Confocal laser-scanning mesoscopy

For laser-scanning confocal mesoscopy, specimens were prepared as outlined above. Fluorescence excitation of GFP was obtained using the 488 nm line set at 5 mW from a multi-line LightHUB-4 laser combiner (Omicron Laserage, Germany). The green emission signal was detected using a PMT (P30-01, Sensstech, UK) with a 550 nm dichroic mirror (DMLP550R, Thorlabs, USA) placed in the emission path and a 525/39 nm bandpass filter (MF525-39, Thorlabs, USA) placed before the detector.

For reflection confocal mesoscopy, incident light was sourced from a 488 nm line set at 1 mW from a multi-line LightHUB-4 laser combiner (Omicron Laserage, Germany). Reflected signal was detected using a PMT (P30-01, Sensstech, UK) with no source-blocking filter in place.

Confocal laser-scanning mesoscopy was carried out using type DF oil immersion ( $n = 1.51$ ) with the Mesolens' correction collars set accordingly to minimise spherical aberration through refractive index mismatch.

### Structural assessment of intra-colony channels

To characterise the structure of intra-colony channels we sought to visualise the distribution of several archetypal structural components of biofilms.

As the biofilms in this study were submerged during imaging in a medium with known refractive index, we were able to determine if channels were filled with substances of differing refractive index (e.g., air) using reflection confocal mesoscopy as above. Solid LB was cast into a 3D-printed imaging chamber and inoculated with JM105 at a density of  $1 \times 10^4$  cfu/ml and incubated for 18–24 h at 37 °C in darkened conditions. Biofilms were mounted in sterile LB medium ( $n = 1.338$ ) prior to imaging.

We then imaged the distribution of non-viable cells in the biofilm based on the approach developed by Asally [30]. Briefly, JM105-miniTn7-HcRed1 colony biofilms were grown for imaging in 3D-printed imaging moulds as outlined previously. LB medium was supplemented with gentamicin (20 µg/ml) and 0.5 µM Sytox green dead-cell stain (S7020, Invitrogen, USA). Cells were seeded at a density of  $1 \times 10^4$  cfu/ml and grown for 18–24 h prior to imaging on the Mesolens in widefield epi-fluorescence mode as described above. A 490 and 580 nm LED from a pE-4000 LED illuminator (CoolLED, UK) were used to excite Sytox Green and HcRed1, respectively. The emission signal was detected using a VNP-29MC CCD detector (Vieworks, South Korea) with 3 × 3 pixel-shift modality enabled and with a triple-bandpass filter ( $470 \pm 10$ ,  $540 \pm 10$  and  $645 \pm 50$  nm) in the emission path.

To visualise the distribution of EPS in the biofilm we stained sialic acid and N-acetylglucosaminyl residues by supplementing solid M9 medium (0.2% glucose (w/v)) [35] with 20 µg/ml gentamicin and 2 µg/ml Alexa594-wheat germ agglutinin (WGA) (W11262, Invitrogen, USA) before inoculating with  $1 \times 10^4$  cfu/ml JM105-miniTn7-*gfp* and growing as previously described. We imaged EPS-stained specimens using widefield epi-fluorescence mesoscopy as before using a 490 nm LED to excite GFP and 580 nm LED to excite Alexa594-WGA.

We determined the lipid localisation throughout the biofilm by staining with Nile Red. We supplemented solid LB medium with 20 µg/ml gentamicin and 10 µg/ml Nile Red (72485, Sigma-Aldrich, USA) before inoculating with  $1 \times 10^4$  cfu/ml JM105-miniTn7-*gfp* and growing as previously described. We then imaged the lipid distribution in relation to the intra-colony channels using widefield epi-fluorescence mesoscopy as before using a 490 nm LED to excite GFP and 580 nm LED to excite Nile Red.

The protein distribution was determined by staining the biofilm with FilmTracer SYPRO Ruby biofilm matrix stain (F10318, Fisher Scientific, USA) which binds to a number of different classes of extracellular protein. Solid LB medium was prepared containing 20 µg/ml gentamicin and a final concentration of 2% (v/v) FilmTracer SYPRO Ruby biofilm matrix stain before inoculating with JM105-miniTn7-*gfp* and growing as previously described. Specimens were imaged using widefield epi-fluorescence

mesoscopy. A 490 and 580 nm LED from a pE-4000 illuminator (CoolLED, UK) were used for GFP and SYPRO Ruby excitation, respectively. Fluorescence emission from GFP and SYPRO Ruby was detected as outlined above. Both channels were acquired sequentially.

#### Disruption and recovery of intra-colony channel structures

To assess the ability of the structures we observe to recover following disruption, single colonies of JM105-miniTn7-*gfp* were grown on solid LB medium supplemented with 20 µg/ml gentamicin and allowed to grow for 10 h at 37 °C in darkened conditions. Following the initial growth step colonies were removed from the incubator and gently mixed with a sterile 10 µl pipette tip to disrupt the channel structures in the growing biofilm. Care was taken to prevent disruption to the underlying solid medium on which the colony was supported. Following disaggregation, the colonies were grown for a further 10 h at 37 °C in darkened conditions prior to imaging. Colonies were then mounted in sterile LB medium and imaged using widefield epi-fluorescence mesoscopy as described above. To determine the effect of channel disruption on the biofilm population, CFUs were enumerated following disruption at regular intervals over a period of time. Briefly, JM105 macro-colonies were prepared as above. A proportion of the colonies were left undisturbed, while others were carefully mixed using a sterile 10 µl pipette tip every 40 min for a period of 8 h. To ensure adequate removal of the biofilm from the surface of the agar, a 6 mm cork-borer was used to punch our colonies and their surround medium before each plug was placed in an individual 2 ml aliquot of sterile LB broth and mixed vigorously for 15 s by vortexing. The cell suspensions were serially diluted and enumerated by spread plating on solid LB, before incubating at 37 °C for 16 h. Colonies were counted and the number of CFU/ml was calculated for each undisrupted and disrupted biofilm. An unpaired *t*-test was used to compare the change in CFU between each condition.

#### Using differentially labelled isogenic strains to observe channels in mixed cultures

The phenomenon of strain sectoring has been previously documented and occurs by mechanical buckling as adjacent colonies expand into each other during radial growth [18, 19]. We investigated whether intra-colony channels were able to cross the strain boundary between sectors by inoculating a low-density mixed culture of JM105-miniTn7-*gfp* and JM105-miniTn7-*HcRed1* at a 1:1 ratio and inoculating a lawn onto solid LB medium containing 20 µg/ml gentamicin. We allowed colonies of each strain to

stochastically collide into adjacent clonal populations during colony expansion and then imaged using widefield mesoscopy after incubation for 20 h at 37 °C in darkened conditions as described above. We used colony PCR to confirm that the miniTn7 insertion, which contained the photoprotein gene, occurred at the same chromosomal location in both strains (*glmS* Fwd.—5' AAC CTG GCA AAT CGG TTA C; *tn7R109* Rev.—5' CAG CAT AAC TGG ACT GAT TTC AG). The miniTn7 transposon inserts at only one *attTn7* site in the chromosome, downstream of *glmS* [37]. We found that both JM105-miniTn7-*gfp* and JM105-miniTn7-*HcRed1* were inserted ~25 base pairs downstream of *glmS*. Therefore, there is no genotypic difference between the strains, save for the inserted photoprotein gene.

#### Fluorescent microsphere uptake assay

To assess the function of the structures we observe, a confluent lawn of fluorescent microspheres was seeded along with the bacterial inoculum at the culturing stage. Two-hundred nanometre multi-excitatory microspheres (Polysciences, Inc., USA) were seeded at a density of  $1 \times 10^{10}$  microspheres/ml and plated along with  $1 \times 10^4$  cfu/ml JM105-miniTn7-*gfp* in a mixed-inoculum. Microsphere translocation was assessed by widefield epi-fluorescence mesoscopy as above with two-channel detection for both the GFP and microsphere fluorescence emission. A triple-bandpass emission filter that transmitted light at  $470 \pm 10$ ,  $540 \pm 10$  and  $645 \pm 50$  nm was placed in the detection path. Sequential excitation of GFP and the fluorescent microspheres was achieved using a 490 and 580 nm LED, respectively, from a pE-4000 LED illuminator (CoolLED, UK). Each channel was acquired sequentially using a CCD camera detector (Stemmer Imaging, UK). All imaging was carried out using water immersion.

#### Assessing the role of intra-colony channels in nutrient uptake

The functional role of the structures which we observe was tested using an arabinose biosensor where GFP expression was controlled by the presence or absence of L-arabinose. The biosensor strain contained the *araBAD* operon with *gfp*-inserted downstream on the promoter and *araBAD* functional genes. The biosensor strain was a gift from colleagues at the James Hutton Institute.

JM105 transformed with the arabinose biosensor plasmid, pJM058, was grown overnight at 37 °C while shaking at 250 rpm in liquid LB medium supplemented with 25 µg/ml chloramphenicol. Overnight cultures were then diluted in fresh LB and grown until  $OD_{600} = 0.5$ . Cells were then pelleted and washed three times with 1x M9 salts. Washed

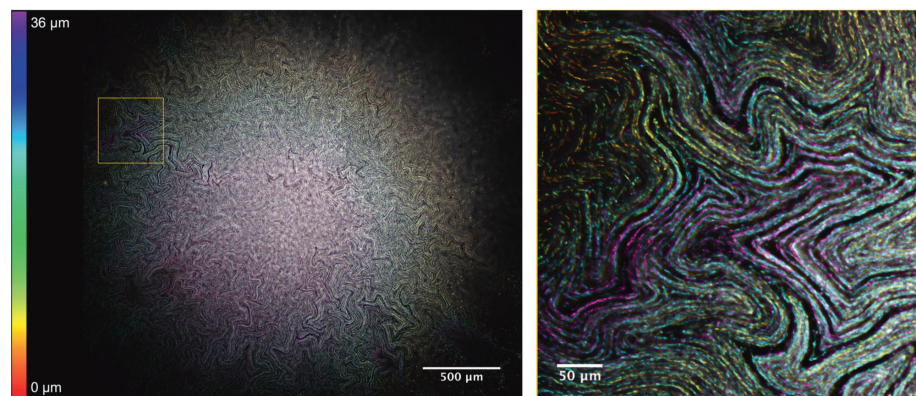


**Fig. 1** Visualising the intra-colony channel system of *E. coli* macro-colony biofilms. A deconvolved 36-μm-thick transverse sub-stack of a mature *E. coli* macro-colony biofilm acquired using widefield mesoscopy. An axial colour-coded LUT has been applied, which indicates

the relative position of each cell within the context of the biofilm. A magnified ROI is presented where individual cells can be clearly resolved. Channel structures are seen to permeate throughout the biofilm and present a 3D topography within the context of the biofilm.

cells were inoculated onto solid M9 minimal medium [35] with L-arabinose as the sole carbon source (0.2%) at a density of  $1 \times 10^4$  cfu/ml and grown for 42–48 h in darkened conditions at 37 °C. Specimens were then prepared for imaging as outlined above.

### Image processing and analysis

Widefield epi-fluorescence mesoscopy z-stacks were deconvolved where specified using with Huygens Professional version 19.04 (Scientific Volume Imaging, The Netherlands, <http://svi.nl>) using a Classic Maximum Likelihood Estimation algorithm. A theoretical point spread function was generated using Huygens Professional with parameters adjusted to suit the experimental setup. Deconvolution was performed using a server with a 64-bit Windows Server 2016 Standard operating system (v.1607), two Intel® Xeon® Silver 4114 CPU processors at 2.20 and 2.19 GHz and 1.0 TB installed RAM. Image analysis was performed using FIJI [38]. Figures presented here were linearly contrast adjusted for presentation purposes where required using FIJI [38].

## Results

### *E. coli* biofilms possess a network of intra-colony channels

The internal architecture of *E. coli* macro-colony biofilms was investigated using conventional widefield epi-fluorescence microscopy, widefield mesoscopy and confocal laser-

scanning mesoscopy. Using widefield mesoscopy it was apparent that *E. coli* (JM105) biofilms contain a network of channel-like structures which permeate the biofilm linking the centre of the colony to the leading edge. The channels measure ~15 μm wide and appear as non-fluorescing regions within the biofilm, which is lined by individual cells in a pole-to-pole arrangement. We applied a Classic Maximum Likelihood Estimation deconvolution algorithm to a sub-sample of a z-stack acquired using the Mesolens in widefield epi-fluorescence mode to improve image quality and reveal the arrangement of individual cells in a mature macro-colony biofilm. We then applied a colour-coded look-up table (LUT) according to the axial position of each optical section within the 36-μm-thick z-stack (Fig. 1). From the axial-coded LUT we can see that the intra-colony channels are not merely 2D lateral arrangements of cells, but that the channels have a 3D topography within the context of the biofilm, resembling canyons and ravines rather than enclosed capillaries.

Imaging of JM105 biofilms using confocal mesoscopy ensured that the deconvolution algorithm used to process widefield Mesolens data did not introduce erroneous structural artefacts. Confocal microscopy provides a marked improvement in signal-to-noise ratio compared with widefield techniques, particularly with thick specimens, resulting in a similar image quality to a deconvolved widefield dataset. Confocal mesoscopy revealed the same channel structures that we identified in widefield imaging experiments presented in Fig. 1 (Supplementary Fig. 2 and Supplementary Movie 1). This concludes that the structures we observed were not introduced as an artefact of image processing.



To demonstrate the benefit of using the Mesolens over conventional microscopes for imaging live biofilms, we also imaged biofilms using a conventional upright widefield epifluorescence microscope with a low magnification, low-NA lens (4×/0.13 NA). We compared the ability of the Mesolens and the conventional microscope to resolve the intra-colony channels and found that there was a clear improvement in the spatial resolution with the Mesolens (Supplementary Fig. 3). The resolution improvement applies to both lateral and axial resolution, and establishes the Mesolens as an ideal imaging technology for 3D imaging of large microbiological specimens with sub-micron resolution, enabling greater than single-cell resolution throughout the entire colony.

### Channels emerge as an inherent property of biofilm formation

The channel structures we have identified appear as dark regions within the biofilm, and so we hypothesised that they may be comprised of a structural matrix. We began investigating the structural makeup of the channels by determining if they were filled with materials of differing refractive index compared with that of the biomass. Using reflection confocal mesoscopy, where signal is detected from reflections of incident light at refractive index boundaries, such as those between bacterial cells and the surrounding growth medium, we tested if the channels were comprised of translocated growth medium or air. A maximum intensity projection of an unlabelled *E. coli* JM105 biofilm acquired in reflection confocal mode showed no reflection signal resembling the intra-colony channels (Fig. 2a). This suggests that the channels must be of a similar refractive index to the surrounding biomass and biofilm matrix and are not occupied by solid growth medium or air.

To determine if the channel structures we observe were occupied by non-viable/non-fluorescing cells, biofilms were grown in the presence of the viability dye, Sytox Green. This dye has an emission peak at 523 nm enabling the use of HcRed1 ( $\lambda_{em}$  618 nm) expressing JM105 *E. coli* cells for two-colour imaging. The false-coloured composite (Fig. 2b) shows a maximum intensity projection of a JM105-miniTn7-HcRed1 biofilm stained with Sytox Green acquired using widefield mesoscopy, where live cells are presented in cyan and non-viable cells are shown in yellow. Subtracting the signal of the non-viable cells from HcRed1-expressing cells to prevent spectral overlap in the emission of the two fluorophores, such that no Sytox-labelled cells were falsely presented in cyan. It was observed that viable and non-viable cells formed two distinct domains within the colony. Here, non-viable cells cluster in the centre of the biofilm while intra-colony channels are not occupied by non-viable/non-fluorescent cells.

To determine if intra-colony channels were filled with exopolysaccharides (EPS) secreted by bacteria within the biofilm, JM105 biofilms were grown in the presence of the lectin-binding dye conjugate Alexa594-WGA. The deconvolved composite image of a JM105-miniTn7-*gfp* biofilm (green) and associated EPS (magenta) shows that EPS are distributed throughout the entire biofilm and are not strictly localised within the channel structures (Fig. 2c). Assessment of the lipid distribution using the lipid-binding dye Nile Red, showed that intra-colony channels are not composed of lipid (Fig. 2d). The protein-specific fluorescent dye, SYPRO Ruby revealed the presence of extracellular protein within the channels (Fig. 2e).

To determine if the formation of intra-colony channels arose as an emergent property of biofilm formation, we tested if the structures were able to re-form following disruption. The colony biofilms were grown to the point of them establishing the formation of channels (Fig. 3a) and then the colony was mixed to create a uniform mass of cells. The colonies were then reimaged following a recovery period of 10 h. The channels reformed in the regions of the biofilm where new growth occurred (Fig. 3b). Interestingly, following continuous disruption over a number of hours, we found that there was a significant decrease ( $P$  value = 0.0423) in the number of CFU in the disrupted biofilms compared with the naïve biofilms (Supplementary Fig. 4). The ability of the channels to form in the same way as a naïve colony suggests that they form as an emergent property of *E. coli* colonial growth on a solid surface.

### Channels result in strain boundaries in mixed isogenic cultures

Growth of two isogenic strains in co-culture, each expressing a different photoprotein, results in sectoring and has been previously described [18–23]. We wished to explore this sectoring property in the context of intra-colony channel formation and to determine if the channels were shared between the strains. When the two isogenic strains sector, the channels do not intersect the boundary between the strains and are retained within a sector (Fig. 4). The confinement of channels was more evident between different populations (i.e., HcRed1 and GFP-expressing), whereas the boundaries between sectors of cells expressing the same photoprotein were less ordered.

### Intra-colony channels represent a novel nutrient acquisition system in *E. coli* biofilms

To investigate whether the intra-colony channels play a role in the transport of substances into the biofilm, the channel system was tested for functional roles by introducing 200 nm diameter fluorescent microspheres to the medium when



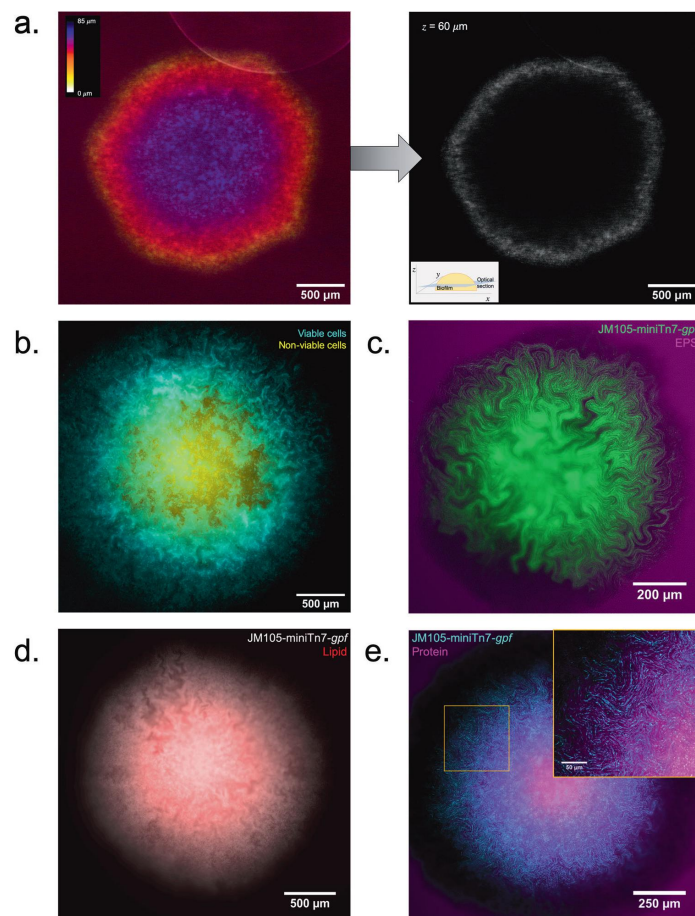


**Fig. 2 Characterising the structure of intra-colony channels.** **a** Maximum intensity projection of an unlabelled JM105 colony acquired using reflection confocal mesoscopy, with a single isolated optical section shown. Reflection imaging determined that intra-colony channels were not occupied by material of differing refractive index to the biomass. The colony-medium interface can be observed clearly, while there is no evident structure within the colony. **b** Signal from non-viable cells (yellow) was subtracted from viable cells to negate any spectral overlap in the emission of Sytox Green and HcRed1. A composite maximum intensity projection of the entire colony is presented. Intra-colony channels in the viable cell population (cyan) did not contain any non-viable cells. **c** Alexa594-WGA-stained EPS

residues (magenta) were not present in the intra-colony channels when compared with elsewhere in the biofilm, meaning channels were not composed of an EPS-based matrix. The high background signal in the surrounding agar is likely owed to non-specific binding of the WGA dye with glycan components of the agar substrate. **d** Nile red-stained lipids (red) clustered in the centre of *E. coli* biofilms while intra-colony channels remain unstained by Nile Red. Therefore, intra-colony channels were not composed of lipids. **e** Emission of SYPRO Ruby-stained extracellular proteins (magenta) mimicked the spatial patterns of intra-colony channels, showing that channels were filled by a protein-based matrix.

preparing the specimen for widefield mesoscopy. The fluorescent microspheres were spread as a dense lawn along with a dilute mid-log JM105-miniTn7-*gfp* culture. A single

optical section, 25 μm above the base of the colony, allows the outline of the colony to be observed at the edges of the image, with the untouched lawn of microspheres outside the

**Fig. 3 Intra-colony channels form as an emergent property of biofilm formation.** **a** An unmixed, naïve control biofilm of JM105-miniTn7-*gfp* with established intra-colony channels. **b** A macro-colony JM105-miniTn7-*gfp* biofilm that was initially grown for 10 h before mechanical disruption and subsequent recovery and regrowth at 37 °C for a further 10 h. Regrowth was accompanied with the re-emergence of intra-colony channels in the outgrown region of the disrupted colony, showing that channel formation is an emergent property of macro-colony biofilm development. The purple circle indicates the boundary of the juvenile colony at the time of disaggregation, where channels have not reformed in the disrupted region.

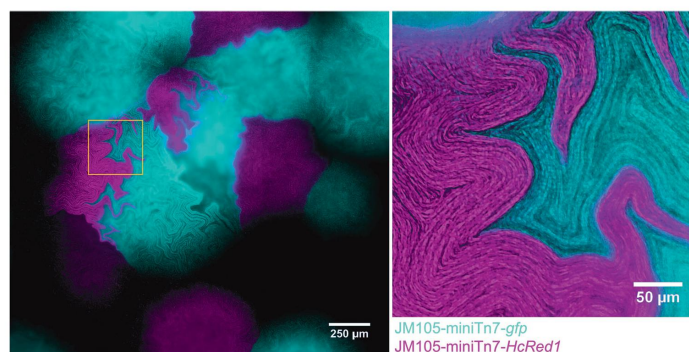
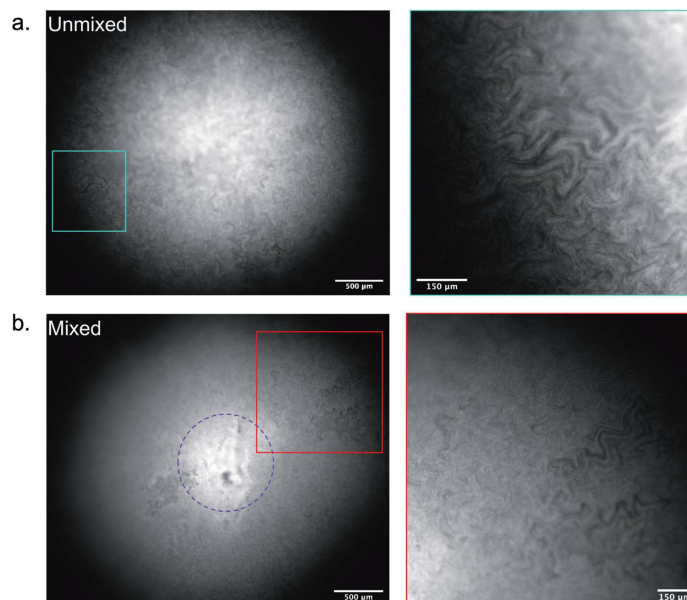


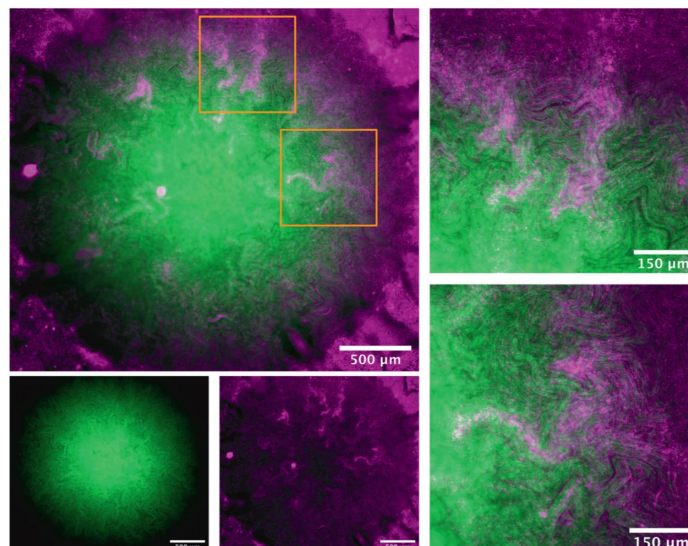
**Fig. 4 Intra-colony channels are confined within clonal populations and unable to cross strain boundaries.** A mixed culture of isogenic JM105 strains which express either GFP (cyan) or HcRed1 (magenta). Each strain sectorized into segregated clonal populations, which have propagated from a single colony-forming unit, and cells

from each sector were unable to cross the strain boundary. The intra-colony channels present within each sector were also unable to cross the strain boundary and were therefore not shared by opposing isogenic colonies.

colony (Fig. 5). The distribution of beads in these areas are homogenous, whereas within the colony the transport of the fluorescent microspheres through the channels reflects the spatial structure of the biofilm. Magnified regions of interest of intra-colony channels show that the channels are acting

as conduits for the transport of microspheres into the biofilm. The transport of microspheres into the channels suggests that these intra-colony structures are involved in the acquisition of substances from the external environment. This suggests the ability of channels to transport small

**Fig. 5 Intra-colony channels facilitate transport of microscopic particles.** A single optical section ~25  $\mu\text{m}$  above the base of the colony shows a mature JM105-miniTn7-*gfp* biofilm (green) and a lawn of 200 nm fluorescent microspheres (magenta). The fluorescent microspheres were transported from a confluent lawn at the base of the colony into the intra-colony channels and directed towards the centre of the colony. Two ROIs are presented from different regions of the colony where fluorescent microspheres were transported into the colony via intra-colony channels.



fluorescent particles could be extended to facilitate uptake of smaller particles and solutes into the colony, and may represent a previously unknown nutrient acquisition system in microbial assemblages.

To further investigate the role of intra-colony channels in biofilm nutrient acquisition, an arabinose-inducible GFP strain (*E. coli* JM105  $P_{BAD}$ -*gfp*) was utilised. Growth of the arabinose-inducible GFP strain on solid minimal medium with L-arabinose as the sole carbon source revealed that the biofilm fluoresced most intensely in regions surrounding the intra-colony channels (Fig. 6). This suggests that the concentration of L-arabinose is highest within the channels compared with the remainder of the biofilm and demonstrates the role of these structures act as a nutrient acquisition and transport mechanism within the colony. This finding challenges the long-held belief that bacterial colony nutrient uptake occurs through passive diffusion from the basal or apical surface of the biofilm through the extracellular matrix, and concurs with previous hypotheses which suggested that large biofilms must develop transport mechanisms to direct nutrients to their centre [1].

## Discussion

This study is the first application of the Mesolens to microbiology and has offered a new approach for imaging large microbial specimens, enabling us to characterise a

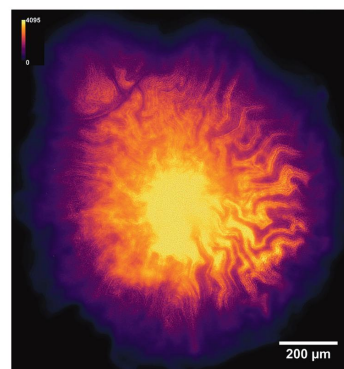


**Fig. 6 Intra-colony channels play a functional role in nutrient acquisition and transport to the centre of bacterial biofilms.** A deconvolved image of a JM105-pJM058 macro-colony biofilm grown on M9 minimal medium with L-arabinose as the sole carbon source. This arabinose biosensor expresses GFP only in the presence of L-arabinose. GFP emission intensity was higher in cells, which line the intra-colony channels compared with cells elsewhere within the biofilm, which shows that the channel structures have a higher concentration of L-arabinose compared with elsewhere within the biofilm. This provides evidence of a functional role in nutrient acquisition and transport for the intra-colony channel system.



novel and hitherto unseen structural aspect of *E. coli* macro-colony biofilms. This emergent functional property of biofilm growth enables nutrient acquisition and transport in these large microbial assemblages and was observed in every macro-colony examined by mesoscopy. Previous biofilm imaging studies have mainly used conventional widefield and laser-scanning microscopy to study biofilm architecture, which are inherently limited by sacrificing spatial resolution and imaging volume. For example, automated tile-scanning microscopes which change the location of the FOV or focal plane have been used to image growing colonies from  $1 \times 10^1$  to  $1 \times 10^4$  cells [39–41]; however, this method often requires long acquisition periods and results in tiling artefacts. With the Mesolens we negate the need for stitching and tiling when imaging multi-millimetre specimens and can image beyond small bacterial aggregates to visualise live bacterial macro-colonies in excess of  $1 \times 10^9$  cells while maintaining sub-micron resolution throughout the entire  $6 \text{ mm}^2$  field. Therefore, in comparison with other conventional large specimen imaging techniques, the Mesolens stands as a novel and improved method for in situ imaging of live bacterial communities. In addition, recent advances in light sheet microscopy [42] and multi-photon microscopy [43, 44] have been applied to biofilm imaging. However, these methods currently cannot resolve sub-micron information over multi-millimetre scales, as with the Mesolens. The same problem accompanies ultrasound [45, 46], optical coherence tomography and photoacoustic tomography [47–49] methods used for mesoscale biofilm imaging, where they cannot properly resolve structures on the order of which we report. We have also studied images of bacterial macro-colonies under a widely available conventional stereomicroscope. Careful comparison with Mesolens images suggests that traces of the channel may be faintly visible in spite of the low resolution of stereomicroscopes in  $x$ ,  $y$  and particularly  $z$  dimensions.

The structures we have identified bear similarities to some other aspects of bacterial community architecture, however it is important to note that the channels we identify are fundamentally different to structures. For example, the water irrigation channels discovered in mushroom-shaped *Pseudomonas* and *Klebsiella* spp. biofilms, which differ from intra-colony channels we observe by their location at the base of large submerged microbial aggregates and often limited to biofilms under flow conditions [31, 50]. There have also been channel-like structures identified in mature bacterial colonies, such as crenulation in *B. subtilis* macro-colonies [29, 30] or the macroscopic folds of *P. aeruginosa* biofilms [27, 28]. It is important to note, that crenulations and folds are all visible as surface structures of the colony and resolvable using photography techniques, whereas the intra-colony channels identified here are present within the

main body of the biofilm and are not observable by viewing the surface of the colony. A similar phenomenon was recently reported in colonies of *Proteus mirabilis* where 100-nm-diameter fluorescent microspheres were observed to penetrate the boundary of the colony through ‘crack-like conduits’ present at the colony edge [51]. However, the authors were unable to resolve any spatial evidence of the conduits themselves.

The spatial arrangement of the intra-colony channels is fractal in nature, with repeating patterns and complex topographies. Upon first glance, channels resemble fractal features found in multi-strain colonies, which form as a result of the mechanical instability between growth and viscous drag of dividing cells [19]. However, these features have only been reported in multi-strain colonies where the fractal dendrites have been composed of live, fluorescing cells [20–23, 52]. The spatial patterns we observe are different to those shown previously. First, the patterns we observe arise within a single population of cells where there are no strain-to-strain interactions to result in the formation of fractal patterns. Given that the intra-colony channels are not occupied by dead non-fluorescing cells (Fig. 2b) it is clear that the bacterial colonies used in this work are not composed of two pseudo-domains (i.e., viable and non-viable cells) which could interact to form complex 3D fractal patterning. Our finding that non-viable cells localise in the centre of the biofilm agrees with previous studies showing that dense microbial aggregates often have dense hypoxic, acidic centres which have diminished access to nutrients [11, 12, 43, 53–57].

The intra-colony channels form as an inherent property of biofilm formation, leading to fractal-like patterns that exhibit plasticity, which is reminiscent of the results of a classical eukaryotic developmental biology experiment by Moscona, where reformation of the channel architecture in marine sponges occurred after disaggregation by passage through a fine silk mesh [58, 59]. The ability of the channels to re-form also suggests that they fulfil a functional role in the context of biofilm biology.

In summary, we have identified a previously undocumented nutrient uptake system in colonial biofilms which challenges the current belief that cells which are out with the reach of underlying nutrient-rich medium are able to gain nutrients beyond diffusion through a homogenous mass of cells their exopolymeric matrix [14–17]. While we have observed these channel structures in several *E. coli* K-12 isolates, it is currently unknown if these channels are limited to only *E. coli* or if they are a widely conserved feature of large microbial aggregates. To assess this requires further study involving a number of phylogenetically diverse strains and subsequent investigation into factors such as cell shape, cell-surface interactions and division mechanics to determine the processes that guide channel

formation. Furthermore, quantitative analysis of these structures is made difficult by the large file size of Mesolens data (i.e., a full-volume three-channel image stack  $\approx 1.5$  TB). Consequently, these data are generally incompatible with most freely available image analysis programmes. Nevertheless, the presence of these channels may represent a route to acquire nutrients throughout complex environmental assemblages of organisms. Moreover, these channels may represent a route to circumvent the chemical protection and resistance phenotype of bacterial biofilms [60], such that rather than relying on antibiotics to penetrate biofilms by diffusion, it may be possible to exploit the intra-colony channels for delivery of antimicrobial agents. Although these observations were made under standard laboratory conditions, given the conserved structure of microbial communities in the environment, the occurrence of these channel structures may also be widespread under environmental conditions. The formation of these channels in the environment would also serve as a potential mechanism to explain how nutrient transport occurs in large microbial communities in nutrient limited conditions. This has yet to be explored in an environmental setting, however the findings presented here offer an overview of how to visualise and resolve these structures by means of optical mesoscopy. This could be further developed to help understand the ecological impact of our observations as the drivers of biofilm formation a natural context are poorly understood [61]. Aside from identifying and characterising intra-colony channels, this study has established the Mesolens as a much needed and powerful tool for studying microbial communities, and by extension could be applied to any aspect of microbial ecology, environmental biology and pathogen microbiology. Ultimately, the identification and characterisation of an intra-colony channel network could therefore have far-reaching applications while providing further understanding on the acquisition of nutrients by microbial communities.

**Acknowledgements** The authors would like to thank Lee McCann (formerly University of Strathclyde, UK) for his technical input with the Mesolens and help with initiating the experiments. In addition, we would like to thank Ainsley Beaton (University of Strathclyde, UK) for the kind gift of the JM105-miniTn7-*gfp* and JM105-miniTn7-*HeRed1* strains, and to Morgan Feeney (University of Strathclyde) for her advice on this manuscript. We also thank Nicola Holden and Jacqueline Marshall (James Hutton Institute, UK) for the kind gift of the pJM058 plasmid which contained the P<sub>BAD</sub>-*gfp* biosensor.

**Funding** This work was supported by the Medical Research Council (MR/K015583/1) and the Natural Environment Research Council (NE/M001415/1). LMR, WBA and GM were funded by the Medical Research Council (MR/K015583/1) and PAH was funded by the Natural Environment Research Council (NE/M001415/1).

**Author contributions** LMR conducted all experiments and analysed all data. LMR, WBA, PAH and GM were responsible for the

experimental design. LMR, WBA, PAH and GM prepared the manuscript.

## Compliance with ethical standards

**Conflict of interest** The authors declare that they have no conflict of interest.

**Publisher's note** Springer Nature remains neutral with regard to jurisdictional claims in published maps and institutional affiliations.

**Open Access** This article is licensed under a Creative Commons Attribution 4.0 International License, which permits use, sharing, adaptation, distribution and reproduction in any medium or format, as long as you give appropriate credit to the original author(s) and the source, provide a link to the Creative Commons license, and indicate if changes were made. The images or other third party material in this article are included in the article's Creative Commons license, unless indicated otherwise in a credit line to the material. If material is not included in the article's Creative Commons license and your intended use is not permitted by statutory regulation or exceeds the permitted use, you will need to obtain permission directly from the copyright holder. To view a copy of this license, visit <http://creativecommons.org/licenses/by/4.0/>.

## References

- Hobley L, Harkins C, MacPhee CE, Stanley-Wall NR. Giving structure to the biofilm matrix: an overview of individual strategies and emerging common themes. *FEMS Microbiol Rev*. 2015;39:649–69.
- Nadell CD, Drescher K, Foster KR. Spatial structure, cooperation and competition in biofilms. *Nat Rev Microbiol*. 2016;14:589.
- Flemming H-C, Wuertz S. Bacteria and archaea on Earth and their abundance in biofilms. *Nat Rev Microbiol*. 2019;17:247–60.
- Costerton JW, Cheng KJ, Geesey GG, Ladd TI, Nickel JC, Dasgupta M, et al. Bacterial biofilms in nature and disease. *Annu Rev Microbiol*. 1987;41:435–64.
- Bixler GD, Bhushan B. Biofouling: lessons from nature. *Philos Trans R Soc Math Phys Eng Sci*. 2012;370:2381–417.
- Chaves Simões L, Simões M. Biofilms in drinking water: problems and solutions. *RSC Adv*. 2013;3:2520–33.
- Percival SL, Suleman L, Vuotto C, Donelli G. Healthcare-associated infections, medical devices and biofilms: risk, tolerance and control. *J Med Microbiol*. 2015;64:323–34.
- Roberts AEL, Kragh KN, Bjarnsholt T, Diggle SP. The limitations of in vitro experimentation in understanding biofilms and chronic infection. *J Mol Biol*. 2015;427:3646–61.
- Carvalho G, Balestrino D, Forestier C, Mathias J-D. How do environment-dependent switching rates between susceptible and persister cells affect the dynamics of biofilms faced with antibiotics? *Npj Biofilms Microbiomes*. 2018;4:6.
- Costerton J. Introduction to biofilms. *Int J Antimicrob Agents*. 1999;11:217–21.
- Serra DO, Richter AM, Klauck G, Mika F, Hengge R. Micro-anatomy at cellular resolution and spatial order of physiological differentiation in a bacterial biofilm. *mBio*. 2013;4:e00103–13.
- Ghanbari A, Dehghany J, Schwebbs T, Mäskén M, Häussler S, Meyer-Hermann M. Inoculation density and nutrient level determine the formation of mushroom-shaped structures in *Pseudomonas aeruginosa* biofilms. *Sci Rep*. 2016;6:32097.
- Sheraton MV, Yam JKH, Tan CH, Oh HS, Mancini E, Yang L, et al. Mesoscopic energy minimization drives *Pseudomonas aeruginosa* biofilm morphologies and consequent stratification of

- antibiotic activity based on cell metabolism. *Antimicrob Agents Chemother.* 2018;62:e02544–17.
14. Libicki SB, Salmon PM, Robertson CR. The effective diffusive permeability of a nonreacting solute in microbial cell aggregates. *Biotechnol Bioeng.* 1988;32:68–85.
  15. Hunt SM, Werner EM, Huang B, Hamilton MA, Stewart PS. Hypothesis for the role of nutrient starvation in biofilm detachment. *Appl Environ Microbiol.* 2004;70:7418–25.
  16. Stewart PS. Diffusion in biofilms. *J Bacteriol.* 2003;185:1485–91.
  17. Guélon T, Mathias J-D, Deffuant G. Influence of spatial structure on effective nutrient diffusion in bacterial biofilms. *J Biol Phys.* 2012;38:573–88.
  18. Rudge TJ, Steiner PJ, Phillips A, Haseloff J. Computational modeling of synthetic microbial biofilms. *ACS Synth Biol.* 2012;1:345–52.
  19. Rudge TJ, Federici F, Steiner PJ, Kan A, Haseloff J. Cell polarity-driven instability generates self-organized, fractal patterning of cell layers. *ACS Synth Biol.* 2013;2:705–14.
  20. Blanchard AE, Lu T. Bacterial social interactions drive the emergence of differential spatial colony structures. *BMC Syst Biol.* 2015;9:59. <https://doi.org/10.1186/s12918-015-0188-5>.
  21. Smith WPJ, Davit Y, Osborne JM, Kim W, Foster KR, Pitt-Francis JM. Cell morphology drives spatial patterning in microbial communities. *Proc Natl Acad Sci.* 2017;114:E280–6.
  22. Goldschmidt F, Regoes RR, Johnson DR. Successive range expansion promotes diversity and accelerates evolution in spatially structured microbial populations. *ISME J.* 2017;11:2112.
  23. Jauffred L, Vejborg RM, Korolev KS, Brown S, Oddershede LB. Chirality in microbial biofilms is mediated by close interactions between the cell surface and the substratum. *ISME J.* 2017;11:1688.
  24. Eriksen RS, Svenningsen SL, Snepken K, Mitarai N. A growing microcolony can survive and support persistent propagation of virulent phages. *Proc Natl Acad Sci.* 2018;115:337–42.
  25. Xiao J, Hara AT, Kim D, Zero DT, Koo H, Hwang G. Biofilm three-dimensional architecture influences in situ pH distribution pattern on the human enamel surface. *Int J Oral Sci.* 2017;9:74–9.
  26. Liu J, Martinez-Corral R, Prindle A, Dong-yeon DL, Larkin J, Gabalda-Sagarra M, et al. Coupling between distant biofilms and emergence of nutrient time-sharing. *Science.* 2017;356:638–42.
  27. Kempes CP, Okegbe C, Mears-Clarke Z, Follows MJ, Dietrich LEP. Morphological optimization for access to dual oxidants in biofilms. *Proc Natl Acad Sci.* 2014;111:208–13.
  28. Jo J, Cortez KL, Cornell WC, Price-Whelan A, Dietrich LE. An orphan cbb3-type cytochrome oxidase subunit supports *Pseudomonas aeruginosa* biofilm growth and virulence. 2017;30:e30205.
  29. Wilking JN, Zaburdaev V, De Volder M, Losick R, Brenner MP, Weitz DA. Liquid transport facilitated by channels in *Bacillus subtilis* biofilms. *Proc Natl Acad Sci.* 2013;110:848–52.
  30. Asally M, Kittisopikul M, Rue P, Du Y, Hu Z, Cagatay T, et al. Localized cell death focuses mechanical forces during 3D patterning in a biofilm. *Proc Natl Acad Sci.* 2012;109:18891–6.
  31. Stoodley P, DeBeer D, Lewandowski Z. Liquid flow in biofilm systems. *Appl Environ Microbiol.* 1994;60:2711–6.
  32. McConnell G, Trägaardh J, Amor R, Dempster J, Reid E, Amos WB. A novel optical microscope for imaging large embryos and tissue volumes with sub-cellular resolution throughout. *eLife.* 2016;5:e18659.
  33. McConnell G, Amos WB. Application of the Mesolens for sub-cellular resolution imaging of intact larval and whole adult *Drosophila*. *J Microsc.* 2018;270:252–8.
  34. Schniete J, Franssen A, Dempster J, Bushell TJ, Amos WB, McConnell G. Fast optical sectioning for widefield fluorescence mesoscopy with the mesolens based on HiLo microscopy. *Sci Rep.* 2018;8:16259.
  35. Elbing KL, Brent R. Recipes and tools for culture of *Escherichia coli*. *Curr Protoc Mol Biol.* 2019;125:e83.
  36. Dempster J, Wokosin DL, McCloskey KD, Girkin JM, Gurney AM. WinFluor: an integrated system for the simultaneous recording of cell fluorescence images and electrophysiological signals on a single computer system. *Br J Pharm.* 2002;137:146.
  37. Lambertsen L, Sternberg C, Molin S. Mini-Tn7 transposons for site-specific tagging of bacteria with fluorescent proteins. *Environ Microbiol.* 2004;6:726–32.
  38. Schindelin J, Arganda-Carreras I, Frise E, Kaynig V, Longair M, Pietzsch T, et al. Fiji: an open-source platform for biological-image analysis. *Nat Methods.* 2012;9:676–82.
  39. Drescher K, Dunkel J, Nadell CD, van Teeffelen S, Grnja I, Wingreen NS, et al. Architectural transitions in *Vibrio cholerae* biofilms at single-cell resolution. *Proc Natl Acad Sci.* 2016;113:E2066–72.
  40. Yan J, Sharo AG, Stone HA, Wingreen NS, Bassler BL. *Vibrio cholerae* biofilm growth program and architecture revealed by single-cell live imaging. *Proc Natl Acad Sci.* 2016;113:E5337–43.
  41. Hartmann R, Singh PK, Pearce P, Mok R, Song B, Díaz-Pascual F, et al. Emergence of three-dimensional order and structure in growing biofilms. *Nat Phys.* 2019;15:251–6.
  42. Lagree K, Desai JV, Finkel JS, Lanni F. Microscopy of fungal biofilms. *Curr Opin Microbiol.* 2018;43:100–7.
  43. Xiao J, Hara AT, Kim D, Zero DT, Koo H, Hwang G. Biofilm three-dimensional architecture influences in situ pH distribution pattern on the human enamel surface. *Int J Oral Sci.* 2017;9:74–9.
  44. Thomsen H, Benkovics G, Fenyvesi É, Farewell A, Malanga M, Ericson MB. Delivery of cyclodextrin polymers to bacterial biofilms—an exploratory study using rhodamine labelled cyclodextrins and multiphoton microscopy. *Int J Pharm.* 2017;531:650–7.
  45. Shemesh H, Goertz DE, van der Sluis LWM, de Jong N, Wu MK, Wesslink PR. High frequency ultrasound imaging of a single-species biofilm. *J Dent.* 2007;35:673–8.
  46. Vaidya K, Osgood R, Ren D, Pichichero ME, Helguera M. Ultrasound imaging and characterization of biofilms based on wavelet de-noised radiofrequency data. *Ultrasound Med Biol.* 2014;40:583–95.
  47. Xi C, Marks D, Schlachter S, Luo W, Boppart SA. High-resolution three-dimensional imaging of biofilm development using optical coherence tomography. *J Biomed Opt.* 2006;11:034001.
  48. Wagner M, Taherzadeh D, Haisch C, Horn H. Investigation of the mesoscale structure and volumetric features of biofilms using optical coherence tomography. *Biotechnol Bioeng.* 2010;107:844–53.
  49. Leite de Andrade MC, Soares de Oliveira MA, Santos F, de AG, dos, Ximenes Vilela P, de B, et al. A new approach by optical coherence tomography for elucidating biofilm formation by emergent *Candida* species. *PLoS ONE.* 2017;12:e0188020.
  50. Drury WJ, Characklis WG, Stewart PS. Interactions of 1 µm latex particles with *Pseudomonas aeruginosa* biofilms. *Water Res.* 1993;27:1119–26.
  51. Xu H, Dauparas J, Das D, Lauga E, Wu Y. Self-organization of swimmers drives long-range fluid transport in bacterial colonies. *Nat Commun.* 2019;10:1792.
  52. Nuñez IN, Matute TF, Del Valle ID, Kan A, Choksi A, Endy D, et al. Artificial symmetry-breaking for morphogenetic engineering bacterial colonies. *ACS Synth Biol.* 2017;6:256–65.
  53. Wimpenny JWT, Coombs JP. Penetration of oxygen into bacterial colonies. *Microbiology.* 1983;129:1239–42.
  54. Peters AC, Wimpenny JWT, Coombs JP. Oxygen profiles in, and in the agar beneath, colonies of *Bacillus cereus*, *Staphylococcus albus* and *Escherichia coli*. *J Gen Microbiol.* 1987;133:1257–63.

55. Jeanson S, Flourey J, Gagnaire V, Lortal S, Thierry A. Bacterial colonies in solid media and foods: a review on their growth and interactions with the micro-environment. *Front Microbiol.* 2015;6:1284.
56. Hwang G, Liu Y, Kim D, Sun V, Aviles-Reyes A, Kajfasz JK, et al. Simultaneous spatiotemporal mapping of in situ pH and bacterial activity within an intact 3D microcolony structure. *Sci Rep.* 2016;6:32841.
57. Webb JS, Thompson LS, James S, Charlton T, Tolker-Nielsen T, Koch B, et al. Cell death in *Pseudomonas aeruginosa* biofilm development. *J Bacteriol.* 2003;185:4585–92.
58. Moscona AA. Aggregation of sponge cells: cell-linking macromolecules and their role in the formation of multicellular systems. *In Vitro.* 1967;3:13–21.
59. Lavrov AI, Kosevich IA. Sponge cell reaggregation: mechanisms and dynamics of the process. *Russ J Dev Biol.* 2014;45: 205–23.
60. Jolivet-Gougeon A, Bonnaure-Mallet M. Biofilms as a mechanism of bacterial resistance. *Drug Disco Today Technol.* 2014;11:49–56.
61. Oliveira NM, Martinez-Garcia E, Xavier J, Durham WM, Kolter R, Kim W, et al. Biofilm formation as a response to ecological competition. *PLoS Biol.* 2015;13:e1002191.